LBNL-40560
UC-410

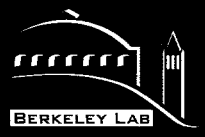

ERNEST ORLANDO LAWRENCE
BERKELEY NATIONAL LABORATORY

Atomic Holography with Electrons and X-rays: Theoretical and Experimental Studies

Patrick M. Len

Materials Sciences Division

June 1997

Ph.D. Thesis

LBNL-40560
UC-410

Atomic Holography with Electrons and X-rays: Theoretical and Experimental Studies

Patrick Michael Len
Ph.D. Thesis

Department of Physics
University of California, Davis

and

Materials Sciences Division
Ernest Orlando Lawrence Berkeley National Laboratory
University of California
Berkeley, CA 94720

June 1997

This work was supported in part by the Office of Naval Research under Contract Nos. N00014-90-5-1457 and N00014-94-1-0162, and by the Director, Office of Energy Research, Office of Basic Energy Sciences, Materials Sciences Division of the U.S. Department of Energy under Contract No. DE-AC03-76SF00098.

Atomic Holography with Electrons and X-rays: Theoretical and Experimental Studies

by

Patrick Michael Len

Patrick Michael Len
March 1997
Physics

Atomic Holography with Electrons and X-rays

Abstract

Gabor first proposed holography in 1948 as a means to experimentally record the amplitude and phase of scattered wavefronts, relative to a direct unscattered wave, and to use such a "hologram" to directly image atomic structure. But imaging at atomic resolution has not yet been possible in the way he proposed. Much more recently, Szöke in 1986 noted that photoexcited atoms can emit photoelectron or fluorescent x-ray wavefronts that are scattered by neighboring atoms, thus yielding the direct and scattered wavefronts as detected in the far field that can then be interpreted as holographic in nature. By now, several algorithms for directly reconstructing three-dimensional atomic images from electron holograms have been proposed (*e.g.* by Barton) and successfully tested against experiment and theory. Very recently, Tegze and Faigel, and Gog *et al.* have recorded experimental x-ray fluorescence holograms, and these are found to yield atomic images that are more free of the kinds of aberrations caused by the non-ideal emission or scattering of electrons. The basic principles of these holographic atomic imaging methods are reviewed, including illustrative applications of the reconstruction algorithms to both theoretical and experimental electron and x-ray holograms. We also discuss the prospects and limitations of these newly emerging atomic structural probes.

Acknowledgments

I would like to thank Professor Charles S. Fadley of the University of California, Davis, for the many years of advice, assistance, and support which made this work possible. I would also like to thank Drs. Ajith Kaduwela, Suntharampillai Thevuthasan for their guidance during the initial years of this work. Thanks to Drs. Jonathan Denlinger, Eli Rotenberg, for the use of their W(110) data collected at the Advanced Light Source beamline 7.0, and Yufeng Chen; and thanks to Drs. Thomas Gog, Gerd Materlik, Dmitri Novikov, and Rachel Eisenhower for their collaborative efforts in implementing Multiple Energy X-ray Holography at the National Synchrotron Radiation Lab at Brookhaven National Lab, and at the Hamburg Synchrotronstrahlungslabor at the Deutsches Elektronen-Synchrotron. Also thanks to my research peers Dr. Scott Ruebush, Dr. Ramon Ynzunza, and Feng Zhang for their advice, input, and camaraderie; Dr. N. R. Canon for ruminative non-physics discussions; and to my parents, my brother, and especially Dr. Fonda Glemba, for their love and understanding.

Research at UC-Davis was supported in part by the Office of Naval Research (Contract Nos. N00014-90-5-1457 and N00014-94-1-0162), by the Director, Office of Energy Research, Office of Basic Energy Sciences, Materials Sciences Division of the U. S. Department of Energy (Contract No. DE-AC03-76SF00098), the National Energy Research Supercomputer Center, and by the International Centre for Diffraction Data.

Table of Contents

Notation, Symbols, and Acronyms

$\mathbf{r}$	position vector in real space
$\mathbf{k}$	wavevector in reciprocal space
$\mathbf{r}'$	position vector in reconstruction space
$u(\mathbf{r})$	real object scattering field
$K(\mathbf{k},\mathbf{r})$	scattering convolution kernel
$A(\mathbf{k})$	scattered wave amplitude
$A_0(\mathbf{k})$	unscattered (reference) wave amplitude
$I(\mathbf{k})$	measured holographic intensity
$I_0(\mathbf{k})$	reference wave intensity
$\chi(\mathbf{k})$	normalized holographic intensity
$U(\mathbf{r}')$	reconstructed image intensity
$\kappa(\mathbf{k},\mathbf{r}')$	reconstruction deconvolution kernel
$f(\mathbf{k})$	scattering factor
k	wavenumber
δk	wavenumber interval
E	energy
δE	energy interval
XPD	X-ray Photoelectron Diffraction
LEED	Low-Energy Electron Diffraction
EEH	Electron Emission Holography
PH	Photoelectron Holography
SWIFT	Scattered Wave Included Fourier Transform
XFH	X-ray Fluorescence Holography
MEXH	Multiple Energy X-ray Holography

Useful Conversions

Electrons:

$$k\left[\text{Å}^{-1}\right] = 0.512365847\sqrt{E[eV]} \tag{i.1}$$

$$\lambda[\text{Å}] = \frac{12.264262}{\sqrt{E[eV]}} \tag{i.2}$$

Photons:

$$k\left[\text{Å}^{-1}\right] = \frac{E[eV]}{1973.2705} \tag{i.3}$$

$$\lambda[\text{Å}] = \frac{12,398.424}{E[eV]} \tag{i.4}$$

Miscellaneous

$$\hbar c\left[\text{eV}\cdot\text{Å}\right] = 1973.2705 \tag{i.5}$$

$$1,021,998.12E_{e^-}[eV] = E^2_{photons}[eV] \tag{i.6}$$

Chapter 1

Basic Principles of Atomic Holography

Abstract

We briefly review the application of Gabor holographic principles to the direct determination of atomic spatial information from photoexcited electron or x-ray diffraction patterns. The basic principles of generating holographic intensities and the numerical reconstruction of images are presented, along with an ideal simulated example. We then conclude with a general overview of this dissertation and the future work suggested by it.

Outline

1.1 Introduction

The elucidation of the atomic structure of condensed matter has long been a goal of crystallography, starting with the geometric investigation of crystalline facets and stacking planes; and proceeding to the modern implementations of x-ray diffraction [1.1]. However, due to the phase problem of conventional diffractometry, atomic positions cannot be directly determined from measuring only intensities, as the information contained in the relative phases between diffracted wavefronts is lost. However, structural information for non-trivial unit cell crystals can be determined from x-ray diffraction patterns by several methods, including pinning down phase information via heavy-ion or isomorphous group substitutions [1.2], and using so-called "direct methods," which

exploit single-scattering from the long-range order (Bragg planes) of a crystal in order to *analytically* extract phase information from relative peak intensities [1.3]. These x-ray diffraction methods are by now very highly developed, and, especially with the aid of high-brightness tunable-energy synchrotron radiation, they are routinely being used to determine atomic structures for many materials, including large macromolecules that can be synthesized as macroscopic single crystals. But the phase problem remains the key hurdle to be solved in order to be certain of obtaining a unique structure from the experimental data, and its solution often involves a complex process.

Likewise, the atomic structures near solid surfaces are often determined from low energy electron diffraction (LEED) [1.4], in which an electron beam instead of an x-ray beam impinges on the sample surface, and the intensities of Bragg-like beams are measured as a function of incident energy. This also is a very powerful structural probe, but it suffers from an *insoluble* phase problem, and the resultant need to compare experiment with multiple-scattering theory in order to determine atomic positions. In this dissertation, we consider two recent approaches for more directly dealing with the phase problem so as to determine local atomic structures more directly: photoelectron holography and x-ray fluorescence holography (with the latter being possible in two different modes).

Gabor outlined in 1948 a "direct method" of *experimentally* recording diffraction phases as well as intensities in an effort to surpass the then current resolution and lens aberration limits of electron microscopy [1.5]. In Gabor's original scheme, an electron wavefront (of wavenumber k_0 and wavelength $\lambda_0 = 2\pi / k_0$) diverging from a point focus illuminates an object as well as a detector (or image plate) directly. The interference pattern at this detector involves the wavefronts scattered by the object, and explicitly records the phases of these wavefronts relative to the direct or reference wavefront (Fig. 1.1(a)). This interference "hologram" thus contains spatial information about the scattering object, which can be retrieved as an image in several ways. Gabor suggested

that the developed image plate could be re-illuminated by a visible light reference wavefront (of wavenumber k and wavelength λ) as shown in Fig. 1.1(b). (Alternatively, the image reconstruction can also be performed numerically using a Fourier-transform-like integral, as first pointed out by Wolf [1.6].) The wavefronts diffracted by the image plate would create two virtual images of the original object visible to the naked eye, and magnified by a factor of $k_0 / k = \lambda / \lambda_0$. Note that since the three-dimensional information of the **r**-space object field $u(\mathbf{r})$ (shown in Fig. 1.1 as an optical mask of the letter "F") is "encoded" holographically into a single-wavenumber two-dimensional **k**-space diffraction pattern $\chi(\hat{\mathbf{k}})$, both a real and twin image of the optical mask are retrieved. This is due to the loss of spatial information perpendicular to the plane of the image plate recording the diffraction pattern [1.7], and is by now overcome in optical holography by recording a volume of holographic intensities by means of a thick recording medium [1.8]. Alternatively, one may record holograms at several wavenumbers that span a volume in **k**-space, as suggested more recently for photoelectron holography by Barton [1.9a].

We are by now all familiar with optical holography, which can produce three-dimensional images with ultimate resolutions at optical wavelengths, or in the 400-800 nanometer (nm) range. But what of imaging smaller objects with either x-rays or electrons as the probing beam? With the advent of synchrotron radiation sources of intense monoenergetic x-ray beams and field emission tips producing similarly well-defined electron beams, Gabor's holographic technique has by now enabled imaging with micrometer = 1000 nm down to $\approx$1 nanometer resolution. In 1952 Baez suggested that Gabor holograms can be formed using x-ray wavefronts [1.10]. Holograms of fabricated and biological samples have by now been recorded and imaged [1.11], and sub-100nm resolution of images has been achieved [1.7]. Also, electron Gabor holograms have been recorded with nanometer resolution to image atomic aggregates and even magnetic flux lines [1.12-1.14].

However, Gabor's goal of ultimately imaging at atomic resolutions in the 0.01-0.1nm (0.1-1.0Å) range had not been attained until recently, due to the lack of a source of sufficiently coherent x-rays or electrons at such short wavelengths. In 1986 Abraham Szöke observed that there is an atomic-scale analog of Gabor's holographic scheme: atoms that are photoexcited in one of their core levels can produce outgoing fluorescent x-ray or photoelectron wavefronts, which then reach a far field detector either directly, or after scattering off of neighboring atoms surrounding the emitter [1.15] (Figs. 1.2(a),(b). In the x-ray fluorescence process (Fig. 1.2(a)), the incident x-ray first excites a core electron to leave behind a core hole; this hole is then filled radiatively to produce a fluorescent x-ray which scatters from neighboring atoms to form the hologram. In the photoelectron emission process, the incident x-ray directly produces an outgoing photoelectron via the photoelectric effect, and this photoelectron scatters to form the hologram (Fig. 1.1(b)). X-ray fluorescence holography thus proceeds via a two-step process, whereas photoelectron holography is via one step. With a sub-Ångstrom source size and wavelength, the amplitudes and phases of such scattered wavefronts from atoms surrounding the emitter can be referenced to the directly emitted wavefront, thus eliminating the phase problem. It was also pointed out a little later by Barton [1.9a,b] and subsequently by Tong *et al.* [1.9c] that, by measuring diffraction patterns at several different wavenumbers, three-dimensional spatial information of the immediate neighborhood surrounding the emitter site could be completely encoded into a three-dimensional **k**-space volume of diffraction intensities $\chi(\mathbf{k})$, from which atomic images free of twin-image effects and other aberrations should be directly obtainable.

1.2 Creation of atomic holographic intensities

The process by which three-dimensional atomic image intensities are numerically reconstructed is to first measure the intensity $I(\mathbf{k})$ from a localized source of x-rays or electrons over some range of directions $\hat{\mathbf{k}} = \mathbf{k} / k$ and perhaps also some range of

wavenumbers k. Normalized holographic intensities $\chi(\mathbf{k})$ are then derived from either $[I(\mathbf{k})-I_0(\mathbf{k})]/\sqrt{I_0(\mathbf{k})}$ or $[I(\mathbf{k})-I_0(\mathbf{k})]/I_0(\mathbf{k})$, where $I(\mathbf{k})$ is the raw measured intensity, and $I_0(\mathbf{k})$ is the intensity that would be measured in the absence of atomic scattering; that is, $I_0(\mathbf{k})$ is the unperturbed intensity of the reference wave. The creation of holographic $I(\mathbf{k})$ and $\chi(\mathbf{k})$ intensities can be understood by first considering the holographic amplitudes $A(\mathbf{k})$ as created by atomic scattering to be a convolution of the **r**-space object field $u(\mathbf{r})$:

$$A(\mathbf{k}) = \iiint_R d^3\mathbf{r} \cdot K(\mathbf{k},\mathbf{r})u(\mathbf{r}), \tag{1.1}$$

where the convolution kernel $K(\mathbf{k},\mathbf{r})$ somehow describes the physics of the emission *and* atomic scattering of the photoexcited wavefronts, and R denotes the maximum radius in real space over which the object exists. This produces a three-dimensional $A(\mathbf{k})$ volume in **k**-space, so as to completely encode three-dimensional spatial information of the object field $u(\mathbf{r})$. Also, $A_0(\mathbf{k})$ is defined to be the far field amplitude that would be measured in the absence of scattering.

However, it is the intensity $I(\mathbf{k})$ (rather than the amplitude $A_0(\mathbf{k})+A(\mathbf{k})$) that is measured in a holographic experiment, and from which normalized holographic intensities $\chi(\mathbf{k})$ are then obtained:

$$\begin{aligned} I(\mathbf{k}) &\equiv |A_0(\mathbf{k}) + A(\mathbf{k})|^2 \\ &= A_0(\mathbf{k})^* A_0(\mathbf{k}) + A(\mathbf{k})^* A_0(\mathbf{k}) + A_0(\mathbf{k})^* A(\mathbf{k}) + A(\mathbf{k})^* A(\mathbf{k}) \\ &= I_0(\mathbf{k}) + A(\mathbf{k})^* A_0(\mathbf{k}) + A_0(\mathbf{k})^* A(\mathbf{k}) + A(\mathbf{k})^* A(\mathbf{k}). \end{aligned} \tag{1.2}$$

The first term is the intensity measured in the absence of scattering ($I_0(\mathbf{k}) \equiv |A_0(\mathbf{k})|^2$); the second and third terms are the holographic amplitudes $A(\mathbf{k})$ referenced to the direct wave $A_0(\mathbf{k})$, while the fourth term is the "self-hologram" term. In most cases $|A_0(\mathbf{k})| >> |A(\mathbf{k})|$

and thus the self-hologram term can be neglected; in particular, for electrons, the self-hologram is less than ≈10% of the holographic amplitudes [1.16], and for x-rays, it is 10^3 to 10^4 times smaller in relative importance.

For the purposes of this discussion, we shall take the normalized hologram intensity to be:

$$\chi(\mathbf{k}) = \frac{I(\mathbf{k}) - I_0(\mathbf{k})}{\sqrt{I_0(\mathbf{k})}}, \tag{1.3}$$

where $I_0(\mathbf{k}) \equiv |A_0(\mathbf{k})|^2$ is the intensity that would be measured in the absence of scattering. For the general system we are considering, then,

$$\begin{aligned}\chi(\mathbf{k}) &= \frac{[I_0(\mathbf{k}) + A_0^*(\mathbf{k})A(\mathbf{k}) + A^*(\mathbf{k})A_0(\mathbf{k})] - I_0(\mathbf{k})}{\sqrt{I_0(\mathbf{k})}} \\ &= \frac{A_0^*(\mathbf{k})A(\mathbf{k}) + A^*(\mathbf{k})A_0(\mathbf{k})}{|A_0(\mathbf{k})|}.\end{aligned} \tag{1.4(a)}$$

Without losing the generality of the above discussion, we can demand that the phase of the far-field amplitude $A_0(\mathbf{k})$ be real (*i.e.*, $A_0(\mathbf{k}) \equiv |A_0(\mathbf{k})|$). This will not in any way affect the holographic information contained in $\chi(\mathbf{k})$, as the phases of the scattered wave amplitudes $A(\mathbf{k})$ are all referenced *relative* to the phase of $A_0(\mathbf{k})$. Thus Eq. (1.4) becomes:

$$\begin{aligned}\chi(\mathbf{k}) &= \frac{|A_0(\mathbf{k})|A(\mathbf{k}) + A^*(\mathbf{k})|A_0(\mathbf{k})|}{|A_0(\mathbf{k})|} \\ &= A(\mathbf{k}) + A^*(\mathbf{k}) \\ &= \iiint_R d^3\mathbf{r} \cdot K(\mathbf{k},\mathbf{r})u(\mathbf{r}) + \iiint_R d^3\mathbf{r} \cdot K^*(\mathbf{k},\mathbf{r})u^*(\mathbf{r}).\end{aligned} \tag{1.4(b)}$$

which can be identified as the terms that will generate the real and twin images, respectively, after reconstruction.

1.3 Direct reconstruction of holographic atomic images

The **r**-space object field $u(\mathbf{r})$ can now be recovered as an image intensity $U(\mathbf{r}')$ in the **r'** image-space from the normalized holographic $\chi(\mathbf{k})$ intensities, by using a **k**-space deconvolution kernel $\kappa(\mathbf{k},\mathbf{r}')$ that is orthogonal to the scattering kernel $K(\mathbf{k},\mathbf{r})$, such that:

$$\iiint_K d^3\mathbf{k}\cdot\kappa^*(\mathbf{k},\mathbf{r}')K(\mathbf{k},\mathbf{r}) \propto \delta(\mathbf{r}-\mathbf{r}'), \tag{1.5(a)}$$

$$\iiint_K d^3\mathbf{k}\cdot\kappa^*(\mathbf{k},\mathbf{r}')K^*(\mathbf{k},\mathbf{r}) \approx 0, \tag{1.5(b)}$$

in order to recover the real image at $\mathbf{r}' = \mathbf{r}$, while suppressing the twin image at $\mathbf{r}' = -\mathbf{r}$. In fact, $\kappa(\mathbf{k},\mathbf{r}')$ need not be orthogonal to $K(\mathbf{k},\mathbf{r})$ everywhere in **k**-space, but only in the range measured in $\chi(\mathbf{k})$ (which can be quite limited in practice), and in the region $|\mathbf{r}| \le R$ surrounding the emitter, which is usually limited by the sampling density of $\chi(\mathbf{k})$ [1.17]. Once such a sufficient $\kappa(\mathbf{k},\mathbf{r}')$ deconvolution kernel is known, the $U(\mathbf{r}')$ object field can be recovered using a **k**-space deconvolution of $\chi(\mathbf{k})$:

$$\begin{aligned}
U(\mathbf{r}') &\equiv \iiint_K d^3\mathbf{k}\cdot\kappa^*(\mathbf{k},\mathbf{r}')\chi(\mathbf{k}) \\
&= \iiint_K d^3\mathbf{k}\cdot\kappa^*(\mathbf{k},\mathbf{r}')\left[\iiint_R d^3\mathbf{r}\cdot K(\mathbf{k},\mathbf{r})u(\mathbf{r}) + \iiint_R d^3\mathbf{r}\cdot K^*(\mathbf{k},\mathbf{r})u^*(\mathbf{r})\right] \\
&= \iiint_R d^3\mathbf{r}\cdot u(\mathbf{r})\left[\iiint_K d^3\mathbf{k}\cdot\kappa^*(\mathbf{k},\mathbf{r}')K(\mathbf{k},\mathbf{r})\right] \\
&\qquad + \iiint_R d^3\mathbf{r}\cdot u^*(\mathbf{r})\left[\iiint_K d^3\mathbf{k}\cdot\kappa^*(\mathbf{k},\mathbf{r}')K^*(\mathbf{k},\mathbf{r})\right] \\
&= \iiint_R d^3\mathbf{r}\cdot u(\mathbf{r})\delta(\mathbf{r}-\mathbf{r}') + 0 \\
&= u(\mathbf{r}').
\end{aligned} \tag{1.6}$$

Thus as long as the scattering process can be well-described by a model convolution kernel $K(\mathbf{k},\mathbf{r})$, then a reconstruction kernel $\kappa(\mathbf{k},\mathbf{r}')$ that satisfies the orthogonality condition (Eqs. 1.5(a)-(b)) can in principle be deduced.

1.4 Basic holographic atomic image reconstruction algorithm

The basic algorithms used in reconstructing atomic holographic images can be understood in the context of a single-scattering (or kinematical) model of point-like scatterers. In such a simple model, the object field becomes:

$$u(\mathbf{r}) = \sum_j \delta(\mathbf{r} - \mathbf{a}_j), \tag{1.7}$$

where the summation is over each of the *j*th scattering sites in the model cluster. The convolution kernel for the scattering process can be expressed as [1.18]:

$$K(\mathbf{k},\mathbf{r}) = \frac{f(\Theta_r^{\mathbf{k}})}{kr} e^{i(\mathbf{k}\cdot\mathbf{r}-kr)}. \tag{1.8}$$

Here e^{-ikr}/kr represents the photoexcited electron or x-ray wavefront that illuminates the (point-like) scattering atoms surrounding the emitter (which is here assumed to emit isotropically for simplicity), $f(\Theta_r^{\mathbf{k}})$ is the complex plane-wave atomic scattering factor ($\equiv |f(\Theta_r^{\mathbf{k}})|\exp[i\psi(\Theta_r^{\mathbf{k}})]$), where $\Theta_r^{\mathbf{k}}$ is the scattering angle, and $\mathbf{k}\cdot\mathbf{r}$ is the additional phase shift of the scattered portion of this wavefront as it reaches the far field detector (Fig. 1.3). Thus the total geometrical path length difference phase between the reference and scattered wavefronts is ($\mathbf{k}\cdot\mathbf{r}$ - kr). This choice for $K(\mathbf{k},\mathbf{r})$ does not include any allowance for anisotropy in magnitude or phase of the outgoing reference wave, which for the simple example of *s*-level photoemission, take the form of an additional factor of $\boldsymbol{\varepsilon}\cdot\mathbf{k}$, where $\boldsymbol{\varepsilon}$ is the polarization vector of the radiation [1.18-1.19]. Thus, in photoemission, reference

wave anisotropy is almost always present. However, for the case considered here of Kα x-ray fluorescence, the outgoing reference wave should be isotropic and randomly polarized, and thus be well described by Eq. (1.8).

Thus in this model, the normalized holographic intensities (Eq. 1.4(b)) becomes:

$$\begin{aligned}\chi(\mathbf{k}) &= \iiint_R d^3\mathbf{r}\cdot K(\mathbf{k},\mathbf{r})u(\mathbf{r}) + c.c. \\ &= \iiint_R d^3\mathbf{r}\cdot \frac{f(\Theta_{\mathbf{r}}^{\mathbf{k}})}{kr} e^{i(\mathbf{k}\cdot\mathbf{r}-kr)} \sum_j \delta(\mathbf{r}-\mathbf{a}_j) + c.c. \\ &= \sum_j \frac{f(\Theta_{\mathbf{a}_j}^{\mathbf{k}})}{ka_j} e^{i(\mathbf{k}\cdot\mathbf{a}_j - ka_j)} + c.c. \end{aligned} \qquad (1.4(c))$$

Another simplifying advantage of x-rays lies in the nature of $f(\Theta_{\mathbf{r}}^{\mathbf{k}})$. Figure 1.4 shows the magnitudes and phases of Ni atomic scattering factors for both x-rays and electrons with wavelength $\lambda = 0.79\text{Å}$ (or wavenumber $k = 8.0\text{Å}^{-1}$). Note that the x-ray scattering factors (Fig. 1.4(a)) are much weaker and more nearly constant in magnitude than those for electrons (Fig. 1.4(b)), and that the scattering phase shifts for x-rays are also much smaller and more nearly constant than those for electrons. Thus, for x-rays $|f(\Theta_{\mathbf{r}}^{\mathbf{k}})| \approx \text{constant} = f_0$, and $\psi(\Theta_{\mathbf{r}}^{\mathbf{k}}) \approx \psi_0 \approx 0$, such that the simplest possible optical scattering kernel results: $K_O(\mathbf{k},\mathbf{r}) \propto e^{i(\mathbf{k}\cdot\mathbf{r}-kr)}$. The reconstruction kernel that is most simply orthogonal to this optical scattering kernel is thus $\kappa_O(\mathbf{k},\mathbf{r}') \equiv e^{i(\mathbf{k}\cdot\mathbf{r}'-kr')}$, as first suggested by Barton and Terminello [1.9b]. Thus for the scattering of fluorescent x-rays, the reconstruction algorithm of Eq. (1.6) becomes to a good approximation:

$$U_A(\mathbf{r}') \equiv \iiint_K d^3\mathbf{k}\cdot e^{-i(\mathbf{k}\cdot\mathbf{r}'-kr')}\chi(\mathbf{k}). \qquad (1.9)$$

In actually displaying an image, we finally take the absolute value of this quantity: $|U_A(\mathbf{r}')|$; the same will be true for other imaging algorithms to follow. This first simple optical reconstruction algorithm (which we will denote as Method A) has been used

recently to obtain direct atomic images from experimental single energy [1.20,1.21] and multiple energy [1.22,1.23] x-ray holographic data sets. And it has also been used with some success in analyzing photoelectron holographic data, as we illustrate for both theoretical simulations and experimental data in the following chapters.

For example, Fig. 1.1(c) shows the optical $\chi(\mathbf{k})$ holographic intensities that were numerically calculated from the transparent "F" mask using Eqs. (1.4) and (1.7)-(1.8). Shown here is the hologram for only one wavenumber (k), but the calculations were carried out over a range of different directions ($\hat{\mathbf{k}}$) and ten different wavenumbers (k) spanning the volume $k_x \times k_y \times k_z = 0.7k_0 \times 0.7k_0 \times 0.03k_0$. Figure 1.1(d) shows the numerically reconstructed real and twin images obtained from the $\chi(\mathbf{k})$ of Fig. 1.1(c). Due to the three-dimensional spatial information that was encoded in the **k**-space volume encompassed by $\chi(\mathbf{k})$, the reconstruction algorithm of Eq. (1.9) suppresses the spurious twin image, while increasing the fidelity of the desired real image (*cf.* Fig. 1.1(b)).

The optical reconstruction algorithm of Method A (Eq. (1.9)) has also been used to reconstruct data from electron holographic data sets, *e.g.* from photoelectron diffraction [1.24-1.28]. However, because of the generally anisotropic nature of the photoemitted source wave, and the strong, non-optical and often multiple nature of electron scattering, the single-scattering optical convolution kernel $K_O(\mathbf{k},\mathbf{r}') \propto e^{i(\mathbf{k}\cdot\mathbf{r}'-kr')}$ does not accurately describe the process by which electron holograms are produced, and consequently this optical reconstruction kernel will not satisfy the orthogonality condition (Eq. (1.5)) for electrons in general. Thus Eq. (1.8), when applied to electron holograms, often results in images which suffer from aberrations and position shifts [1.29-1.32], a point to which we return later in this dissertation.

Various modifications have been made to the basic optical reconstruction algorithm of Method A (Eq. 1.9), and to the definition of the reconstruction integral (Eq. (1.6)) itself [1.33-1.37], in order to account for the non-optical nature of electron scattering, of which four methods will be discussed here. The first of these, which we will

call Method $\tilde{A}$ is a straightforward attempt to remove the effects of the complex electron scattering factor $f(\Theta^{\mathbf{k}}_{\mathbf{r}'})$ by dividing it out in the transform kernel. This has been termed the "Scattered-Wave Included Fourier Transform" (SWIFT) by Tonner *et al.* [1.33], and it can be written as:

$$U_{\tilde{A}}(\mathbf{r}') \equiv \iiint_K d^3\mathbf{k} \cdot \frac{e^{-i(\mathbf{k}\cdot\mathbf{r}'-kr')}}{f(\Theta^{\mathbf{k}}_{\mathbf{r}'})} \chi(\mathbf{k}). \tag{1.10}$$

Another direct method (Method B) proposed by Tong and co-workers [1.34a], and Wu and Lapeyre [1.34b], has been to recognize that the atomic backscattering region for electrons is approximately optical in nature. That is, for scattering angles not too far from 180°, both $|f(\Theta^{\mathbf{k}}_{\mathbf{r}})|$ and $\psi(\Theta^{\mathbf{k}}_{\mathbf{r}})$ are very nearly constant, conditions which minimize their contributions to image aberrations [1.34]; this is clearly seen in the curves for Ni in Fig. 1.4. Therefore only small-solid-angle $\chi(\mathbf{k})$ windows centered on backscattering directions are used in imaging backscattering atoms in the transform of Eq. (1.9). The atomic image intensity obtained is given by:

$$U_B(\mathbf{r}') \equiv \iiint_K d^3\mathbf{k} \cdot e^{-i(\mathbf{k}\cdot\mathbf{r}'-kr')} w(\alpha, \Theta^{\mathbf{k}}_{-\mathbf{r}'}) \chi(\mathbf{k}). \tag{1.11}$$

where $w(\alpha, \Theta^{\mathbf{k}}_{-\mathbf{r}'})$ is a window function that has value of unity inside the cones of half-angle α (typically $\approx 30°$) centered on the reconstruction axis $-\mathbf{r}'$, and is zero everywhere else. Since holographic information describing forward scattering atoms (if they are present) is also included in this region in $\mathbf{k}$-space, they can also in principle be imaged, even though atomic forward scattering is less optical-like. This reconstruction method may seem less direct than that of Method A in that one needs to know *a priori* the cone half-angle α of the backscattering region where scattering phase shifts are approximately constant. However, this α can easily be determined with no prior knowledge of the

scattering nature of the system being imaged, for example, by the trial-and-error method of closing α from the full angular $\chi(\mathbf{k})$ range, until the reconstructed atomic images of backscatterers ceases to change in position.

More recently, an imaging algorithm that recognizes the complete quantum mechanical nature of photoelectron propagation and scattering (here, Method C) has been proposed by Rous and Rubin [1.35]. In the first Born approximation, this method can be related to the imaging algorithm of Method A by:

$$U_C(\mathbf{r}') \equiv \frac{d}{dr'}\left[r' \cdot \mathrm{Re}\left[\iiint_K d^3\mathbf{k} \cdot e^{-i(\mathbf{k}\cdot\mathbf{r}'-kr')}\chi(\mathbf{k})\right]\right]. \tag{1.12}$$

This form suggests that this method will reduce the relative importance of near-origin ($r \approx 0$) signals imaged by Method A, while emphasizing images more distant from the emitter. However, the two terms present in the derivative in r makes this less conclusive.

The final reconstruction algorithm (Method D) considered here is due to Hoffman and Schindler [1.36], and is not strictly speaking holographic in nature. But it also is a so-called "direct method" for analyzing photoelectron diffraction data so as to in a single step estimate the atomic positions, usually of backscattering atoms under adsorbates. Its form is given by:

$$U_D(\mathbf{r}') = \sum_{\hat{\mathbf{k}}} \Delta\sigma_{\hat{\mathbf{k}}} \exp\left[r' \cdot \int_k dk \cdot \chi_{theory}(\mathbf{k},\mathbf{r}')\chi(\mathbf{k})\right], \tag{1.13}$$

where $\chi_{theory}(\mathbf{k},\mathbf{r}')$ is calculated via a single-scattering model:

$$\chi_{theory}(\mathbf{k},\mathbf{r}') = \mathrm{Re}\left[\frac{e^{i(kr'-\mathbf{k}\cdot\mathbf{r}')}}{kr'} f(\Theta^{\mathbf{k}}_{\mathbf{r}'})\right]. \tag{1.14}$$

Thus Eq. (1.13) is a redefinition of the deconvolution integral of Eq. (1.6), but it still relies on the orthogonality of a theoretically calculated single-scattering model $\chi_{theory}(\mathbf{k},\mathbf{r}')$ with the experimental $\chi(\mathbf{k})$, whose exponentiated dot product over **k**-space as defined above will produce image intensity peaks at atomic positions. This method inherently assumes individual scans of intensity with photon energy over the range k of the integral, and then a coarse sum over directions $\hat{\mathbf{k}}$, as weighted ideally by the solid angle $\Delta\sigma_{\hat{\mathbf{k}}}$ each subtends.

In summary, atomic resolution holography can in principle be done using localized sources of either fluorescent x-rays or photoelectrons, but the atomic scattering of x-rays is most nearly ideal, and this suggests that a simple optical reconstruction kernel as in Eq. (1.9) can be straightforwardly used to directly obtain atomic images from holographic x-ray intensities. This simple kernel will also be seen to successfully image some atoms using photoelectron holographic data. However, more sophisticated reconstruction kernels and deconvolution integrals will probably be necessary in the future to account for the non-ideal nature of the propagation and scattering of photoelectrons and thus obtain the most accurate atomic images from holographic electron intensities. This dissertation explores the applications of these methods to both electron and x-ray holography.

1.5 Dissertation Overview

The next chapter (Chapter 2) discusses the FORTRAN77 implementation of the algorithms that generate, normalize, and reconstruct images from holographic diffraction data.

Chapters 2-5 consider various aspects of photoelectron holography, including the optimum type of **k**-space sampling density to use for a given problem and with a specific choice of imaging algorithm. The various algorithms proposed to date are applied to various theoretical data sets, and to a very large experimental data set recently obtained at the Advanced Light Source by Denlinger, Rotenberg, *et al.* [1.38].

Chapter 3 demonstrates the effects on the fidelity of atomic images reconstructed via Methods A and B of using different **k**-space sampling densities in theoretical single-scattering holographic Cu(001) photoelectron diffraction data. We thus address here the minimum number of data points (and thus the minimum experimental time) that needs to be taken in order to achieve accurate atomic imaging.

Chapter 4 compares the fidelity of atomic images reconstructed via Methods A, B, C, and D as based on different **k**-space sampling densities in theoretical single-scattering holographic photoelectron diffraction data calculated for Cu-Ni pentamers and Cu/Ni(001) clusters. The advantages and disadvantages of the different methods are discussed.

Chapter 5 deals with experimental data, and compares images reconstructed from experimental and theoretical single and multiple scattering models for surface and bulk atom emission from W(110) via Methods A, $\tilde{A}$, B, C, and D. This is a "model" next-generation data set.

Chapters 6-8 deal with the much more newly demonstrated technique of x-ray fluorescence holography, in some cases comparing it as to advantages and disadvantages with photoelectron holography.

Due to the more ideal scattering nature of x-rays compared to electrons, the advantages of reconstructed images from x-ray fluorescent holograms (XFH) relative to holographic photoelectron diffraction data are discussed in Chapter 6, along with theoretical modeling aimed at assessing concerns involving the experimental implementation of XFH. In particular, the degree of statistical accuracy necessary to adequately image near-neighbor atoms is assessed, and this is directly related to the time duration of potential experiments of this type. Limitations associated with the fact that XFH as shown in Fig. 1(a) can be performed at one (or at most a few) wavenumbers are also considered.

A second x-ray holographic method is the optical reciprocal (or time-reversed) case of XFH, as shown in Fig. 1.2(c). This method makes use of scattering by the incident

beam to produce variations in the local field strength at a certain fluorescence emitter, with the angle-integrated fluorescence intensity now being used only to monitor this field strength as a function of incidence direction. This method has been termed multiple energy x-ray holography (MEXH), and it makes it possible to record x-ray holograms at several different wavenumbers so as to acquire a full volume of holographic **k**-space intensities. The two different x-ray holographic methods are further illustrated in Fig. 1.5. The atomic images experimentally obtainable via XFH and MEXH from a model cluster of Fe(001) are demonstrated using single scattering model holographic x-ray data in Chapter 7.

Chapter 8 explores the effect of the polarization of the incident radiation on atomic images reconstructed from experimental and theoretical data sets for $\alpha - Fe_2O_3(001)$. This is in fact the first experimental data for MEXH to be published. Polarization has a major influence on MEXH data via the Thomson scattering cross section as it affects the incident x-ray beam or reference wave.

Finally, Chapter 9 concludes with a discussion of the prospects and limitations of atomic holography with electrons and x-rays.

References

[1.1] *Historical Atlas of Crystallography,* J. Lima-de-Faria, ed., The International Union of Crystallography (Kluwer Academic Publishers, Dordrecht, 1990).

[1.2] T. L. Blundell and L. N. Johnson, *Protein Crystallography* (New York: Academic Press, 1976), 136.

[1.3] J. Karla and H. A. Hauptmann, Acta Crys. **3** (1950) 18.

[1.4] M.A. Van Hove and S.Y. Tong, eds., *Surface Crystallography by LEED* (Springer-Verlag, New York, 1979).

[1.5] D. Gabor, Nature (London) **161** (1948) 777.

[1.6] E. Wolf, Opt. Comm. **1** (1969) 153, and J. Opt. Soc. Am. **60** (1970) 18.

[1.7] C. Jacobsen, M. Howells, J. Kirz, and S. Rothman, J. Opt. Soc. Am. A 7 (1990) 1847.

[1.8] R. R. A. Syms, *Practical Volume Holography* (Oxford: Clarendon Press, 1990) 21.

[1.9] (a) J. J. Barton, Phys. Rev. Lett. **61** (1988) 1356, and Phys. Rev. Lett. **67** (1991) 3106. (b) J. J. Barton and L. J. Terminello, paper presented at the Third International Conference on the Structure of Surfaces, Milwaukee, July 1990, and in *Structure of Surfaces III,* S. Y. Tong, M. A. Van Hove, X. Xide, and K. Takanayagi, eds., (Springer Verlag, Berlin 1991), 107. (c) S. Y. Tong, H. Huang, and C. M. Wei, Phys. Rev. B **46** (1992) 2452, and references therein.

[1.10] A. V. Baez, J. Opt. Soc. Am. **42** (1952) 756.

[1.11] (a) C. Jacobsen, in *X-ray Microscopy in Biology and Medicine,* K. Shinohara, K. Yada, H. Kihara, and T. Saito, eds. (Japan Scientific Societies Press, Tokyo, 1990) 167. (b) S. Lindaas, M. Howells, C. Jacobsen, and A. Kalinovsky, J. Opt. Soc. Am. A **13** (1996) 1788.

[1.12] (a) A. Tonomura, ed., *Electron Holography,* Springer Series in Optical Sciences, Vol. 70 (Springer-Verlag, Berlin, 1993). (b) A. Tonomura, Phys. World **7** (1994) 39, and references therein.

[1.13] H. Schmid, H.-W. Fink, and J. Kreuzer, J. Vac. Sci. Technol. B **13** (1995) 2428, and references therein.

[1.14] A. Orchowski, W. D. Rau, and H. Lichte, Phys. Rev. Lett. **74** (1995) 399, and references therein.

[1.15] A. Szöke, in *Short Wavelength Coherent Radiation: Generation and Applications,* T. Attwood and J. Boker, eds., AIP Conference Proceedings No. 147, (AIP, New York, 1986) 361.

[1.16] S. Thevuthasan, G. S. Herman, A. P. Kaduwela, R. S. Saiki, Y. J. Kim, W. Niemczura, M. Burger, and C. S. Fadley, Phys. Rev. Lett. **67** (1991) 469.

[1.17] P. M. Len, S. Thevuthasan, A. P. Kaduwela, M. A. Van Hove, and C. S. Fadley, Surf. Sci. **365** (1996) 535.

[1.18] C. S. Fadley, in *Synchrotron Radiation Research: Advances in Surfaces and Interface Science*, R. Z. Bachrach, ed., (Plenum Press, New York, 1992). (b) D. J. Friedman, C. S. Fadley, J. Electron Spec. Relat. Phenom. **51** (1990) 689.

[1.19] D. K. Saldin, G. R. Harp, and B. P. Tonner, Phys. Rev. B **45** (1992) 9629.

[1.20] M. Tegze, and G. Faigel, Europhys. Lett **16** (1991) 41.

[1.21] M. Tegze, and G. Faigel, Nature **380** (1996) 49.

[1.22] T. Gog, P. M. Len, G. Materlik, D. Bahr, C. Sanchez-Hanke, and C. S. Fadley, Phys. Rev. Lett. **76** (1996) 3132.

[1.23] T. Gog, R.-H. Menke, F. Arfelli, P. M. Len, C. S. Fadley, and G. Materlik, Synch. Rad. News **9** (1996) 30.

[1.24] (a) B. L. Petersen, L. J. Terminello, J. J. Barton, and D. A. Shirley, J. Electron Spec. Relat. Phenom. **75** (1995) 229, and references therein. (b) H. Wu, G. J. Lapeyre, H. Huang, and S. Y. Tong, Phys. Rev. Lett. **71** (1993) 251, and references therein. (c) M. Zharnikov, M. Weinelt, P. Zebisch, M. Stichler, and H.-P. Steinrück, Surf. Sci. **334** (1995) 114, and references therein. (d) R. Denecke, R. Eckstein, L. Ley, A. E. Bocquet, J. D. Riley, and R. C. G. Leckey, Surf. Sci. **331-333** (1995) 1085. (e) J. G. Tobin, G. D. Waddill, H. Hi, and S. Y. Tong, Surf. Sci. **334** (1995) 263, and references therein.

[1.25] (a) H. Li, S. Y. Tong, D. Naumovic, A. Stuck, and J. Osterwalder, Phys. Rev. B **47** (1993) 10036. (b) D. K. Saldin, G. R. Harp, and X. Chen, Phys. Rev. B **48** (1993) 8234, and references therein.

[1.26] (a) Z.-L. Han, S. Hardcastle, G. R. Harp, H. Li, X.-D. Wang, J. Zhang, and B. P. Tonner, Surf. Sci. **258** (1991) 313, and references therein. (b) I. H. Hong, S. C. Shyu, Y. C. Chou, and C. M. Wei, Phys. Rev. B **52** (1995) 16884, and references therein.

[1.27] (a) M. A. Mendez, C. Glück, J. Guerrero. P. L. de Andres, K. Heinz, D. K. Saldin, and J. B. Pendry, Phys. Rev. B **45** (1992) 9402, and references therein. (b) C. M. Wei, S. Y. Tong, H. Wedler, M. A. Mendez, and K. Heinz, Phys. Rev. Lett. **72** (1994) 2434, and references therein.

[1.28] S. Y. Tong, H. Huang, and X. Q. Guo, Phys. Rev. Lett. **69** (1992) 3654.

[1.29] P. M. Len, S. Thevuthasan, C. S. Fadley, A. P. Kaduwela, and M. A. Van Hove, Phys. Rev. B **50** (1994) 11275.

[1.30] D. K. Saldin, G. R. Harp, B. L. Chen, and B. P. Tonner, Phys. Rev. B **44** (1991) 2480.

[1.31] S. Thevuthasan, G. S. Herman, A. P. Kaduwela, T. T. Tran, Y. J. Kim, R. S. Saiki, and C. S. Fadley, J. Vac. Sci. Technol. A **10** (1992) 2261.

[1.32] P. Hu and D. A. King, Phys. Rev. B **46** (1992) 13615.

[1.33] (a) B. P. Tonner, Z.-L. Han, G. R. Harp, and D. K. Saldin, Phys. Rev. B **43** (1991) 14423. (b) D. K. Saldin, K. Reuter, P. L. De Andres, H. Wedler, X. Chen, J. B. Pendry, and K. Heinz, Phys. Rev. B **54** (1996) 8172.

[1.34] (a) S. Y. Tong, H. Li, and H. Huang, Phys. Rev. B **51** (1995) 1850. (b) H. Wu and G. J. Lapeyre, Phys. Rev B **51** (1995) 14549.

[1.35] P. J. Rous and M. H. Rubin, Surf. Sci. **316** (1994) L1068.

[1.36] P. Hofmann, K.-M. Schindler, V. Fritzsche, S. Bao, A. M. Bradshaw, and D. P. Woodruff, J. Vac. Sci. Tech. A. **12** (1994) 2045, Surf. Sci. **337** (1995) 169, and references therein.

[1.37] X. Chen and D. K. Saldin, Phys. Rev. B **50** (1994) 17463.

[1.38] P. M. Len, J. D. Denlinger, E. Rotenberg, S. Kevan, B. P. Tonner, and C. S. Fadley, to be submitted to Phys. Rev. B.

Figure captions

Figure 1.1. (a)-(b) An idealized numerical demonstration of the creation and inversion of single-wavenumber optical Gabor in-line holograms. (a) A point source of coherent radiation of wavelength λ_0 at the origin illuminates a transparent mask with point scatterers creating the letter "F" and spanning some coordinate space **r**, as well as an image plate. This image plate is then exposed by a direct wavefront, as well as by the wavefronts scattered by the mask, which in their coherent superposition produce a holographic interference pattern. (b) The developed image plate is later re-illuminated by a reference wavefront of wavelength λ. The wavefronts diffracted by the image plate produces a virtual (real) image of the mask at positions **r**, and a virtual conjugate twin image at the inverse positions **-r**. (c)-(d) An analogous demonstration of the creation and inversion of optical multiple wavenumber holograms. (c) A multiple wavenumber normalized $\chi(\mathbf{k})$ hologram data set (of which only one wavenumber is shown) is calculated from the object field $u(\mathbf{r})$ by means of an **r**-space convolution, using a kernel $K(\mathbf{k},\mathbf{r})$ that describes the emission and scattering physics involved (here, optical scattering in the far-field regime). (d) The object field $u(\mathbf{r})$ is recovered as an image intensity $U(\mathbf{r}')$ by a **k**-space deconvolution of $\chi(\mathbf{k})$, using a kernel $\kappa(\mathbf{k},\mathbf{r}')$ that is sufficiently orthogonal to $K(\mathbf{k},\mathbf{r})$ (in fact, the optical kernel of Eq. (1.9)). Note that the conjugate twin image $U(\mathbf{r}'=-\mathbf{r})$ has been suppressed, due to the volume of **k**-space enclosed in the multiple wavenumber $\chi(\mathbf{k})$ considered here.

Figure 1.2. Atomic-scale analogs of Gabor holography. (a) The first scheme suggested by Szöke [1.15] for x-ray fluorescence holography (XFH), in which an excitation x-ray first creates an inner-shell hole in one of many equivalent fluorescing atoms, and this atom then emits fluorescent x-ray wavefronts that illuminate neighboring atoms, as well as a far field detector. This detector senses the interference between the direct wavefront, and wavefronts scattered by the neighboring atoms. Moving the detector over a large solid-

angle range builds up a holographic interference pattern. (b) Analogous to (a), but for the single-step process of core-level photoelectron emission. Here, the scattering of the outgoing photoelectron produces the hologram, and it is recorded in the same manner as in x-ray fluorescence holography. (c) Multiple energy x-ray holography (MEXH), the time-reversed case of (a), as suggested by Gog *et al.* [1.22], where a coherent far field excitation x-ray illuminates and photoexcites an emitter, but also scatters from atoms neighboring the emitter in passing to it. The emitting atom senses the interference between the direct wavefront and wavefronts elastically scattered by the neighboring atoms. The net photoexcitation strength is then detected by a stationary, large solid-angle detector. Moving the far field source over a large solid-angle range builds up a holographic interference pattern. In all three of the cases shown here, atomic images can be reconstructed numerically.

Figure 1.3. Scattering geometry between a photoemitter and a neighboring scattering atom. The photoemitter is placed at the origin, while the neighboring scatterer is located at the relative position **r**. The far field detector lies in the direction **k**. The portion of the direct wavefront that is scattered by the neighboring atom into the detector at **r** depends on the scattering angle $\Theta_{\mathbf{r}}^{\mathbf{k}}$ between **r** and **k**.

Figure 1.4. Ni scattering factor magnitudes ($|f(\Theta_{\mathbf{r}}^{\mathbf{k}})|$) and phases ($\psi(\Theta_{\mathbf{r}}^{\mathbf{k}})$), as a function of scattering angle $\Theta_{\mathbf{r}}^{\mathbf{k}}$ for (a) x-rays at $k = 8.0\text{Å}^{-1}$ ($E = 15.79\text{keV}$. (b) electrons at $k = 8.0\text{Å}^{-1}$ ($E = 244\text{eV}$). $\Theta_{\mathbf{r}}^{\mathbf{k}} = 0°$ is the forward scattering direction, and $\Theta_{\mathbf{r}}^{\mathbf{k}} = 180°$ is the backscattering direction.

Figure 1.5. Atomic x-ray holographic techniques, showing the relationship of the external excitation radiation source and detector, with respect to the use of atomic x-ray fluorescence. (a) X-ray fluorescence holography (XFH) (*cf.* Fig. 1.2(a)). (b) Multiple

energy x-ray holography (MEXH) (*cf.* Fig. 1.2(c)). Note that since XFH and MEXH are optical reciprocal cases, wavefront paths are time-reversed with respect to each other.

(a)

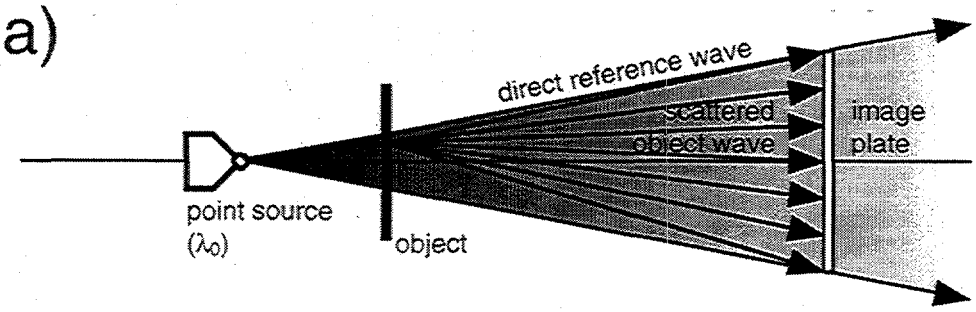

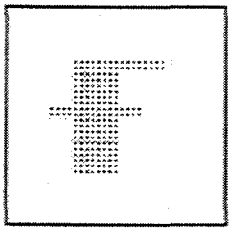

Transparent mask
with point scatterers
($20\lambda_0 \times 20\lambda_0$)

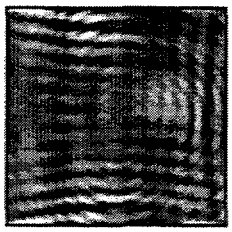

holographic
interference pattern
($0.7k_0 \times 0.7k_0$)

(b)

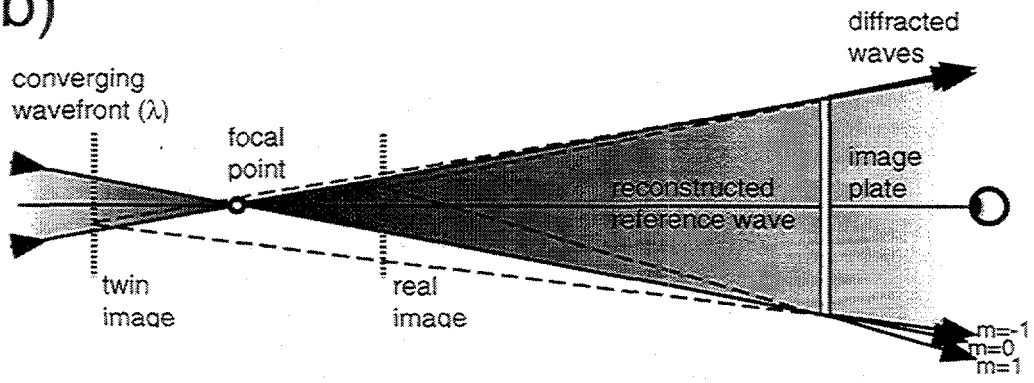

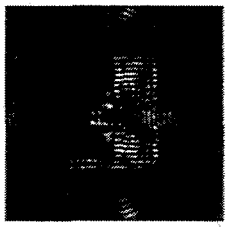

twin image
($20\lambda \times 20\lambda$)

real image
($20\lambda \times 20\lambda$)

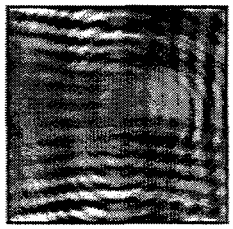

holographic
interference pattern
($0.7k \times 0.7k$)

Fig. 1.1(a)-(b)

(c)

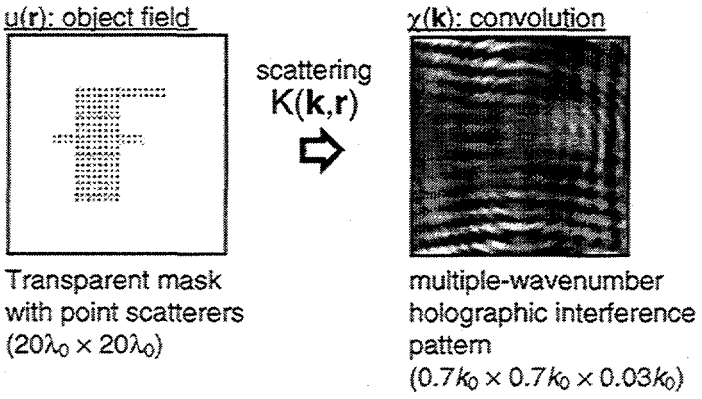

(d)

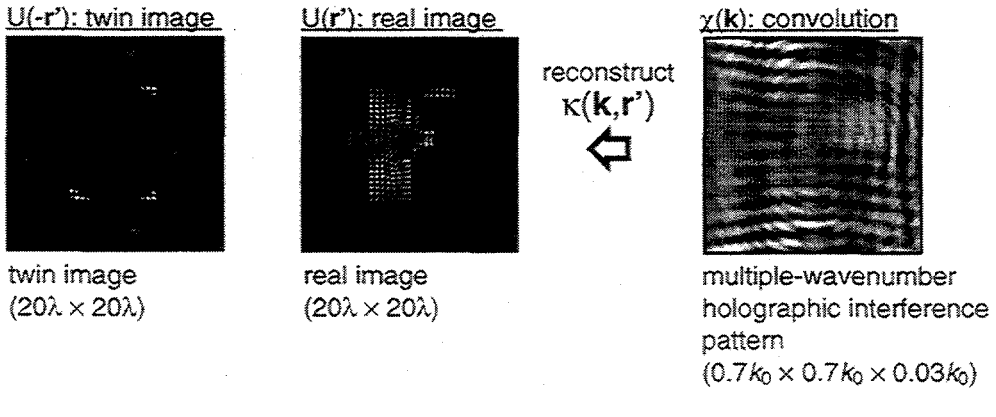

Fig. 1.1(c)-(d)

(a) XFH

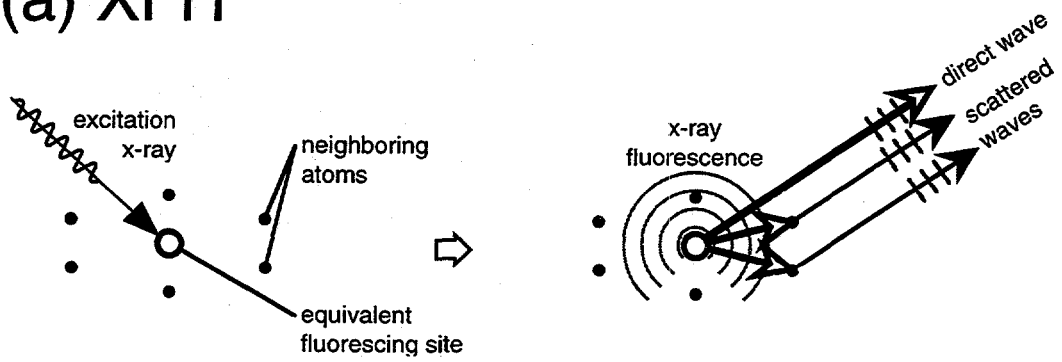

(b) PH

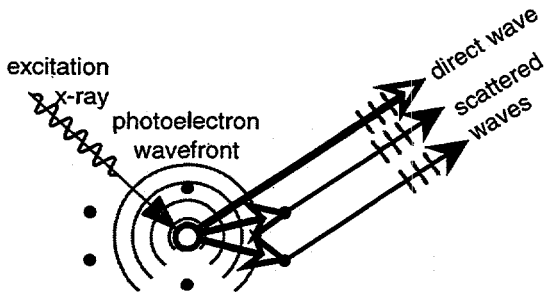

(c) MEXH

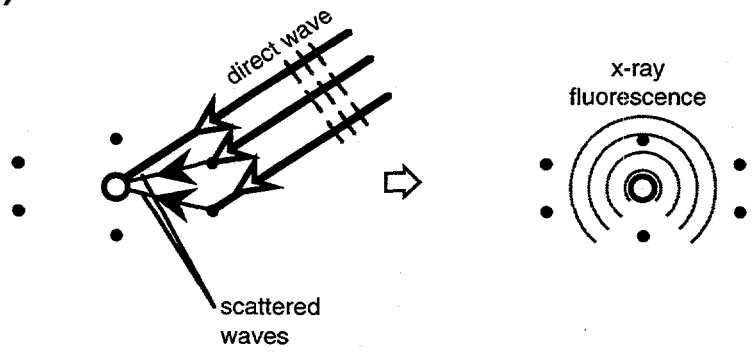

Fig. 1.2

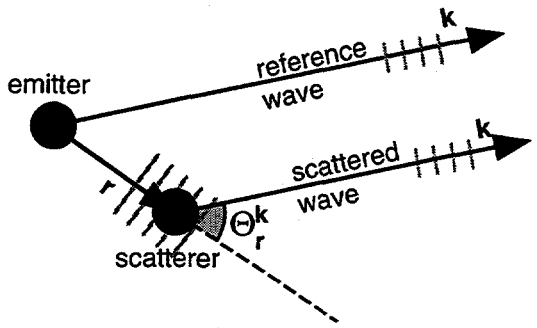

Fig. 1.3

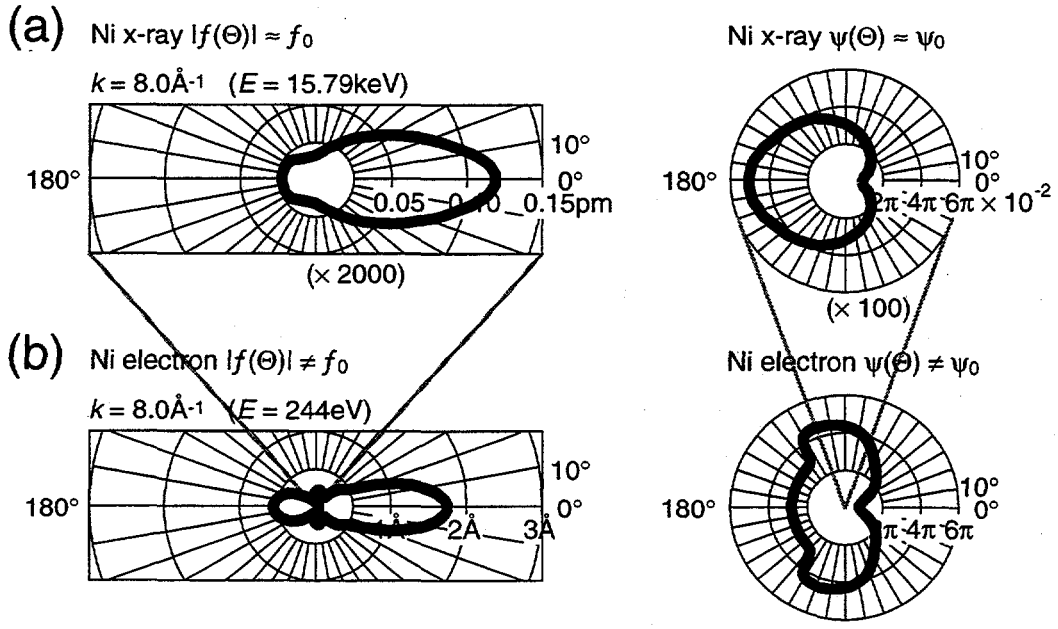

Fig. 1.4

(a) XFH

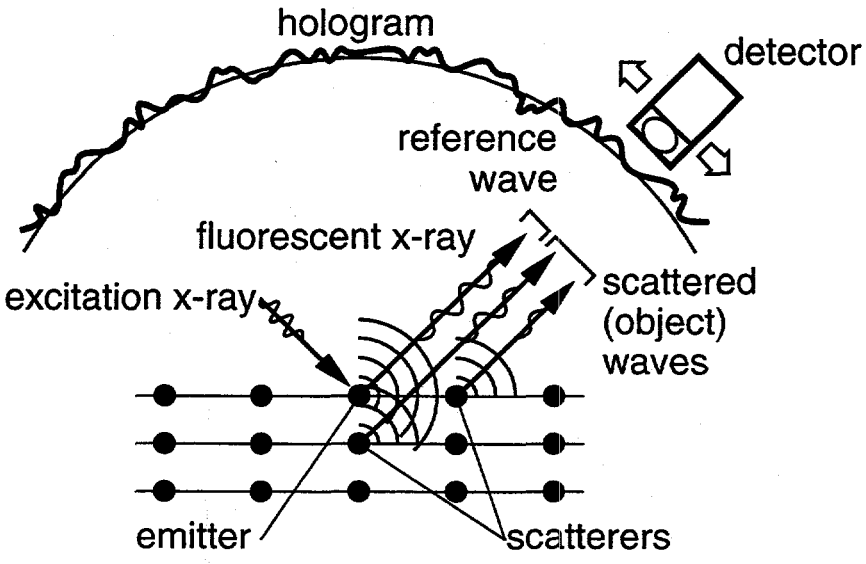

(b) MEXH

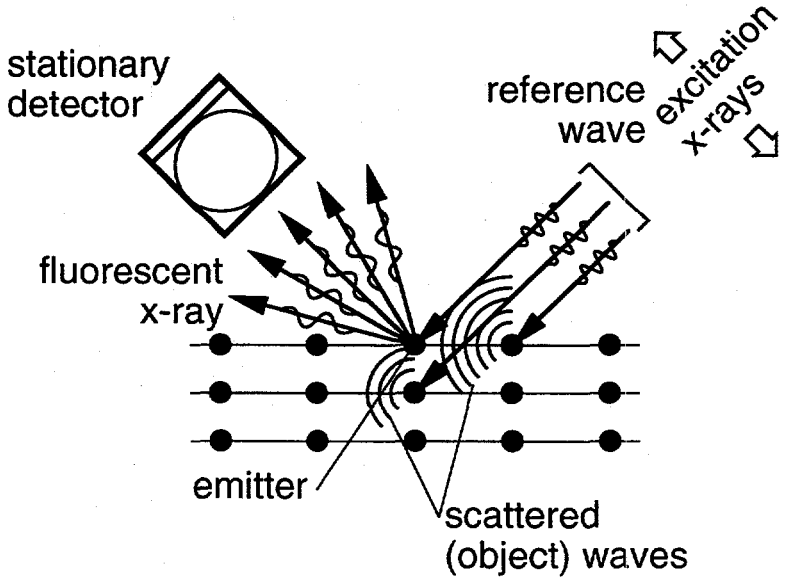

Fig. 1.5

Chapter 2

Overview of Theoretical Methodology and Numerical Programs Used in Atomic Holography

Abstract

This chapter briefly describes the theoretical methodology and the FORTRAN77 programs used in this study of atomic electron and x-ray holography, covering in more detail programs that numerically reconstruct atomic images from normalized holographic $\chi(\mathbf{k})$ intensity data sets.

Outline

2.1 Introduction

In the course of developing atomic electron and x-ray holography as a practical probe of atomic structure, various programs have been developed to generate holographic electron (*ssc-vib.f, scat.f*) and x-ray (*Xray-holo.f*) diffraction pattern intensities. Since in practice the reference wavefront $I_0(\mathbf{k})$ cannot be analytically known and must be deduced from the experimental raw holographic $I(\mathbf{k})$ intensities, several programs to extract $I_0(\mathbf{k})$ and subsequently calculate the normalized holographic $\chi(\mathbf{k})$ intensities have also been

developed (*Io-magk.f, Io-khat.f, Filter.f, Fit-Io.m*). Finally, despite the aesthetic allure of experimentally illuminating such holographic diffraction patterns with a reference wavefront in order to recover visible real-space atomic images, programs to numerically reconstruct atomic images in a more convenient and practical manner have been developed (*HoloInvert.f*), given the computing power readily available on supercomputers, workstations, and more recently, desktop personal computers.

Some of these programs were developed prior to the present study (*ssc-vib.f, scat.f*), but most were written by the author, and/or represent significant modifications of earlier programs.

2.2 Programs to calculate holographic photoelectron diffraction intensities

ssc-vib.f

ssc-vib.f is a FORTRAN77 program developed by Friedman and Fadley [2.1] that calculates raw $I(\mathbf{k})$ or ideally normalized $\chi(\mathbf{k})$ x-ray photoelectron diffraction (XPD) intensities from single-scattering model clusters. Included in this programs are the effects of interchannel interference between the spherical-wave corrected $\ell_f = \ell_i \pm 1$ final states, inelastic attenuation, surface refraction due to the inner potential, incident photoexcitation and detector geometry, and finite angular acceptance of the detector. Also, Thevuthasan has included the effects of correlated Debye-Waller vibrations, due to the model of Sagurton *et al.* [2.2]. The methodology for calculating the single-scattering photoelectron diffraction intensities is discussed in the section below.

scat.f

scat.f is a FORTRAN77 program package developed by Chen *et al.* [2.3] that calculates raw $I(\mathbf{k})$ or ideally normalized $\chi(\mathbf{k})$ x-ray photoelectron diffraction (XPD) intensities from both single- and multiple-scattering model clusters. The separable Green's function matrix formalism of Rehr and Albers [2.4] is used, and all of the effects discussed

above are also incorporated. *scat.f* seeks to more efficiently calculate diffraction intensities by avoiding repetitive and/or negligible scattering events. The version of *scat.f* used in this work (version 3.50) was still in its final testing stage, but the comparison of results from *scat.f* closely corresponds with previous multiple-scattering calculations [2.5] and experimental O/W(110) data [2.6]. *scat.f* was significantly faster than previous multiple scattering packages [2.5] and thus was used for the large-scale computations needed to simulate the W(110) experimental data in Chapter 5.

We now present a brief discussion of the separable Green's function approach of Rehr and Albers, and follow with a full quantitative description of the quantities involved in this approach to first order (*i.e.*, single scattering). Raw photoelectron intensities, for the most simple case of a single photoemitter, and fixed polarized incident excitation sample geometry (where $\hat{\mathbf{e}} = \hat{\mathbf{e}}_2 = \hat{\mathbf{z}}$, and thus $m_f = m_i$) are given by [2.5]:

$$I(\mathbf{k}) \propto \sum_{\ell_f, m_f} \left| \left[(-i)^{\ell_f} e^{i\delta_{\ell_f}(k)} R_{\ell_f}(k) \left\langle \ell_f m_f \middle| (10) \middle| \ell_i m_i \right\rangle \right] \left[G_{00}^{(0)}(\mathbf{k}) + G_{00}^{(1)}(\mathbf{k}) + \ldots + G_{00}^{(N)}(\mathbf{k}) \right] \right|^2, \qquad (2.1)$$

where the quantities within the first set of brackets describe the radial and angular parts of the photoemitter's dipole transition matrix element, including the radial wave function phase shifts $\delta_{\ell_f}(k)$ and the radial matrix elements $R_{\ell_f}(k)$, which are either calculated using the atomic program *CROSSECT* [2.7], or within the *scat.f* program package itself; both calculations are based on a methodology discussed in the work of Goldberg *et al.*, who also tabulate these quantities for a variety of atoms and energies [2.8]. As shown in Fig. 2.1(a), the quantities within the second set of brackets respectively represent the direct (unscattered) wave, the singly-scattered wave, and the subsequently *N*thly-scattered wave contributions to the total photoelectron diffraction intensity seen by the far field detector.

For the purposes of this discussion, we will neglect the effect of wavefront refraction at the surface caused by the presence of an inner potential. The direct wave propagator contribution can be expressed as [2.5]:

$$G_{00}^{(0)}(\mathbf{k}) \approx Y_{l_f}^{m_f}(\theta_{\hat{\mathbf{e}}}^{\mathbf{k}}, \phi_{hv}^{\mathbf{k}}) e^{-L_0/2\Lambda_e}, \tag{2.2}$$

where the inelastic attenuation is described by the $e^{-L_0/2\Lambda_e}$ factor, where L_0 is the distance propagated by the direct wave in the bulk, and Λ_e is the mean free electron path in the bulk [2.9]. Similarly the singly-scattered wave propagator can be expressed as [2.5]:

$$G_{00}^{(1)}(\mathbf{k}) \approx \sum_j \frac{e^{i(\mathbf{k}\cdot\mathbf{a}_j - ka_j)}}{a_j} f_k(\Theta_{\mathbf{a}_j}^{\mathbf{k}}) e^{-L_j/2\Lambda_e} W_j(T, \Theta_{\mathbf{a}_j}^{\mathbf{k}}), \tag{2.3}$$

where the sum is over a set of atomic single scattering sites labeled j and at positions $\mathbf{a}_j$. $e^{i(\mathbf{k}\cdot\mathbf{a}_j - ka_j)}/a_j$ represents the $1/r$ attenuation of the emitter-scatterer path, and the optical path length difference between the direct and singly-scattered wavefronts. Inelastic attenuation is described by the $e^{-L_j/2\Lambda_e}$ factor, where L_j is the distance propagated by the singly-scattered wave in the bulk. The atomic scattering factor $f_k(\Theta_{\mathbf{a}_j}^{\mathbf{k}})$ in Eq. (2.3) is given as [2.5]:

$$f_k(\Theta_{\mathbf{a}_j}^{\mathbf{k}}) = \frac{1}{2ik} \sum_{\ell=0}^{\ell_{max}} (2\ell+1)(e^{2i\delta_\ell} - 1) P_\ell(\cos\Theta_{\mathbf{a}_j}^{\mathbf{k}}) C_\ell(ka_j). \tag{2.4}$$

This scattering factor is calculated from the scattering phase shifts δ_l that are produced from a program package such as *MUFPOT* [2.10], or are determined from within the *scat.f* program itself. The $C_\ell(ka_j)$ spherical Hankel function corrects for the curved-wave nature of the emitter-scatterer wavefront, and can be expressed as:

$$C_\ell(ka_j) = \sqrt{\frac{1+\ell(\ell+1)}{2(ka_j)^2}}\, e^{i\ell(\ell+1)/2ka_j}. \tag{2.5}$$

The effect of temperature-dependent Debye-Waller vibrations is accounted for in Eq. (2.3) by the $W_j(T,\Theta^{\mathbf{k}}_{\mathbf{a}_j})$ factor, which is given by [2.11]:

$$W_j(T,\Theta^{\mathbf{k}}_{\mathbf{a}_j}) = \exp\left[-2k^2(1-\cos\Theta^{\mathbf{k}}_{\mathbf{a}_j})\left\langle u^2(T)\right\rangle\right], \tag{2.6}$$

and the mean-squared displacement of the atomic position is given by [2.11]:

$$\left\langle u^2(T)\right\rangle = \frac{3\hbar^2 T}{Mk_B\theta_D^2}, \tag{2.7}$$

where T is the absolute temperature, M is the atomic mass, and θ_D is the Debye temperature.

In order to show how the Rehr-Albers formalism may be extended to higher scattering orders, we now shift the level of our discussion to a more qualitative nature. For an Nthly scattered wave described by the $G_{00}^{(N)}(\mathbf{k})$ propagator in Eq. (2.1), it can be shown that the propagation of this wave is expressible in a separable way (Fig. 2.1(b)) [2.4,2.5]:

$$G_{00}^{(N)}(\mathbf{k}) \propto \sum_{\substack{\text{all possible}\\ \text{scattering paths}}} G_1 \cdot t_1 \cdot G_2 \cdot t_2 \cdot G_3 \cdot t_3 \cdots t_N \cdot G_{N+1}(\mathbf{k}) \tag{2.8}$$

In this simplified notation, the direct wavefront would then be given by $G_{00}^{(0)} \approx G_1(\mathbf{k})$, and the singly-scattered wavefront would then be given by:

$$G_{00}^{(1)} \propto \sum_{\substack{\text{all possible}\\ \text{scattering paths}}} G_1 \cdot t_1 \cdot G_2(\mathbf{k}), \tag{2.9}$$

with the t_1 scattering matrix being identified with the scattering factor $f_k(\Theta^{\mathbf{k}}_{\mathbf{a}_j})$ of Eq. (2.4) above.

For the purposes of this dissertation, Nth-scattering events were calculated as long as they contributed to no less that 2% of the total raw diffraction intensity. From inspection of running *scat.f* with lower cut-off values, no appreciable difference in calculated intensities was seen, such that a cut-off value of 2% was used in order to make maximum use of CPU time.

2.2 Programs to calculate holographic x-ray diffraction intensities

Xray-holo.f

Xray-holo.f is a FORTRAN77 program that calculates normalized holographic x-ray $\chi(\mathbf{k})$ intensities from single-scattering model clusters. This code was originally adapted by Thevuthasan from the electron holographic $I(\mathbf{k})$ intensity program *ssc-vib.f* [2.1], as the physics that describes x-ray scattering is a much simplified analog of the single-scattering model of electron diffraction. Specifically, the photoexcitation cross-section and photoemitted source wave are assumed to be isotropic for the x-ray cases studied in this work, and no Debye-Waller temperature effects are included. Isotropic x-ray fluorescence should be rigorously true in the case of the Kα transitions considered in this dissertation, since the initial hole is in the spherically-symmetric 1*s* level. The neglect of Debye-Waller effects can also be justified, as the main effect of sample temperature is to reduce the contrast of holographic diffraction fringes, mainly from backscattering atoms [2.11]. However, a sufficient number of counts can be made to compensate for the detrimental effect of Debye-Waller vibrations on contrast, as demonstrated by room temperature experiments [2.12-2.14]. For Mo, with an atomic weight of 95.94g/mol, and a Debye temperature of 400K, the mean squared displacement at $T = 300$K is thus:

$$\langle u^2(T)\rangle = \frac{3(1.0545\times10^{-34}\,J\cdot s)^2(300K)(6.022\times10^{23}\,atoms/mol)}{(0.09594kg/mol)(1.381\times10^{-23}\,J/K)(400K)^2}$$
$$= 2.843\times10^{-23}m^2 \qquad (2.7(a))$$
$$= 0.0028\text{Å}^2,$$

which then leads to the following Debye-Waller factors for forward ($\Theta^{\mathbf{k}}_{\mathbf{a}_j} = 0°$), side ($\Theta^{\mathbf{k}}_{\mathbf{a}_j} = 90°$) and backscattering ($\Theta^{\mathbf{k}}_{\mathbf{a}_j} = 180°$) geometries for Mo Kβ x-rays ($k = 10.1\text{Å}^{-1}$):

$$W_j(T,\Theta^{\mathbf{k}}_{\mathbf{a}_j} = 0°) \equiv 1.,$$
$$W_j(T,\Theta^{\mathbf{k}}_{\mathbf{a}_j} = 90°) = \exp\left[-2(10.1\text{Å}^{-1})^2(1-\cos(90°))(0.028\text{Å}^2)\right] = 0.5648, \qquad (2.6(a))$$
$$W_j(T,\Theta^{\mathbf{k}}_{\mathbf{a}_j} = 90°) = \exp\left[-2(10.1\text{Å}^{-1})^2(1-\cos(180°))(0.028\text{Å}^2)\right] = 0.3190.$$

Thus, provided that contrast problems can be resolved, Debye-Waller attenuation of diffraction is not expected to otherwise affect reconstructed atomic images, as this effect ranges less than an order of magnitude over all scattering directions.

Inelastic attenuation of x-rays is also expected to be negligible in our calculations for several reasons. First, the attenuation lengths are very long (≈ μm). Also, the Borrmann effect of anomalous non-dispersive scattering [2.15] is disregarded, as considering a cluster large enough for such an effect to become important ($V \approx \mu m^3$) would be too computationally unwieldy ($N_{scatterers} \approx 10^{11}$, assuming $10^{-11}\mu m^3$ / scatterer) for even supercomputers. Finally, we are primarily interested in imaging the short-range atomic structure around a given emitter, and so the inclusion of such distant scatterers has no effect on these components of the resulting hologram [2.12].

Xray-holo.f consists of a family of related programs (Progs. 2.1-2.3) to calculate x-ray holographic $\chi(\mathbf{k})$ intensities for a number of different experimental geometries:

Table 2.1. *Xray-holo.f* program family

Xray-holo.f	XFH, or MEXH with unpolarized incident radiation
Xray-holo-p1.f	MEXH with horizontally polarized incident radiation
Xray-holo-p2.f	MEXH with vertically polarized incident radiation

Input file format

All the *Xray-holo.f* programs use the same input file and format (*Xray-holo.in*):

Example 2.1. *Xray-holo.in* sample file

`Fe-bcc:0d`	name of atomic cluster coordinate file
`Fe:sf`	name of x-ray scattering factor file
`10.`	$\theta_0 \equiv$ starting polar angle (in degrees) as measured with respect to the sample surface
`5.`	$\delta\theta \equiv$ size of polar angle steps (in degrees)
`16`	$n\theta \equiv$ number of polar angle steps (in degrees)
`0.`	$\phi_0 \equiv$ starting azimuthal angle (in degrees)
`5.`	$\delta\phi \equiv$ size of azimuthal angle steps (in degrees)
`72`	$n\phi \equiv$ number of azimuthal angle steps (in degrees)
`8.0`	$k_0 \equiv$ starting wavenumber (in $Å^{-1}$)
`0.1`	$\delta k \equiv$ size of wavenumber steps (in $Å^{-1}$)
`11`	$nk \equiv$ number of wavenumber steps (in $Å^{-1}$)
`Fe-bcc:xK`	name of normalized holographic $\chi(\mathbf{k})$ file

Of note are the parameters that specify at which points in **k**-space (k,θ,ϕ) to calculate normalized holographic x-ray $\chi(\mathbf{k})$ intensities. These points are equally spaced with respect to wavenumber (δk) and angular $(\delta\theta,\delta\phi)$ intervals. Polar angle θ is measured from the plane of the surface (*i.e.*, $\theta = 90°$ is the surface normal).

Two data files are subsequently read in by *Xray-holo.f*: the atomic cluster coordinate file, and the x-ray scattering factor file.

X-ray scattering factor file

This data file is a listing of the real and imaginary components of the complex x-ray scattering factor $f_k(\Theta) = f_0(k,\Theta) + f_1(k) + if_2(k)$, where Θ is the angle between the

incident (**k**) and scattered (**k'**) wavefronts, $f_0(\Theta)$ is the scattering angle-dependent component of the scattering factor, and f_1 and f_2 are the dispersive-specific components of the scattering factor. These parameters can be adapted from published tables [2.16] using commercial or public domain interpolation applications (*e.g., Mathematica*© [2.17], *spline* [2.18], *etc.*). The published tables usually give values of $f_0(k \sin\Theta / 2\pi)$, in relative units of the electron scattering strength, *i.e.*, the Thomson scattering factor, which is for unpolarized incident radiation [2.19]:

$$T_{unpolarized}(\Theta) \equiv \sqrt{\frac{d\sigma}{d\Omega}} = \left(\frac{e^2}{mc^2}\right)\sqrt{\frac{(1+\cos^2\Theta)}{2}}. \tag{2.10}$$

For polarized incident radiation, the Thomson scattering factor for a single electron is given by:

$$T_{polarized}(\Theta_{\hat{\mathbf{e}}}^{\mathbf{k}'}) \equiv \sqrt{\frac{d\sigma}{d\Omega}} = \left(\frac{e^2}{mc^2}\right)\sqrt{\sin^2\Theta_{\hat{\mathbf{e}}}^{\mathbf{k}'}}, \tag{2.11}$$

where $\Theta_{\hat{\mathbf{e}}}^{\mathbf{k}'}$ is the angle between the polarization vector of the incident radiation $\hat{\mathbf{e}}$, and the direction **k'** of the scattered radiation.

In this dissertation, the raw $f_0(k \sin\Theta / 2\pi)$ table values have been interpolated to a wavenumber and scattering angle dependent scattering factor $f_0(k,\Theta)$ for $0° \le \Theta \le 180°$, using the *Interpolate[]* function of *Mathematica*© [2.17], and setting

$$\left.\frac{\partial f_0(k,\Theta)}{\partial\Theta}\right|_{\Theta=0°} = 0, \tag{2.12}$$

$$\left.\frac{\partial f_0(k,\Theta)}{\partial\Theta}\right|_{\Theta=180°} = 0, \tag{2.13}$$

in order to ensure smooth and unkinked forward and backscattering peaks. Also listed in Ref. [2.16] are the real and imaginary parts of the dispersive contributions to the scattering factor, $f_1(k)$ and $f_2(k)$, which are incorporated into the complete complex scattering factor as $f_k(\Theta) = f_0(k,\Theta) + f_1(k) + if_2(k)$. The scattering factor for a given wavenumber k is finally listed at 1° intervals from $\Theta = 0°$ to 180°; different wavenumber scattering factors (as specified in *Xray-holo.in*) are then listed sequentially:

Example 2.2. Scattering factor file format

Wavenumber (in $Å^{-1}$)	Scattering angle (in 1° intervals)	Real part of scattering factor (in electrons)	Imaginary part of scattering factor (in electrons)
k	$\Theta°$	$f_0(k,\Theta) + f_1(k)$	$f_2(k)$

All scattering factor values are in relative units of electrons, which are then converted to absolute scattering factor units within *Xray-holo.f*, depending on the polarization of the incident x-rays, as discussed above. Figure 2.2(a) shows the atomic scattering factor for a single Fe atom for $k = 10.30Å^{-1}$ x-rays, in relative electron units. Figures 2.2(b)-(d) shows the Thomson scattering factor for a single electron incident with (b) unpolarized, (c) horizontally polarized, and (d) vertically polarized incident radiation. For the three programs in Table 2.1, the final scattering factors are calculated from multiplying the electron unit scattering factor $f_k(\Theta)$ with the appropriate Thomson scattering factor, whether for unpolarized (Eq. (2.10) and Fig. 2.2(b)) incident radiation, or polarized (Eq. (2.11) and Figs. 2.2(c)-(d)) incident radiation. Scattering angles Θ and polarization angles $\Theta_{\hat{\epsilon}}^{\mathbf{k}'}$ for each emitter-scatterer pair are then determined within *Xray-holo.f*, in order to linearly interpolate the relative $f_k(\Theta)$ scattering factor, or to calculate the appropriate Thomson scattering factor, respectively.

Cluster coordinate file

Common to *ssc-vib.f*, the cluster coordinate file lists the (x,y,z) coordinates of each atom, whether it is an emitter (code = 1) or scatterer (0), and its type (always 1, since we have so far considered only arrays of one kind of emitter and scatterer). The emitter need not be at the origin, as relative emitter-scatterer vectors are calculated in *Xray-holo.f*. Example 2.3 shows an Fe[001] trimer coordinate file, with a single emitter in the middle of two scatterers oriented perpendicular to a hypothetical Fe(001) surface.

Example 2.3. Fe[001] trimer

x (in Å)	y (in Å)	z (in Å)	emitter (1) or scatterer (0)	species type (≡ 1)
0.00	0.00	2.96	0	1
0.00	0.00	0.00	1	1
0.00	0.00	-2.96	0	1

In the current implementation of *Xray-holo.f*, only clusters containing a single emitter and atomic species can be considered. Should either more than one unique emitter site, or more than one scattering atomic species needs to be considered, then the following procedure has been used as an alternative to significant reworking of *Xray-holo.f* A single modification can be made to *Xray-holo.f* such that raw complex $A_n(\mathbf{k})$ amplitudes are separately output for each *n*th emitter/scatterer combination. Then each of these $A_n(\mathbf{k})$ amplitudes are coherently summed to obtain the holographic intensities $I(\mathbf{k}) = \sum_n A_n^*(\mathbf{k}) A_n(\mathbf{k})$, from which normalized holographic intensities $\chi(\mathbf{k}) = (I(\mathbf{k}) - N)/N$ are obtained, where N is the total number of different emitter/scatterer combinations involved, and $I_0(\mathbf{k})$ has been normalized to unity.

Xray-holo.f main subroutine

The main subroutine of *Xray-holo.f* is a multiply nested loop that calculates normalized holographic $\chi(\mathbf{k})$ intensities over different wavenumbers (k) and directions

(θ,ϕ) in **k**-space, where the innermost nested loop in curly brackets is the single scattering convolution integral of Eqs. (1.8) and (1.4(c)), for discrete point scatterers located at $\mathbf{r} = \mathbf{a}_j$:

$$\chi(\mathbf{k}) \equiv \left| 1 + \sum_j \frac{f(\Theta^{\mathbf{k}}_{\mathbf{a}_j})}{ka_j} e^{i(\mathbf{k}\cdot\mathbf{a}_j - ka_j)} \right|^2 - 1. \tag{2.14}$$

Xray-holo.f output format

Xray-holo.f writes out normalized holographic $\chi(\mathbf{k})$ intensities for consecutive increasing wavenumber (k), polar angle (θ), and azimuthal angle (ϕ) values.

Example 2.4 *Xray-holo.f* output format

Wavenumber (in Å^{-1})	Polar angle (in degrees)	Azimuthal angle (in degrees)	Normalized holographic intensity
k	θ	ϕ	$\chi(k,\theta,\phi)$

2.4 Programs to normalize raw holographic intensities

Three FORTRAN77 programs, along with a *Mathematica*© macro, calculate the normalized holographic $\chi(\mathbf{k})$ intensities from raw holographic $I(\mathbf{k})$ intensities via:

$$\chi(\mathbf{k}) \equiv \frac{I(\mathbf{k}) - I_0(\mathbf{k})}{\sqrt{I_0(\mathbf{k})}}, \tag{2.15}$$

where the methods by which the background $I_0(\mathbf{k})$ is calculated are discussed in detail below:

Table 2.2. Holographic data normalization programs

Io-magk.f	Normalizes each different set of variable-energy $I(\mathbf{k})$ data points separately by subtraction of an average constant background
Io-khat.f	Normalizes each different set of variable-direction $I(\mathbf{k})$ data points separately by removal of a linear background
Filter.f	Normalizes each different set of variable-energy data points separately by removal of low-frequency components
Fit-Io.m	Normalizes with respect to both energy and polar angle by removal of a low-order polynomial fit

Io-magk.f

Io-magk.f (Prog. 2.4) normalizes raw $I(\mathbf{k})$ intensities by calculating $I_0(\mathbf{k})$ as an average value for each set of different scanned-energy (scanned-wavenumber) data points I_0^k, averaging over directions at each different wavenumber k [2.20]:

$$I_0^k = \frac{\iint_S k^2 d\sigma_{\hat{\mathbf{k}}} I_k(\hat{\mathbf{k}})}{\iint_S k^2 d\sigma_{\hat{\mathbf{k}}}}. \tag{2.16}$$

Io-khat.f

Io-khat.f (Prog. 2.5) normalizes raw $I(\mathbf{k})$ intensities by calculating $I_0(\mathbf{k})$ as a linear fit for each set of scanned-energy (scanned-wavenumber) data points $I_0^{\hat{\mathbf{k}}}(k)$ at a given direction $\hat{\mathbf{k}}$ [2.21]:

$$I_0^{\hat{\mathbf{k}}}(k) = a_{\hat{\mathbf{k}}} + b_{\hat{\mathbf{k}}} k, \tag{2.17}$$

Filter.f

Filter.f (Prog. 2.6) normalizes raw $I(\mathbf{k})$ intensities by calculating $I_0^k(\mathbf{k})$ as the low-frequency angular components for each different scanned-angle $I(\mathbf{k})$ data set at a given energy (wavenumber), as suggested by Harp *et al.* [2.22]:

$$I_0^k(\mathbf{k}) = \frac{\iint_S k^2 d\sigma_{\hat{\mathbf{k}}} e^{-\sigma^2(\mathbf{k}-\mathbf{k}')^2} I_k(\mathbf{k}')}{\iint_S k^2 d\sigma_{\hat{\mathbf{k}}}} \tag{2.18}$$

where σ is a variable parameter which smooths the original $I(\mathbf{k})$ over a certain length scale in $|\mathbf{k}-\mathbf{k}'|$. Thus data points at $I(\mathbf{k})$ are smoothed with data located at relative positions $(\mathbf{k}-\mathbf{k}')$, and these other data points $I(\mathbf{k}')$ are weighted by the Gaussian function $e^{-\sigma^2(\mathbf{k}-\mathbf{k}')^2}$. Note that as $\sigma \rightarrow 0$, this procedure degenerates into the *Io-magk.f* normalization scheme. *Filter.f* has been found to be most appropriate to find $I_0(\mathbf{k})$ when the most significant correction to the raw $I(\mathbf{k})$ intensities is the removal of low-angular frequency geometric absorption effects in x-ray holograms [2.13]. Equation (2.5) has also been used to remove high-frequency scattering components in x-ray fluorescence holograms [2.12]. For electron holographic $I(\mathbf{k})$ intensities, this method has been used to remove localized forward scattering features [2.22,2.23], and a version of *Filter.f* has been modified by Ruebush to specifically remove high-angular frequency noise from experimental electron diffraction patterns [2.24].

Input file format

All of the above normalization programs (*Io-magk.f, Io-khat.f, Filter.f*) use the same input file and format (*Io.in*):

Example 2.2. *Io.in* sample file

`Fe-bcc:Ik`	raw $I(\mathbf{k})$ intensity file (arb. units)
`Fe-bcc:xK`	normalized intensity $\chi(\mathbf{k})$ file (arb. units)
`72`	$n\theta \equiv$ number of polar angle steps (in degrees)
`37`	$n\phi \equiv$ number of azimuthal angle steps (in degrees)
`0.0`	$nk \equiv$ number of wavenumber steps (in $Å^{-1}$)
`0.15`	σ (for *Filter.f*) (in Å)

Fit-Io.m

Fit-Io.m (Prog. 2.7) is a *Mathematica*© macro file that enables a raw $I(\mathbf{k})$ data set to be read in and normalized by the *Mathematica*© kernel, where $I_0(\mathbf{k})$ is determined by:

$$I_0(\mathbf{k}) = a_{00} + \sum_{m=1}^{3}\sum_{n=1}^{3} a_{mn} k^m \cos[(2n-1)\theta]. \tag{2.19}$$

This three-dimensional **k**-space polynomial fit with respect to both wavenumber k and polar angle θ is CPU intensive, as typical $I(\mathbf{k})$ and $\chi(\mathbf{k})$ data sets comprise of up to 10^3-10^4 intensities. Such data sets are normalized using *Fit-Io.m* in 10^2-10^3 minutes of CPU time on a Sun SPARC2 workstation. The number of coefficients (above, $1 \le m,n \le 6$) can be truncated or expanded as need arises. The number of coefficients needed to adequately normalize $I(\mathbf{k})$ intensities can be determined by the inspection and imaging of the $I_0(\mathbf{k})$ and $\chi(\mathbf{k})$ intensities that are determined in the normalization process. Normally, the above sums should be restricted to $(m,n) \le (3,3)$ to avoid removing valid diffraction features from the data set. Figure 2.3(a) shows a raw theoretical $I(\mathbf{k})$ data set calculated for surface W 4*f* photoemission from a multiple-scattering W(110) cluster (*cf.* Chapter 5). The theoretical background $I_0(\mathbf{k})$, and normalized $\chi(\mathbf{k})$ data sets corresponding to Fig. 2.3(a) are shown in Fig. 2.3(b)-(c), respectively. Since the background $I_0(\mathbf{k})$ cannot be known analytically (unless a theoretical $I(\mathbf{k})$ data set is considered, as here), Figs. 2.4(b)-(c) and 2.5(b)-(c) show progressively higher-order wavenumber and polar angle fits of Eq. (2.19) to the raw theoretical $I(\mathbf{k})$ data set of Fig. 2.3(a). For comparison, the theoretical background $I_0(\mathbf{k})$ is shown in Figs. 2.4(a) and 2.5(a). As can be seen in Figs. 2.4-2.5, the lower order polynomial fits of $(m,n) \le (1,1)$ (Fig. 2.4(b)) and $(m,n) \le (2,2)$ (Fig. 2.4(c)) do not adequately reproduce the fine structure features of the theoretical background $I_0(\mathbf{k})$ of Fig. 2.4(a). However, the $(m,n) \le (3,3)$ polynomial fit of Fig. 2.5(b) generally reproduces the bright feature seen at $(k,\theta) \approx (5\text{Å}^{-1}, 80°)$ in Fig. 2.5(a), as does the $(m,n) \le$

(6,6) polynomial fit of Fig. 2.5(c), which also reproduces the azimuthal bands seen in Fig. 2.5(a). However, caution should be exercised when extending the polynomial fit to higher orders, as finer features that will begin to be included in $I_0(\mathbf{k})$ may actually correspond to holographic modulations. The best methodology is simply to reconstruct images from progressively higher order polynomial fit normalized $\chi(\mathbf{k})$ data sets, until these images no longer appreciably improve in fidelity.

Table 2.3 shows the a_{mn} coefficients for the polynomial $I_0(\mathbf{k})$ fit to the theoretical surface emission $I(\mathbf{k})$ of Fig. 2.1(a), where $|a_{00}|$ has been normalized to 1.

Table 2.3 a_{mn} Coefficients for $(m,n) \leq (6,6)$

a_{mn}	$n=0$	1	2	3	4	5	6
$m=0$	-1.0	1.8	3.4	1.6	0.34	1.6	-0.021
1	0.54	0.83	-1.5	0.75	0.19	0.74	-0.079
2	0.73	-1.4	3.1	-1.3	-0.22	-1.3	0.22
3	0.22	0.73	-1.2	0.63	0.12	0.56	-0.096
4	0.025	-0.21	0.14	0.16	-0.45	-0.11	0.017
5	8.4e-4	0.032	-1.3e-3	0.022	7.9e-3	0.011	-1.2e-3
6	3.1e-5	1.8e-3	5.5e-3	-1.2e-3	4.9e-4	4.7e-4	2.0e-5

In Table 2.3, the a_{mn} coefficients for $(m,n) \leq (3,3)$ are on the order of unity, while those for $(3,3) \leq (m,n) \leq (6,6)$ are for the most part an order of magnitude less. However, it also appears from the entries that it may be necessary to take n higher than m, and up to as high as 5. But this should be tested for each case using the image criterion mentioned above.

The file names of the raw $I(\mathbf{k})$, background $I_0(\mathbf{k})$, and normalized $\chi(\mathbf{k})$ data sets must be explicitly written into the macro file, as well as the number of k, θ, and ϕ steps in these data sets.

2.5 Programs to reconstruct atomic images

HoloInvert.f

HoloInvert.f is a FORTRAN77 program that reconstructs image intensities from either normalized electron or x-ray holographic $\chi(\mathbf{k})$ intensities. *HoloInvert.f* consists of a family of related programs to calculate image $U(\mathbf{r}')$ intensities via different reconstruction algorithms:

Table 2.4. *HoloInvert.f* program family

HoloInvert.f	Method A reconstruction algorithm
HoloInvert:2.0a.f	Method $\tilde{A}$ reconstruction algorithm
HoloInvert:2.0b.f	Method B reconstruction algorithm
HoloInvert:2.0c.f	Method C reconstruction algorithm
HoloInvert:2.0d.f	Method D reconstruction algorithm

Input file format

All the *HoloInvert.f* programs use the same input file and format (*HoloInvert.in*):

Example 2.3 Sample *HoloInvert.in* format for three-dimensional volume reconstruction

`Fe-bcc:xK`			normalized hologram $\chi(\mathbf{k})$ file (in arb. units)
`16`			$n\theta \equiv$ number of polar angle steps (in degrees)
`72`			$n\phi \equiv$ number of azimuthal angle steps (in degrees)
`10`			$nk \equiv$ number of wavenumber steps (in $Å^{-1}$)
`0.0`			rotation angle $\Delta\phi$ (in degrees)
`Fe-bcc:xyz:Ur`			image intensity $U(\mathbf{r}')$ (in arb. units)
`-6.0`	`6.0`	`0.1`	x_1', x_2', dx' (in Å)
`-6.0`	`6.0`	`0.1`	y_1', y_2', dy' (in Å)
`-6.0`	`6.0`	`0.1`	z_1', z_2', dz' (in Å)

Of note are the parameters that specify at which points in real space ($\mathbf{r}' = (x',y',z')$) to calculate image $U(\mathbf{r}')$ intensities. The 1, 2, or 3 dimensional region to be covered in a given reconstruction is specified by the appropriate beginning and ending (x_1', y_1', z_1'), (x_2', y_2', z_2') limits (highlighted in boldface). Example 2.3 above is thus for a

reconstruction covering a volume of ±6.0 Å in all three directions. Examples 2.4-2.5 show image reconstruction parameters for the [100] axis and the (001) plane, respectively.

The rotation angle $\Delta\phi$ is defined as the counterclockwise rotation angle of the hologram with respect to the fixed reconstruction axes x', y', and z', which in effect rotates reconstructed images with respect to the real-space region being reconstructed. This feature allows the alignment of images reconstructed from $\chi(\mathbf{k})$ data that is not already aligned azimuthally with respect to a low-index direction (*e.g.*, [100]).

Example 2.4 Sample *HoloInvert.in* format for [100] axis reconstruction

Fe-bcc:xK			normalized hologram $\chi(\mathbf{k})$ file (in arb. units)
16			$n\theta \equiv$ number of polar angle steps (in degrees)
72			$n\phi \equiv$ number of azimuthal angle steps (in degrees)
10			$nk \equiv$ number of wavenumber steps (in $Å^{-1}$)
0.0			rotation angle $\Delta\phi$ (in degrees)
Fe-bcc:x100:Ur			image intensity $U(\mathbf{r}')$ (in arb. units)
-6.0	6.0	0.1	x_1', x_2', dx' (in Å)
0.0	0.0	0.1	y_1', y_2', dy' (in Å)
0.0	0.0	0.1	z_1', z_2', dz' (in Å)

Example 2.5 Sample *HoloInvert.in* format for (001) plane reconstruction

Fe-bcc:xK			normalized hologram $\chi(\mathbf{k})$ file (in arb. units)
16			$n\theta \equiv$ number of polar angle steps (in degrees)
72			$n\phi \equiv$ number of azimuthal angle steps (in degrees)
10			$nk \equiv$ number of wavenumber steps (in $Å^{-1}$)
0.0			rotation angle $\Delta\phi$ (in arb. units)
Fe-bcc:xy001:Ur			image intensity $U(\mathbf{r}')$
-6.0	6.0	0.1	x_1', x_2', dx' (in Å)
-6.0	6.0	0.1	y_1', y_2', dy' (in Å)
0.0	0.0	0.1	z_1', z_2', dz' (in Å)

The image region of interest need not be either centered, nor pass through the origin. Example 2.6 shows the parameters for imaging the (002) plane of Fe(001) that is 1.453 Å above the emitter plane:

Example 2.6 Sample *HoloInvert.in* format for (002) plane reconstruction

Fe-bcc:xK			normalized hologram $\chi(\mathbf{k})$ file
16			$n\theta \equiv$ number of polar angle steps (in degrees)
72			$n\phi \equiv$ number of azimuthal angle steps (in degrees)
10			$nk \equiv$ number of wavenumber steps (in $Å^{-1}$)
0.0			rotation angle $\Delta\phi$
Fe-bcc:xy001:Ur			image intensity $U(\mathbf{r}')$
-6.0	6.0	0.1	x_1', x_2', dx' (in Å)
-6.0	6.0	0.1	y_1', y_2', dy' (in Å)
1.435	1.435	0.1	z_1', z_2', dz' (in Å)

In this manner, any directions of the form [*h*00], [0*k*0], [00*l*], or planes of the form (*h*00), (0*k*0), (00*l*) can be imaged.

By specifying the (counterclockwise) rotation angle $\Delta\phi$ of the hologram with respect to the reconstructed image reference frame, all directions of the form [*hk*0], as well as planes of the form (*hk*0) can be imaged. Examples 2.7-2.8 show input parameters for the (110) and (120) planes for bulk Fe(001), respectively:

Example 2.7 Sample format for (110) plane reconstruction

Fe-bcc:xK			normalized hologram $\chi(\mathbf{k})$ file (in arb. units)
16			$n\theta \equiv$ number of polar angle steps (in degrees)
72			$n\phi \equiv$ number of azimuthal angle steps (in degrees)
10			$nk \equiv$ number of wavenumber steps (in $Å^{-1}$)
45.0			rotation angle $\Delta\phi$ (in degrees)
Fe-bcc:xz110:Ur			image intensity $U(\mathbf{r}')$ (in arb. units)
-6.0	6.0	0.1	x_1', x_2', dx' (in Å)
-6.0	6.0	0.1	y_1', y_2', dy' (in Å)
0.0	0.0	0.1	z_1', z_2', dz' (in Å)

Example 2.8 Sample format for (120) plane reconstruction

Fe-bcc:xK			normalized hologram $\chi(\mathbf{k})$ file (in arb. units)
16			$n\theta \equiv$ number of polar angle steps (in degrees)
72			$n\phi \equiv$ number of azimuthal angle steps (in degrees)
11			$nk \equiv$ number of wavenumber steps (in $Å^{-1}$)
26.56505118			rotation angle $\Delta\phi$ (in degrees)
Fe-bcc:xz120:Ur			image intensity $U(\mathbf{r}')$
-6.0	6.0	0.1	x_1', x_2', dx' (in Å)
-6.0	6.0	0.1	y_1', y_2', dy' (in Å)
0.0	0.0	0.1	z_1', z_2', dz' (in Å)

Image reconstructions in general [*hkl*] directions or (*hkl*) planes are not supported in this version of *HoloInvert.f*, though such directions/planes would be possible through the incorporation of full Euler rotation operations on the orientation of the hologram, with respect to the image reconstruction reference frame.

Note that image resolutions (dx', dy', dz') need not be identical for each different direction, as long as they are non-zero. This stems from the nature of the algorithm that determines from the input parameters at which $\mathbf{r}' = (x', y', z')$ points the image $U(\mathbf{r}')$ intensities are to be calculated.

Hologram data file format

The hologram data file format is identical to the hologram data output format from *Xray-holo.f*, where normalized holographic $\chi(\mathbf{k})$ intensities are listed for consecutive increasing wavenumber (k), polar angle (θ), and azimuthal angle (ϕ) values. Note that the data is explicitly in the format of an $nk \times n\theta \times n\phi$ matrix; any missing values in **k**-space must be explicitly listed as zero.

Example 2.9 Hologram data file format

Wavenumber (in $Å^{-1}$)	Polar angle (in degrees)	Azimuthal angle (in degrees)	Normalized holographic intensity
k	θ	ϕ	$\chi(k,\theta,\phi)$

Also important is that the $\chi(\mathbf{k})$ data intervals for wavenumber (δk) and angular ($\delta\theta$, $\delta\phi$) spacings must be identical for all entries. Numerous commercial programs can be used to interpolate holographic image intensity data sets onto a constant $\delta k \times \delta\theta \times \delta\phi$ **k**-space lattice if this is not initially the case. One that was used in this dissertation is the *Fit[]* function of *Mathematica*© [2.17].

HoloInvert.f main subroutine

The main subroutine of *HoloInvert.f* (Prog. 2.8) is a multiply nested loop containing the numerical evaluation of the reconstruction algorithm of Method A (Eq. (1.9)) for image intensities located at **r'**:

$$U_A(\mathbf{r}') = \sum_{\theta} \cos\theta \sum_{\phi} \sum_{k} k^2 \chi(k,\theta,\phi) e^{i(\mathbf{k}\cdot\mathbf{r}' - kr')} . \qquad (2.20)$$

In actually representing the final image, it is the absolute value of this quantity that is plotted over the **r'** space; the same is true for the other images Ã, B, and C discussed below. Because θ is here defined as a takeoff angle relative to the surface instead of the often-used polar angle $\theta' = 90° - \theta$ measured relative to the normal, we note that the factor $k^2 \cos\theta'$ in this sum is just the non-constant factor in a volume element in **k**-space of the form $k^2 \delta k \sin\theta' \delta\theta' \delta\phi'$.

The wavenumber summation is the innermost loop, such that the geometric path length difference $(\mathbf{k}\cdot\mathbf{r}' - kr')$ needs to be evaluated only once for each different (θ,ϕ) direction in the $\chi(\mathbf{k})$ data set for each image intensity at **r'**.

It should be noted on closer inspection that *HoloInvert.f* is neither fully vectorized nor optimized, but it nonetheless already performs moderately well on Sun SPARC2 workstations, evaluating 10^4 data point $\chi(\mathbf{k})$ holograms to generate 10^4 image $U(\mathbf{r}')$ intensities within 10^2 minutes. Performance on CRAY supercomputers indicates at least

an order of magnitude or better increase in evaluation times. The motivation behind the implementation of *HoloInvert.f* was to translate Eq. (2.5) into FORTRAN77 using the most straightforward and transparent code. Use of more sophisticated integration summation methods (*e.g.* trapezoidal rule, Simpson's rule, *etc.*), was not found to significantly improve image fidelity. Thus, the simple Reimann integration summation used here is adequate to reconstruct image $U(\mathbf{r}')$ intensities of sufficient fidelity in *HoloInvert.f*, while keeping this code as simple and compact as possible for any further modifications.

2.6 Modifications to the HoloInvert.f main subroutines to treat other imaging methods

Method $\tilde{A}$

For Method $\tilde{A}$ (Prog. 2.9), an additional data file is read in by *HoloInvert:2.0a.f*: the scattering factor file *fk.in*, which has the same format as the scattering factor files read by *Xray-holo.f* (*cf.* Ex. 2.2).

The main numerical evaluation subroutine of the reconstruction algorithm of Method $\tilde{A}$ (Eq. (1.10)) then becomes:

$$U_{\tilde{A}}(\mathbf{r}') = \sum_{\theta} \cos\theta \sum_{\phi} \sum_{k} k^2 \chi(k,\theta,\phi) \frac{e^{i(\mathbf{k}\cdot\mathbf{r}'-kr')}}{f_k(\Theta^{\mathbf{k}}_{\mathbf{r}'})}, \tag{2.21}$$

where the scattering factor $f_k(\Theta^{\mathbf{k}}_{\mathbf{r}'})$ is interpolated via a linear interpolation subroutine (*cf. Xray-holo.f*) for each unique scattering angle Θ between $\mathbf{r}'$ and $\mathbf{k}$. There is no dependence on the radiation polarization here, and so this program cannot be used to correct fully for the more complex x-ray case in which Thomson scattering of polarized incoming radiation may have to be allowed for. (An alternative method to correct for this effect is discussed in Chapter 8). Note also that this method requires knowing the identity of the atom at each site in order to specify $f_k(\Theta^{\mathbf{k}}_{\mathbf{r}'})$. If only one type of atom is present, this is trivial, but

if not, then some sort of trial and error procedure and/or prior knowledge of approximate atomic positions is required.

Method B

The additional data file read in by *HoloInvert:2.0b.f* (Prog. 2.10) is *window.in*, which merely specifies the half-angle size α of the window function $w(\alpha, \Theta^{\mathbf{k}}_{-\mathbf{r}'})$ in degrees.

The main numerical evaluation subroutine of the reconstruction algorithm of Method B (Eq. (1.11)) then becomes:

$$U_B(\mathbf{r}') = \sum_{\theta} \cos\theta \sum_{\phi} \sum_{k} k^2 \chi(k,\theta,\phi) e^{i(\mathbf{k}\cdot\mathbf{r}'-kr')} w(\alpha, \Theta^{\mathbf{k}}_{-\mathbf{r}'}), \tag{2.22}$$

where $w(\alpha, \Theta^{\mathbf{k}}_{-\mathbf{r}'})$ is an if-then conditional statement that allows the $\chi(\mathbf{k})$ contribution to the numerical integral summation to be non-zero if the angle $\Theta^{\mathbf{k}}_{-\mathbf{r}'}$ is smaller than the window half-angle α. The included cone is here abruptly terminated at its edge, with no smooth transition between included points and excluded points. Although this can introduce additional fine structure in the resulting transform, it is the method used in prior applications of this method to photoelectron diffraction data.

Method C

The additional data file read in by *HoloInvert:2.0c.f* (Prog. 2.11) is *rous.in*, which is the image intensity $U_A(\mathbf{r}')$ output from *HoloInvert.f*.

The main numerical evaluation subroutine of the reconstruction algorithm of Method C (Eq. (1.12)) is identical to Method A (Eq. (1.9)), but image intensities are evaluated for points $\mathbf{r}_+' = \mathbf{r}' + dr'\hat{\mathbf{r}}'$ that lie radially outward from the origin, where $dr' \equiv$ 0.01Å and a fixed small number. Thus image $U_A(\mathbf{r}_+')$ intensities are computed that can be used together with $U_A(\mathbf{r}')$ to implement the reconstruction algorithm of Method C:

$$U_C(\mathbf{r}') = \frac{(r'+dr')\,\mathrm{Re}\left[U_A(\mathbf{r}_+')\right] - r'\,\mathrm{Re}\left[U_A(\mathbf{r}')\right]}{dr'}. \tag{2.23}$$

Step sizes dr' were varied, and found to have little effect on image reconstructed via Method C, as long as dr' was smaller than the finest imagible features desired.

Method D

Similar to *HoloInvert:2.0a.f*, the additional data file read in by *HoloInvert:2.0d.f* (Prog. 2.12) is *fk.in*.

The main numerical evaluation subroutine of the reconstruction algorithm of Method D (Eq. (1.13)) is different than those of Methods A-C:

$$U_D(\mathbf{r}') = \sum_{\theta}\cos\theta\sum_{\phi}\exp\left[r'\sum_{k}\chi(k,\theta,\phi)\chi_{theoretical}(k,\theta,\phi,x',y',z')\right], \tag{2.24}$$

where the single-scattering calculated intensities are given by

$$\chi_{theoretical}(k,\theta,\phi,x',y',z') \equiv \mathrm{Re}\left[f_k(\Theta_{\mathbf{r}'}^{\mathbf{k}})\frac{e^{i(\mathbf{k}\cdot\mathbf{r}'-kr')}}{kr'}\right]. \tag{2.25}$$

The $\cos\theta$ factor is here preserved from the volume element in **k**-space that is present in the other methods in order to provide some weighting based on the solid angle encompassed by each direction, but in keeping with the form used by Hofmann and Schindler in their original proposal of this method [2.25], there is no k^2 factor in the sum on k.

2.7 Graphical presentation of reconstructed atomic images

All of the reconstructed images in this work have been processed by *HoloGraph.m*, a *Mathematica*© macro developed by Budge [2.26] that plots these images as *Postscript*© files [2.27]. These Postscript files are then translated into PICT format using *Ghostview*© [2.28], cropped with *GraphicConverter*© [2.29], and then realized in their final form using *ClarisDraw*© to add labels, axes, scales, *etc.* [2.30].

2.8 Concluding remarks

In this chapter we have given a brief overview of the basic theoretical methodology and the resulting computer programs used in this study of atomic x-ray and electron holography, as well as more specific instructions and examples for the programs that were developed especially for this work.

References

[2.1] D. J. Friedman and C. S. Fadley, J. Electron Spectrosc. Relat. Phenom. **57** (1991) 223.

[2.2] M. Sagurton, E. L. Bullock, and C. S. Fadley, Surf. Sci. **182** (1987) 287.

[2.3] Y. Chen, H. Wu, and D. A. Shirley, private communication.

[2.4] J. J. Rehr and R. C. Albers, Phys. Rev. B **41** (1990) 8139.

[2.5] A. P. Kaduwela, D. J. Friedman, and C. S. Fadley, J. Electron. Spectrosc. Relat. Phenom. **57** (1991) 223.

[2.6] R. X. Ynzunza, unpublished results.

[2.7] M. T. Manson and S. Skillman.

[2.8] S. M. Goldberg, C. S. Fadley, and S. Kono, J. Electron Spect. Relat. Phenom. **21** (1981) 285.

[2.9] M. P. Seah and W. A. Dench, Surf. Interface Anal. **1** (1977) 2.

[2.10] T. L. Loucks, *Augmented Plane Wave Method* (W. A. Benjamin, Inc., New York, 1967).

[2.11] A. W. Zangwill, *Physics at Surfaces* (Cambridge University Press, Cambridge, 1988) 171.

[2.12] M. Tegze and G. Faigel, Europhys. Lett. **16** (1991) 41, and Nature **380** (1996) 49.

[2.13] (a) T. Gog, P. M. Len, G. Materlik, D. Bahr, C. Sanchez-Hanke, and C. S. Fadley, Phys. Rev. Lett. **76** (1996) 3132. (b) P. M. Len, T. Gog, D. Novikov, R. A. Eisenhower, G. Materlik, and C. S. Fadley, submitted to Phys. Rev. B.

[2.14] D. Novikov, private communication.

[2.15] B.W. Batterman and H. Cole, Rev. Mod. Phys. **36** (1964) 681.

[2.16] *International Tables for X-ray Crystallography*, edited by K. Lonsdale (Reidel, Dordrecht, 1968), Vol. III.

[2.17] Wolfram Research Inc.

[2.18] SunOS release 4.1, Sun Microsystems Inc.

[2.19] L. V. Azaroff, *Elements of X-ray Crystallography* (McGraw-Hill, New York, 1968), 87.

[2.20] L. J. Terminello, B. L. Petersen, and J. J. Barton, J. Electron Spectrosc. Relat. Phenom. **75** (1995) 229, and references therein.

[2.21] C. M. Wei, J. H. Hong, P. R. Jeng, S. C. Shyu, and Y. C. Chou, Chem. Phys. Lett. **228** (1994) 513, and references therein.

[2.22] G. R. Harp, D. K. Saldin, X. Chen, Z.-L. Han, and B. P. Tonner, J. Electron Spectrosc. Relat. Phenom. **57** (1991) 331.

[2.23] R. Denecke, R. Eckstein, L. Ley, A. E. Bocquet, J. D. Riley, and R. C. G. Leckey, Surf. Sci. **331-333** (1995) 1085.

[2.24] S. D. Ruebush, Ph. D. dissertation, University of California, Davis, CA, June 1996.

[2.25] O. Schaff, P. Hofmann, C. J. Hirschmugl, A. Theobald, V. Fernandez, K.-M. Schindler, A. M. Bradshaw, N. Booth, R. Davis, and D. P. Woodruff, J. Electron Spec. Relat. Phenom. **76** (1995) 85, and references therein.

[2.26] A. Budge, private communication.

[2.27] Adobe Systems, Inc.

[2.28] L. P. Deutsch and M. Lentczner, Aladdin Enterprises.

[2.29] T. Lemke, Lemke Software.

[2.30] Claris Corporation.

Program Listings

Program 2.1. *Xray-holo.f.*

Program 2.2. *Xray-holo-p1.f.*

Program 2.3. *Xray-holo-p2.f.*

Program 2.4. *Io-magk.f.*

Program 2.5. *Io-khat.f.*

Program 2.6. *Filter.f.*

Program 2.7. *Fit-Io.m.*

Program 2.8. *HoloInvert.f.*

Program 2.9. *HoloInvert:2.0a.f.*

Program 2.10. *HoloInvert:2.0b.f.*

Program 2.11. *HoloInvert:2.0c.f.*

Program 2.12. *HoloInvert:2.0d.f.*

Figure captions

Figure 2.1. (a) Schematic representation of the direct, singly-scattered, and *N*thly-scattered wave propagation contributions to the diffraction intensity measured by the far field detector at ∞. (b) Schematic representation of the seperable Green's function expression for the *N*thly-scattered wave propagator of (a).

Figure 2.2. Scattering factor magnitudes for $k = 5.220\text{Å}^{-1}$ ($E = 10.30$keV) x-rays incident on atomic Fe. Θ is the angle between the incident ($\mathbf{k}$) and scattered ($\mathbf{k}'$) wavevectors. (a) Fe atomic scattering factor, in relative units of electrons. (b)-(d) Thomson electron scattering factors, in absolute units of $r_e = e^2 / mc^2 \equiv 2.818 \times 10^{-5}\text{Å}$, for (b) unpolarized, (c) vertically polarized, and (d) horizontally polarized incident x-rays.

Figure 2.3. Schematic **k**-space volume representations of theoretical data sets for surface W $4f_{7/2}$ emission, as viewed down along $[\bar{1}\,\bar{1}\,0]$ (top panels), and down along $[00\,\bar{1}]$ (bottom panels). The intensities in the lower right-hand quadrant have been removed to show the intensity surface at the constant minimum wavenumber. (a) Raw theoretical $I(\mathbf{k})$ data set. (b) Theoretical $I_0(\mathbf{k})$ background. (c) Theoretical normalized $\chi(\mathbf{k})$ data set.

Figure 2.4. As Fig. 2.3, but for (a) Theoretical $I_0(\mathbf{k})$ background (*cf.* Fig. 2.3(b)). (b) $I_0(\mathbf{k})$ as determined by a least-squares $(m,n) \leq (1,1)$ fit in wavenumber and polar angle of Eq. (2.19) to the raw $I(\mathbf{k})$ intensities of Fig. 2.3(a). (c) $I_0(\mathbf{k})$ as determined by a least-squares $(m,n) \leq (2,2)$ fit in wavenumber and polar angle of Eq. (2.19) to the raw $I(\mathbf{k})$ intensities of Fig. 2.3(a).

Figure 2.5. As Fig. 2.4, but for (b) $(m,n) \leq (3,3)$, and (c) $(m,n) \leq (6,6)$ fits.

Program 2.1. *Xray-holo.f*

```
c  Xray-holo.f
c  xray hologram generator
c  may 92, s. thevuthasan
c  aug 92, p. len (comments and modifications)
c  aug 95, p. len (modification for energy scans)
c  sep 95, p. len (optimization for energy scans, 1 emitter only)
c  sep 96, p. len (finalized form)
c
        parameter (natmax = 500000, itypMx = 5, nemiMx = 20)
        parameter (pi = 3.141592653589793)
        parameter (r0 = 2.8179409238e-05)
c
        real I, I0, imff, imf1, imf2, kr, krkr, xj(3), k0
        real k(30), theta(90), phi(360)
        complex amplitude(30,90,360), e, ff
        integer atmtyp(natmax), indxEm(nemiMx), nEmitr, numtyp
        character*40 File_Ar, File_fk, File_xK
        real imf(30,0:180), ref(30,0:180), xjAtom(natmax,3)
c
c  read in the input file
        open (unit = 10, file = 'Xray-holo.in')
          read (10,*) File_Ar
          read (10,*) File_fk
          read (10,*) theta0
          read (10,*) dtheta
          read (10,*) ntheta
          read (10,*) phi0
          read (10,*) dphi
          read (10,*) nphi
          read (10,*) k0
          read (10,*) dk
          read (10,*) nk
          read (10,*) File_xK
        close (10)
        backscatter = 1e6
c
c  initialization of theta, phi, and k arrays
        do 80 itheta = 1, ntheta
          theta(itheta) = theta0 + (itheta-1)*dtheta
          theta(itheta) = theta(itheta)*pi/180.
80      continue
        do 90 iphi = 1, nphi
          phi(iphi) = phi0 + (iphi-1)*dphi
          phi(iphi) = phi(iphi)*pi/180.
90      continue
        do 100 ik = 1, nk
          k(ik) = k0 + (ik-1)*dk
100     continue
c
c  read in the coordinate file
        open (unit = 20, file = File_Ar)
        numtyp = 0
        nEmitr = 0
        do 200 jatom = 1, natmax
          read (20, *, end = 2)
&             (xjAtom(jatom,ixyz),ixyz=1,3), isEmitr, atmtyp(jatom)
          numtyp = max0(atmtyp(jatom), numtyp)
          if (isEmitr .eq. 1) then
            nEmitr = nEmitr + 1
            indxEm(nEmitr) = jatom
          endif
200     continue
2       close (20)
        natoms = jatom - 1
c
c  reading in the scattering factor file
        open (unit = 30, file = File_fk)
        do 300 ik = 1, nk
          do 300 ithetark = 0, 180
          read (30,*) dummy, ref(ik,ithetark), imf(ik,ithetark)
300     continue
```

```
      close (30)
c
c  calculation of the k vector
cccc     hbar = 1.0545726663e-34
cccc     c = 2.99792458e08
cccc     eVmtoJA = 1e-10*1.6021773349e-19
cccc     k = (energy*eVmtoJA)/(hbar*c)
c
c  start of the hologram intensity calculations
      open (unit = 40, file = File_xK)
c
c  loop over theta
     do 500 itheta = 1, ntheta
c
c  loop over phi
       do 600 iphi = 1, nphi
c
c  loop over emitters
         do 700 iemitr = 1, nEmitr
c
c  loop over atoms
           do 800 jatom = 1, natoms
c
c  emitter can't scatter onto itself
            if (jatom .eq. indxEm(iemitr)) go to 800
c
c  coordinates for j'th atom, with emitter at origin
            do 900 jxyz = 1, 3
900           xj(jxyz) = xjAtom(jatom, jxyz) -
&                        xjAtom(indxEm(iemitr), jxyz)
            r = sqrt(xj(1)**2 + xj(2)**2 + xj(3)**2)
c
c  skip atoms that lie outside backscattering cut-off
            if (xj(3) .lt. 0.0 .and. r .gt. backscatter) go to 800
c
c  finding scattering angle
      thetark = aacos((xj(1)*cos(theta(itheta))*cos(phi(iphi)) +
     &                 xj(2)*cos(theta(itheta))*sin(phi(iphi)) +
     &                 xj(3)*sin(theta(itheta))) / r)
c
c  loop over energies
            ithetark = int(thetark)
            delta = abs(thetark - ithetark)
           do 1000 ik = 1, nk
c
c  calculate diffraction attenuation
             kr = k(ik)*r
             krkr = kr*(1. - cos(thetark))
             e = cmplx(cos(krkr), sin(krkr))/kr
c
c  interpolation of scattering factor ff
c
             ref1 = ref(ik,ithetark)
             ref2 = ref(ik,ithetark + 1)
             imf1 = imf(ik,ithetark)
             imf2 = imf(ik,ithetark + 1)
c
             reff = ref1 + (ref2 - ref1)*delta
             imff = imf1 + (imf2 - imf1)*delta
c
             ff = cmplx(reff, imff)
c
c  calculation of the scattered amplitude
             amplitude(ik,itheta,iphi) = amplitude(ik,itheta,iphi) +
     &         + e*ff*r0*sqrt((1.0 + cos(thetark)**2)/2.0)
cccc     write(*,*) amplitude(ik,itheta,iphi),
cccc      &     e*ff*r0*sqrt((1.0 + cos(thetark)**2)/2.0),ik,itheta,iphi,jatom
c
c  end loop over energies
1000        continue
c
c  end loop over atoms
800       continue
c
c  end loop over emitters
```

```
700          continue
c
c  end loop over phi
600       continue
c
c  end loop over theta
500     continue
c
c  write loop
         I0 = 1.0
         do 2000 ik = 1, nk
           do 2000 itheta = 1, ntheta
             do 2000 iphi = 1, nphi
               I = (cabs(amplitude(ik,itheta,iphi) + 1.0))**2
               xK = (I - I0)/sqrt(I0)
cccc           write (40,*) theta(itheta)*180./pi, phi(iphi)*180./pi,
cccc     &      amplitude(ik,itheta,iphi)
              write (40,4000) k(ik), theta(itheta)*180./pi, phi(iphi)*180./pi, xK
2000     continue
         close (40)
4000     format(3f7.2,2x,e14.7)
         end
c
         function aacos(costhetark)
c  allows for a small amount of roundoff error when cos(thetark) is
c  calculated as a dot product.
c
         if (abs(costhetark) .gt. 1.0001) stop 'Error 1 in aacos'
         if (abs(costhetark) .gt. 1) costhetark = sign(1.0, costhetark)
         aacos = acos(costhetark)
         return
         end
```

Program 2.2. *Xray-holo-p1.f*

```
c  Xray-holo.f
c  xray hologram generator
c  may 92, s. thevuthasan
c  aug 92, p. len (comments and modifications)
c  aug 95, p. len (modification for energy scans)
c  sep 95, p. len (optimization for energy scans, 1 emitter only)
c  nov 95, p. len (addition of synchrotron polarization effects)
c  sep 96, p. len (finalized form)
c
        parameter (natmax = 500000, itypMx = 5, nemiMx = 20)
        parameter (pi = 3.141592653589793)
        parameter (r0 = 2.8179409238e-05)
c
        real I, I0, imff, imf1, imf2, kr, krkr, xj(3), k0
        real k(30), theta(90), phi(360)
        complex amplitude1(30,90,360), amplitude2(30,90,360), e, ff
        integer atmtyp(natmax), indxEm(nemiMx), nEmitr, numtyp
        character*40 File_Ar, File_fk, File_xK
        real imf(30,0:180), ref(30,0:180), xjAtom(natmax,3)
c
c  read in the input file
        open (unit = 10, file = 'Xray-holo.in')
          read (10,*) File_Ar
          read (10,*) File_fk
          read (10,*) theta0
          read (10,*) dtheta
          read (10,*) ntheta
          read (10,*) phi0
          read (10,*) dphi
          read (10,*) nphi
          read (10,*) k0
          read (10,*) dk
          read (10,*) nk
          read (10,*) File_xK
        close (10)
        backscatter = 1e6
c
c  initialization of theta, phi, and k arrays
       do 80 itheta = 1, ntheta
         theta(itheta) = theta0 + (itheta-1)*dtheta
         theta(itheta) = theta(itheta)*pi/180.
80      continue
        do 90 iphi = 1, nphi
          phi(iphi) = phi0 + (iphi-1)*dphi
          phi(iphi) = phi(iphi)*pi/180.
90      continue
        do 100 ik = 1, nk
          k(ik) = k0 + (ik-1)*dk
100     continue
c
c  read in the coordinate file
        open (unit = 20, file = File_Ar)
        numtyp = 0
        nEmitr = 0
        do 200 jatom = 1, natmax
          read (20, *, end = 2)
&             (xjAtom(jatom,ixyz),ixyz=1,3), isEmitr, atmtyp(jatom)
          numtyp = max0(atmtyp(jatom), numtyp)
          if (isEmitr .eq. 1) then
            nEmitr = nEmitr + 1
            indxEm(nEmitr) = jatom
          endif
200     continue
2       close (20)
        natoms = jatom - 1
c
c  reading in the scattering factor file
       open (unit = 30, file = File_fk)
        do 300 ik = 1, nk
          do 300 ithetark = 0, 180
          read (30,*) dummy, ref(ik,ithetark), imf(ik,ithetark)
```

```
300     continue
        close (30)
c
c  calculation of the k vector
cccc    hbar = 1.0545726663e-34
cccc    c = 2.99792458e08
cccc    eVmtoJA = 1e-10*1.6021773349e-19
cccc    k = (energy*eVmtoJA)/(hbar*c)
c
c  start of the hologram intensity calculations
        open (unit = 40, file = File_xK)
c
c  loop over theta
       do 500 itheta = 1, ntheta
c
c  loop over phi
         do 600 iphi = 1, nphi
c
c  loop over emitters
           do 700 iemitr = 1, nEmitr
c
c  loop over atoms
             do 800 jatom = 1, natoms
c
c  emitter can't scatter onto itself
               if (jatom .eq. indxEm(iemitr)) go to 800
c
c  coordinates for j'th atom, with emitter at origin
               do 900 jxyz = 1, 3
900              xj(jxyz) = xjAtom(jatom, jxyz) -
&                           xjAtom(indxEm(iemitr), jxyz)
               r = sqrt(xj(1)**2 + xj(2)**2 + xj(3)**2)
c
c  skip atoms that lie outside backscattering cut-off
               if (xj(3) .lt. 0.0 .and. r .gt. backscatter) go to 800
c
c  finding scattering angle
        thetark = aacos((xj(1)*cos(theta(itheta))*cos(phi(iphi)) +
     &                  xj(2)*cos(theta(itheta))*sin(phi(iphi)) +
     &                  xj(3)*sin(theta(itheta))) / r)
c
c  loop over energies
               ithetark = int(thetark)
               delta = abs(thetark - ithetark)
              do 1000 ik = 1, nk
c
c  calculate diffraction attenuation
                 kr = k(ik)*r
                 krkr = kr*(1. - cos(thetark))
                 e = cmplx(cos(krkr), sin(krkr))/kr
c
c  interpolation of scattering factor ff
c
                 ref1 = ref(ik,ithetark)
                 ref2 = ref(ik,ithetark + 1)
                 imf1 = imf(ik,ithetark)
                 imf2 = imf(ik,ithetark + 1)
c
                 reff = ref1 + (ref2 - ref1)*delta
                 imff = imf1 + (imf2 - imf1)*delta
c
                 ff = cmplx(reff, imff)
c
c  calculation of the scattered amplitude
                 call calc_polarization(xj,theta(itheta),phi(iphi),psi)
                 cpsi = cos(psi)
                 spsi = sin(psi)
                 amplitude1(ik,itheta,iphi) = amplitude1(ik,itheta,iphi) +
     &             + e*ff*r0*cpsi*cpsi
                 amplitude2(ik,itheta,iphi) = amplitude2(ik,itheta,iphi) +
     &             + e*ff*r0*spsi*cpsi
cccc     &                   + e*ff*r0*sqrt((1.0 + cos(thetark)**2)/2.0)
cccc    write(*,*) amplitude(ik,itheta,iphi),
cccc     &     e*ff*r0*sqrt((1.0 + cos(thetark)**2)/2.0),ik,itheta,iphi,jatom
c
```

```
c  end loop over energies
1000           continue
c
c  end loop over atoms
800           continue
c
c  end loop over emitters
700          continue
c
c  end loop over phi
600       continue
c
c  end loop over theta
500     continue
c
c  write loop
        I0 = 1.0
        do 2000 ik = 1, nk
          do 2000 itheta = 1, ntheta
            do 2000 iphi = 1, nphi
              I = (cabs(amplitude1(ik,itheta,iphi) + 1.0))**2
     &         + (cabs(amplitude2(ik,itheta,iphi)))**2
              xK = (I - I0)/sqrt(I0)
cccc          write (40,*) theta(itheta)*180./pi, phi(iphi)*180./pi,
cccc     &     amplitude(ik,itheta,iphi)
             write (40,4000) k(ik), theta(itheta)*180./pi, phi(iphi)*180./pi, xK
2000     continue
        close (40)
4000     format(3f7.2,2x,e14.7)
        end
c
        function aacos(costhetark)
c  allows for a small amount of roundoff error when cos(thetark) is
c  calculated as a dot product.
c
        if (abs(costhetark) .gt. 1.0001) stop 'Error 1 in aacos'
        if (abs(costhetark) .gt. 1) costhetark = sign(1.0, costhetark)
        aacos = acos(costhetark)
        return
        end
c
        subroutine calc_polarization(xj,theta,phi,psi)
c  calculates the effect of polarized incident synchrotron radiation
c
        real xj(3), theta, phi, opp, adj, psi
c
        ctheta = cos(theta)
        cphi = cos(phi)
        stheta = sin(theta)
        sphi = sin(phi)
c
        opp = -xj(1)*sphi + xj(2)*cphi
        adj = xj(1)*ctheta*cphi + xj(2)*ctheta*sphi + xj(3)*stheta
c
        psi = atan2(opp,adj)
cccc    cpsi = cos(psi)
cccc    c2psi = cpsi*cpsi
c
        return
        end
```

Program 2.3. *Xray-holo-p2.f*

```
c  Xray-holo.f
c  xray hologram generator
c  may 92, s. thevuthasan
c  aug 92, p. len (comments and modifications)
c  aug 95, p. len (modification for energy scans)
c  sep 95, p. len (optimization for energy scans, 1 emitter only)
c  nov 95, p. len (addition of synchrotron polarization effects)
c  sep 96, p. len (finalized form)
c
        parameter (natmax = 500000, itypMx = 5, nemiMx = 20)
        parameter (pi = 3.141592653589793)
        parameter (r0 = 2.8179409238e-05)
c
        real I, I0, imff, imf1, imf2, kr, krkr, xj(3), k0
        real k(30), theta(90), phi(360)
        complex amplitude1(30,90,360), amplitude2(30,90,360), e, ff
        integer atmtyp(natmax), indxEm(nemiMx), nEmitr, numtyp
        character*40 File_Ar, File_fk, File_xK
        real imf(30,0:180), ref(30,0:180), xjAtom(natmax,3)
c
c  read in the input file
        open (unit = 10, file = 'Xray-holo.in')
          read (10,*) File_Ar
          read (10,*) File_fk
          read (10,*) theta0
          read (10,*) dtheta
          read (10,*) ntheta
          read (10,*) phi0
          read (10,*) dphi
          read (10,*) nphi
          read (10,*) k0
          read (10,*) dk
          read (10,*) nk
          read (10,*) File_xK
        close (10)
        backscatter = 1e6
c
c  initialization of theta, phi, and k arrays
        do 80 itheta = 1, ntheta
          theta(itheta) = theta0 + (itheta-1)*dtheta
          theta(itheta) = theta(itheta)*pi/180.
80      continue
        do 90 iphi = 1, nphi
          phi(iphi) = phi0 + (iphi-1)*dphi
          phi(iphi) = phi(iphi)*pi/180.
90      continue
        do 100 ik = 1, nk
          k(ik) = k0 + (ik-1)*dk
100     continue
c
c  read in the coordinate file
        open (unit = 20, file = File_Ar)
        numtyp = 0
        nEmitr = 0
        do 200 jatom = 1, natmax
          read (20, *, end = 2)
&              (xjAtom(jatom,ixyz),ixyz=1,3), isEmitr, atmtyp(jatom)
          numtyp = max0(atmtyp(jatom), numtyp)
          if (isEmitr .eq. 1) then
            nEmitr = nEmitr + 1
            indxEm(nEmitr) = jatom
          endif
200     continue
2       close (20)
        natoms = jatom - 1
c
c  reading in the scattering factor file
        open (unit = 30, file = File_fk)
        do 300 ik = 1, nk
          do 300 ithetark = 0, 180
          read (30,*) dummy, ref(ik,ithetark), imf(ik,ithetark)
```

```
300     continue
        close (30)
c
c  calculation of the k vector
cccc    hbar = 1.0545726663e-34
cccc    c = 2.99792458e08
cccc    eVmtoJA = 1e-10*1.6021773349e-19
cccc    k = (energy*eVmtoJA)/(hbar*c)
c
c  start of the hologram intensity calculations
        open (unit = 40, file = File_xK)
c
c  loop over theta
       do 500 itheta = 1, ntheta
c
c  loop over phi
         do 600 iphi = 1, nphi
c
c  loop over emitters
           do 700 iemitr = 1, nEmitr
c
c  loop over atoms
             do 800 jatom = 1, natoms
c
c  emitter can't scatter onto itself
               if (jatom .eq. indxEm(iemitr)) go to 800
c
c  coordinates for j'th atom, with emitter at origin
               do 900 jxyz = 1, 3
900              xj(jxyz) = xjAtom(jatom, jxyz) -
&                           xjAtom(indxEm(iemitr), jxyz)
               r = sqrt(xj(1)**2 + xj(2)**2 + xj(3)**2)
c
c  skip atoms that lie outside backscattering cut-off
               if (xj(3) .lt. 0.0 .and. r .gt. backscatter) go to 800
c
c  finding scattering angle
       thetark = aacos((xj(1)*cos(theta(itheta))*cos(phi(iphi)) +
     &                 xj(2)*cos(theta(itheta))*sin(phi(iphi)) +
     &                 xj(3)*sin(theta(itheta))) / r)
c
c  loop over energies
               ithetark = int(thetark)
               delta = abs(thetark - ithetark)
              do 1000 ik = 1, nk
c
c  calculate diffraction attenuation
                kr = k(ik)*r
                krkr = kr*(1. - cos(thetark))
                e = cmplx(cos(krkr), sin(krkr))/kr
c
c  interpolation of scattering factor ff
c
                ref1 = ref(ik,ithetark)
                ref2 = ref(ik,ithetark + 1)
                imf1 = imf(ik,ithetark)
                imf2 = imf(ik,ithetark + 1)
c
                reff = ref1 + (ref2 - ref1)*delta
                imff = imf1 + (imf2 - imf1)*delta
c
                ff = cmplx(reff, imff)
c
c  calculation of the scattered amplitude
                call calc_polarization(xj,theta(itheta),phi(iphi),psi)
                cpsi = cos(psi)
                spsi = sin(psi)
                amplitude1(ik,itheta,iphi) = amplitude1(ik,itheta,iphi) +
     &            + e*ff*r0*cpsi*cpsi
                amplitude2(ik,itheta,iphi) = amplitude2(ik,itheta,iphi) +
     &            + e*ff*r0*spsi*cpsi
cccc     &                  + e*ff*r0*sqrt((1.0 + cos(thetark)**2)/2.0)
cccc    write(*,*) amplitude(ik,itheta,iphi),
cccc     &     e*ff*r0*sqrt((1.0 + cos(thetark)**2)/2.0),ik,itheta,iphi,jatom
c
```

```
c  end loop over energies
1000           continue
c
c  end loop over atoms
800           continue
c
c  end loop over emitters
700          continue
c
c  end loop over phi
600       continue
c
c  end loop over theta
500     continue
c
c  write loop
        I0 = 1.0
        do 2000 ik = 1, nk
          do 2000 itheta = 1, ntheta
            do 2000 iphi = 1, nphi
              I = (cabs(amplitude1(ik,itheta,iphi) + 1.0))**2
     &         + (cabs(amplitude2(ik,itheta,iphi)))**2
              xK = (I - I0)/sqrt(I0)
cccc          write (40,*) theta(itheta)*180./pi, phi(iphi)*180./pi,
cccc     &     amplitude(ik,itheta,iphi)
             write (40,4000) k(ik), theta(itheta)*180./pi, phi(iphi)*180./pi, xK
2000     continue
        close (40)
4000     format(3f7.2,2x,e14.7)
        end
c
        function aacos(costhetark)
c  allows for a small amount of roundoff error when cos(thetark) is
c  calculated as a dot product.
c
        if (abs(costhetark) .gt. 1.0001) stop 'Error 1 in aacos'
        if (abs(costhetark) .gt. 1) costhetark = sign(1.0, costhetark)
        aacos = acos(costhetark)
        return
        end
c
        subroutine calc_polarization(xj,theta,phi,psi)
c  calculates the effect of polarized incident synchrotron radiation
c
        real xj(3), theta, phi, opp, adj, psi
c
        ctheta = cos(theta)
        cphi = cos(phi)
        stheta = sin(theta)
        sphi = sin(phi)
c
        opp = -xj(1)*stheta*cphi - xj(2)*stheta*sphi - xj(3)*ctheta
        adj = xj(1)*ctheta*cphi + xj(2)*ctheta*sphi + xj(3)*stheta
c
        psi = atan2(opp,adj)
cccc    cpsi = cos(psi)
cccc    c2psi = cpsi*cpsi
c
        return
        end
```

Program 2.4. *Io-magk.f*

```
c  Io-magk.f
c
c  this program reads in different energy holograms,
c  then normalizes them with respect to each other
c
c  jul 95,     p. len
c  sep 96,     p. len  (final form)
c
c  initialization and parameterization
         real theta(90,360), phi(90,360), xK(200,90,360)
cccc     real kx(10,90,360), ky(10,90,360), kz(10,90,360)
         real xK0(200), xK1(200)
         integer ntheta, nphi
         character*80 rawxK, normxK
         parameter(pi = 3.141592654)
         parameter(degtorad = pi/360.0)
         real ctheta(90,360)
c
c  read in reconstruction integration parameters
         open(unit = 10, file = 'Io.in')
           read(10,10) rawxK
           read(10,*) ntheta
           read(10,*) nphi
cccc       read(10,*) k0
cccc       read(10,*) dk
           read(10,*) nk
           read(10,10) normxK
           read(10,*) sigma
         close(10)
10       format(a40)
c
c  main read-in routine
         open(unit = 20, file = rawxK)
         do 100 ik = 1, nk
           do 101 itheta = 1, ntheta
             do 102 iphi = 1, nphi
               read (20,*) k(ik), theta(itheta,iphi), phi(itheta,iphi),
     &                     xK(ik,itheta,iphi)
102            continue
101          continue
100      continue
         close(20)
c
c  calculation of cos and sin functions.  All input angles are
c  now converted to radians.
          do 201 itheta = 1, ntheta
            do 202 iphi = 1, nphi
              ctheta(itheta,iphi) = cos(theta(itheta,iphi)*degtorad)
202           continue
201         continue
c
         do 300 ik = 1, nk
           xK0(ik) = 0.0
           do 301 itheta = 1, ntheta
             do 302 iphi = 1, nphi
               xK0(ik) = xK0(ik) + xK(ik,itheta,iphi)*ctheta(itheta,iphi)
               xK1(ik) = xK1(ik) + ctheta(itheta,iphi)
302          continue
301        continue
         write(*,*) ik, xK0(ik), xK1(ik), xK0(ik)/xK1(ik)
300      continue
c
         open (unit = 40, file = normxK)
cccc     open (unit = 50, file = 'test')
         do 400 ik = 1, nk
           do 401 itheta = 1, ntheta
             do 402 iphi = 1, nphi
               write(40,4000) k(ik), theta(itheta,iphi), phi(itheta,iphi),
     &   xK(ik,itheta,iphi)-(xK0(ik)/xK1(ik))
cccc     write(50,*) phi(itheta,iphi), xK(ik,itheta,iphi)-(xK0(ik)/xK1(ik))
402          continue
```

```
401         continue
400       continue
cccc4000 format(2f7.2,2x,e14.7)
4000      format(3f7.2,2x,e14.7)
c
          close(40)
          stop
          end
```

Program 2.5. *Io-khat.f*

```
c  Io-khat.f
c
c  fits a least squares line for I0 removal from scanned-energy data
c  sep 96      p. len  (final form)
c
        character*80 file_in, file_out
        real theta(30,120), phi(30,120)
        real xK(200,30,120)
        real xK1(200), xK0(200)
c
        open (unit = 10, file = 'Io.in')
          read (10,1) file_in
          read (10,*) ntheta
          read (10,*) nphi
          read (10,*) nk
          read (10,1) file_out
          read (10,*) sigma
        close (10)
1       format (a40)
c
        open (unit = 20, file = file_in)
        do 200 ik = 1, nk
          do 200 itheta = 1, ntheta
            do 200 iphi = 1, nphi
              read (20,*) k(ik), theta(itheta,iphi), phi(itheta,iphi),
     &                    xK(ik,itheta,iphi)
200     continue
        close(20)
c
        do 300 itheta = 1, ntheta
          do 300 iphi = 1, nphi
            do 310 ik = 1, nk
              xK1(ik) = xK(ik,itheta,iphi)
ccccc         call calc_xK0(xK1, nk, xK0)
310         continue
            call calc_xK0(xK1, nk, xK0)
            do 320 ik = 1, nk
              xK(ik,itheta,iphi) = xK1(ik) - xK0(ik)
320         continue
300     continue
c
        open (unit = 40, file = file_out)
        do 400 ik = 1, nk
          do 400 itheta = 1, ntheta
            do 400 iphi = 1, nphi
              write (40,4) k(ik), theta(itheta,iphi), phi(itheta,iphi),
     &                     xK(ik,itheta,iphi)
400     continue
        close (40)
cccc4   format(2f6.1,2x,e14.7)
4       format(3f6.1,2x,e14.7)
        stop
        end
c
        subroutine calc_xK0(xK1, nk, xK0)
c
        real xK1(200), xK0(200), k(200)
c
        do 1000 ik = 1, nk
          k(ik) = real(ik)
1000    continue
c
        call lstsqr(k, xK1, nk, a, b)
c
        do 1100 ik = 1, nk
          xK0(ik) = a*real(ik) + b
1100    continue
        return
        end
c
        subroutine lstsqr(x, y, n, a, b)
```

```
c
c  calculates the coefficients of the equation y = ax + b that best fits
c  the data supplied in the arrays x and y, using a least squares fit
c  t. m. r. ellis, _fortran 77 programming, 2nd ed._
c
        integer n
        real x(n), y(n), a, b
c
        integer i
        real xsum, ysum, xysum, x2sum
c
        xsum = 0.
        ysum = 0.
        xysum = 0.
        x2sum = 0.
c
        do 2000 i = 1, n
          xsum = xsum + x(i)
          ysum = ysum + y(i)
          xysum = xysum + x(i)*y(i)
          x2sum = x2sum + x(i)*x(i)
2000    continue
c
        a = (xsum*ysum - n*xysum)/(xsum*xsum - n*x2sum)
        b = (ysum - a*xsum)/n
        return
        end
```

Program 2.6. *Filter.f*

```
c  Filter.f
c
c  this program reads in different energy holograms,
c  then convolutes them with a gaussian, in order to
c  remove high-frequency x(K') fringes associated with
c  atoms far away from the emitter, producing a low-
c  pass filtered x(K).  low-pass filtered x(K) is then
c  subtracted from the raw x(K) to obtain a high-pass
c  filtered x(K)
c
c  jul 95,      p. len
c  aug 95,      p. len (corrections)
c  sep 96,      p. len (finalized form)
c
c  initialization and parameterization
         real theta(45,180), phi(45,180), xK(30,45,180)
         real kx(30,45,180), ky(30,45,180), kz(30,45,180)
         real k(30), k0, kkx, kky, kkz
         integer ntheta, nphi
cccc     character*40 rawxK, lopassxK
         character*80 rawxK, hipassxK, lopassxK
         parameter(pi = 3.141592654)
         parameter(degtorad = pi/180.0)
         real ctheta(45,180)
c
c  read in reconstruction integration parameters
         open(unit = 10, file = 'GaussxK.in')
           read(10,10) rawxK
           read(10,*) ntheta
           read(10,*) nphi
cccc       read(10,*) k0
cccc       read(10,*) dk
           read(10,*) nk
           read(10,10) hipassxK
cccc       read(10,10) lopassxK
           read(10,*) sigma
cccc       read(10,*) symmetry
         close(10)
10       format(a80)
c
c  initialize k
        do 90 ik = 1, nk
          k(ik) = k0 + (ik-1)*dk
90      continue
c
c  main read-in routine
         open(unit = 20, file = rawxK)
         do 100 ik = 1, nk
           do 101 itheta = 1, ntheta
             do 102 iphi = 1, nphi
               read (20,*) k(ik), theta(itheta,iphi), phi(itheta,iphi),
     &                     xK(ik,itheta,iphi)
102            continue
101          continue
100      continue
         close(20)
c
c  calculation of cos and sin functions.  All input angles are
c  now converted to radians.
        do 200 itheta = 1, ntheta
          do 201 iphi = 1, nphi
            ctheta(itheta,iphi) = cos(theta(itheta,iphi)*degtorad)
            stheta = sin(theta(itheta,iphi)*degtorad)
            cphi = cos(phi(itheta,iphi)*degtorad)
            sphi = sin(phi(itheta,iphi)*degtorad)
            do 202 ik = 1, nk
              kx(ik,itheta,iphi) = k(ik)*ctheta(itheta,iphi)*cphi
              ky(ik,itheta,iphi) = k(ik)*ctheta(itheta,iphi)*sphi
              kz(ik,itheta,iphi) = k(ik)*stheta
202           continue
201        continue
```

```
200      continue
c
c  loop over each direction in x(K)
         open (unit = 30, file = lopassxK)
         open (unit = 31, file = hipassxK)
         do 300 ik = 1, nk
           do 301 itheta = 1, ntheta
cccc         do 302 iphi = 1, symmetry
             do 302 iphi = 1, nphi
               xKlo = 0.0
               A = 0.0
c  integrate over all K' directions in x(K')
cccc           do 303 jk = 1, nk
         jk = ik
                  do 304 jtheta = 1, ntheta
                   do 305 jphi = 1, nphi
c  find the Gaussian weighing function
                     kkx = (kx(ik,itheta,iphi) - kx(jk,jtheta,jphi))
                     kky = (ky(ik,itheta,iphi) - ky(jk,jtheta,jphi))
                     kkz = (kz(ik,itheta,iphi) - kz(jk,jtheta,jphi))
                     deltak2 = kkx*kkx + kky*kky + kkz*kkz
                    egauss = exp(-deltak2/(sigma*sigma))
                     xKlo = xKlo +
     &                      xK(jk,jtheta,jphi)*egauss*ctheta(jtheta,jphi)
                     A = A + egauss*ctheta(jtheta,jphi)
305                continue
304                continue
cccc303          continue
                 xKlo = xKlo/A
                 xKhi = xK(ik,itheta,iphi) - xKlo
cccc             write(30,3000) theta(itheta,iphi), phi(itheta,iphi), xKlo
                 write(31,3000) k(ik), theta(itheta,iphi), phi(itheta,iphi), xKhi
302            continue
301          continue
300      continue
cccc3000 format(2f6.1,2x,e14.7)
3000     format(3f6.1,2x,e14.7)
         close(30)
         close(31)
c
         stop
         end
```

Program 2.7. *Fit-Io.m*

```
inputfile = OpenRead["raw:Ik"];
iKraw = ReadList[inputfile, {Number,Number,Number,Number}];
Close[inputfile];

stream1 = OpenAppend["normalized:xK",
FormatType -> OutputForm];

stream2 = OpenAppend["background:Io",
FormatType -> OutputForm];

unused = (1 + k + k^2 + k^3 + k^4 + k^5 + k^6)*
     + Cos[theta Degree] + Cos[3*theta Degree] + Cos[5*theta Degree]
     + Cos[7*theta Degree] + Cos[9*theta Degree] + Cos[11*theta Degree])

iK = Interpolation[iKraw];

io = Fit[iKraw, {1, k, Power[k, 2], Power[k, 3], Power[k, 4], Power[k, 5],

    Power[k, 6], Cos[Times[Degree, theta]],

    Times[k, Cos[Times[Degree, theta]]],

    Times[Power[k, 2], Cos[Times[Degree, theta]]],

    Times[Power[k, 3], Cos[Times[Degree, theta]]],

    Times[Power[k, 4], Cos[Times[Degree, theta]]],

    Times[Power[k, 5], Cos[Times[Degree, theta]]],

    Times[Power[k, 6], Cos[Times[Degree, theta]]],

    Cos[Times[3, Degree, theta]], Times[k, Cos[Times[3, Degree, theta]]],

    Times[Power[k, 2], Cos[Times[3, Degree, theta]]],

    Times[Power[k, 3], Cos[Times[3, Degree, theta]]],

    Times[Power[k, 4], Cos[Times[3, Degree, theta]]],

    Times[Power[k, 5], Cos[Times[3, Degree, theta]]],

    Times[Power[k, 6], Cos[Times[3, Degree, theta]]],

    Cos[Times[5, Degree, theta]], Times[k, Cos[Times[5, Degree, theta]]],

    Times[Power[k, 2], Cos[Times[5, Degree, theta]]],

    Times[Power[k, 3], Cos[Times[5, Degree, theta]]],

    Times[Power[k, 4], Cos[Times[5, Degree, theta]]],

    Times[Power[k, 5], Cos[Times[5, Degree, theta]]],

    Times[Power[k, 6], Cos[Times[5, Degree, theta]]],

    Cos[Times[7, Degree, theta]], Times[k, Cos[Times[7, Degree, theta]]],

    Times[Power[k, 2], Cos[Times[7, Degree, theta]]],

    Times[Power[k, 3], Cos[Times[7, Degree, theta]]],

    Times[Power[k, 4], Cos[Times[7, Degree, theta]]],

    Times[Power[k, 5], Cos[Times[7, Degree, theta]]],

    Times[Power[k, 6], Cos[Times[7, Degree, theta]]],

    Cos[Times[9, Degree, theta]], Times[k, Cos[Times[9, Degree, theta]]],

    Times[Power[k, 2], Cos[Times[9, Degree, theta]]],
```

```
    Times[Power[k, 3], Cos[Times[9, Degree, theta]]],

    Times[Power[k, 4], Cos[Times[9, Degree, theta]]],

    Times[Power[k, 5], Cos[Times[9, Degree, theta]]],

    Times[Power[k, 6], Cos[Times[9, Degree, theta]]],

    Cos[Times[11, Degree, theta]], Times[k, Cos[Times[11, Degree, theta]]],

    Times[Power[k, 2], Cos[Times[11, Degree, theta]]],

    Times[Power[k, 3], Cos[Times[11, Degree, theta]]],

    Times[Power[k, 4], Cos[Times[11, Degree, theta]]],

    Times[Power[k, 5], Cos[Times[11, Degree, theta]]],

    Times[Power[k, 6], Cos[Times[11, Degree, theta]]]},

{k,theta,phi}];

stream3 = OpenAppend["background:co-eff",
FormatType -> OutputForm];
      Write[stream3, io];

Do[
  Do[
    Do[
      xK = (iK[k,theta,phi] - N[io])/Abs[N[io]];
      Write[stream1, theta, "   ", phi, "   ", FortranForm[xK]];
      Write[stream2, theta, "   ", phi, "   ", FortranForm[N[io]]],
    {phi, 0, 355, 5}],
  {theta, 40, 85, 5}],
{k, 3.85, 7.45, 0.1}];

Close[stream1];
Close[stream2];
Exit
```

Program 2.8. *HoloInvert.f*

```
c  HoloInvert.f
c
c  this program reconstructs atomic images from holographic intensities.
c
c  please acknowledge use of this program.  please contact:
c  p. m. len
c  physics department
c  university of california, davis
c  davis, ca  95616
c
c  mahalo nui loa (hawaiian, "thank you very much")
c
c  s. thevuthasan, may 93            original program
c  a. p. kaduwela, jan 95            reoptimized for scalar machines
c  p. m. len, mar 96          final modifications
c  p. m. len, sep 96          final modifications
c
c  to compile this code on a cray:
c  cf77 -Zv HoloInvert.f -o HoloInvert
c
c  to compile this code on a SUN:
c  f77 -r8 -i4 -O3 HoloInvert.f -o HoloInvert
c
c  initialization and parameterization
        real k(40), x(256), y(256), z(256)
        real k0, krkr, theta(18,72), phi(18,72), xK(40,18,72)
        real stheta(18,72), ctheta(18,72)
        real kx(18,72), ky(18,72), kz(18,72)
        complex kern, dUr, Ur
        integer nx, nz, nk, ntheta, nphi
        character*80 FilexK, FileUr
        parameter(pi = 3.141592654)
        parameter(degtorad = pi/180.0)
c
c  read in reconstruction integration parameters
        open(unit = 10, file = 'HoloInvert.in')
          read(10,10) FilexK
          read(10,*) ntheta
          read(10,*) nphi
cccc      read(10,*) k0
cccc      read(10,*) dk
          read(10,*) nk
          read(10,*) rotate
          read(10,10) FileUr
          read(10,*) xmin, xmax, dx
          read(10,*) ymin, ymax, dy
          read(10,*) zmin, zmax, dz
        close(10)
        nx = ((xmax - xmin)/dx) + 1
        ny = ((ymax - ymin)/dy) + 1
        nz = ((zmax - zmin)/dz) + 1
c       k0 = 0.5121365847*sqrt(energy)
10      format(a80)
c
c  initialization of k, x, y, and z arrays
        do 60 ix = 1, nx
          x(ix) = xmin + (ix-1)*dx
60      continue
        do 70 iy = 1, ny
          y(iy) = ymin + (iy-1)*dy
70      continue
        do 80 iz = 1, nz
          z(iz) = zmin + (iz-1)*dz
80      continue
cccc    do 90 ik = 1, nk
cccc      k(ik) = k0 + (ik-1)*dk
cccc90  continue
c
c  main read-in routine
        open(unit = 20, file = FilexK)
        do 100 ik = 1, nk
```

```
          do 101 itheta = 1, ntheta
            do 102 iphi = 1, nphi
              read(20,*) k(ik), theta(itheta,iphi), phi(itheta,iphi),
     &                   xK(ik,itheta,iphi)
              theta(itheta,iphi) = theta(itheta,iphi)*degtorad
              phi(itheta,iphi) = (phi(itheta,iphi) - rotate)*degtorad
102         continue
101       continue
100     continue
        close(20)
c
c  initialization of angles and trigonometrics
        do 200 itheta = 1, ntheta
          do 200 iphi = 1, nphi
            ctheta(itheta,iphi) = cos(theta(itheta,iphi))
            stheta(itheta,iphi) = sin(theta(itheta,iphi))
            kx(itheta,iphi) = ctheta(itheta,iphi)*cos(phi(itheta,iphi))
            ky(itheta,iphi) = ctheta(itheta,iphi)*sin(phi(itheta,iphi))
            kz(itheta,iphi) = stheta(itheta,iphi)
200     continue
c
c  loop over each position in U(r)
        open(unit = 30, file = FileUr)
        do 300 ix = 1, nx
          do 301 iy = 1, ny
            do 302 iz = 1, nz
            dUr = (0., 0.)
            r = sqrt(x(ix)*x(ix) + y(iy)*y(iy) + z(iz)*z(iz))
c  integrate over hologram solid angle
            do 303 itheta = 1, ntheta
              do 304 iphi = 1, nphi
              xkx = x(ix)*kx(itheta,iphi)
              yky = y(iy)*ky(itheta,iphi)
              zkz = z(iz)*kz(itheta,iphi)
c  phase-sum over different wavenumbers
                do 305 ik = 1, nk
                  krkr = k(ik)*(xkx + yky + zkz) - k(ik)*r
                  kern = cmplx(cos(krkr),sin(krkr))
        dUr = dUr + xK(ik,itheta,iphi)*kern*k(ik)*k(ik)*ctheta(itheta,iphi)
305             continue
c  end phase-sum
304           continue
303           continue
              Ur = dUr
              write(30,30) x(ix), y(iy), z(iz), Ur
cccc          write(30,30) Ur
c  end hologram solid angle integration
302         continue
301       continue
300     continue
c  end loop over each position in U(r)
cccc30  format(2(2x,e12.5))
30      format(3(2x,f6.2),2(2x,e12.5))
c
        close(30)
        end
```

Program 2.9. *HoloInvert:2.0a.f*

```
c  HoloInvert.f
c  version 2.0a
c
c  this program reconstructs atomic images from holographic intensities.
c
c  please acknowledge use of this program.  please contact:
c  p. m. len
c  physics department
c  university of california, davis
c  davis, ca  95616
c
c  s. thevuthasan, may 93            original program
c  a. p. kaduwela, jan 95            reoptimized for scalar machines
c  p. m. len, mar 96          final modifications
c  p. m. len, jul 96          implementation of SWIFT
c  p. m. len, sep 96            final modifications
c
c  to compile this code on a cray:
c  cf77 -Zv HoloInvert.f -o HoloInvert
c
c  to compile this code on a SUN:
c  f77 -r8 -i4 -O3 HoloInvert.f -o HoloInvert
c
c  initialization and parameterization
        real k(40), x(256), y(256), z(256)
        real k0, krkr, theta(18,72), phi(18,72), xK(40,18,72)
       real stheta(18,72), ctheta(18,72)
        real kx(18,72), ky(18,72), kz(18,72)
        complex kern, dUr, Ur
        integer nx, nz, nk, ntheta, nphi
        character*80 FilexK, FileUr
        parameter(pi = 3.141592654)
        parameter(degtorad = pi/180.0)
c
        real fk(40,0:180)
c
c  read in reconstruction integration parameters
        open(unit = 10, file = 'HoloInvert.in')
          read(10,10) FilexK
          read(10,*) ntheta
          read(10,*) nphi
cccc      read(10,*) k0
cccc      read(10,*) dk
          read(10,*) nk
          read(10,*) rotate
          read(10,10) FileUr
          read(10,*) xmin, xmax, dx
          read(10,*) ymin, ymax, dy
          read(10,*) zmin, zmax, dz
        close(10)
        nx = ((xmax - xmin)/dx) + 1
        ny = ((ymax - ymin)/dy) + 1
        nz = ((zmax - zmin)/dz) + 1
c       k0 = 0.5121365847*sqrt(energy)
10      format(a80)
c
        call read_fk(nk,fk)
c
c  initialization of k, x, y, and z arrays
        do 60 ix = 1, nx
          x(ix) = xmin + (ix-1)*dx
60      continue
        do 70 iy = 1, ny
          y(iy) = ymin + (iy-1)*dy
70      continue
        do 80 iz = 1, nz
          z(iz) = zmin + (iz-1)*dz
80      continue
cccc    do 90 ik = 1, nk
cccc      k(ik) = k0 + (ik-1)*dk
cccc90  continue
```

```
c
c  main read-in routine
         open(unit = 20, file = FilexK)
         do 100 ik = 1, nk
           do 101 itheta = 1, ntheta
             do 102 iphi = 1, nphi
               read(20,*) k(ik), theta(itheta,iphi), phi(itheta,iphi),
     &                    xK(ik,itheta,iphi)
              theta(itheta,iphi) = theta(itheta,iphi)*degtorad
              phi(itheta,iphi) = (phi(itheta,iphi) - rotate)*degtorad
102          continue
101        continue
100      continue
         close(20)
c
c  initialization of angles and trigonometrics
        do 200 itheta = 1, ntheta
          do 200 iphi = 1, nphi
            ctheta(itheta,iphi) = cos(theta(itheta,iphi))
            stheta(itheta,iphi) = sin(theta(itheta,iphi))
            kx(itheta,iphi) = ctheta(itheta,iphi)*cos(phi(itheta,iphi))
            ky(itheta,iphi) = ctheta(itheta,iphi)*sin(phi(itheta,iphi))
            kz(itheta,iphi) = stheta(itheta,iphi)
200      continue
c
c  loop over each position in U(r)
         open(unit = 30, file = FileUr)
         do 300 ix = 1, nx
           do 301 iy = 1, ny
             do 302 iz = 1, nz
             dUr = (0., 0.)
             r = sqrt(x(ix)*x(ix) + y(iy)*y(iy) + z(iz)*z(iz))
c  integrate over hologram solid angle
             do 303 itheta = 1, ntheta
               do 304 iphi = 1, nphi
               xkx = x(ix)*kx(itheta,iphi)
               yky = y(iy)*ky(itheta,iphi)
               zkz = z(iz)*kz(itheta,iphi)
               costhetark = (xkx + yky + zkz)/r
c  phase-sum over different wavenumbers
                 do 305 ik = 1, nk
                   call interpolate_ff(ik,costhetark,fk,ff)
                     krkr = k(ik)*(xkx + yky + zkz) - k(ik)*r
                     kern = cmplx(cos(krkr),sin(krkr))
        dUr = dUr + xK(ik,itheta,iphi)*kern*k(ik)*k(ik)*ctheta(itheta,iphi)/ff
305                continue
c  end phase-sum
304              continue
303            continue
               Ur = dUr
cccc           write(30,30) Ur
               write(30,30) x(ix), y(iy), z(iz), Ur
c  end hologram solid angle integration
302          continue
301        continue
300      continue
c  end loop over each position in U(r)
cccc30   format(2(2x,e12.5))
30       format(3(2x,f6.2),2(2x,e12.5))
c
         close(30)
         end
c
        subroutine read_fk(nk, fk)
c  this subroutine reads in the scattering factor magnitudes that are output
c  from fkSWIFT.f
c
        real fk(nk,0:180)
c
        open(unit = 40, file = 'fk.in')
        do 400 ik = 1, nk
          read(40,*) k_no_use
          do 400 itheta = 0, 180
            read(40,*) fk(ik,itheta)
400     continue
```

```
      close(40)
      return
      end
c
      subroutine interpolate_ff(ik, costhetark, fk, ff)
c  this subroutine interpolates the scattering factor magnitude for the angle
c  thetark, given cos(thetark)
c
      real costhetark, fk(11,0:180)
c
      thetark = aacos(costhetark)
      ithetark = int(thetark)
      delta = abs(thetark - ithetark)
c
      ff1 = fk(ik,ithetark)
      if (ithetark .eq. 180) then ithetark = 178
      ff2 = fk(ik,ithetark + 1)
c
      ff = ff1 + (ff2 - ff1)*delta
c
      return
      end
c
      function aacos(costhetark)
c  this function calculates acos(cos(thetark), but allows for a small amount
c  of round-off error when cos(thetark) is calculated as a dot product
c
      real costhetark, aacos
c
      if (abs(costhetark) .gt. 1.0001) stop 'Error 1 in aacos'
      if (abs(costhetark) .gt. 1) costhetark = sign(1., costhetark)
      aacos = acos(costhetark)
      return
      end
```

Program 2.10. *HoloInvert:2.0b.f*

```
c  HoloInvert.f
c  version 2.0b
c
c  this program reconstructs atomic images from holographic intensities.
c
c  please acknowledge use of this program.  please contact:
c  p. m. len
c  physics department
c  university of california, davis
c  davis, ca  95616
c
c  s. thevuthasan, may 93            original program
c  a. p. kaduwela, jan 95            reoptimized for scalar machines
c  p. m. len, mar 96          final modifications
c  p. m. len, jul 96          implementation of small cone routine
c  p. m. len, sep 96            final modifications
c
c  to compile this code on a cray:
c  cf77 -Zv HoloInvert.f -o HoloInvert
c
c  to compile this code on a SUN:
c  f77 -r8 -i4 -O3 HoloInvert.f -o HoloInvert
c
c  initialization and parameterization
        real k(40), x(256), y(256), z(256)
        real k0, krkr, theta(18,72), phi(18,72), xK(40,18,72)
       real stheta(18,72), ctheta(18,72)
        real kx(18,72), ky(18,72), kz(18,72)
        complex kern, dUr, Ur
        integer nx, nz, nk, ntheta, nphi
        character*80 FilexK, FileUr
        parameter(pi = 3.141592654)
        parameter(degtorad = pi/180.0)
c
c  read in reconstruction integration parameters
        open(unit = 10, file = 'HoloInvert.in')
          read(10,10) FilexK
          read(10,*) ntheta
          read(10,*) nphi
cccc      read(10,*) k0
cccc      read(10,*) dk
          read(10,*) nk
          read(10,*) rotate
          read(10,10) FileUr
          read(10,*) xmin, xmax, dx
          read(10,*) ymin, ymax, dy
          read(10,*) zmin, zmax, dz
        close(10)
        nx = ((xmax - xmin)/dx) + 1
        ny = ((ymax - ymin)/dy) + 1
        nz = ((zmax - zmin)/dz) + 1
c       k0 = 0.5121365847*sqrt(energy)
10      format(a80)
c
        call read_window(coswindow)
c
c  initialization of k, x, y, and z arrays
        do 60 ix = 1, nx
          x(ix) = xmin + (ix-1)*dx
60      continue
        do 70 iy = 1, ny
          y(iy) = ymin + (iy-1)*dy
70      continue
        do 80 iz = 1, nz
          z(iz) = zmin + (iz-1)*dz
80      continue
cccc    do 90 ik = 1, nk
cccc      k(ik) = k0 + (ik-1)*dk
cccc90  continue
c
c  main read-in routine
```

```
        open(unit = 20, file = FilexK)
        do 100 ik = 1, nk
          do 101 itheta = 1, ntheta
            do 102 iphi = 1, nphi
              read(20,*) theta(itheta,iphi), phi(itheta,iphi),
     &                   xK(ik,itheta,iphi)
              theta(itheta,iphi) = theta(itheta,iphi)*degtorad
              phi(itheta,iphi) = (phi(itheta,iphi) - rotate)*degtorad
102         continue
101       continue
100     continue
        close(20)
c
c  initialization of angles and trigonometrics
        do 200 itheta = 1, ntheta
          do 200 iphi = 1, nphi
            ctheta(itheta,iphi) = cos(theta(itheta,iphi))
            stheta(itheta,iphi) = sin(theta(itheta,iphi))
            kx(itheta,iphi) = ctheta(itheta,iphi)*cos(phi(itheta,iphi))
            ky(itheta,iphi) = ctheta(itheta,iphi)*sin(phi(itheta,iphi))
            kz(itheta,iphi) = stheta(itheta,iphi)
200     continue
c
c  loop over each position in U(r)
        open(unit = 30, file = FileUr)
        do 300 ix = 1, nx
          do 301 iy = 1, ny
            do 302 iz = 1, nz
            dUr = (0., 0.)
            r = sqrt(x(ix)*x(ix) + y(iy)*y(iy) + z(iz)*z(iz))
c  integrate over hologram solid angle
            do 303 itheta = 1, ntheta
              do 304 iphi = 1, nphi
              xkx = x(ix)*kx(itheta,iphi)
              yky = y(iy)*ky(itheta,iphi)
              zkz = z(iz)*kz(itheta,iphi)
              costhetark = abs((xkx + yky + zkz)/r)
                if (costhetark .gt. coswindow) then
c  phase-sum over different wavenumbers
                  do 305 ik = 1, nk
                    krkr = k(ik)*(xkx + yky + zkz) - k(ik)*r
                    kern = cmplx(cos(krkr),sin(krkr))
        dUr = dUr + xK(ik,itheta,iphi)*kern*k(ik)*k(ik)*ctheta(itheta,iphi)
305               continue
                endif
c  end phase-sum
304           continue
303         continue
            Ur = dUr
cccc        write(30,30) Ur
            write(30,30) x(ix), y(iy), z(iz), Ur
c  end hologram solid angle integration
302       continue
301     continue
300   continue
c  end loop over each position in U(r)
cccc30  format(2(2x,e12.5))
30    format(3(2x,f6.2),2(2x,e12.5))
c
        close(30)
        end
c
        subroutine read_window(coswindow)
c  this subroutine reads in the small-cone half-angle
c
        real window, coswindow
c
        open(unit = 40, file = 'window.in')
          read(40,*) window
        close(40)
        coswindow = cos(window*3.141592654/180.)
        return
        end
```

Program 2.11. *HoloInvert:2.0c.f*

```
c  HoloInvert.f
c  version 2.0c
c
c  this program reconstructs atomic images from holographic intensities.
c
c  please acknowledge use of this program.  please contact:
c  p. m. len
c  physics department
c  university of california, davis
c  davis, ca  95616
c
c  s. thevuthasan, may 93            original program
c  a. p. kaduwela, jan 95            reoptimized for scalar machines
c  p. m. len, mar 96          final modifications
c  p. m. len, jul 96          implementation of rous-rubin algorithm
c  p. m. len, sep 96            final modifications
c
c  to compile this code on a cray:
c  cf77 -Zv HoloInvert.f -o HoloInvert
c
c  to compile this code on a SUN:
c  f77 -r8 -i4 -O3 HoloInvert.f -o HoloInvert
c
c  initialization and parameterization
        real k(40), x(256), y(256), z(256)
        real k0, krkr, theta(18,72), phi(18,72), xK(40,18,72)
       real stheta(18,72), ctheta(18,72)
        real kx(18,72), ky(18,72), kz(18,72)
        complex kern, dUr, Ur, Ur0(256,256)
        integer nx, nz, nk, ntheta, nphi
        character*80 FilexK, FileUr
        parameter(pi = 3.141592654)
        parameter(degtorad = pi/180.0)
c
c  read in reconstruction integration parameters
        open(unit = 10, file = 'HoloInvert.in')
          read(10,10) FilexK
          read(10,*) ntheta
          read(10,*) nphi
cccc      read(10,*) k0
cccc      read(10,*) dk
          read(10,*) nk
          read(10,*) rotate
          read(10,10) FileUr
          read(10,*) xmin, xmax, dx
          read(10,*) ymin, ymax, dy
          read(10,*) zmin, zmax, dz
        close(10)
        nx = ((xmax - xmin)/dx) + 1
        ny = ((ymax - ymin)/dy) + 1
        nz = ((zmax - zmin)/dz) + 1
c       k0 = 0.5121365847*sqrt(energy)
10      format(a80)
c
        call read_Ur0(121,121,Ur0)
        dr = 0.01
c
c  initialization of k, x, y, and z arrays
        do 60 ix = 1, nx
          x(ix) = xmin + (ix-1)*dx
60      continue
        do 70 iy = 1, ny
          y(iy) = ymin + (iy-1)*dy
70      continue
        do 80 iz = 1, nz
          z(iz) = zmin + (iz-1)*dz
80      continue
cccc    do 90 ik = 1, nk
cccc      k(ik) = k0 + (ik-1)*dk
cccc90  continue
c
```

```
c  main read-in routine
        open(unit = 20, file = FilexK)
        do 100 ik = 1, nk
          do 101 itheta = 1, ntheta
            do 102 iphi = 1, nphi
              read(20,*) theta(itheta,iphi), phi(itheta,iphi),
     &                   xK(ik,itheta,iphi)
             theta(itheta,iphi) = theta(itheta,iphi)*degtorad
             phi(itheta,iphi) = (phi(itheta,iphi) - rotate)*degtorad
102         continue
101       continue
100     continue
        close(20)
c
c  initialization of angles and trigonometrics
       do 200 itheta = 1, ntheta
         do 200 iphi = 1, nphi
           ctheta(itheta,iphi) = cos(theta(itheta,iphi))
           stheta(itheta,iphi) = sin(theta(itheta,iphi))
           kx(itheta,iphi) = ctheta(itheta,iphi)*cos(phi(itheta,iphi))
           ky(itheta,iphi) = ctheta(itheta,iphi)*sin(phi(itheta,iphi))
           kz(itheta,iphi) = stheta(itheta,iphi)
200     continue
c
c  loop over each position in U(r)
        open(unit = 30, file = FileUr)
        do 300 ix = 1, nx
          do 301 iy = 1, ny
            do 302 iz = 1, nz
            dUr = (0., 0.)
            r = sqrt(x(ix)*x(ix) + y(iy)*y(iy) + z(iz)*z(iz))
c  integrate over hologram solid angle
            do 303 itheta = 1, ntheta
              do 304 iphi = 1, nphi
               xkx = x(ix)*(1. + dr/r)*kx(itheta,iphi)
               yky = y(iy)*(1. + dr/r)*ky(itheta,iphi)
               zkz = z(iz)*(1. + dr/r)*kz(itheta,iphi)
c  phase-sum over different wavenumbers
                  do 305 ik = 1, nk
                     krkr = k(ik)*(xkx + yky + zkz) - k(ik)*(r + dr)
                     kern = cmplx(cos(krkr),sin(krkr))
        dUr = dUr + xK(ik,itheta,iphi)*kern*k(ik)*k(ik)*ctheta(itheta,iphi)
305               continue
c  end phase-sum
304             continue
303           continue
              Ur = dUr
              Ur = ((r+dr)*Ur - r*Ur0(ix,iz))/dr
cccc          write(30,30) Ur
              write(30,30) x(ix), y(iy), z(iz), Ur
c  end hologram solid angle integration
302         continue
301       continue
300     continue
c  end loop over each position in U(r)
cccc30   format(2(2x,e12.5))
30      format(3(2x,f6.2),2(2x,e12.5))
c
        close(30)
        end
c
        subroutine read_Ur0(nx,nz,Ur0)
c  this subroutine reads in the optically-reconstructed image intensities
c
        complex Ur0(nx,nz)
c
        open(unit = 50, file = 'rous.in')
        do 500 ix = 1, nx
          do 500 iz = 1, nz
          read(50,*) a, b
          Ur0(ix,iz) = cmplx(a,b)
500     continue
        close(50)
        return
        end
```

Program 2.12. *HoloInvert:2.0d.f*

```
c  HoloInvert.f
c  version 2.0d
c
c  this program reconstructs atomic images from holographic intensities.
c
c  please acknowledge use of this program.  please contact:
c  p. m. len
c  physics department
c  university of california, davis
c  davis, ca  95616
c
c  s. thevuthasan, may 93            original program
c  a. p. kaduwela, jan 95            reoptimized for scalar machines
c  p. m. len, mar 96          final modifications
c  p. m. len, jul 96          implementation of Hofmann-Schindler
c  p. m. len, sep 96            final modifications
c
c  to compile this code on a cray:
c  cf77 -Zv HoloInvert.f -o HoloInvert
c
c  to compile this code on a SUN:
c  f77 -r8 -i4 -O3 HoloInvert.f -o HoloInvert
c
c  initialization and parameterization
       real k(40), x(256), y(256), z(256)
       real k0, krkr, theta(18,72), phi(18,72), xK(40,18,72)
      real stheta(18,72), ctheta(18,72)
       real kx(18,72), ky(18,72), kz(18,72)
       complex kern, dUr
       real Ur_ave, Ur(256,256,256)
       integer nx, nz, nk, ntheta, nphi
       character*80 FilexK, FileUr
       parameter(pi = 3.141592654)
       parameter(degtorad = pi/180.0)
c
       real fk(40,0:180)
c
c  read in reconstruction integration parameters
       open(unit = 10, file = 'HoloInvert.in')
         read(10,10) FilexK
         read(10,*) ntheta
         read(10,*) nphi
         read(10,*) k0
         read(10,*) dk
         read(10,*) nk
         read(10,*) rotate
         read(10,10) FileUr
         read(10,*) xmin, xmax, dx
         read(10,*) ymin, ymax, dy
         read(10,*) zmin, zmax, dz
       close(10)
       nx = ((xmax - xmin)/dx) + 1
       ny = ((ymax - ymin)/dy) + 1
       nz = ((zmax - zmin)/dz) + 1
c      k0 = 0.5121365847*sqrt(energy)
10     format(a80)
c
       call read_fk(nk,fk)
c
c  initialization of k, x, y, and z arrays
       do 60 ix = 1, nx
         x(ix) = xmin + (ix-1)*dx
60     continue
       do 70 iy = 1, ny
         y(iy) = ymin + (iy-1)*dy
70     continue
       do 80 iz = 1, nz
         z(iz) = zmin + (iz-1)*dz
80     continue
       do 90 ik = 1, nk
         k(ik) = k0 + (ik-1)*dk
```

```
90      continue
c
c  main read-in routine
        open(unit = 20, file = FilexK)
        do 100 ik = 1, nk
          do 101 itheta = 1, ntheta
            do 102 iphi = 1, nphi
              read(20,*) theta(itheta,iphi), phi(itheta,iphi),
     &                   xK(ik,itheta,iphi)
              theta(itheta,iphi) = theta(itheta,iphi)*degtorad
              phi(itheta,iphi) = (phi(itheta,iphi) - rotate)*degtorad
102         continue
101       continue
100     continue
        close(20)
c
c  initialization of angles and trigonometrics
        do 200 itheta = 1, ntheta
          do 200 iphi = 1, nphi
            ctheta(itheta,iphi) = cos(theta(itheta,iphi))
            stheta(itheta,iphi) = sin(theta(itheta,iphi))
            kx(itheta,iphi) = ctheta(itheta,iphi)*cos(phi(itheta,iphi))
            ky(itheta,iphi) = ctheta(itheta,iphi)*sin(phi(itheta,iphi))
            kz(itheta,iphi) = stheta(itheta,iphi)
200     continue
c
c  loop over each position in U(r)
        nxyz = 0
        do 300 ix = 1, nx
          do 301 iy = 1, ny
            do 302 iz = 1, nz
            dUr = (0., 0.)
            r = sqrt(x(ix)*x(ix) + y(iy)*y(iy) + z(iz)*z(iz))
c  integrate over hologram solid angle
            do 303 itheta = 1, ntheta
              do 304 iphi = 1, nphi
              xkx = x(ix)*kx(itheta,iphi)
              yky = y(iy)*ky(itheta,iphi)
              zkz = z(iz)*kz(itheta,iphi)
              costhetark = (xkx + yky + zkz)/r
c  phase-sum over different wavenumbers
                do 305 ik = 1, nk
                  call interpolate_ff(ik,costhetark,fk,ff)
                    krkr = k(ik)*(xkx + yky + zkz) - k(ik)*r
                    kern = cmplx(cos(-krkr),sin(-krkr))
        dUr = dUr + xK(ik,itheta,iphi)*kern*ff/(100.*k(ik))
305             continue
        Ur(ix,iy,iz) = Ur(ix,iy,iz) + ctheta(itheta,iphi)*exp(real(dUr))
c  end phase-sum
304           continue
303         continue
cccc        write(30,30) Ur
        Ur(ix,iy,iz) = abs(Ur(ix,iy,iz))
        Ur_ave = Ur_ave + Ur(ix,iy,iz)
c  end hologram solid angle integration
            nxyz = nxyz + 1
302       continue
301     continue
300   continue
c
      Ur_ave = Ur_ave/real(nxyz)
      open(unit = 30, file = FileUr)
      do 320 ix = 1, nx
        do 320 iy = 1, ny
          do 320 iz = 1, nz
          r2 = x(ix)*x(ix) + y(iy)*y(iy) + z(iz)*z(iz)
          if (r2 .ne. 0.) then
cccc            write(30,30) (Ur_ave - Ur(ix,iy,iz)), 0.
            write(30,30) x(ix), y(iy), z(iz), (Ur_ave - Ur(ix,iy,iz)), 0.
          else
cccc            write(30,30) 0., 0.
            write(30,30) x(ix), y(iy), z(iz), 0., 0.
          endif
320   continue
cccc
```

```
cccc30   format(2(2x,e12.5))
30       format(3(2x,f6.2),2(2x,e12.5))
c
         close(30)
         end
c
         subroutine read_fk(nk, fk)
c  this subroutine reads in the scattering factor magnitudes that are output
c  from fkSWIFT.f
c
         real fk(nk,0:180)
c
         open(unit = 40, file = 'fk.in')
         do 400 ik = 1, nk
           read(40,*) k_no_use
           do 400 itheta = 0, 180
             read(40,*) fk(ik,itheta)
400      continue
         close(40)
         return
         end
c
         subroutine interpolate_ff(ik, costhetark, fk, ff)
c  this subroutine interpolates the scattering factor magnitude for the angle
c  thetark, given cos(thetark)
c
         real costhetark, fk(11,0:180)
c
         thetark = aacos(costhetark)
         ithetark = int(thetark)
         delta = abs(thetark - ithetark)
c
         ff1 = fk(ik,ithetark)
         if (ithetark .eq. 180) then ithetark = 178
         ff2 = fk(ik,ithetark + 1)
c
         ff = ff1 + (ff2 - ff1)*delta
c
         return
         end
c
         function aacos(costhetark)
c  this function calculates acos(cos(thetark), but allows for a small amount
c  of round-off error when cos(thetark) is calculated as a dot product
c
         real costhetark, aacos
c
         if (abs(costhetark) .gt. 1.0001) stop 'Error 1 in aacos'
         if (abs(costhetark) .gt. 1) costhetark = sign(1., costhetark)
         aacos = acos(costhetark)
         return
         end
```

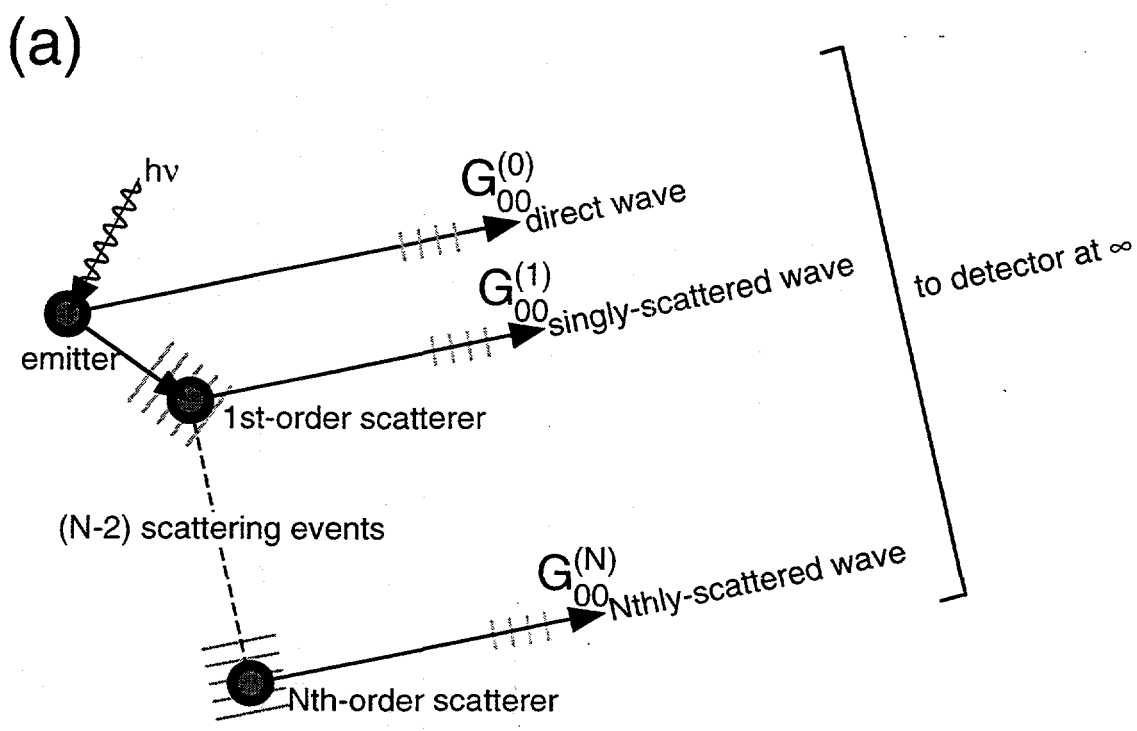

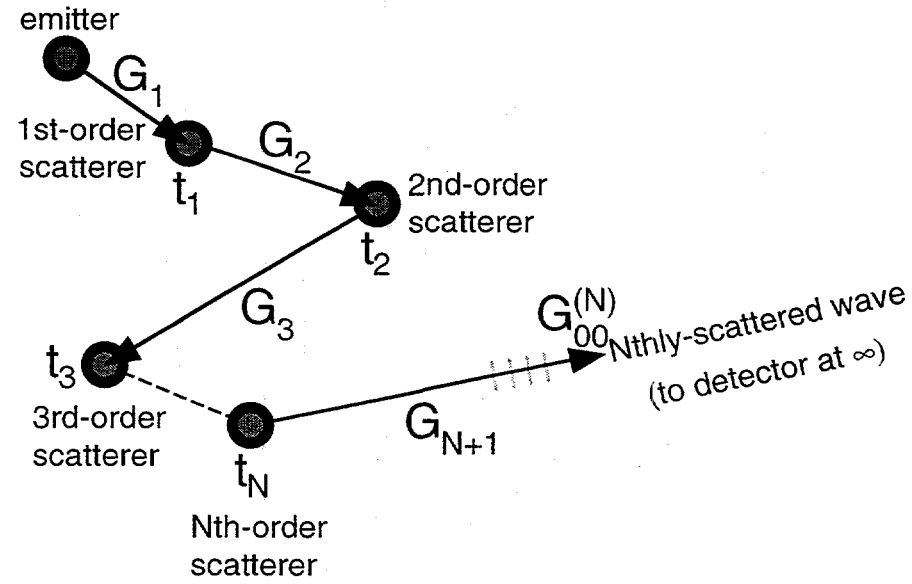

Fig. 2.1

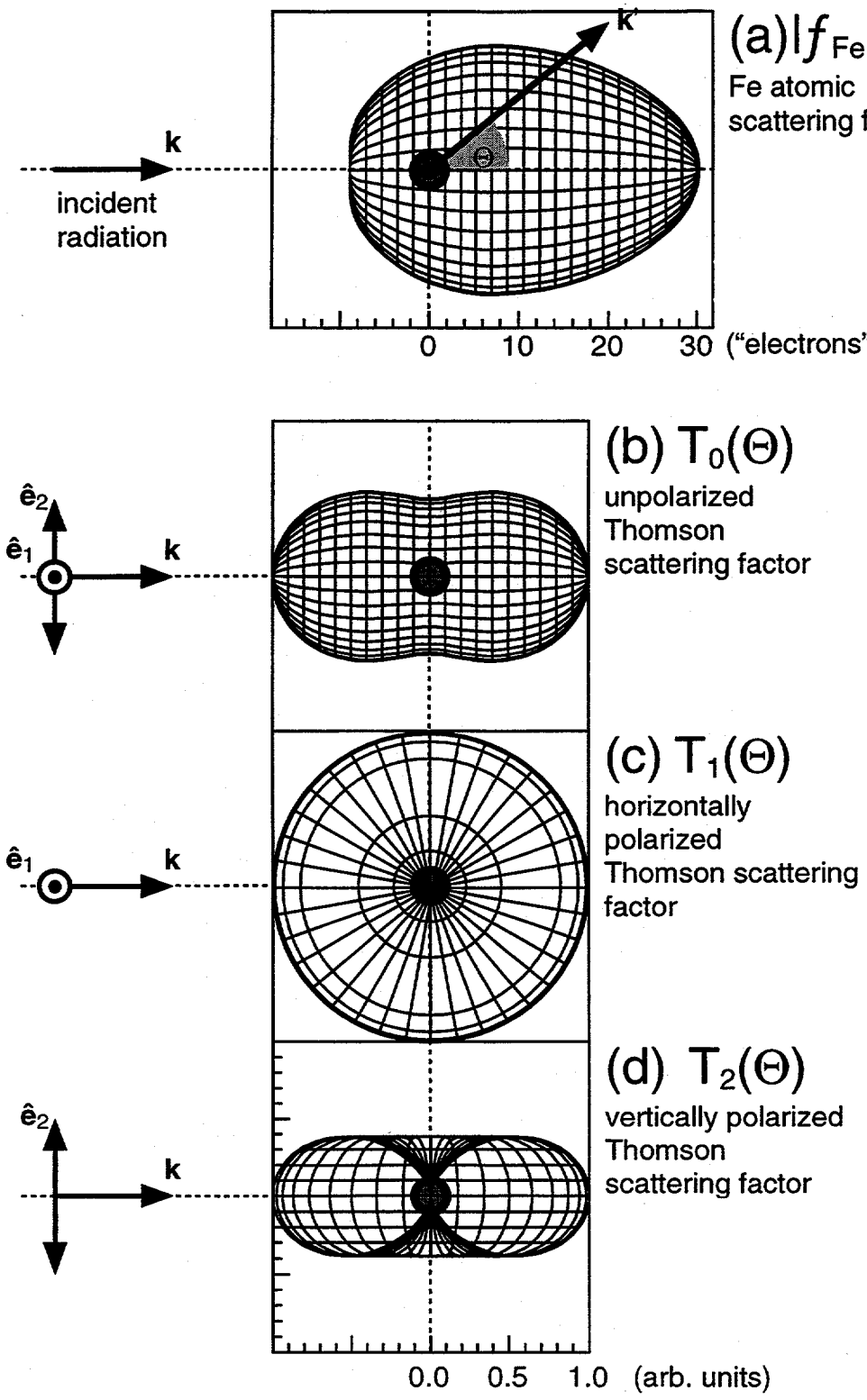

Fig. 2.2

2.3. Theoretical surface W$f_{7/2}$ photoelectron diffraction patterns

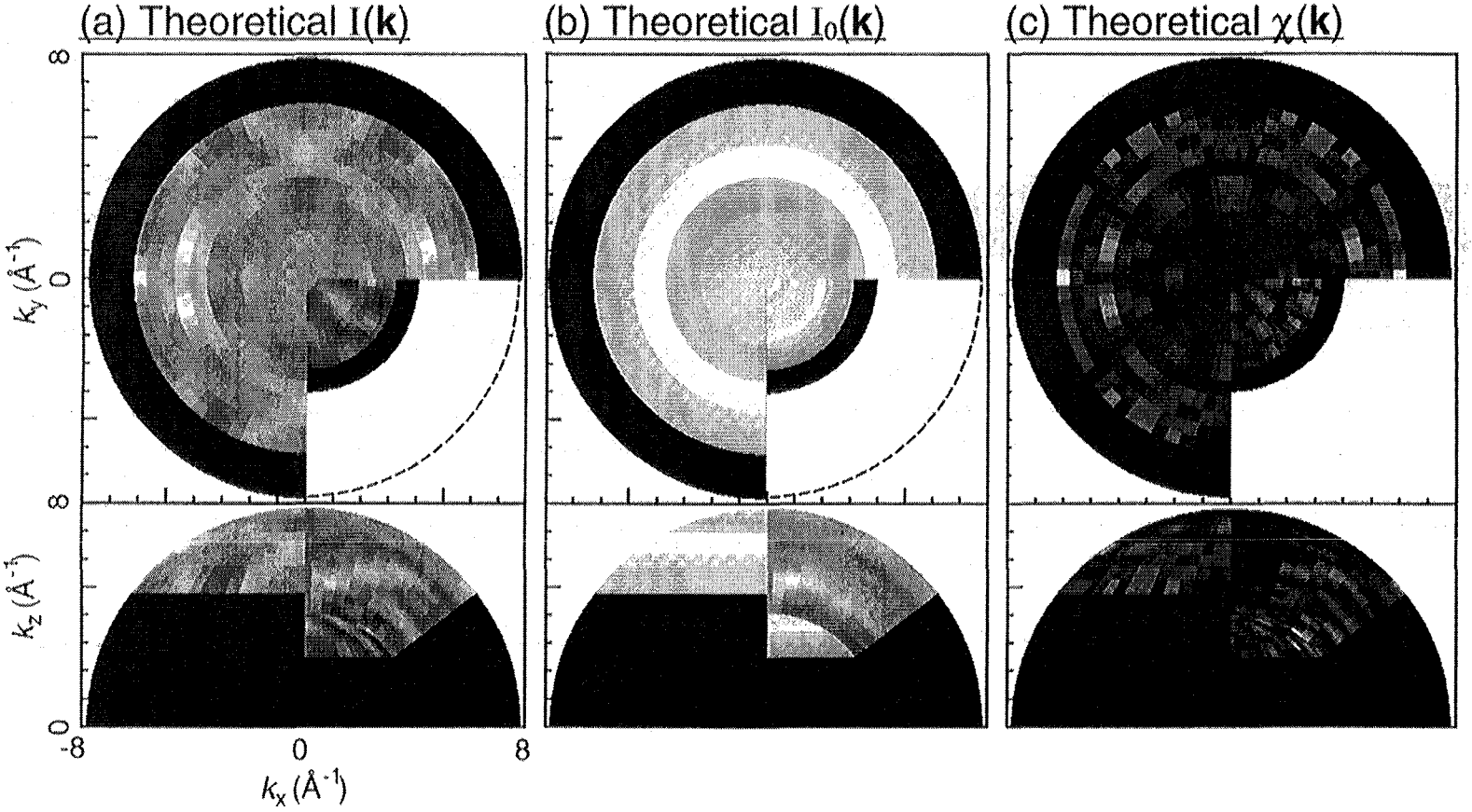

Fig. 2.3

2.4. Theoretical surface W$f_{7/2}$ photoelectron diffraction patterns

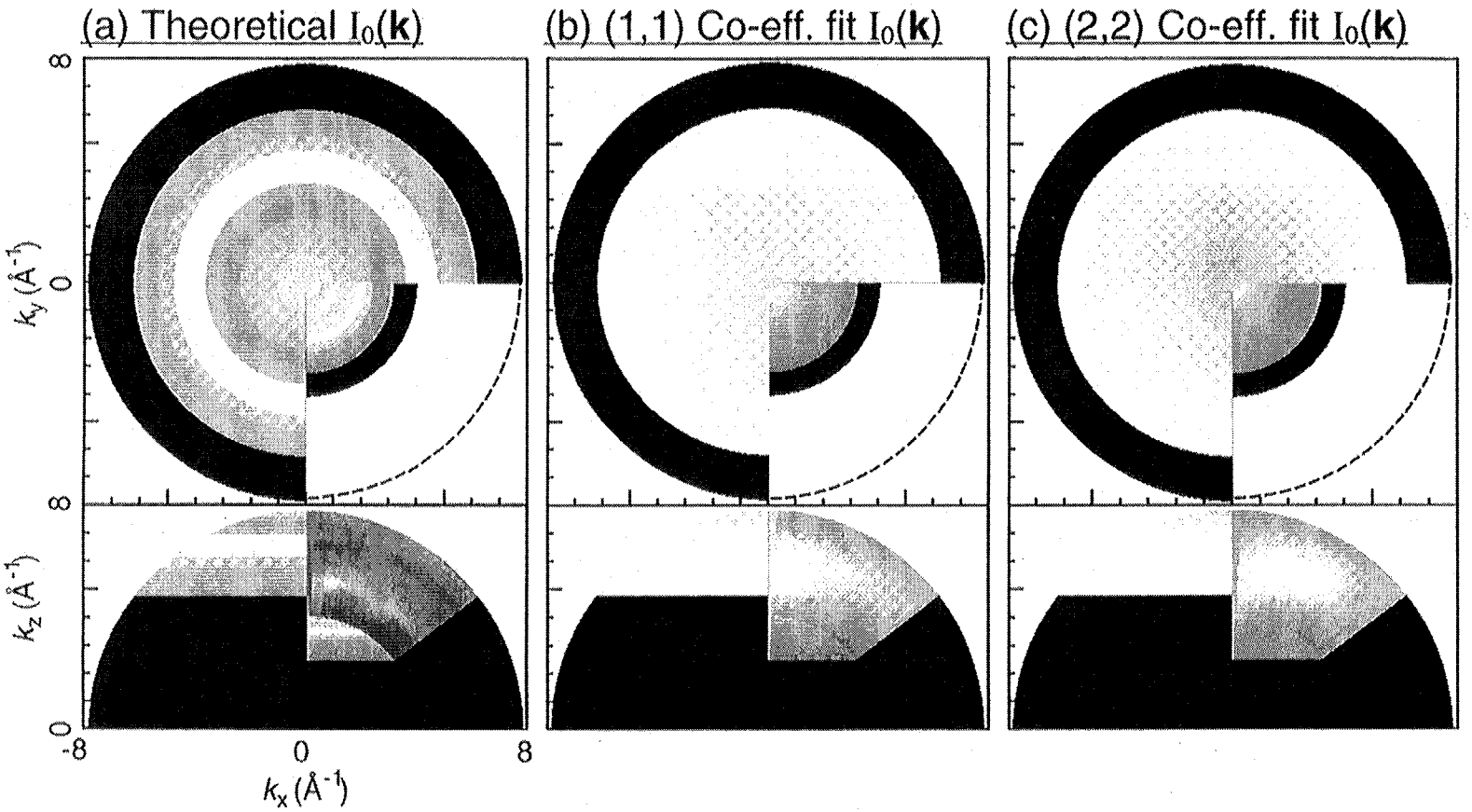

Fig. 2.4

2.5. Theoretical surface $Wf_{7/2}$ photoelectron diffraction patterns

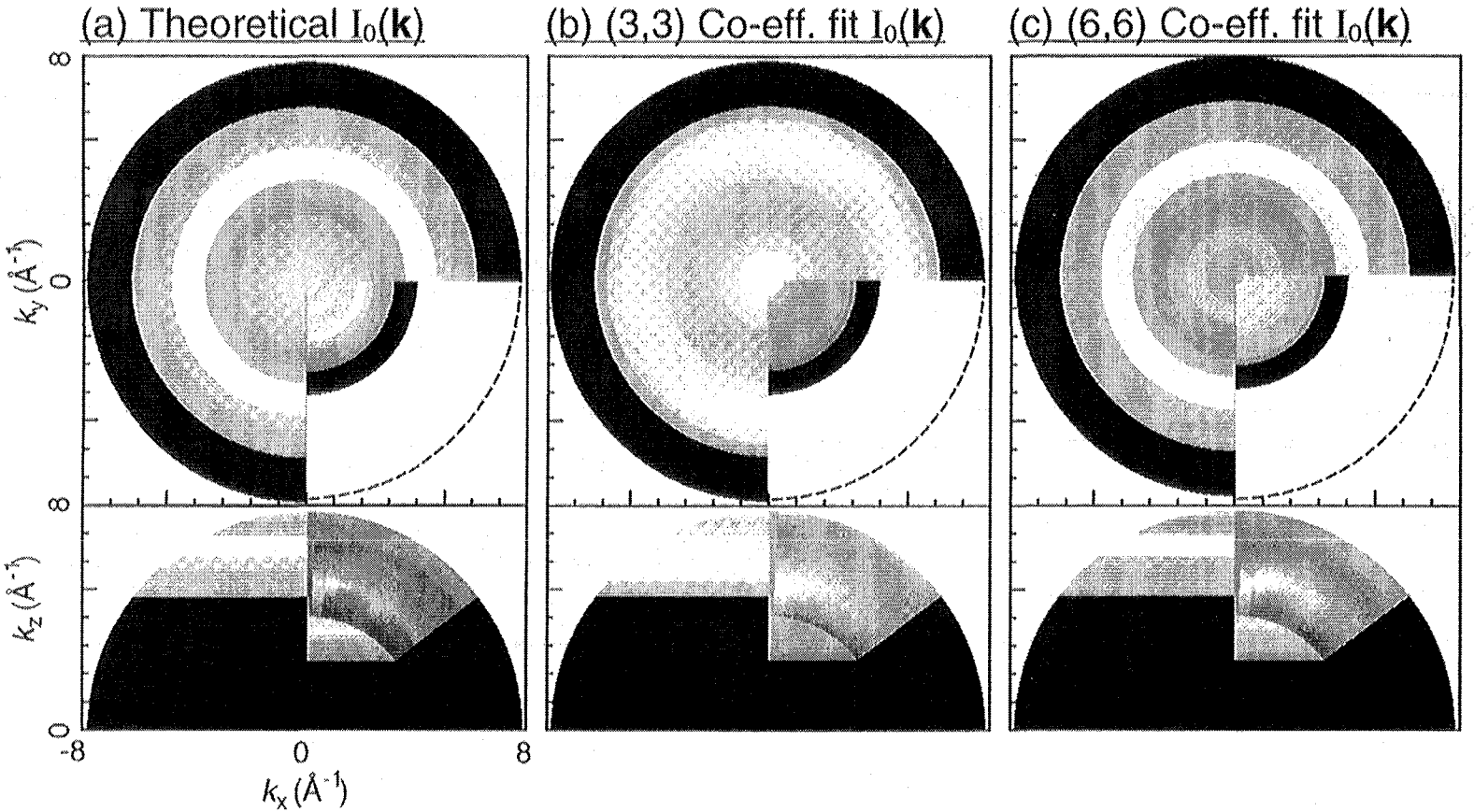

Fig. 2.5

Chapter 3

Optimization of **k**-Space Sampling in Atomic Holography

Abstract

Photoelectron diffraction data and other diffraction data associated with electron emission can be transformed as to holographically image atomic structure near surfaces. Two limiting-case approaches to acquire a **k**-space volume of these holographic diffraction intensities have previously been proposed: several different wavevector scanned-angle data sets, or several different direction scanned-wavenumber data sets. A continuum of different sampling densities in the direction and magnitude of **k** exists in such holography, spanning the two limits previously discussed. Using model diffraction calculations for localized electron emission (*e.g.*, core photoelectron emission) from Cu(001) clusters, we explore the full range of **k**-space sampling possible, and find that the intermediate sampling regime between the extreme scanned-angle and scanned-wavenumber choices results in optimum image quality for the original image reconstruction scheme of Barton and others, and also for a variant method that involves using only a small cone of data in **k**-space for each image transform. General rules for optimizing image quality for a given data set volume of **k**-space are also discussed and used to evaluate the sampling choices made in some prior experimental studies.

Outline

3.1 Introduction

In recent years, there have been several theoretical and experimental studies of different types of electron emission holography, with the aim of generating three-dimensional images of atoms near surfaces [3.1-3.12]. These methods make use of the intensity distributions of photoelectrons [3.2-3.8], Auger electrons [3.9], backscattered Kikuchi electrons [3.10], and diffuse and fractional-order features in low-energy electron [3.11] and positron [3.12] diffraction. X-ray fluorescence holography has also been proposed as a related method [3.1,3.13,3.14]. The intensity modulations that are interpreted as a hologram are produced by the scattering of an outgoing electron (or fluorescent x-ray) wavefront originating from a localized atomic source (*e.g.*, a core-level photoelectron) by the atoms neighboring the emitter, with the unscattered outgoing wavefront component serving as the reference wave in the hologram [3.1]. If the electron intensity in the far field at a given outgoing wavevector $\mathbf{k}$ is $I(\mathbf{k})$, and the corresponding intensity in the absence of any scattering is $I_0(\mathbf{k})$, then the normalized hologram intensity used in forming images is defined as either $\chi(\mathbf{k}) = [I(\mathbf{k}) - I_0(\mathbf{k})]/I_0(\mathbf{k})$ or $\chi(\mathbf{k}) = [I(\mathbf{k}) - I_0(\mathbf{k})]/\sqrt{I_0(\mathbf{k})}$. Whether considered in a single scattering model or a more accurate multiple scattering model, such electron holograms are not ideal in a classic sense due to the strong nature of electron-atom scattering [3.15,3.16-3.18], and various methods have been proposed for correcting the resulting aberrations in images [3.19,3.20].

Atomic images $U(\mathbf{r}')$ at relative positions $\mathbf{r}'$ with respect to the emitter at the origin are reconstructed via a $\mathbf{k}$-space deconvolution of normalized holographic $\chi(\mathbf{k})$ intensities, and in the most general sense this algorithm (here, Method A) can be expressed as [3.2]:

$$U_A(\mathbf{r}') \equiv \iiint_K d^3\mathbf{k} \cdot e^{-i(\mathbf{k}\cdot\mathbf{r}' - kr')}\chi(\mathbf{k}), \tag{3.1}$$

where the integration is over the **k**-space volume of the $\chi(\mathbf{k})$ data set, and the deconvolution kernel $e^{i(\mathbf{k}\cdot\mathbf{r}'-kr')}$ is based on the back-propagation of the optical path length difference between the reference and object waves.

Since $I(\mathbf{k})$ and $\chi(\mathbf{k})$ data is experimentally recorded with respected to wavenumber (k) and direction ($\hat{\mathbf{k}}$), then Eq. (3.1) can be expressed in spherical coordinates in **k**-space:

$$U_A(\mathbf{r}') \equiv \int_k dk \iint_\Omega d\sigma_{\mathbf{k}} e^{-i(\mathbf{k}\cdot\mathbf{r}'-kr')}\chi(\mathbf{k}), \tag{3.2}$$

where we define the solid-angle integration increment $d\sigma_{\mathbf{k}} \equiv k^2 d\sigma_{\hat{\mathbf{k}}} \equiv k^2 \cos\theta d\theta d\phi$, and θ is the polar inclination angle (surface normal $\theta \equiv 90°$). Also, the average angular integration increment in **k**-space is defined as $|d\hat{\mathbf{k}}| \approx \sqrt{d\sigma_{\mathbf{k}}}$.

Historically, the basic **k**-space reconstruction algorithm of Method A was arrived at via two equivalent approaches motivated by the experimental methods of measuring $I(\mathbf{k})$ intensities. One such approach was motivated by the historical recording of scanned-angle $I_k(\hat{\mathbf{k}})$ diffraction patterns at a fixed wavenumber k [3.3]. Atomic images reconstructed from such a single-wavenumber scanned-angle normalized $\chi_k(\hat{\mathbf{k}})$ data set suffer from twin images and other image artifacts [3.2(a),3.4,3.15]. By recording several different wavenumbers of these scanned-angle $I_k(\hat{\mathbf{k}})$ data sets, Eq. (3.2) becomes in the limit of coarse wavenumber intervals ($dk \rightarrow \delta k$) and fine angular resolution ($d\sigma_{\mathbf{k}}$) [3.2(b)]:

$$U_A^{dk\rightarrow\delta k}(\mathbf{r}') \equiv \sum_k k^2 \delta k e^{ikr'} \iint_\Omega d\sigma_{\hat{\mathbf{k}}} e^{-i\mathbf{k}\cdot\mathbf{r}'}\chi(\mathbf{k}). \tag{3.3}$$

Among the first experimental images obtained using this method were for bulk Cu(001) by Terminello *et al.* [3.5(a)], and for bulk Pt(111) by Petersen *et al.* [3.5(b),(c)].

The other limiting approach of recording $I(\mathbf{k})$ intensities was motivated to the historical measurement of scanned-wavenumber $I_{\hat{\mathbf{k}}}(k)$ for a fixed $\hat{\mathbf{k}}$ direction. Transforming such a single-direction scanned-wavenumber normalized $\chi_{\hat{\mathbf{k}}}(k)$ data set via Eq. (3.2) does not yield localized atomic images, but only path length differences of different scatterers around a given emitter [3.6]. By recording several different directions of these scanned-wavenumber $I_{\hat{\mathbf{k}}}(k)$ data sets, Eq. (3.2) becomes in the limit of fine wavenumber intervals (dk) and coarse angular resolution ($d\sigma_{\hat{\mathbf{k}}} \rightarrow \delta\sigma_{\hat{\mathbf{k}}}$) [3.2(c)]:

$$U_A^{d\sigma_{\hat{\mathbf{k}}}\rightarrow\delta\sigma_{\hat{\mathbf{k}}}}(\mathbf{r}') \equiv \sum_{\hat{\mathbf{k}}} \delta\sigma_{\hat{\mathbf{k}}} \int_k k^2 dk e^{-i(\mathbf{k}\cdot\mathbf{r}'-kr')}\chi(\mathbf{k}). \tag{3.4}$$

Among the first experimental images obtained with this approach were for Cu(001)-c(2×2)-Au by Tobin *et al.* [3.7(a)], and for Si(111)-($\sqrt{3}\times\sqrt{3}$)R30°-Al by Wu *et al.* [3.7(b)].

It is apparent that Eqs. (3.3) and (3.4) are merely equivalent expressions of Eq. (3.2), simply involving a switch in the order of integration and summation over the magnitude and direction of $\mathbf{k}$. However, there has been a previous proposal to distinguish these algorithms as distinctly unique reconstruction methods on the basis of the $I(\mathbf{k})$ and $\chi(\mathbf{k})$ data sets resolutions, whether scanned-angle/coarse-wavenumber, or coarse-angle/scanned-wavenumber [3.8(e)]. This distinction is artificial, since all experimental data in reality involves finite steps in both magnitude and direction, these two algorithms can be considered interchangeable when applied to any actual $\chi(\mathbf{k})$. Furthermore, $\chi(\mathbf{k})$ data sets can be obtained with a continuum of choices from scanned-angle/coarse-wavenumber to coarse-angle/scanned-wavenumber, with a set of any of these choices spanning a certain volume in $\mathbf{k}$-space. This has been demonstrated in experiments subsequent to the preliminary studies [3.5,3.7], where atomic images have obtained from photoelectron $\chi(\mathbf{k})$ data sets that have resolutions between the scanned-angle/coarse-wavenumber and coarse-angle/scanned wavenumber limits [3.8].

A further variation in the holographic analysis of $\chi(\mathbf{k})$ data proposed independently by Tong *et al.* [3.21(a)] and Wu and Lapeyre [3.21(b)] is to carry out the imaging transform for each point $\mathbf{r}$ over only a small cone of directions in the full $\chi(\mathbf{k})$ data set, and to emphasize the imaging of backscattering atoms along the negative axis of this cone. This "small-cone" procedure is designed to selectively include backscattering contributions to $\chi(\mathbf{k})$ that are more nearly ideal in nature, resulting in more accurate holographic images. This is equivalent in Eq. (3.3) or Eq. (3.4) to limiting $d\sigma_{\hat{\mathbf{k}}}$ ($\delta\sigma_{\hat{\mathbf{k}}}$) to a specific set of directions within a cone with a half-angle of typically 20°-30°, and $\mathbf{r}'$ to directions along the negative axis of this cone, with the cone then being swept over the full set of $\chi(\mathbf{k})$ data:

$$U_B(\mathbf{r}') \equiv \iiint_K d^3\mathbf{k} \cdot e^{-i(\mathbf{k}\cdot\mathbf{r}'-kr')} w(\alpha, \Theta^{\mathbf{k}}_{-\mathbf{r}'}) \chi(\mathbf{k}), \tag{3.5}$$

where $w(\alpha, \Theta^{\mathbf{k}}_{-\mathbf{r}'})$ is a window function that has value of unity inside the cones of half-angle α centered on the reconstruction axis $-\mathbf{r}'$, and is zero everywhere else. This method (here, Method B) shows promise of reducing the artifacts in imaging backscattering atoms, but it is also clear that, in reducing the effective angular $\chi(\mathbf{k})$ range transformed, the inherent resolution of each atom in space will be degraded [3.21(b)]. In addition, as we will demonstrate below, this variation in the use of Eqs. (3.3) or (3.4) does not alter the limitations on image quality that may arise due to the type of $\mathbf{k}$-sampling employed.

Another important point to consider in the analysis of such $\chi(\mathbf{k})$ data is the manner of choosing the normalizing intensity $I_0(\mathbf{k})$. The most correct normalization is clearly to use the intensity in the absence of any diffraction effects, and this is easily derived in a theoretical calculation. This is thus the normalization that we will use throughout this theoretical study, as we require a scheme that can be used over the full range of $\mathbf{k}$ sampling choices. From an experimental point of view, determining this three-dimensional $I_0(\mathbf{k})$ is however more difficult, as it involves both the angle and wavenumber

dependence of the photoelectric cross section, and other geometric factors related to the electron escape and the photon-electron experimental geometry. Fitting some sort of linear or low-order spline curve to data obtained over either angles or wavenumbers is one way to estimate an experimental $I_0(\mathbf{k})$. However, either of these limiting choices can effectively wash out some/all of the diffraction structure in the other dimension not considered in the fit. For example, fitting scanned-wavenumber data for each individual direction with a linear function as advocated by Wei *et al.* [3.22] effectively removes most of the *angular* variation in intensity associated with forward scattering atoms, thus much diminishing their intensities in holographic images [3.8(a)]. In Chapter 5 of this dissertation, we demonstrate that sufficient data in both angle and wavenumber taken that a truly three-dimensional $I_0(\mathbf{k})$ can be obtained by some more complex fitting procedure. In this way, the full holographic information content of the data can be maintained throughout the remainder of the analysis. Our calculations are thus representative of what would be obtained with this more general approach, but we nonetheless expect our general conclusions concerning $\mathbf{k}$ sampling to hold even with the more approximate $I_0(\mathbf{k})$ choices mentioned above.

In this chapter, we will compare atomic images obtained from theoretical $\chi(\mathbf{k})$ curves for a model Cu surface over the full range of reasonable choices for sampling a given volume of $\mathbf{k}$-space, and point out certain criteria that should be useful for optimizing image quality in future experimental studies. Our theoretical calculations have been performed for clusters of Cu atoms simulating Cu(001) surfaces, and have been carried out at the single-scattering level [3.23]. Additional image aberrations may arise due to multiple scattering effects, *or* in certain forward scattering geometries, multiple scattering may even improve images due to defocusing effects [3.20]. However, prior work and spot checks of our results using multiple scattering calculations for Ni(001) [3.24,3.25] indicate that our overall conclusions will not be influenced by these effects. The geometries of the two-layer 25-atom Cu clusters used in all of our calculations are shown

in Figs. 3.1(a) and 3.1(d): the cluster in (a) places the emitter in the surface layer, with only backscattering and side-scattering neighbors, and that in (d) places the emitter in the second layer and below the surface, now with forward- as well as side-scattering neighbors. The calculated $\chi(\mathbf{k})$ and $U_A(\mathbf{r}')$ reconstructions in this work, being for only two-layer slabs of Cu(001), cannot thus be compared directly with experimental $\chi(\mathbf{k})$ data or reconstructed atomic images from bulk Cu(001) [3.5(a)], but should nonetheless permit drawing conclusions concerning the best type of $\mathbf{k}$ sampling to use for a given method. Electron wavenumbers ranged from $k_{\min} = 10.0\text{Å}^{-1}$ to $k_{\max} = 13.0\text{Å}^{-1}$, for a wavenumber span of $\Delta k = k_{\max} - k_{\min} = 3.0\text{Å}^{-1}$, corresponding to kinetic energies of $E_{\min} \approx 381\text{eV}$ to $E_{\min} \approx 644\text{eV}$. This range is comparable to that used in some prior experimental studies [3.5,3.7]. Intensities were calculated over the full $\Delta\Omega_{\hat{\mathbf{k}}} = 2\pi$ solid-angle above the surface. The emitting atom is at the center of each cluster in the x and y coordinates parallel to the surface. The reference electron wave outgoing from the emitter is assumed to be isotropic in character (*i.e.*, with $\ell = 0$) to avoid having to assume a specific type of electron excitation process (*e.g.*, *s*, *p*, *d*, or *f* core excitation, Auger, *etc.*), whereas the scattered wave components exhibit the full anisotropy in magnitude and phase associated with electron-atom scattering [3.23]. Our results should thus apply at least semi-quantitatively to *all* forms of electron emission holography, although *source-wave anisotropy* in each specific case could lead to additional image aberrations, as discussed elsewhere [3.21,3.11(c),3.26]. Scattering phase shifts were calculated in a standard way [3.23,3.24], and the inelastic attenuation length ranged for Cu from 10.5Å (for $k_{\min} = 10.0\text{Å}^{-1}$) to 13.7Å (for $k_{\max} = 13.0\text{Å}^{-1}$). Vibrational effects were included using Debye-Waller factors for Cu corresponding to a temperature of 300K [3.23,3.24]. In most of the images reported here, the equivalent Eqs. (3.3) and (3.4) were used over the full solid-angle of the data, although we return at the end of the paper to point out that similar conclusions are obtained even when the small-cone approach mentioned above is used.

3.2 χ(k) data sets spanning the scanned-angle and scanned-wavenumber sampling extremes

Figure 3.2 illustrates the different choices of **k**-space sampling considered. In (a), the **k** points in a representative $\chi(\mathbf{k})$ data set over a given volume of **k** space are shown as a stacked set of planar polar net projections, with each one spanning the full $\Delta\Omega_{\hat{\mathbf{k}}} = 2\pi$ solid-angle. Intensities for different k are stacked vertically. Single $\chi(\mathbf{k})$ data elements (of which each corner can be considered to represent a single electron diffraction intensity measurement) for the different sampling choices used in this paper are shown in Figs. 3.2(b)-(f): (b) represents our closest approach to the scanned-angle limit, and (f) to the scanned-wavenumber limit. Each $\chi(\mathbf{k})$ data set we have considered contains a total of 64,800 data points, so that each $\chi(\mathbf{k})$ element in Figs. 3.2(b)-(f) contains the same volume in **k**-space. The symmetry of the (001) clusters in Fig. 3.1 further means that only 1/8th of 64,800 or 8,100 independent intensities would actually have to be measured or calculated for the present system; a similar degree of reduction would apply to any low-index single crystal surface. In an experimental sense, each of our sampling choices in Fig. 3.2 would thus take the same amount of data accumulation time. Any differences in atomic images obtained from these five $\chi(\mathbf{k})$ data sets will then be primarily due to their differing angular and wavenumber resolutions (*i.e.*, choices of $\delta\hat{\mathbf{k}}$ and δk). The average spacing between directions can be calculated from $|\delta\hat{\mathbf{k}}| \approx \sqrt{2\pi k_{\max}^2 / N_D}$, where N_D is the number of different directions in the $\chi(\mathbf{k})$ data set. The spacing between different wavenumbers (or energies) can be found from $\delta k = \Delta k / (N_k - 1)$, where N_E is the number of different wavenumbers (energies) considered in the data set. The numbers N_D and N_k are given next to their respective $\chi(\mathbf{k})$ data elements.

Before applying the imaging algorithm (Eq. (3.1) or Eq. (3.2)) to these multiple-wavenumber data sets, a Hanning window of the form $H(\theta) = \cos^2\theta$ (where the polar angle θ is measured from the surface normal) was applied to all $\chi(\mathbf{k})$ intensities [3.27].

The effective angular range of $\chi(\mathbf{k})$ is approximately halved by the use of this window function, but this was found to improve the atomic images somewhat by reducing spurious features due to the abrupt termination of the data set at its solid-angle edges; it also had the effect of smoothing out any slight differences between the angular boundaries of the data sets due to the varying number of discrete (θ,ϕ) directions involved. For the special case of the small-cone method to be discussed later, no Hanning window was used. No other correction procedures were applied to these $\chi(\mathbf{k})$ data sets before calculating images from them, in order to avoid masking the effects on the atomic images of varying **k**-space sampling density.

3.3 Effect of k-space sampling on atomic images

We now show atomic images derived from the $\chi(\mathbf{k})$ data sets in Figs. 3.2(b)-(f) by applying the equivalent imaging algorithms of Eqs. (3.1) and (3.2) in high-symmetry planes parallel to and perpendicular to the surface of the cluster. The image planes are shown in Figs. 3.1(b), 3.1(c), and 3.1(e). Figure 3.3 presents images for the backscattering Cu cluster in Fig. 3.1(a) in the (001) or *xy* plane including the emitter (Fig. 3.1(b)), and Fig. 3.4 shows images for the same cluster in the (100) plane (Fig. 3.1(c)), again including the emitter. The white crosses indicate the actual atomic positions in the cluster. We also note that we have in all cases used a strictly linear gray scale so as to more clearly show the weaker, and potentially confusing, features in each image. Other image presentation techniques have been used in the literature, including color scales that effectively suppress weaker features [3.7,3.9,3.10] or three-dimensional surfaces that only represent image intensity above a certain cutoff [3.5,3.11(c)], and thus completely eliminate weaker features. Thus, the images shown here may not appear to be as aesthetically pleasing as some prior holographic images, but we believe they represent more accurately the overall image quality that we want to assess as a function of **k** sampling.

Figures 3.3 and 3.4 make it clear that the images for 18 wavenumbers (energies) and for 50 wavenumbers in panels (b) and (c) are the most reliable, with spurious peaks and noise arising in the other three panels (a), (d) and (e) that correspond to **k**-space sampling closer to the scanned-angle and scanned-wavenumber limits of Eqs. (3.3) and (3.4). *There is thus an intermediate set of sampling choices that is expected to give better holographic images.* Figure 3.4 also indicates that both backscattering and side scattering atoms may be locatable in the images for optimum sampling, with side scatterers actually being the more easily discernible. Figure 3.5 presents images for the cluster including forward scattering of Fig. 3.1(d) in the (100) plane (Fig. 3.1(e)). Panels 3.5(b)-(d) with N_E = 18-113 wavenumbers now yield the most reliable images compared to the other two panels. However, the atomic positions of the forward scatterers are not as clearly resolved in three dimensions as the backscattering atoms are in Fig. 3.4, showing extreme elongation along the forward scattering direction due to high forward scattering anisotropies [3.20(a),3.26]. Panels (a)-(c) also show a purely artifactual peak at y= 0.0Å and $z \approx$ 2.0Å. *Imaging forward scattering atoms is thus expected to be inherently more difficult in electron emission holography, even with an optimized sampling of* **k***-space,* but Fig. 3.5(d) indicates that biasing the **k**-sampling towards a larger number of wavenumbers yields better results. This improvement is probably due to the increased averaging over different anistropies and phase shifts at the different wavenumbers involved.

We note that the general locations and widths of the atomic peaks in Figs. 3.3, 3.4, and 3.5 are *not* dependent on changes in the angular and wavenumber resolution of a $\chi(\mathbf{k})$ data set. The overall position uncertainty of atomic images depends on the total angular and wavenumber span ($\Delta\Omega_{\hat{\mathbf{k}}}$ and Δk, respectively) of a given $\chi(\mathbf{k})$ data set in **k**-space [3.26,3.28], parameters which were made identical for all five cases considered.

The deterioration of image quality in the upper and lower panels of Figs. 3.3-3.5 can be viewed simply as Fourier transform aliasing [3.27] due to an increase in either the

spacing in magnitude or the spacing in direction in **k**-space at the two extremes of sampling. Two criteria for optimizing images emerge from such a consideration. First, atomic images obtained from a $\chi(\mathbf{k})$ data set that is too coarse in wavenumber resolution (*i.e.*, too large a δk and going toward the scanned-angle limit) can have distinct spurious image peaks at radial distances $R_k = m\pi/\delta k$ from the emitter, where m is a non-zero integer [3.25]. These spurious image peaks are especially strong in directions extending from the emitter backwards from forward scattering nearest-neighbor and next-nearest-neighbor atoms [3.25]. The atomic images of the forward scattering Cu cluster (Fig. 3.5) best illustrate this effect. In Fig. 3.5(a), for which $\delta k = 3.0\text{Å}^{-1}$, the large wavenumber step in $\chi(\mathbf{k})$ causes spurious peaks spaced every $\pi/[3.0\text{Å}^{-1}] \approx 1.05\text{Å}$ down into the cluster along the $[01\bar{1}]$ and $[0\bar{1}\,\bar{1}]$ directions. In order to keep a region of at least 6.0Å in radius free from these peaks, an wavenumber resolution corresponding to $\delta k \leq \pi/[6.0\text{Å}]$, thus requiring at least seven different electron wavenumbers, would be required for this region of **k**-space. Figs. 3.3(b)-(e), 3.4(b)-(e), and 3.5(b)-(e) thus represent cases that are well-behaved as to this first criterion.

A second criterion arises when considering the scanned-wavenumber limit, since a similar problem occurs when the spacing between directions ($|\delta\hat{\mathbf{k}}|$) becomes too large. In fact, Harp *et al.* have shown that the radius R_D around an emitting atom over which images are expected to be reliable is given by $R_D \leq \pi/|\delta\hat{\mathbf{k}}|$ [3.28]. The scanned-wavenumber $\chi(\mathbf{k})$ data sets of Figs. 3.3(c)-(e) have direction resolutions that make R_D = 3.47Å, 2.31Å, and 1.74Å, respectively, providing an explanation for the deterioration of these images as well. To keep at least the region over a 6Å radius around the emitter free from this type of noise, an average resolution of $|\delta\hat{\mathbf{k}}| \leq \pi/[6.0\text{Å}]$, or at least 3900 spatial directions, would be needed. This second criterion is satisfied in Figs. 3.3(a)-(c), 3.4(a)-(c), and 3.5(a)-(c).

Putting these two criteria together directly shows why the images in Figs. 3.3(b)-(c), 3.4(b)-(c), and 3.5(b)-(c) are in general the most free of artifacts.

3.4 Optimization of resolution in wavenumber and direction for χ(k) data sets

Thus, a scanned-angle $\chi(\mathbf{k})$ data set that is too coarse in wavenumber resolution (too large a δk), or a scanned-wavenumber $\chi(\mathbf{k})$ data set that is too coarse in direction (too large a $|\delta\hat{\mathbf{k}}|$) can result in degraded atomic images outside of the distances R_k and R_D from the emitter, respectively. In fact, maximizing *both* R_k and R_D at the same self-consistent value for the present $\chi(\mathbf{k})$ of 64,800 data points would require 9 different wavenumbers, and an angular grid of $(|\delta\hat{\mathbf{k}}_\theta|,|\delta\hat{\mathbf{k}}_\phi|) = (2°,2°)$, or 8,100 directions. This results in an $R_k = \pi/\delta k = \pi/[\Delta k/(N_k-1)] = 8.38$Å, and an $R_D = \pi/|\delta\hat{\mathbf{k}}|$ $\approx \pi/\sqrt{2\pi k_{\max}^2/N_D} \approx 8.68$Å. However, R_k and R_D do not have to be so large when imaging the clusters in this paper (as the farthest scatterers here are only 3.25Å from the emitters), or indeed in many experimental applications. In order to keep image degradation outside of a smaller radius of only $R_k = R_D = 6.0$Å for our clusters, a $\chi(\mathbf{k})$ data set for the $(\Delta k, \Delta\Omega_{\hat{\mathbf{k}}})$ range considered here must include at least $N_k \geq (\Delta k/\delta k)+1 = (R_k\Delta k/\pi)+1 \approx 7$ different electron wavenumbers, and $N_D \geq \Delta\Omega_{\hat{\mathbf{k}}} k_{\max}^2/|\delta\hat{\mathbf{k}}|^2 = 2\pi k_{\max}^2 R_D^2/\pi^2 \approx 3{,}900$ different $\chi(\mathbf{k})$ directions, corresponding roughly to a $(|\delta\hat{\mathbf{k}}_\theta|,|\delta\hat{\mathbf{k}}_\phi|) = (3°,3°)$ angular data mesh. The volume element in such a "minimal" data set is schematically shown in Fig. 3.6(a), and it is slightly larger than the ones shown in Fig. 3.2, yielding a total of only 25,200 $\chi(\mathbf{k})$ intensities to span the same volume of **k**-space (or only 39% of the previous total of 64,800). In addition, the spatial symmetry of our example Cu(001) surfaces means that only 1/8th of this number or about 3,150 unique $\chi(\mathbf{k})$ intensities would need to be measured experimentally in order to obtain reasonable atomic images. In Fig. 3.6, we show atomic images for the backscattering (Figs. 6(b),(c)) and the forward scattering (Fig. 3.6(d)) Cu clusters obtained from such an optimized "minimal" $\chi(\mathbf{k})$ data set containing just enough data points to push image noise and aberrations due to coarse **k**-space sampling to the edges of the image. All of these images are well behaved, although that for the (100) plane of the

forward scattering cluster (Fig. 3.6(d)) not surprisingly again shows distorted features above the surface due to forward scattering anisotropies and non-constant scattering phase shifts, as well as the spurious peak at $x = 0.0$Å, $y \approx 2.0$Å. Also, at the bottom corners of Fig. 3.6(d), weaker spurious peaks evidently due to coarse wavenumber resolution appear at $(y,z) \approx (\pm 4.44$Å, -4.44Å) or a distance of 6.30Å from the emitter; these in fact correspond to the kinds of features expected at $R_k = \pi / \delta k = 6.30$Å [3.25]. Another Fourier transform artifact is also visible in Fig. 3.6(d), where even weaker peaks are found at $\pi / \Delta k \approx 1.05$Å intervals between the coarse-wavenumber peaks and the origin. This effect is simply due to the finite wavenumber span (Δk) of the $\chi(\mathbf{k})$ data set that was Fourier-transformed [3.21], and these weaker peaks correspond to attenuated sidelobes of the primary aliased peaks.

It is now of interest to apply these general criteria for **k**-space sampling to a few prior experimental studies using full-solid-angle photoelectron holography to image near-surface atoms. In Refs. [3.5(a)] and [3.5(b)], a display analyzer with high resolution in direction was used, so we can assume that R_D is effectively large. The wavenumber steps involved in these two studies lead to the real limits on maximum image radius: $R_k = 7.85$Å in Ref. [3.5(a)] and $R_k = 15.7$Å in Ref. [3.5(b)]. The data sets in both of these studies appear to be adequate for imaging near-neighbor atoms over the range discussed by these authors. In Ref. [3.7(a)], we estimate R_D to be only 2.29Å, such that images of even nearest-neighbor atoms at distances of 2-3Å might be expected to be surrounded by coarse-angle noise (*cf.* Figs. 3.3(d) and 3.4(d), which have a comparable R_D), while R_k is effectively much larger due to smooth-curve interpolation of scanned-wavenumber $\chi(\mathbf{k})$ data with initially rather fine steps of only 2eV. In Ref. [3.7(b)], $R_D = 4.63$Å, and is borderline, but probably sufficient, for the distances ≤ 5Å over which images were generated in this study, while $R_k = 20.9$Å and therefore puts no real limit on image size. Of the four data sets considered here, the latter two nominally scanned-wavenumber studies could have benefited from data taken with smaller steps in direction, and a

corresponding increase could have been made in the wavenumber step size so as to yield the same overall data acquisition times.

Finally, we consider the influence of **k**-space sampling on the use of the previously-mentioned small-cone inversion method to reduce artifacts in imaging backscattering atoms [3.21]. Figure 3.7 shows images reconstructed using the small-cone method of Eq. (3.5), with a cone half-angle width of 30°, or $\Delta\Omega_{\hat{\mathbf{k}}} = 0.27\pi$, of the backscattering Cu cluster in the (100) plane in Fig. 3.1(c). These images are obtained from $\chi(\mathbf{k})$ data sets based upon the individual **k**-space elements of Figs. 3.2(b)-(f); no Hanning window was used here. To permit a fully parallel comparison with our prior results, these images were calculated along both the negative and positive axes of the cones. However, we point out that the small-cone approach has been specifically constructed to focus on imaging backscattering atoms for which the non-idealities in scattering anisotropy are the least problematic, so images of forward scattering are not expected to be particularly useful with this method. Similar to the images for $\Delta\Omega_{\hat{\mathbf{k}}} = 2\pi$ discussed above, the intermediate **k**-space sampling choices of Figs. 3.7(b)-(d) give the most reliable backscattering atomic images, compared to the more nearly limiting-case scanned-angle and scanned-wavenumber images of Figs. 3.7(a) and 3.7(e), respectively. This is due to the fact that the small-cone method is inescapably still a Fourier transform that is susceptible to Fourier artifacts. Therefore, avoiding these artifacts when imaging backscattering atoms using this method still requires experimental $\chi(\mathbf{k})$ data sets that have the minimal wavenumber and angular **k**-space resolutions we have quantified above. All of the elongated features for $z > 0$ are simply artifacts due to the use of the small cone method along the positive cone axes. Figure 3.6(e) also shows the yz = (100) atomic image of the backscattering cluster of Fig. 3.1(c), reconstructed via the small-cone method from the minimal $\chi(\mathbf{k})$ data set of Fig. 3.6(a). This image is relatively free of the coarse resolution aberrations and noise present in the limiting cases of Figs. 3.7(a) and 3.7(e), although it does have a strong alias peak at $(y,z) \approx$ (0.0Å, -4.0Å) that could be eliminated by using a slightly greater number of

wavenumbers (see *e.g.*, Fig. 3.7(b)). Thus, the small-cone method also is found to benefit from the same sort of optimization of **k**-space sampling that we have been discussing, and conversely to exhibit image degradation if these criteria are not minimally met.

3.5 Concluding remarks

We have pointed out that scanned-angle and scanned-wavenumber $\chi(\mathbf{k})$ data sets for electron emission holography represent two limits of a continuum of choices in the sampling of electron **k** for holographic imaging of surface atomic structures. Going too far toward either of these limits is found to produce undesired noise and aberrations in the resulting atomic images, but simple criteria have been proposed to permit determining the optimum resolution in wavenumber (δk) and in direction ($|\delta \hat{\mathbf{k}}|$) so as to most efficiently use data acquisition time. Some prior experimental studies considered represent a mixture of satisfying and not satisfying these criteria. These criteria are also found to apply to holographic inversions based upon the small-cone approach. For the example Cu(001) surface investigated here, symmetry reduction of the data set finally yields a total of about 3,000 intensities that would need to be measured to obtain reasonable images within a sphere of radius 6.0Å centered on the emitter, a number that is quite feasible using third-general synchrotron radiation beamlines. For the wavenumber range of $10.0\text{Å}^{-1} \leq k \leq 13.0\text{Å}^{-1}$ considered here, imaging forward scattering atoms (as compared to backscattering atoms) is inherently more difficult, even with optimized **k**-space sampling, although this behavior might be improved by going to lower wavenumbers for which forward scattering is diminished in relative importance and becomes more nearly isotropic in nature.

References

[3.1] A. Szöke, in: *Short Wavelength Coherent Radiation: Generation and Applications,* eds. D. T. Atwood and J. Boker, AIP Conf. Proc. No. 147 (AIP, New York, 1986), 361.

[3.2] J. J. Barton, Phys. Rev. Lett. **61** (1988) 1356, and Phys. Rev. Lett. **67** (1991) 3106. (b) J. J. Barton and L. J. Terminello, paper presented at the Third International Conference on the Structure of Surfaces, Milwaukee, July 1990, and in *Structure of Surfaces III,* eds. S. Y. Tong, M. A. Van Hove, X. Xide, and K. Takanayagi (Springer Verlag, Berlin, 1991) 107. (c) S. Y. Tong, H. Huang, and C. M. Wei, Phys. Rev. B **46** (1992) 2452, and references therein.

[3.3] P. J. Orders and C. S. Fadley, Phys. Rev. B **27** (1983) 781, and references therein.

[3.4] (a) G. R. Harp, D. K. Saldin, and B. P. Tonner, Phys. Rev. B **42** (1990) 9199. (b) S. Thevuthasan, R. X. Ynzunza, E. D. Tober, C. S. Fadley, A. P. Kaduwela, and M. A. Van Hove, Phys. Rev. Lett. **70** (1993) 595, and references therein.

[3.5] (a) L. J. Terminello, J. J. Barton, and D. A. Lapiano-Smith, J. Vac. Sci. Technol. B **10** (1992) 2088, and Phys. Rev. Lett. **70** (1993) 599. (b) B. L. Petersen, L. J. Terminello, J. J. Barton, and D. A. Shirley, Chem. Phys. Lett. **220** (1994) 46; (c) B. L. Petersen, Ph. D. Thesis (University of California-Berkeley, 1995).

[3.6] D. H. Rosenblatt, J. G. Tobin, M. G. Mason, R. F. Davis, S. D. Kevan, D. A. Shirley, C. H. Li, and S. Y. Tong, Phys. Rev. B **23** (1981) 3828.

[3.7] (a) J. G. Tobin, G. D. Waddill, H. Li, and S. Y. Tong, Phys. Rev. Lett. **70** (1993) 4150. (b) H. Wu, G. J. Lapeyre, H. Huang, and S. Y. Tong, Phys. Rev. Lett. **71** (1993) 251.

[3.8] (a) L. J. Terminello, B. L. Petersen, and J. J. Barton, J. Electron Spec. Relat. Phenom. **75** (1995) 229, and references therein. (b) H. Wu, G. J. Lapeyre, H. Huang, and S. Y. Tong, Phys. Rev. Lett. **71** (1993) 251, and references therein. (c) M. Zharnikov, M. Weinelt, P. Zebisch, M. Stichler, and H.-P. Steinrück, Thin

Sol. Films **275** (1996) 266, and references therein. (d) R. Denecke, R. Eckstein, L. Ley, A. E. Bocquet, J. D. Riley, R. C. G. Leckey, Surf. Sci. **331-333** (1995) 1085. (e) J. G. Tobin, G. D. Waddill, H. Hi, S. Y. Tong, Surf. Sci. **334** (1995) 263, and references therein.

[3.9] (a) H. Li, S. Y. Tong, D. Naumovic, A. Stuck, and J. Osterwalder, Phys. Rev. B **47** (1993) 10036. (b) D. K. Saldin, G. R. Harp, and X. Chen, Phys. Rev. B **48** (1993) 8234, and references therein..

[3.10] (a) Z.-L. Han, S. Hardcastle, G. R. Harp, H. Li, X.-D. Wang, J. Zhang, and B. P. Tonner, Surf. Sci. **258** (1991) 313, and references therein. (b) I. H. Hong, P. R. Jeng, S. C. Shyu, Y. C. Chou, and C. M. Wei, Surf. Sci. Lett. **312** (1994) 743.

[3.11] (a) M. A. Mendez, C. Glück, J. Guerrero, P. L. de Andres, K. Heinz, D. K. Saldin, and J. B. Pendry, Phys. Rev. B **45** (1992) 9402, and references therein. (b) C. M. Wei, S. Y. Tong, H. Wedler, M. A. Mendez, and K. Heinz, Phys. Rev. Lett. **72** (1994) 2434, and references therein. (c) D. K. Saldin and X. Chen, Phys. Rev. B **52** (1995) 2941, and references therein.

[3.12] S. Y. Tong, H. Huang, and X. Q. Guo, Phys. Rev. Lett. **69**, 3654 (1992).

[3.13] M. Tegze and G. Faigel, Europhys. Lett. **16** (1991) 41, and Nature **380** (1996) 49.

[3.14] (a) T. Gog, P. M. Len, G. Materlik, D. Bahr, C. Sanchez-Hanke, and C. S. Fadley, Phys. Rev. Lett. **76** (1996) 3132. (b) T. Gog, R.-H. Menke, F. Arfelli, P. M. Len, C. S. Fadley, G. Materlik, Synch. Rad. News **9** (1996) 30. (c) P. M. Len, T. Gog, G. Materlik, and C. S. Fadley, Phys. Rev. B Rapid Comm **55** (1997) 3323. (d) P. M. Len, T. Gog, D. Novikov, R. A. Eisenhower, G. Materlik, and C. S. Fadley, submitted to Phys. Rev. B.

[3.15] P. M. Len, S. Thevuthasan, C. S. Fadley, A. P. Kaduwela, and M. A. Van Hove, Phys. Rev. B **50** (1994) 11275.

[3.16] D. K. Saldin, G. R. Harp, B. L. Chen, and B. P. Tonner, Phys. Rev. B **44** (1991) 2480.

[3.17] S. Thevuthasan, G. S. Herman, A. P. Kaduwela, T. T. Tran, Y. J. Kim, R. S. Saiki, and C. S. Fadley, J. Vac. Sci. Technol. A **10** (1992) 2261.

[3.18] P. Hu and D. A. King, Phys. Rev. B **46** (1992) 13615.

[3.19] B. P. Tonner, Z.-L. Han, G. R. Harp, and D. K. Saldin, Phys. Rev. B **43** (1991) 14423.

[3.20] (a) S. Thevuthasan, G. S. Herman, A. P. Kaduwela, T. T. Tran, Y. J. Kim, R. S. Saiki, C. S. Fadley, and M. A. Van Hove, J. Vac. Sci. Tech. A **10** (1992) 2261. (b) P. Hu and D. A. King, Phys. Rev. B **46** (1992) 13615.

[3.21] (a) S. Y. Tong, H. Li, and H. Huang, Phys. Rev. B **51** (1995) 1850. (b) H. Wu and G. J. Lapeyre, Phys. Rev. B **51** (1995) 14549.

[3.22] C. M. Wei, J. H. Hong, P. R. Jeng, S. C. Shyu, and Y. C. Chou, Chem. Phys. Lett. **228** (1994) 513.

[3.23] (a) C. S. Fadley, in: Synchrotron Radiation Research: Advances in Surfaces and Interface Science, ed. R.Z. Bachrach, (Plenum Press, New York, 1992); (b) D. J. Friedman, C. S. Fadley, J. Elec. Spec. **51** (1990) 689.

[3.24] A. P. Kaduwela, D. J. Friedman, and C. S. Fadley, J. Electron Spectrosc. Relat. Phenom. **57** (1991) 223.

[3.25] P. M. Len, F. Zhang, S. Thevuthasan, A. P. Kaduwela, M. A. Van Hove, and C. S. Fadley, J. Electron Spectrosc. Relat. Phenom. **76** (1995) 351. (b) S. Thevuthasan, P. M. Len, and C. S. Fadley, unpublished results.

[3.26] D. K. Saldin, G. R. Harp, and B. P. Tonner, Phys. Rev. B **45** (1992) 9629.

[3.27] E. O. Brigham, *The Fast Fourier Transform and its Applications* (Prentice-Hall, New Jersey, 1988).

[3.28] G. R. Harp, D. K. Saldin, X. Chen, Z.-L. Han, and B. P. Tonner, J. Electron Spectrosc. Relat. Phenom. **70** (1991) 331.

Figure captions

Figure 3.1. (a) 25-atom Cu cluster with only backscattering and side-scattering neighbors to an emitter at the surface. (b),(c) Planes used for imaging in the cluster of (a): (b) (001) plane including the emitter, $z = 0.0$Å. (c) (100) plane including the emitter, $x = 0.0$Å. (d) 25-atom Cu cluster with the emitter below the surface and forward scattering neighbors included. (e) (100) plane including the emitter, $x = 0.0$Å.

Figure 3.2. Schematic **k**-space representation of a $\chi(\mathbf{k})$ data set (a) and various choices of individual data set elements (b)-(f). The data set elements represent varying wavenumber and angular resolutions (or equivalently, choices of δk and $\delta\hat{\mathbf{k}}$), but all contain the same overall volume in **k**-space and from $\chi(\mathbf{k})$ data sets containing the same total number of 64,800 data points.

Figure 3.3. Atomic images $|U_A(\mathbf{r}')|$ obtained for the backscattering cluster of Fig. 3.1(a) from various $\chi(\mathbf{k})$ data sets based upon the individual **k**-space elements of Figs. 3.2(b)-(f). Images here are in the (001) plane containing the emitter (Fig. 3.1(b)). Actual atomic positions are indicated with white crosses, and the two axes are marked off in 1Å units.

Figure 3.4. As Fig. 3.3, but in the (100) plane containing the emitter (Fig. 3.1(c)).

Figure 3.5. As Fig. 3.4, but for the 25-atom cluster of Fig. 3.1(d) including also forward scattering atoms, and imaging in the (100) plane containing the emitter (Fig. 3.1(e)).

Figure 3.6 (a) An optimized "minimal" data set element for a $\chi(\mathbf{k})$ consistent with accurate imaging within a radius of 6.0Å around the emitter, and containing only 25,200 data points. (b),(c) Atomic images $|U_A(\mathbf{r}')|$ obtained from this $\chi(\mathbf{k})$ data set, calculated for the backscattering cluster of Fig. 3.1(a): (b) imaging in the (001) plane containing the

emitter, and (c) in the (100) plane containing the emitter. (d) Atomic image calculated for the forward scattering cluster of Fig. 3.1(d) in the (001) plane containing the emitter. (e) Atomic image $|U_B(\mathbf{r}')|$ obtained using the small-cone method of Tong *et al.* [3.21(a)], and of Wu and Lapeyre [3.21(b)] for the backscattering cluster of Fig. 3.1(a) in the (100) plane containing the emitter. Actual atomic positions are indicated with white crosses, and the two axes are marked off in 1Å units.

Figure 3.7 Atomic images $|U_B(\mathbf{r}')|$ obtained from the method of Tong *et al.*[3.21(a)], and of Wu and Lapeyre [3.21(b)], where only a small angular cone of half-angle 30° centered along backscattering directions is used in the imaging algorithms of Eqs. (1) or (2). These calculations are for the backscattering cluster of Fig. 3.1(a), from various $\chi(\mathbf{k})$ data sets based upon the individual **k**-space elements of Figs. 3.2(b)-(f). Images here are in the (100) plane containing the emitter (Fig. 3.1(c)). Actual atomic positions are indicated with white crosses, and the two axes are marked off in 1Å units. The small-cone method has also been used for the minimal-data-set image shown in Fig. 3.6(e).

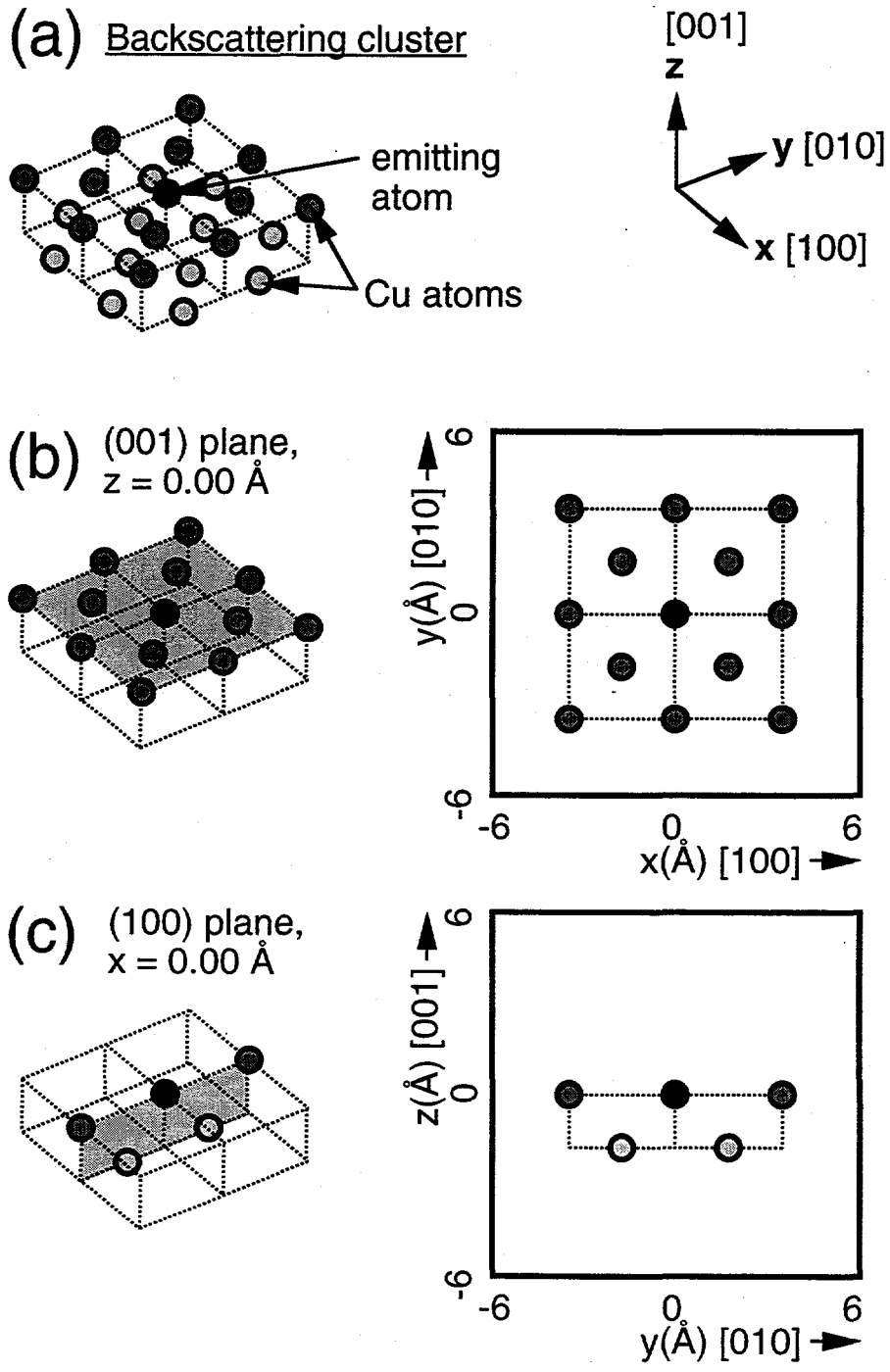

Figs. 3.1(a)-(c)

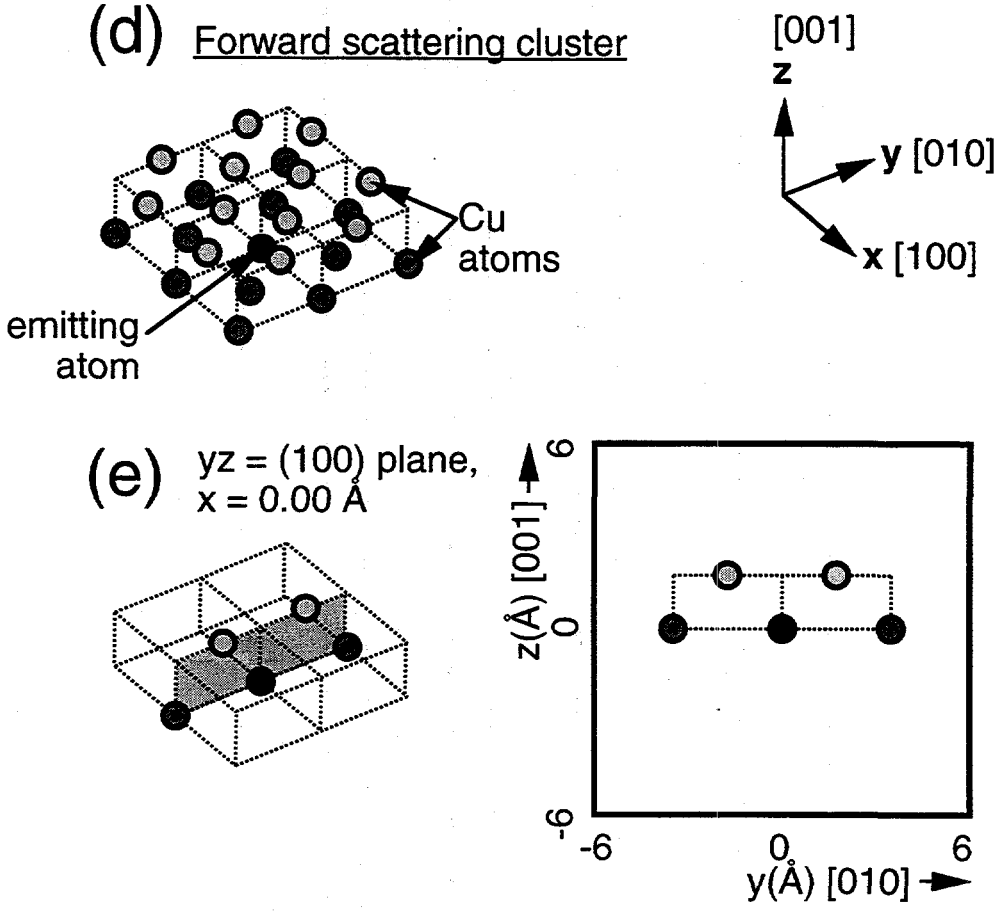

Figs. 3.1(d)-(e)

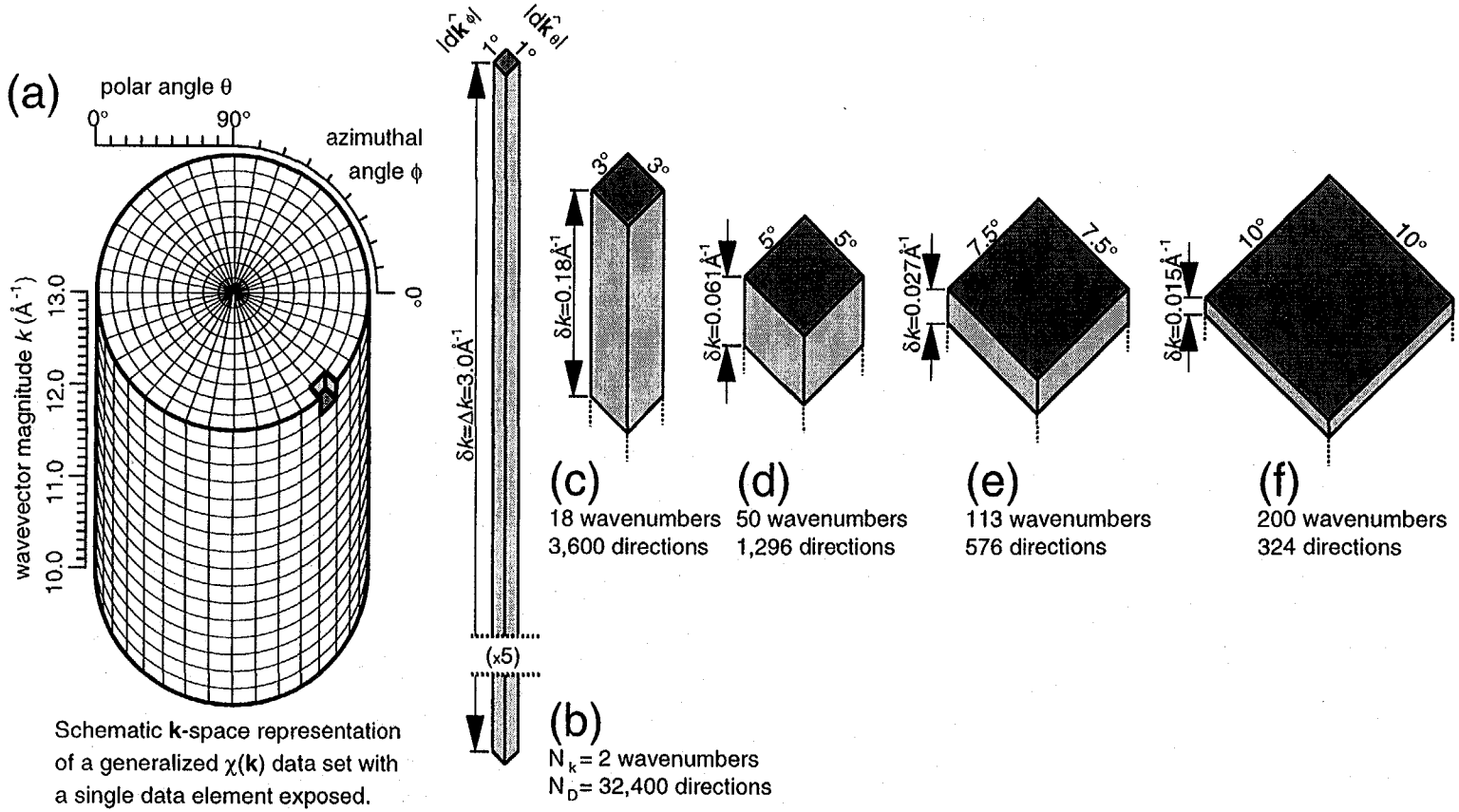

Schematic **k**-space representation of a generalized $\chi(\mathbf{k})$ data set with a single data element exposed.

Fig. 3.2

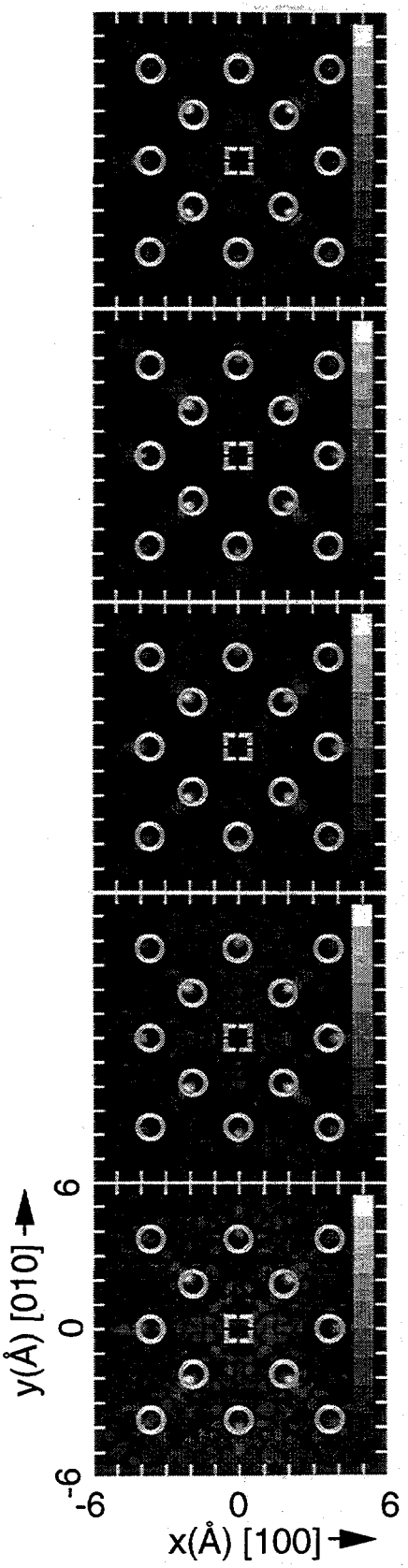

(a)
backscattering Cu(001)
Method A, (001) plane
N_k = 2 wavenumbers
N_E = 32,400 directions
($\delta k = 3.0 Å^{-1}$; $\delta\theta \times \delta\phi = 1° \times 1°$)

(b)
backscattering Cu(001)
Method A, (001) plane
N_k = 18 wavenumbers
N_E = 3,600 directions
($\delta k = 0.18 Å^{-1}$; $\delta\theta \times \delta\phi = 3° \times 3°$)

(c)
backscattering Cu(001)
Method A, (001) plane
N_k = 50 wavenumbers
N_E = 1,296 directions
($\delta k = 0.061 Å^{-1}$; $\delta\theta \times \delta\phi = 5° \times 5°$)

(d)
backscattering Cu(001)
Method A, (001) plane
N_k = 113 wavenumbers
N_E = 576 directions
($\delta k = 0.027 Å^{-1}$; $\delta\theta \times \delta\phi = 7.5° \times 7.5°$)

(e)
backscattering Cu(001)
Method A, (001) plane
N_k = 200 wavenumbers
N_E = 324 directions
($\delta k = 0.015 Å^{-1}$; $\delta\theta \times \delta\phi = 10° \times 10°$)

Fig. 3.3

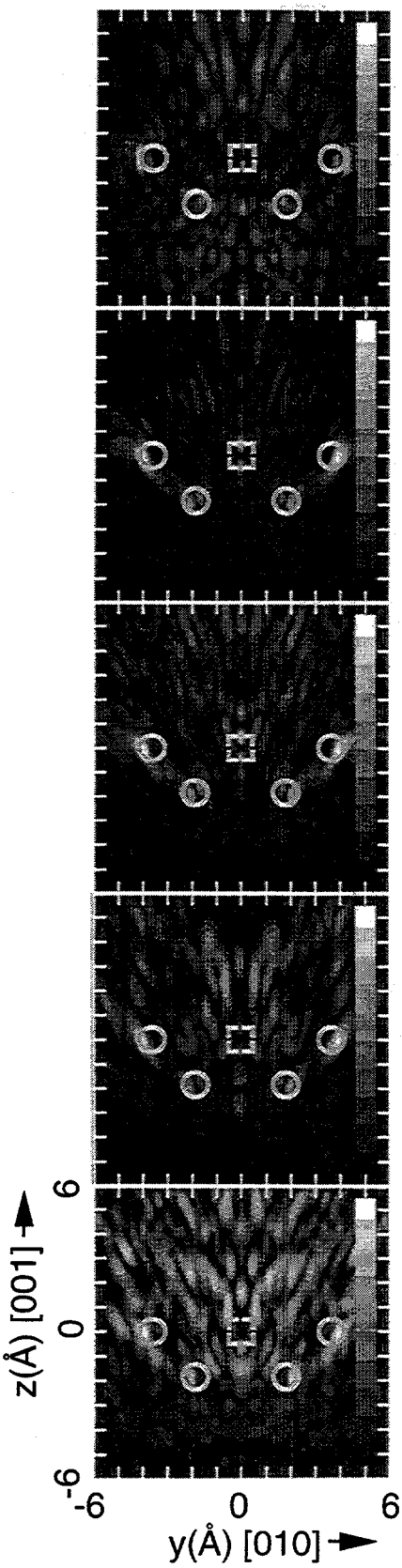

(a)
backscattering Cu(001)
Method A, (100) plane
N_k = 2 wavenumbers
N_E = 32,400 directions
($\delta k = 3.0 Å^{-1}$; $\delta\theta \times \delta\phi = 1° \times 1°$)

(b)
backscattering Cu(001)
Method A, (100) plane
N_k = 18 wavenumbers
N_E = 3,600 directions
($\delta k = 0.18 Å^{-1}$; $\delta\theta \times \delta\phi = 3° \times 3°$)

(c)
backscattering Cu(001)
Method A, (100) plane
N_k = 50 wavenumbers
N_E = 1,296 directions
($\delta k = 0.061 Å^{-1}$; $\delta\theta \times \delta\phi = 5° \times 5°$)

(d)
backscattering Cu(001)
Method A, (100) plane
N_k = 113 wavenumbers
N_E = 576 directions
($\delta k = 0.027 Å^{-1}$; $\delta\theta \times \delta\phi = 7.5° \times 7.5°$)

(e)
backscattering Cu(001)
Method A, (100) plane
N_k = 200 wavenumbers
N_E = 324 directions
($\delta k = 0.015 Å^{-1}$; $\delta\theta \times \delta\phi = 10° \times 10°$)

Fig. 3.4

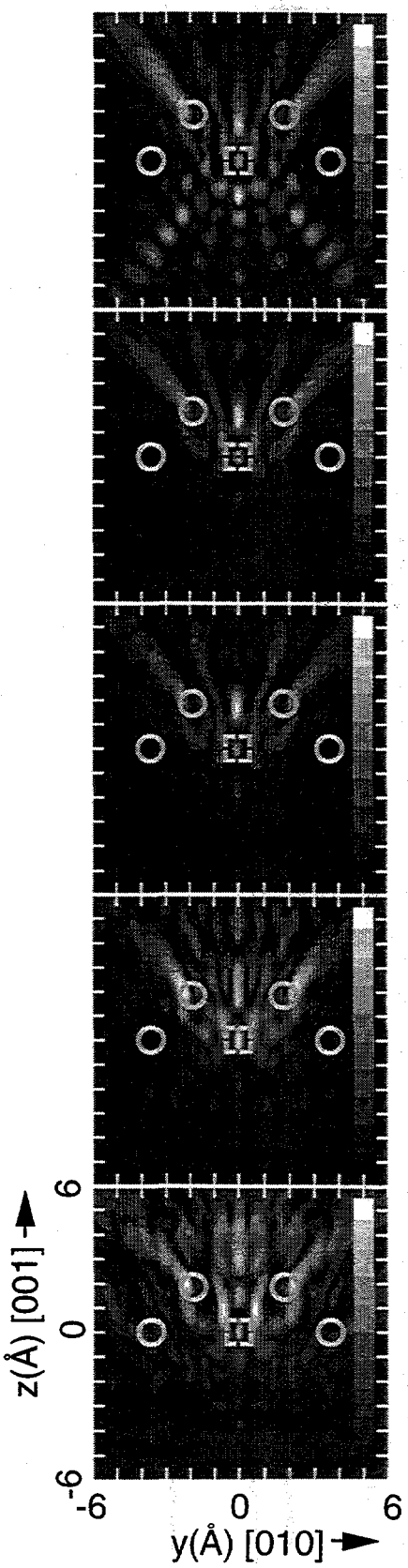

(a)
forward scattering Cu(001)
Method A, (100) plane
N_k = 2 wavenumbers
N_E = 32,400 directions
(δk = 3.0Å^{-1}; $\delta\theta$ x $\delta\phi$ = 1° x 1°)

(b)
forward scattering Cu(001)
Method A, (100) plane
N_k = 18 wavenumbers
N_E = 3,600 directions
(δk = 0.18Å^{-1}; $\delta\theta$ x $\delta\phi$ = 3° x 3°)

(c)
forward scattering Cu(001)
Method A, (100) plane
N_k = 50 wavenumbers
N_E = 1,296 directions
(δk = 0.061Å^{-1}; $\delta\theta$ x $\delta\phi$ = 5° x 5°)

(d)
forward scattering Cu(001)
Method A, (100) plane
N_k = 113 wavenumbers
N_E = 576 directions
(δk = 0.027Å^{-1}; $\delta\theta$ x $\delta\phi$ = 7.5° x 7.5°)

(e)
forward scattering Cu(001)
Method A, (100) plane
N_k = 200 wavenumbers
N_E = 324 directions
(δk = 0.015Å^{-1}; $\delta\theta$ x $\delta\phi$ = 10° x 10°)

Fig. 3.5

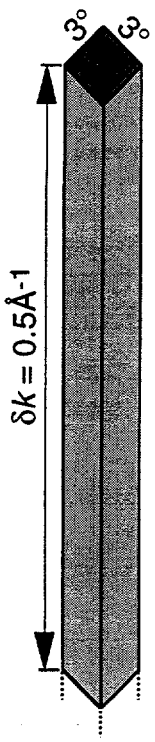

(a)
single $\chi(\mathbf{k})$
data element
N_k = 7 wavenumbers
N_E = 3,600 directions
(25,200 total
data points)

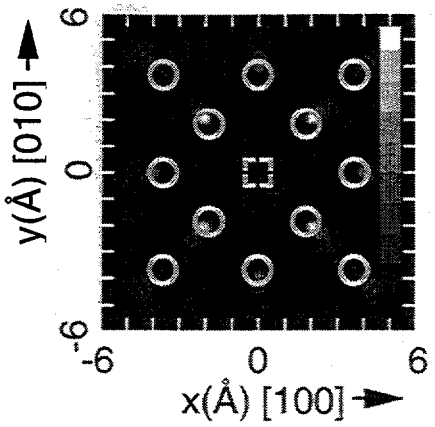

(b)
backscattering Cu(001)
Method A, (001) plane
N_k = 7 wavenumbers
N_E = 3,600 directions
($\delta k = 0.5Å^{-1}$; $\delta\theta_x\,\delta\phi = 3°\times 3°$)

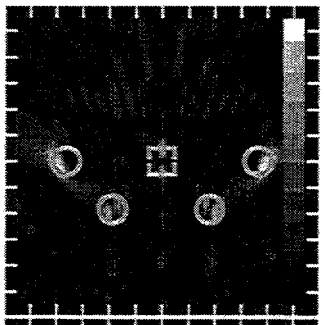

(c)
backscattering Cu(001)
Method A, (100) plane
N_k = 7 wavenumbers
N_E = 3,600 directions
($\delta k = 0.5Å^{-1}$; $\delta\theta_x\,\delta\phi = 3°\times 3°$)

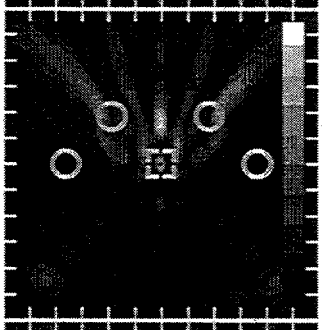

(d)
forward scattering Cu(001)
Method A, (100) plane
N_k = 7 wavenumbers
N_E = 3,600 directions
($\delta k = 0.5Å^{-1}$; $\delta\theta_x\,\delta\phi = 3°\times 3°$)

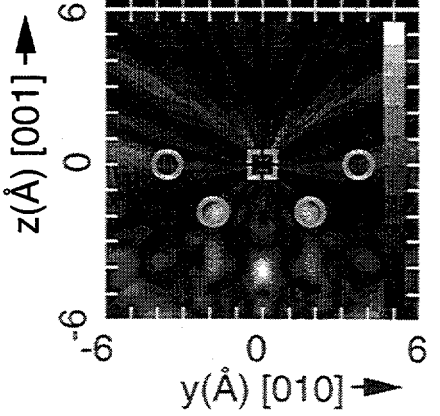

(e)
backscattering Cu(001)
Method B, (100) plane
N_k = 7 wavenumbers
N_E = 3,600 directions
($\delta k = 0.5Å^{-1}$; $\delta\theta_x\,\delta\phi = 3°\times 3°$)

Fig. 3.6

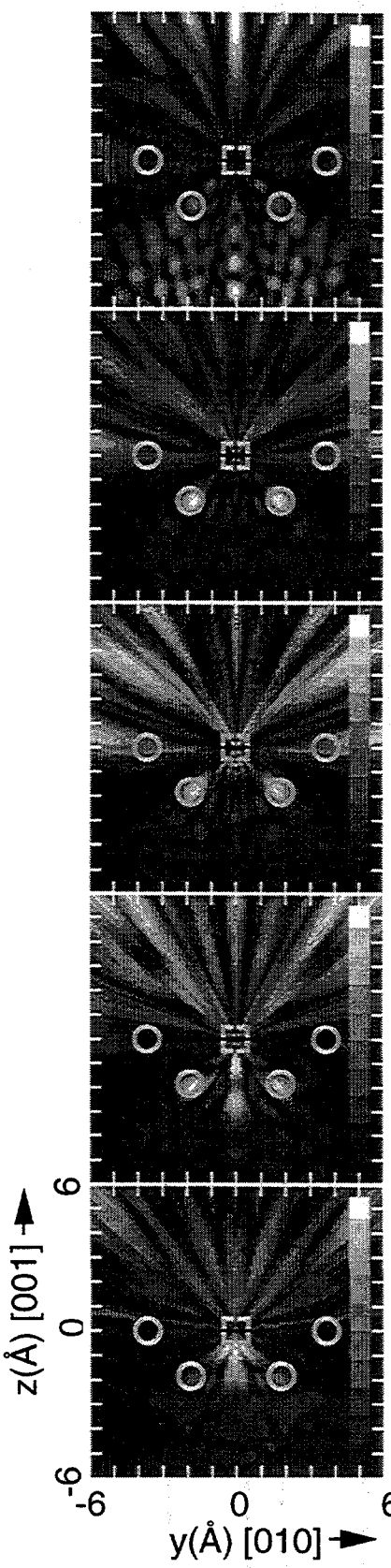

(a)
backscattering Cu(001)
Method B, (100) plane
N_k = 2 wavenumbers
N_E = 32,400 directions
($\delta k = 3.0 Å^{-1}$; $\delta\theta_x\, \delta\phi = 1° \times 1°$)

(b)
backscattering Cu(001)
Method B, (100) plane
N_k = 18 wavenumbers
N_E = 3,600 directions
($\delta k = 0.18 Å^{-1}$; $\delta\theta_x\, \delta\phi = 3° \times 3°$)

(c)
backscattering Cu(001)
Method B, (100) plane
N_k = 50 wavenumbers
N_E = 1,296 directions
($\delta k = 0.061 Å^{-1}$; $\delta\theta_x\, \delta\phi = 5° \times 5°$)

(d)
backscattering Cu(001)
Method B, (100) plane
N_k = 113 wavenumbers
N_E = 576 directions
($\delta k = 0.027 Å^{-1}$; $\delta\theta_x\, \delta\phi = 7.5° \times 7.5°$)

(e)
backscattering Cu(001)
Method B, (100) plane
N_k = 200 wavenumbers
N_E = 324 directions
($\delta k = 0.015 Å^{-1}$; $\delta\theta_x\, \delta\phi = 10° \times 10°$)

Fig. 3.7

Chapter 4

Optimal Atomic Imaging by Photoelectron Holography

Abstract

Several recent papers have dealt with the question of whether large-scale photoelectron diffraction data spanning a significant range in both angle and wavenumber can be analyzed as holograms so as to directly produce three-dimensional images of near-surface atomic structure. Data is thus taken over some volume in the photoelectron wavevector **k**-space, and then transformed to obtained atomic images. In this work, we review four analysis methods proposed to date for deriving atomic positions directly from photoelectron diffraction data and consider the application of them to theoretical diffraction patterns calculated from various single-scattering model clusters. This permits making some general conclusions as to domains of applicability and the optimization of **k**-space sampling so as to minimize data acquisition time, while still assuring atomic images that are free of coarse **k**-sampling aberrations. We conclude that holographic imaging of atoms does not require exceedingly large photoelectron diffraction data sets, with a few thousand data points being a suitable minimum, and we also comment on the relative merits of the four different imaging algorithms.

Outline

4.1 Introduction

Photoexcited atoms near surfaces can emit electron wavefronts that can reach a distant detector either directly or after scattering off of neighboring atoms. The photoelectron diffraction pattern resulting from the interference of these wavefronts can be normalized as $\chi(\mathbf{k}) = [I(\mathbf{k})-I_0(\mathbf{k})]/I_0(\mathbf{k})$ or $[I(\mathbf{k})-I_0(\mathbf{k})]/\sqrt{I_0(\mathbf{k})}$, where $I(\mathbf{k})$ is the electron intensity detected at a given electron wavevector $\mathbf{k}$ (= k (wavenumber) × $\hat{\mathbf{k}}$ (direction)), and $I_0(\mathbf{k})$ is the corresponding intensity in the absence of any scattering. Szöke first pointed out that these $\chi(\mathbf{k})$ data sets could be interpreted as holograms, where the direct electron wavefronts are considered as reference waves, and the scattered wavefronts as object waves [4.1]. A number of theoretical and experimental papers have subsequently discussed the reconstruction of three-dimensional atomic images from $\chi(\mathbf{k})$ data sets based on photoelectrons [4.2-4.16], Auger electrons [4.17], backscattered Kikuchi electrons [4.18], diffuse low energy electrons [4.19] and positrons [4.20], as well as from fluorescent x-rays [4.1,4.21]. In this paper, we will review the four major atomic imaging methods that have been suggested to date for photoelectron holography, consider the application of them to various classes of atomic models (simple Cu/Ni and large Cu/Ni(001) clusters), present general conclusions as to the optimal **k**-space sampling resolution necessary to minimize data acquisition times while assuring atomic image fidelity with any of these methods, and compare these methods as to their advantages and disadvantages.

Our methodology will be to compute holographic data over a certain volume in **k**-space for various choices of **k**-sampling by using the well-known single scattering cluster model [4.22], to invert these data so as to produce atomic images using four important imaging algorithms that have been proposed to date, and to thus draw conclusions concerning the optimum procedures for holographically imaging atoms. Although using a multiple scattering approach [4.23] would certainly be a more accurate way to calculate such holograms, the thousands of individual calculations that would be needed are at

present prohibitively long from the point of view of calculation time. In any case, because all of the transform methods we will consider inherently attempt to project out the single scattering character from a given data set, we expect the present single-scattering simulations to be a good representation of the best possible behavior of a real experimental holographic inversion. Additional complications due to incomplete cancellation of multiple scattering effects in the inversion process for an experimental data set are of course possible.

4.2 Review of image reconstruction methods

The basic reconstruction algorithm (here denoted Method "A") for extracting atomic images from $\chi(\mathbf{k})$ data sets was developed by Barton [4.2], and Tong and co-workers [4.3] and is a **k**-space Fourier transform with a kernel based on the ideal path-length difference phase factor ($e^{i(\mathbf{k}\cdot\mathbf{r}'-kr')}$), as extended over both angular and wavenumber ranges. The atomic image intensity $U_A(\mathbf{r}')$ at a location **r'** relative to the emitter as origin is given by:

$$U_A(\mathbf{r}') = \int_k dk e^{-ikr'} \iint_S d\sigma_{\mathbf{k}} e^{i\mathbf{k}\cdot\mathbf{r}'} \chi(\mathbf{k}), \tag{4.1}$$

where the solid angle element is given by $d\sigma_{\mathbf{k}} = k^2 \cos\theta d\theta d\phi$. This method has been extensively used in imaging surface overlayers and near-surface structures [4.4-4.5].

Various other image reconstruction methods have also been developed in addition to Method A, as the path-length difference kernel does not sufficiently image atoms when the electron scattering in a system is strongly non-ideal or non-isotropic in nature [4.6-4.9].

A second method proposed independently by Tong and co-workers [4.10], and Wu and Lapeyre [4.11] (Method "B") limits the transform of Eq. (4.1) to the

backscattering contribution to $\chi(\mathbf{k})$ for which the scattering is most nearly ideal, and which thus corresponds to imaging atoms beneath the emitting atom as seen from the detector. This is done by limiting the solid angle of $\chi(\mathbf{k})$ used in reconstructing backscattering images at $\mathbf{r}'$ to $\hat{\mathbf{k}}$ directions within a cone centered on the $-\hat{\mathbf{r}}'$ axis. This algorithm can be written as:

$$U_B(\mathbf{r}') = \int_k dk e^{-ik|\mathbf{r}'|} \iint_S d\sigma_{\mathbf{k}} e^{i\mathbf{k}\cdot\mathbf{r}'} \chi(\mathbf{k}) \cdot w(\alpha, \Theta^{\hat{\mathbf{k}}}_{-\hat{\mathbf{r}}'}), \tag{4.2}$$

and is identical to Eq. (4.1) except for the window function $w(\alpha, \Theta^{\hat{\mathbf{k}}}_{-\hat{\mathbf{r}}'})$, which is most simply equal to unity where $|\Theta^{\hat{\mathbf{k}}}_{-\hat{\mathbf{r}}'}| \leq \alpha$ (typically $\approx 30°$) and is zero elsewhere. Method B also has been demonstrated to reconstruct successful atomic images from experimental $\chi(\mathbf{k})$ data [4.11-13].

A third method due to Rous and Rubin [4.14] (Method "C") involves a reconstruction kernel that recognizes the quantum mechanical nature of electron propagation and atomic scattering, at least at the level of the first Born approximation. The resulting imaging algorithm is given by:

$$U_C(\mathbf{r}') = \frac{d}{dr'}\left[r' \cdot \mathrm{Re}\left[\int_k dk e^{-ik|\mathbf{r}'|} \iint_S d\sigma_{\mathbf{k}} e^{i\mathbf{k}\cdot\mathbf{r}'} \chi(\mathbf{k}) \right] \right] = \frac{d}{dr'}\left[r' \cdot \mathrm{Re}\left[U_A(\mathbf{r}') \right] \right], \tag{4.3}$$

with the second form showing its close relationship to Eq. (4.1). According to Rous and Rubin, the image intensity $U_C(\mathbf{r}')$ should be proportional to the potential field of the scattering atoms.

A somewhat different method of obtaining atomic positions from $\chi(\mathbf{k})$ data due to Hofmann and Schindler [4.15] (Method "D") emphasizes the analysis of scanned-wavenumber photoelectron diffraction data with k as the primary variable, although several directions $\hat{\mathbf{k}}$ are also measured. This method uses a theoretically calculated single

scattering $\chi_{theoretical}(\mathbf{k},\mathbf{r}')$ as a transform kernel over a single-direction scanned-wavenumber data set, with such transforms then being exponentiated and summed over different directions via the empirically derived formula:

$$U_D(\mathbf{r}') = \sum_{\hat{\mathbf{k}}} \Delta\sigma_{\hat{\mathbf{k}}} \exp\left[r' \cdot \int_k dk \chi_{theoretical}(\mathbf{k},\mathbf{r}')\chi(\mathbf{k}) \right], \tag{4.4}$$

where:

$$\chi_{theoretical}(\mathbf{k},\mathbf{r}') = \mathrm{Re}\left[\frac{e^{i(kr-\mathbf{k}\cdot\mathbf{r}')}}{kr'} f(\Theta^{\hat{\mathbf{k}}}_{\hat{\mathbf{r}}'}) \right], \tag{4.5}$$

and $f(\Theta^{\hat{\mathbf{k}}}_{\hat{\mathbf{r}}'})$ is the scattering factor for electron wavefronts scattered from direction $\hat{\mathbf{r}}'$ to direction $\hat{\mathbf{k}}$. The exponent in Eq. (4.4) can be interpreted as an inner product between the theoretical $\chi_{theoretical}(\mathbf{k},\mathbf{r}')$ and the experimental $\chi(\mathbf{k})$, over a range of wavenumbers k. An image intensity $U_D(\mathbf{r}')$ is then built up by arithmetically summing (but not summing with phase information preserved as in the other three methods) these inner products for many different directions. This method also has been successful in deriving adsorbate geometries on surfaces [4.16], but it is not holographic in a strict sense.

4.3 $\chi(\mathbf{k})$ k-space parameters

Figure 4.1 shows the schematic **k**-space representation of a $\chi(\mathbf{k})$ data set that spans directions in the upper 2π hemisphere above a sample surface, and wavenumbers (kinetic energies) in the range $8.11\text{Å}^{-1} \le k \le 11.25\text{Å}^{-1}$ ($250\text{eV} \le E \le 482\text{eV}$), as viewed along the $[00\bar{1}]$ and $[\bar{1}00]$ directions (Figs. 4.1(a)-(b), respectively). Individual $\chi(\mathbf{k})$ measurements are located at each intersection in this **k**-space representation. The $\chi(\mathbf{k})$

data elements in the first quadrant have been removed to show the $\chi(|\mathbf{k}| = 8.11\text{Å}^{-1})$ **k**-space surface.

In this angular and wavenumber range, it would be most ideal to collect **k**-space data points with as fine a resolution in direction ($|\delta\hat{\mathbf{k}}|$) and wavenumber ($\delta|\mathbf{k}|=\delta k$) as possible, in order to be sure of recording all major turning points in the $\chi(\mathbf{k})$ intensities, avoid any coarse **k**-space resolution transform artifacts in the atomic images reconstructed using Methods A-D, and thus improve the discrimination of the atomic image peak signals from the background noise. However, the ultimate number of $\chi(\mathbf{k})$ intensities that can be measured will always be limited by experimental time constraints. One question that arises immediately is thus: *What is the minimum number of experimental* $\chi(\mathbf{k})$ *measurements necessary in a given angular and wavenumber range to ensure minimally resolved atomic images within a certain radius R of the emitter?* However, even if we are given this number of $\chi(\mathbf{k})$ data points in some volume in **k**-space, measurements can still be taken with **k**-space resolutions ranging from fine-in-angle/coarse-in-wavenumber to coarse-in-angle/fine-in-wavenumber. Thus, a second question arises: *How should an experimental* $\chi(\mathbf{k})$ *data set best be resolved in* **k***-space given this limited number of available intensity measurements in order to optimally resolve atoms?* In this paper, in order to fairly compare the atomic images produced by each of Methods A-D, we will first determine the minimum $\chi(\mathbf{k})$ data set that will produce satisfactory atomic images from each method. Then the effect of different **k**-space sampling choices relative to this minimal $\chi(\mathbf{k})$ data set on the images reconstructed by all of the methods will be investigated, and the images produced by each method from their respectively optimally resolved $\chi(\mathbf{k})$ data sets will finally be compared.

All of the calculated $\chi(\mathbf{k})$ data sets considered in this paper have the *overall* angular and wavenumber range of the schematic data set of Fig. 4.1. The average angular **k**-spacing between data points is then given by $|\delta\hat{\mathbf{k}}| \approx \sqrt{2\pi k_{\max}^2 / N_D}$, where N_D is the number of different directions chosen for a given $\chi(\mathbf{k})$ data set. The spacing between

different wavenumber holographic intensities is given by $\delta k = (k_{max} - k_{min})/(N_k - 1)$, where N_k is the number of different wavenumbers in the same $\chi(\mathbf{k})$ data set.

Figures 4.2(a) and 4.3(a) respectively show the $yz = (100)$ planar cuts of the simple five atom Cu/Ni and large 203 atom Cu/Ni(001) clusters considered in this study. Note that the emitters are taken to be Cu atoms in four-fold hollow sites on an Ni(001) substrate with the same Ni vertical spacings as in the Ni lattice; thus we will be attempting to image only backscattering Ni atoms and side-scattering Cu atoms. Such backscattering and side scattering cases are in fact those for which the most accurate and encouraging holographic atomic images have been derived from experimental data to date [4.5a,4.5b,4.11-4.13,4.18,4.19a]. The Cu $2p \rightarrow s+d$ photoelectron diffraction patterns as calculated using a single scattering model [4.22] for each cluster are shown in Figs. 4.2(b)-(c) and Figs. 4.3(b)-(c), in the same manner as Figs. 4.1(a)-(b). In arriving at these, an experimental temperature of 300K was simulated by including Debye-Waller vibration effects [4.22,4.23]. Inelastic attenuation of photoelectrons due to scattering beneath the bulk surface was also simulated with inelastic attenuation lengths ranging from 6.08Å (for $k_{min} = 8.11 \text{Å}^{-1}$) to 8.44Å (for $k_{max} = 11.25 \text{Å}^{-1}$). The incident unpolarized radiation and outgoing photoelectron path make an arbitrary fixed angle of 72°.

The normalized photoelectron hologram was found from the calculated intensities by calculating $\chi(k\hat{\mathbf{k}}) = [I(k\hat{\mathbf{k}}) - I_0(k\hat{\mathbf{k}})]/I_0(k\hat{\mathbf{k}})$. Although different normalization schemes have been used in prior photoelectron holography studies [4.24], we have here chosen to derive $I_0(k\hat{\mathbf{k}})$ in the most straightforward way, as a simple linear background over the N_E intensities along a given direction $\hat{\mathbf{k}}$. Thus, the data along each direction have a single linear background subtracted from them, and there is no direct linkage between the backgrounds for different directions, except via the fact that $I(k\hat{\mathbf{k}})$ will be a continuous function of direction, and this will indirectly link the linear $I_0(k\hat{\mathbf{k}})$'s, especially for data taken with closer spacings in direction. This linear normalization scheme strongly attenuates forward scattering images, as the holographic forward scattering modulations in

$I(\mathbf{k})$ will vary slowly along forward scattering directions, and as such would tend to be subtracted as part of the linear background $I_0(k\hat{\mathbf{k}})$ [4.24a]. However, this normalization scheme will be sufficient for present purposes, as we are considering only backscattering and side scattering clusters in this paper. In addition, we have made spot checks for some cases considered here as to what happens when a more desirable and accurate three-dimensional smooth-curve fit is made to $I(k\hat{\mathbf{k}})$ in deriving $I_0(k\hat{\mathbf{k}})$ [4.28], and find that this has a negligible effect on the images of the backscattering and side-scattering atoms.

Table 4.1 below shows the angular ($|\delta\hat{\mathbf{k}}|$) and wavenumber (δk) **k**-space resolutions required by Nyquist sampling considerations in order to avoid transform alias aberrations within different radii R from the emitter [4.25,4.26]; such consideration lead to $|\delta\mathbf{k}|$ or $\delta k = \pi / R$. Note that the total number of data points given in Table 4.1 are for measurements spanning the entire 2π hemisphere above the cluster. For the clusters considered here, the symmetry-reduced solid angle area would be 1/8th of this; thus the actual number of inequivalent intensity measurements would be given by $N_{total} \div 8$, as indicated in parentheses in the last column. In order to keep a larger volume of space around the emitter artifact-free, finer sampling of this region of **k**-space is required, and more $\chi(\mathbf{k})$ data points in different directions (N_D) and at different wavenumbers (N_k) are needed. However, if we are, for example, only interested in imaging the backscattering Ni atoms that are 2.43Å distant from the emitter, it is expected that only $N_{total} = N_D \times N_k \approx$ 10^3 to 10^4 $\chi(\mathbf{k})$ data points (or only 10^2 to 10^3 unique data points with symmetry reduction) would be required.

Table 4.1
k-space parameters for increasingly finer resolution $\chi(\mathbf{k})$ data sets

Radius of artifact-free volume R	Required **k**-space resolution $\lvert\delta\hat{\mathbf{k}}\rvert, \delta k = \frac{\pi}{R}$	Number (resolution) of different directions N_D ($\delta\theta \times \delta\phi$)	Number of different wavenumbers N_k	Total number of (symmetry-reduced) $\chi(\mathbf{k})$ data points $N_{total} = N_D \times N_k$
(a) 2Å	1.57Å^{-1}	324 (10°×10°)	3	972 (÷8 ≈ 122)
(b) 3	1.047	900 (6°×6°)	4	3,600 (÷8 = 450)
(c) 4	0.785	1,296 (5°×5°)	5	6,480 (÷8 = 810)
(d) 5	0.628	2,016 (4°×4°)	6	12,420 (÷8 ≈ 1,553)

4.4. Effect of k-space resolution on atomic images

Figures 4.4-4.7 show the atomic images of the small Cu-emitting/Ni-backscattering cluster of Fig. 4.2(a), reconstructed using Methods A-D, respectively, from the calculated single-scattering $\chi(\mathbf{k})$ data set of Figs. 4.2(b)-(c). Within each figure, the images were reconstructed from this $\chi(\mathbf{k})$ with the different **k**-space resolutions given in Table 4.1.

As expected for all of Methods A-D, the Ni atomic images 2.43Å distant from the emitter are unresolved in the images of Figs. 4.4-4.7(a), reconstructed from $\chi(\mathbf{k})$ data with a resolution only sufficient to adequately resolve atomic images within $R \leq 2$Å from the emitter. Peaks that seem to be identifiable as the Ni backscatterers at this **k**-space resolution of only 972 $\chi(\mathbf{k})$ data points are seen in the images obtained by Method B (Fig. 4.5(a)), but these peaks are significantly shifted away from their actual positions of (y,z) = (±1.76Å,-1.76Å), and are in fact due to the coarse-wavenumber alias features spaced at $\Delta R = \pi / \delta k = \pi / (1.57\text{Å}^{-1}) = 2$Å intervals along the $[01\bar{1}]$ and $[0\bar{1}\,\bar{1}]$ backscattering directions [4.25,4.26].

As expected, increasing the **k**-space resolution of the $\chi(\mathbf{k})$ data set results in better resolved atomic images. In the images reconstructed from the intermediate resolved $\chi(\mathbf{k})$ data set of 3,600 data points (Figs. 4.4-4.7(b)), the Ni backscattering images are now discernible in all of Methods A-D. But the sharpest and clearest images are for Method A.

Figures 4.4-4.7(c) show the images obtained by Methods A-D from the $\chi(\mathbf{k})$ data set of 6,480 data points. The backscattering Ni images are now unambiguously resolved at very near to their correct positions by each method at this **k**-space resolution, which we take to be the minimum number required here to successfully use all four Methods A-D on an identical $\chi(\mathbf{k})$ data set.

Figures 4.4-4.7(d) now show the images obtained from the finest resolved $\chi(\mathbf{k})$ set considered here, of 12,420 intensities. These atomic images are slightly more resolved, with a further reduction of background noise from the images reconstructed from the previous resolution $\chi(\mathbf{k})$ set. Method D retains the most background noise of all four for this case, with the possibility of incorrectly assigning an atom to a position directly below the emitter at $(y,z) \approx (0\text{Å},-3\text{Å})$. Overall, Method D thus seems the most difficult to cleanse of image artifacts.

Note the presence of a weak artifact peak at $(y,z) \approx (0\text{Å},-2\text{Å})$ in most of Figs 4.4-4.7(b)-(d). This artifact is expected due to the imaging kernel $e^{i(\mathbf{k}\cdot\mathbf{r}'-kr')}$ which is used in some way by all four methods (Eqs. (4.1)-(4.4)). When data for a single $\hat{\mathbf{k}}$ direction in $\chi(\mathbf{k})$ is reconstructed, the locus of this kernel is an image intensity paraboloid passing through the location of a scatterer, with a position offset possibly due to scattering phase shifts [4.3]. As more $\hat{\mathbf{k}}$ directions are sampled in Eqs. (4.1) or (4.2), the intersection of many paraboloids will overlap at the atomic scattering locations. However, if there are only a few $\hat{\mathbf{k}}$ directions in a given $\chi(\mathbf{k})$ data set, there will be a smaller number of paraboloids that intersect at the actual scattering locations, compared to the weak spurious intersections of these paraboloids along low-index directions [4.27]. It is such spurious intersections that are seen here.

We have so far demonstrated that only 10^3 to 10^4 $\chi(\mathbf{k})$ data points (or only 10^2 to 10^3 unique data points with symmetry reduction) would be necessary to satisfactorily define the images of Ni backscattering atoms 2.43Å distant from a Cu emitter. As expected from Nyquist sampling considerations, a $\chi(\mathbf{k})$ data set with a **k**-space resolution

to resolve images within $R \leq 3$Å (3,600 →450 intensities with symmetry reduction) is marginally adequate to resolve these Ni backscattering atoms, and a finer **k**-space resolution to resolve images within $R \leq 4$Å (6,480→810 intensities) is required to unambiguously image these Ni atoms *by all four methods.* As for finer $\chi(\mathbf{k})$ data sets, resolving atomic images within a radius more than the photoelectron inelastic attenuation length of 6-8Å would be much more arduous from an experimental point of view. Such a finely resolved data set for $R \leq 8$Å would have $N_{total} = 46{,}656 \rightarrow 5{,}832$ intensities. Thus 10^4 to 10^5 data points in this volume of **k**-space without symmetry reduction would be the maximum number resulting in improved atomic images, as more data points in this volume would not be significantly beneficial.

As a more realistic demonstration of the adequacy of various **k**-space sampling resolutions, we now consider the imaging of a much larger cluster simulating a 1ML Cu overlayer on Ni(001) (Fig. 4.3(a)). The images using Methods A-D obtained from the calculated Cu/Ni(001) $\chi(\mathbf{k})$ of Figs. 4.3(b)-(c) and with the resolution of Table 4.1(c) (6,480 intensities without symmetry reduction) are shown in Figs. 4.8-4.11(a). As before, the images of the Ni backscattering atoms at $(y,z) = (\pm 1.76\text{Å}, -1.76\text{Å})$ are reasonably well-resolved by all four methods at this resolution, as are the in-plane Cu neighbors that are now present at $(y,z) = (\pm 3.52\text{Å}, 0\text{Å})$ in the images generated by Methods A, C, and D (Figs. 4.8,10-11(a)). In the image obtained by Method B (Fig. 4.9(a)), the side scattering Cu images are absent, due to the lack of sufficient $\chi(\mathbf{k})$ intensities for the small cone regions used for images in the xy = (001) plane of the emitter. This represents a weakness of Method B in not resolving as well such in-plane neighbors as Methods A, C, and D. These side scattering Cu atoms are imaged by Method D (Fig. 4.11(a)), even though the calculated $\chi_{theoretical}(\mathbf{k},\mathbf{r}')$ for Method D used here only included the scattering factor $f(\Theta_{\mathbf{r}'}^{\hat{\mathbf{k}}})$ for Ni atoms, rather than also for Cu atoms in the surface plane. This is adequate for the present example, as the scattering factors for Cu and Ni are very similar, but a fully correct $\chi_{theoretical}(\mathbf{k},\mathbf{r}')$ transform kernel for Eq. (4.3) involving atoms of more than one

type would require *a priori* knowledge of the approximate position and localization of each type of atom being imaged. Once again, Method D retains the highly level of background artifact features for this case with 6,480 intensities.

We now consider in Table 4.2 below different choices of **k**-space resolutions that range from the Nyquist resolution for both directions and wavenumbers to resolve images within a 4Å radius (Table 4.1(c) and Table 4.2(a)), to more coarse-in-direction/fine-in-wavenumber resolutions, *but still with the same minimal number of 6,480 intensities expected to ensure well-resolved atomic images and leading to the same expected data acquisition time* (Table 4.2(b)-(d)). Figs. 4.8-4.11(b)-(d) show the Cu/Ni(001) images obtained by Methods A-D from $\chi(\mathbf{k})$ data sets with the given in Table 4.2(b)-(d). It can be seen that the best resolved images of the backscattering Ni atoms for Methods A-D result from an $\chi(\mathbf{k})$ data set that is *slightly* more coarse-in-angle/fine-in-wavenumber (Figs 4.8-4.11(b)) than the **k**-space resolution of Table 4.2(a). This is probably primarily due to a better subtraction of the linear $I_0(k\hat{\mathbf{k}})$ background from the raw $I(\mathbf{k})$ data, because of the greater number of wavenumber data points (N_E = 11) in a given direction $\hat{\mathbf{k}}$. Even though the direction resolution $|\delta\hat{\mathbf{k}}|$ is coarser than required by Nyquist considerations, the advantage of more wavenumbers and better $I_0(k\hat{\mathbf{k}})$ background subtraction here outweighs the added noise from the coarse-in-direction resolution of only 576 directions for Methods A-D. However, increasing the number of wavenumbers in Figs. 4.8-4.11(b) at the expense of the number of directions has the simultaneous undesirable effect of suppressing the in-plane Cu atom images that are clearly present in Figs. 4.8(a), 4.10(a), and 4.11(a). Therefore, it is a matter of choice between these two types of **k**-space resolutions (Table 4.2(a) and (b)) that would depend on the particular problem at hand.

Table 4.2
k-space parameters for increasingly coarse-in-direction/fine-in-wavenumber $\chi(\mathbf{k})$ data sets of approximately 6,480 intensities

Direction **k**-space resolution $\lvert\delta\hat{\mathbf{k}}\rvert$ $(\delta\theta \times \delta\phi)$	Wave-number **k**-space resolution δk	Number of different directions N_D	Number of different wavenumbers N_k	Total number of (symmetry-reduced) $\chi(\mathbf{k})$ data points $N_{total} = N_D \times N_k$
(a) 0.785Å^{-1} (5°×5°)	0.785Å^{-1}	1,296	5	6,480 (÷8 = 810)
(b) 1.17 (7.5°×7.5°)	0.314	576	11	6,336 (÷8 = 792)
(c) 1.57 (10°×10°)	0.165	324	20	6,480 (÷8 = 810)
(d) 2.35 (15°×15°)	0.0714	144	45	6,480 (÷8 = 810)

Increasing the number of different wavenumber measurements for each single direction further is *not* found to be beneficial, however. In Figs. 4.8-4.11(c)-(d), the more coarse-in-direction/fine-in-wavenumber $\chi(\mathbf{k})$ data sets of Table 4.2(c)-(d) result in images that are clearly degraded from the images of Figs. 4.8-4.11(b), which may be taken as optimally benefiting from having somewhat more wavenumbers. For the extreme case of the few-directions/many-wavenumbers $\chi(\mathbf{k})$ data set of Table 4.2(d), the Ni backscattering images obtained by Methods A-D (Figs. 4.8-4.11(d)) are in fact no longer discernible to any degree. There are too few directions to establish atomic images here, as only the spurious intersections associated with the $e^{i(\mathbf{k}\cdot\mathbf{r}'-kr')}$ kernel are seen here along the [001] axis of symmetry at $(y,z) \approx (0\text{Å}, \pm 1.5\text{Å})$, $(0\text{Å}, -4\text{Å})$, as discussed above for images reconstructed from coarse-in-direction $\chi(\mathbf{k})$ data sets. *Thus, increasing the number of different wavenumber measurements at the expense of different directions in a* $\chi(\mathbf{k})$ *data set is beneficial to only a moderate degree from using data with equally resolved direction and wavenumber resolution as called for from Nyquist considerations.* In disagreement with this conclusion, there has in fact been a recent proposal to consider the extreme fine-in-wavenumber/coarse-in-direction and course-in-wavenumber/fine-in-direction **k**-space sampling choices as two distinct atomic structure probes [4.5b]. However, these choices simply represent extremes of a continuous range of **k**-space

sampling, of which the optimal choice we have shown to be in the intermediate range of roughly equally resolved direction and wavenumber data steps [Ref. 4.25 and this chapter]. Thus, this distinction of methods [4.5b] seems artificial, and not consistent with the optimal use of the holographic methodology.

An overall comparison of Methods A-D can now be made at this point, based upon the optimal **k**-space resolved images of Figs. 4.8-4.11(a),(b). Note that the backscattering Ni images produced by Method A (Fig. 4.8(b)) are split. Image aberrations of this type are generally the result of using the Helmholtz-Kirchoff equation in Eq. (4.1), which is only completely valid for optical-like wave propagation and scattering [4.2,4.3]. Aside from incorporating explicit correction factors into Eq. (4.1) to account for the obvious non-optical nature of source and scattered electron wavefronts [4.6-4.9], Methods B-D constitute modified approaches to Eq. (4.1) that implicitly try to take account of the actual behavior of these wavefronts.

Method B produces singular atomic peaks (Figs. 4.9(a)(b)) where Method A reconstructs split images in the second case (Fig. 4.9(b)). This is easily understood as Eq. (4.2) uses only $\chi(\mathbf{k})$ regions where the atomic scattering factors for electrons are approximately stationary [4.11]. Use of Method B has also been shown to improve atomic images where the source wave has a large initial ℓ state, such that the window function $w(\alpha,\Theta^{\hat{\mathbf{r}}}_{-\hat{\mathbf{r}}_j})$ would only see a small portion of this source wave anisotropy [4.10]. However, note that the atomic images of Method B are less resolved than the images of Methods A, C-D. This is the result of the smaller angular range of $\chi(\mathbf{k})$ used in the cone windows of Eq. (4.2), where $\alpha = 30°$ means that only 0.27π is transformed for any given image point, compared to the nearly 2π angular range imaged by Eqs. (4.1), (4.3), and (4.4) in Methods A, C, and D, respectively [4.25,4.26]. Thus the main advantage of using Method B would seem to be in cases where correcting for the degree of source and/or scattered wave anisotropies is worth the loss of image resolution and sensitivity to in-plane side scattering atoms involved in applying Eq. (4.2).

As noted above, the splitting of the Method A images in Fig. 4.8(b) can in part be caused by the non-optical propagation nature of the source and scattered electron wavefronts, which is accounted for at least in the first Born Approximation by Method C [4.14]. In fact, the images reconstructed by Method C (Fig. 4.10(b)) are *slightly* more localized than those of Method A, aside from the fringe-like modulations that are due to the fact that only the real part of the complex transform of Eq. (4.3) is used in deriving image intensities, and thus the image reflects a loss of coherent (complex) information [4.26]. It could be advantageous to implement Method C for imaging systems with buried emitters and forward-scattering neighbors, as there would then be a significant degree of propagation of the source and scattered wavefronts through the bulk. This propagation should be better described quantum mechanically by Eq. (4.3) than for overlayer systems, where these wavefronts propagate mainly through the vacuum, and as such can be described more adequately by Eq. (4.1) in this region.

Method D also produces images with arc-like fringes (Fig. 4.11(b)), with the high frequency of these being due to only the real portion of Eq. (4.5) being used, and phase information thus being lost (similar to Method C). This algorithm describes the full anisotropy of atomic electron scattering, insofar as it is included in the scattering factor $f(\Theta_{\hat{\mathbf{r}}'}^{\hat{\mathbf{r}}})$ used in Eq. (4.5). Because the same scattering factor was used here in both the generation of $\chi(\mathbf{k})$ and the reconstruction of atomic images with Method D, the intensity peaks in Fig. 4.11(b) should ideally correspond identically to actual atomic positions. However, the background artifacts in Method D prevent totally ruling out the possible presence of atoms in certain positions along low-index directions, as indicated by the faint spurious features along y = 0 in the images produced by Eqs. (4.4)-(4.5). Artifacts of this sort do not appear in images in previous published work using this technique [4.16], but this is perhaps due to black-on-white intensity scales that cut off lower intensities at an arbitrary level. Due to the single scattering model used in Eqs. (4.4)-(4.5) to generate $\chi_{theoretical}(\mathbf{k},\mathbf{r}')$, Method D should perform best for systems where single scattering events

dominate, as for example, for overlayers (such as the case illustrated here, and in previous adsorbate studies [4.15,4.16]).

Therefore in cases where Method A does not reconstruct adequate atomic images due to significant non-optical behavior of the source and scattered wavefronts, Methods B-D can produce images of at least comparable, or for backscattering atoms perhaps even improved fidelity, at differing costs of resolution or image coherence and background level. The $\chi(\mathbf{k})$ data resolution that results in adequately resolved atomic images for Methods A-D only needs to be slightly finer than that called for by the Nyquist criteria ($|\delta\hat{\mathbf{k}}|, \delta k = \pi / R$) in order to resolve atoms at a given distance R from the emitter. This ensures that a minimal amount of $\chi(\mathbf{k})$ measurements need to be taken (and thus minimizes the data acquisition time), while still assuring adequately resolved atomic images within this region of interest around the emitter. With this minimal number of $\chi(\mathbf{k})$ data points in a given volume of **k**-space, it is to a certain degree advantageous for imaging backscatterers (but not side scattering in-plane neighbors) to take data with resolution slightly coarser than the Nyquist criterion with respect to direction, and thus finer with respect to wavenumber, with one benefit being that the slightly finer wavenumber resolution permits better subtracting out a $I_0(k\hat{\mathbf{k}})$ background. However, atomic images can be degraded to the point of being totally unresolved if the number of different wavenumbers N_k is increased too much at the expense of decreasing the number of different directions N_D. In general, optimal image quality is found for about 5-10 wavenumbers and an angular spacing of about 5°-10°.

4.5 Concluding remarks

We have demonstrated the effects of varying **k**-space resolution on images obtained by four recently proposed imaging algorithms by applying them to calculated photoelectron diffraction data. We have shown generally how one can use the Nyquist criterion to minimize the size of a $\chi(\mathbf{k})$ data set while simultaneously insuring adequately

resolved atomic images within a given radius of the emitter. Given this total number of required intensity measurements, we have also considered how to best resolve this $\chi(\mathbf{k})$ data set with respect to the number of directions versus the number of wavenumbers, with a slight preference for higher wavenumber resolution which can leads to cleaner backscattering images. We have shown that holographic imaging of atoms should not require large data sets with very fine **k**-space resolution in both wavenumber and direction [4.16], but rather that of the order of 6,400 total intensities (which can be symmetry reduced to only about 800-1000 intensities for many surfaces) is sufficient to fully resolve the first sphere of neighbors around a given emitter. We have also compared the image quality as produced by these four imaging algorithms, as judged from inversions of $\chi(\mathbf{k})$ data sets that have been optimized for each method. Overall, the full transform Method A of Eq. (4.1) seems to be the most robust in yielding atomic images in both back-scattering and side-scattering directions. The small-cone Method B of Eq. (4.2) improves somewhat the positions of backscattering atoms and should be useful for some systems, but it does this at the cost of reduced overall resolution and the loss of side-scattering information. The quantum-mechanically motivated Method C yields images of very similar type to those from Method A, but because it makes use of only one of the complex components in its arguments, has the negative aspect of higher-frequency noise artifacts in the image background. It would nonetheless be interesting to apply Method C to experimental data for the first time, as has just been done by our group [4.28]. The non-holographic Method D appears to be the least robust in producing atomic images, as judged by the presence of arc-like background features in most images and a higher background level in general compared to the other three methods.

References

[4.1] A. Szöke, in: Short Wavelength Coherent Radiation: Generation and Applications, eds. D. T. Atwood and J. Boker, AIP Conf. Proc. No. 147 (AIP, New York, 1986), 361.

[4.2] (a) J. J. Barton, Phys. Rev. Lett. **61** (1988) 1356. (b) J. J. Barton, Phys. Rev. Lett. **67** (1991) 3106.

[4.3] S. Y. Tong, H. Huang, and C. M. Wei, Phys. Rev. B **46** (1992) 2452.

[4.4] (a) R. Denecke, R. Eckstein, L. Ley, A. E. Bocquet, J. D. Riley, R. C. G. Leckey, Surf. Sci. **331-333** (1995) 1085. (b) B. L. Petersen, L. J. Terminello, J. J. Barton, and D. A. Shirley, Chem. Phys. Lett. **220** (1994) 46. (c) L. J. Terminello, J. J. Barton, and D. A. Lapiano-Smith, J. Vac. Sci. Technol. B **10** (1992) 2088, and Phys. Rev. Lett. **70** (1993) 599.

[4.5] (a) M. Zharnikov, M. Weinelt, P. Zebisch, M. Stichler, H.-P. Steinrück, Surf. Sci. **334** (1995) 114, and references therein. (b) J. G. Tobin, G. D. Waddill, H. Li, and S. Y. Tong, Surf. Sci. **334** (1995) 263, and references therein. (c) H. Wu, G. J. Lapeyre, H. Huang, and S. Y. Tong, Phys. Rev. Lett. **71** (1993) 251.

[4.6] B. P. Tonner, Z.-L. Han, G. R. Harp, and D. K. Saldin, Phys. Rev. B **43** (1991) 14423.

[4.7] G. R. Harp, D. K. Saldin, X. Chen, Z.-L. Han and B. P. Tonner, J. Electron Spectrosc. Relat. Phenom. **70** (1991) 331.

[4.8] (a) S. Thevuthasan, R. X. Ynzunza, E. D. Tober, C. S. Fadley, A. P. Kaduwela, and M. A. Van Hove, Phys. Rev. Lett. **70** (1993) 595. (b) T. T. Tran, S. Thevuthasan, Y. J. Kim, D. J. Friedman, and C. S. Fadley, Phys. Rev. B **45** (1992) 12106, and Surf. Sci. **281** (1993) 270. (c) S. Thevuthasan, G. S. Herman, A. P. Kaduwela, T. T. Tran, Y. J. Kim, R. S. Saiki, C. S. Fadley, and M. A. Van Hove, J. Vac. Sci. Tech. A **10** (1992) 2261. (d) G. S. Herman, S. Thevuthasan, T. T. Tran, Y. J. Kim, and C. S. Fadley, Phys. Rev. Lett. **68** (1992) 650.

[4.9] P. Hu and D. A. King, Phys. Rev. B **46** (1992) 13615.

[4.10] S. Y. Tong, H. Li, and H. Huang, Phys. Rev. B **51** (1995) 1850.

[4.11] H. Wu and G. J. Lapeyre, Phys. Rev. B **51** (1995) 14549.

[4.12] J. M. Roesler, M. T. Sieger, T. Miller, T.-C. Chiang, Surf. Sci. **329** (1995) L588.

[4.13] M. T. Sieger, J. M. Roesler, D.-S. Lin, T. Miller, and T.-C. Chiang, Phys. Rev. Lett. **73** (1994) 3117.

[4.14] P. J. Rous and M. H. Rubin, Surf. Sci. **316** (1994) L1068.

[4.15] P. Hofmann and K. M. Schindler, Phys. Rev. B **47** (1993) 13942.

[4.16] P. Hofmann, K.-M. Schindler, V. Fritzsche, S. Bao, A. M. Bradshaw, and D. P. Woodruff, J. Vac. Sci. Tech. A **12** (1994) 2045, and Surf. Sci. **337** (1995) 169.

[4.17] (a) H. Li, S. Y. Tong, D. Naumovic, A. Stuck, and J. Osterwalder, Phys. Rev. B **47** (1993) 10036. (b) D. K. Saldin, G. R. Harp, and X. Chen, Phys. Rev. B **48** (1993) 8234, and references therein.

[4.18] (a) Z.-L. Han, S. Hardcastle, G. R. Harp, H. Li, X.-D. Wang, J. Zhang, and B. P. Tonner, Surf. Sci. **258** (1991) 313, and references therein. (b) P. R. Jeng, I. H. Hong, Y. C. Chou, and C. M. Wei, Phys. Rev. B **51** (1995) 13645, and references therein.

[4.19] (a) M. A. Mendez, C. Glück, J. Guerrero, P. L. de Andres, K. Heinz, D. K. Saldin, and J. B. Pendry, Phys. Rev. B **45** (1992) 9402, and references therein. (b) C. M. Wei, S. Y. Tong, H. Wedler, M. A. Mendez, and K. Heinz, Phys. Rev. Lett. **72** (1994) 2434, and references therein.

[4.20] S. Y. Tong, H. Huang, and X. Q. Guo, Phys. Rev. Lett. **69** (1992) 3564.

[4.21] (a) M. Tegze and G. Faigel, Europhys. Lett. **16** (1991) 41. (b) P. M. Len, S. Thevuthasan, C. S. Fadley, A. P. Kaduwela, and M. A. Van Hove, Phys. Rev. B **50** (1994) 11275. (c) M. Tegze and G. Faigel, Nature **380** (1996) 49. (d) T. Gog, P. M. Len, G. Materlik, D. Bahr, C. Sanchez-Hanke, and C. S. Fadley, Phys. Rev. Lett. **76** (1996) 30.

[4.22] (a) C. S. Fadley, in: Synchrotron Radiation Research: Advances in Surfaces and Interface Science, ed. R.Z. Bachrach, (Plenum Press, New York, 1992). (b) D. J. Friedman, C. S. Fadley, J. Electron Spec. Relat. Phenom. **51** (1990) 689.

[4.23] A. P. Kaduwela, D. J. Friedman, and C. S. Fadley, J. Electron Spec. Relat. Phenom. **57** (1991) 223.

[4.24] (a) C. M. Wei, J. H. Hong, P. R. Jeng, S. C. Shyu, and Y. C. Chou, Chem. Phys. Lett. **228** (1994) 513. (b) L. J. Terminello, B. L. Petersen, and J. J. Barton, J. Electron Spec. Relat. Phenom. **75** (1995) 229.

[4.25] P. M. Len, S. Thevuthasan, A. P. Kaduwela, M. A. Van Hove, and C. S. Fadley, Surf. Sci. **365** (1996) 535, and references therein.

[4.26] P. M. Len, F. Zhang, S. Thevuthasan, A. P. Kaduwela, M. A. Van Hove, and C. S. Fadley, J. Electron Spec. Relat. Phenom. **76** (1995) 351.

[4.27] M. T. Sieger, private communication.

[4.28] P. M. Len, C. S. Fadley, and G. Materlik, to appear in *X-ray and Inner-Shell Processes: 17th International Conference*, R. L. Johnson, H. Schmidt-Boeckering, and B. F. Sonntag (eds.), AIP Conference Proceedings No. 389 (AIP, New York, 1997).

Figure captions

Figure 4.1. Schematic **k**-space representation of a $\chi(\mathbf{k})$ data set spanning the full 2π hemisphere above a surface, with photoelectron wavevector magnitudes in the range $8.11\text{Å}^{-1} \leq k \leq 11.25\text{Å}^{-1}$ ($250\text{eV} \leq E \leq 482\text{eV}$). Each mesh intersection represents a single $\chi(\mathbf{k})$ intensity measurement. The $\chi(\mathbf{k})$ data points in the first quadrant are cut away to show the $\chi(|\mathbf{k}| = 8.11\text{Å}^{-1})$ surface. (a) View along the $[00\bar{1}]$ direction. (b) View along the $[\bar{1}00]$ direction.

Figure 4.2. (a) yz = (100) planar cut of a small Cu/Ni cluster used in a first set of simulations. (b)-(c) Single scattering $\chi(\mathbf{k})$ calculated for Cu $2p \rightarrow s+d$ photoemission from the cluster of (a), with the same angular and wavenumber range as the schematic data set shown in Fig. 4.1.

Figure 4.3. (a) yz = (100) planar cut of an equivalent emitter site of a large, 203 atom Cu/Ni(001) cluster used in a second set of simulations. (b)-(c) Single scattering $\chi(\mathbf{k})$ calculated for Cu $2p \rightarrow s+d$ photoemission from the cluster of (a), with the same angular and wavenumber range as the schematic data set shown in Fig. 4.1.

Figures 4.4-4.7. Atomic images obtained from the small Cu/Ni cluster $\chi(\mathbf{k})$ of Figs. 4.2(b)-(c), and based upon the different **k**-space sampling resolutions of Table 4.1(a)-(d). Images here are in the yz = (100) plane (Fig. 4.2(a)). Actual atomic positions are indicated with white crosses, and the two axes are marked off in 1Å units. Figure 4.4. Atomic images $|U_A(\mathbf{r}')|$ reconstructed using Method A and Eq. (4.1). Figure 4.5. Atomic images $|U_B(\mathbf{r}')|$ reconstructed using Method B and Eq. (4.2), where the half-angle of the small cone is $\alpha = 30°$. Figure 4.6. Atomic images $|U_C(\mathbf{r}')|$ reconstructed using Method C and Eq. (4.3). Figure 4.7. Atomic images $U_D(\mathbf{r}')$ reconstructed using Method D and Eqs. (4.4) and (4.5).

Figures 4.8-4.11. As Figs. 4.4=4.7, but for atomic images obtained from the larger Cu/Ni(001) cluster $\chi(\mathbf{k})$ of Figs. 4.3(b)-(c), based upon the increasingly more coarse-in-direction/fine-in-wavenumber **k**-space sampling resolutions of Table 4.2(a)-(d). Figure 4.8. Atomic images $|U_A(\mathbf{r}')|$ reconstructed using Method A. Figure 4.9. Atomic images $|U_B(\mathbf{r}')|$ reconstructed using Method B, where the half-angle of the small cone is $\alpha = 30°$. Figure 4.10. Atomic images $|U_C(\mathbf{r}')|$ reconstructed using Method C. Figure 4.11. Atomic images $U_D(\mathbf{r}')$ reconstructed using Method D.

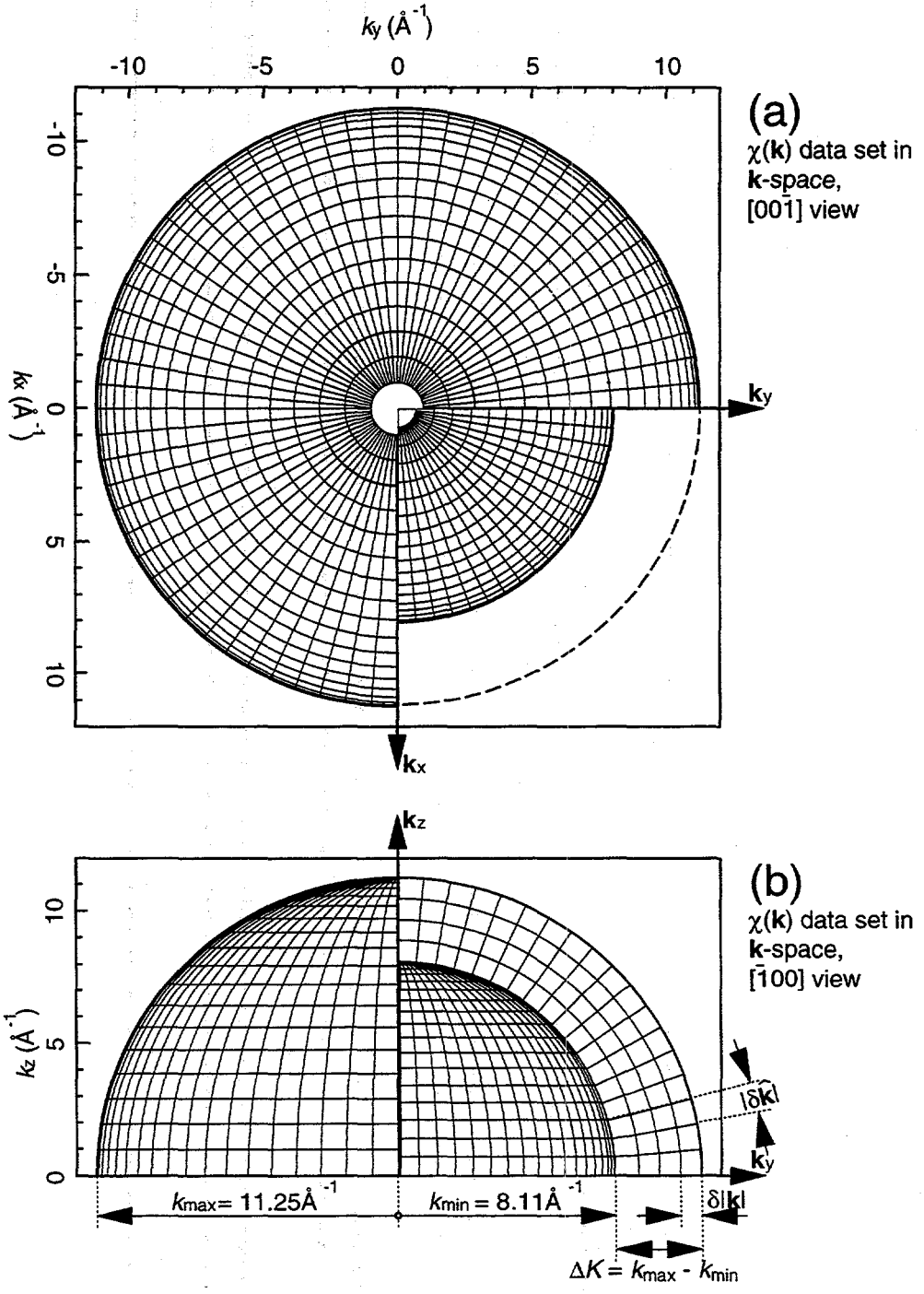

Fig. 4.1

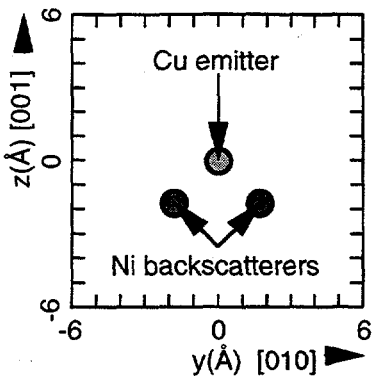

(a)
Cu/Ni cluster,
(100) plane

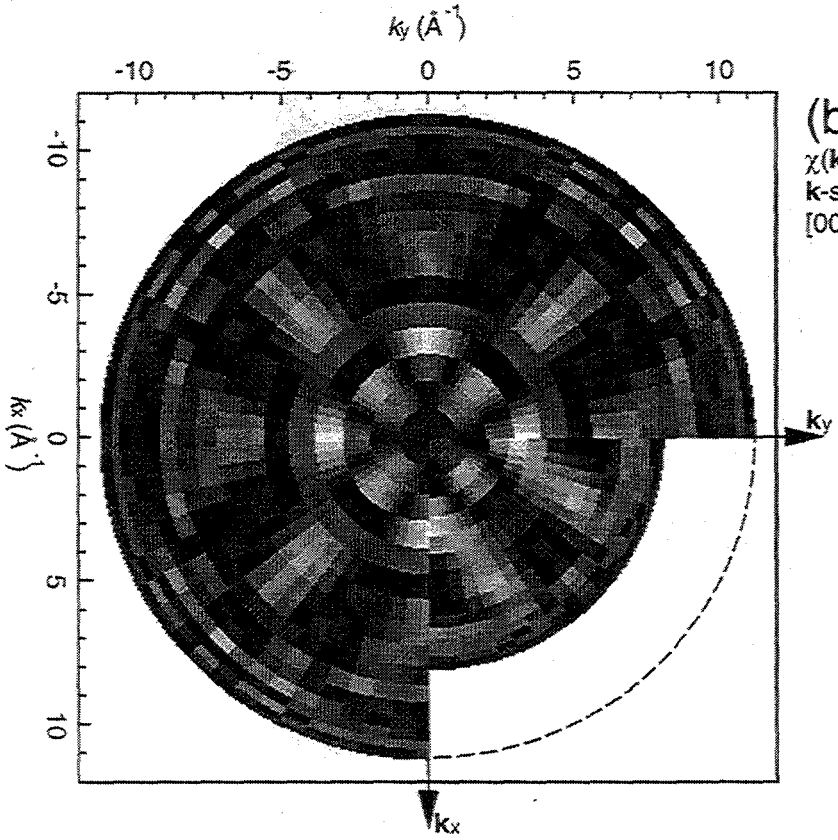

(b)
$\chi(\mathbf{k})$ data set in
k-space,
[00$\bar{1}$] view

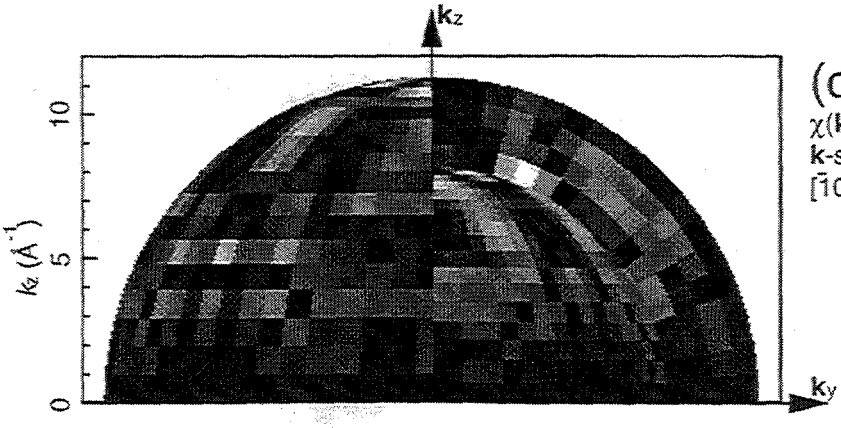

(c)
$\chi(\mathbf{k})$ data set in
k-space,
[$\bar{1}$00] view

Fig. 4.2

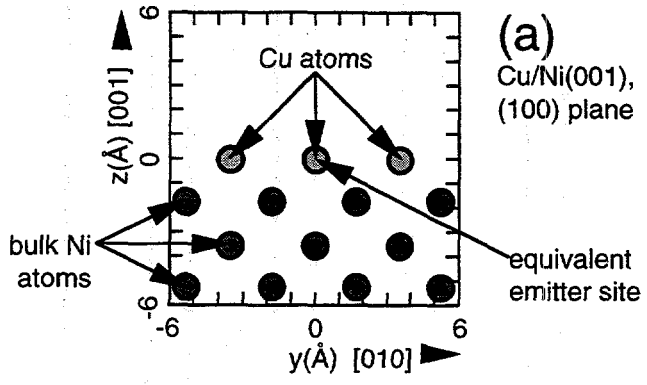

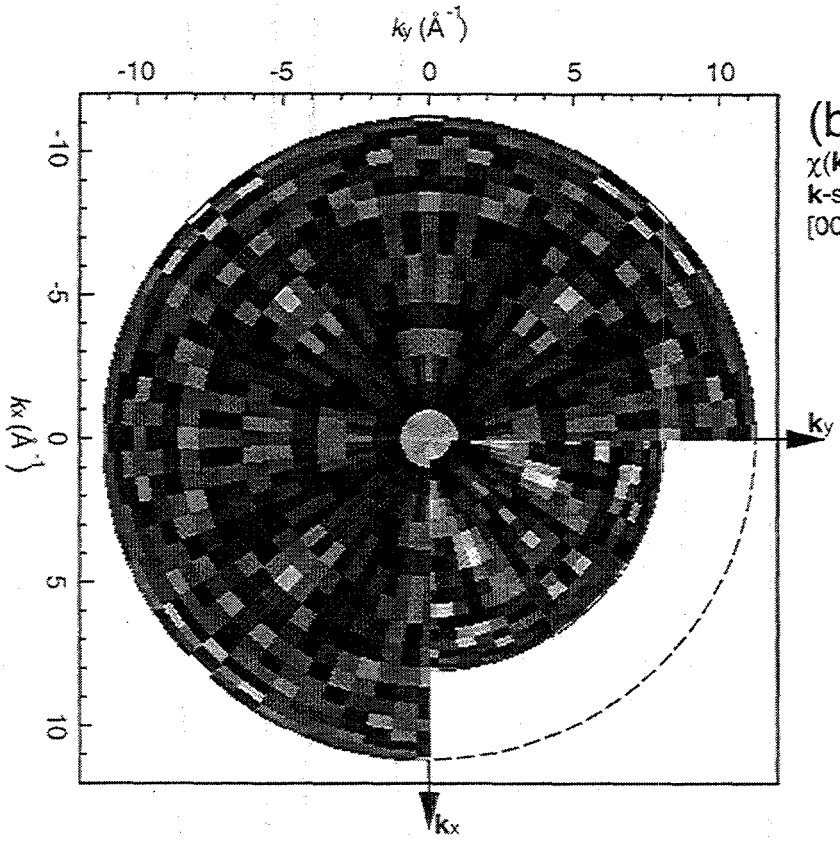

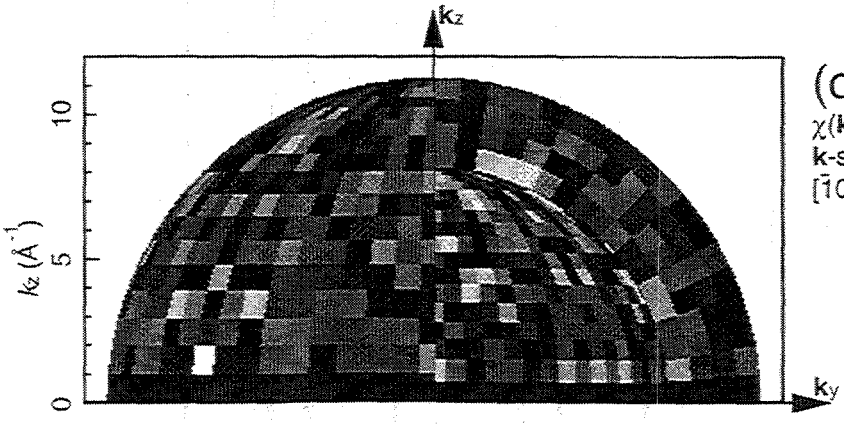

Fig. 4.3

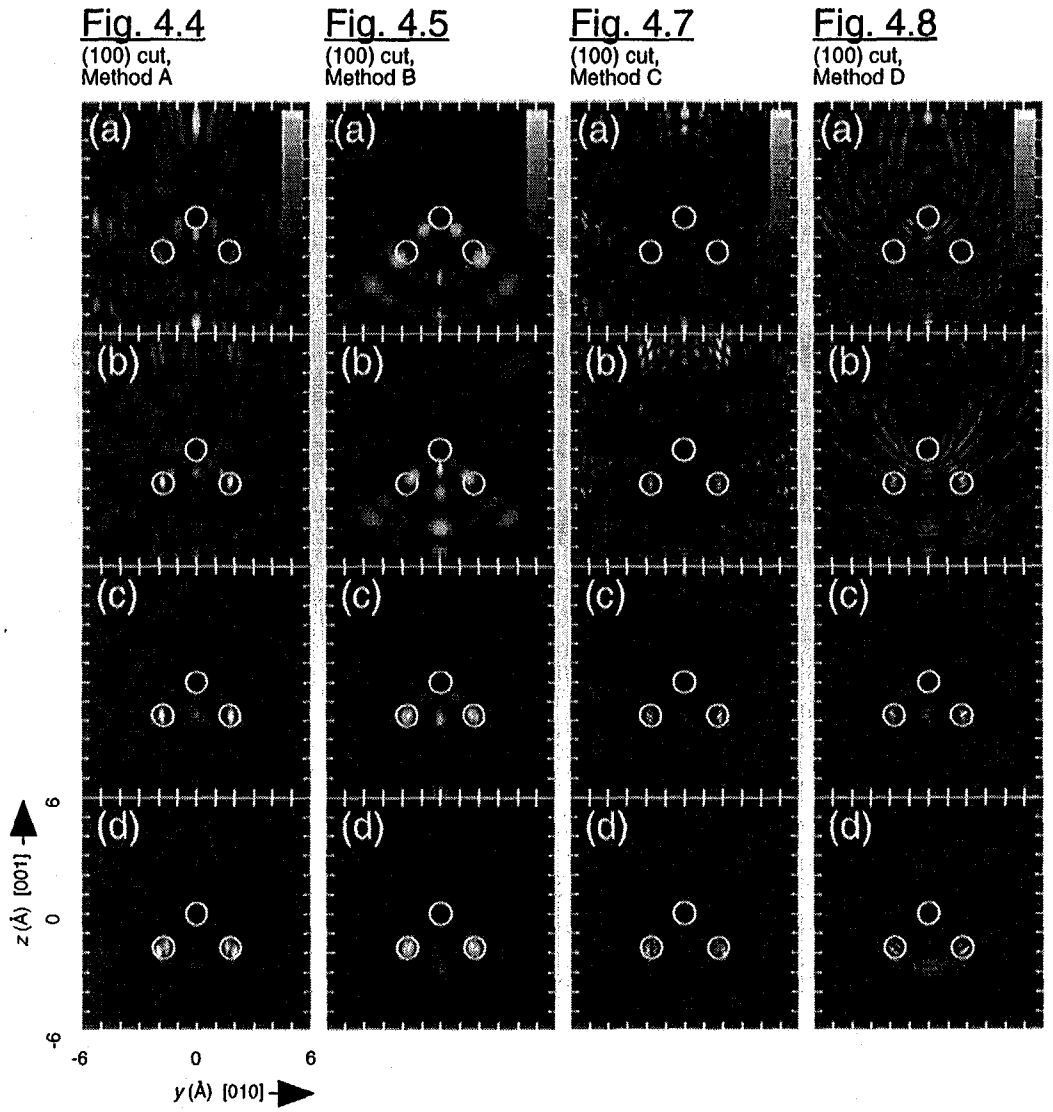

Figs. 4.4-4.7

Fig. 4.8
(100) cut,
Method A

Fig. 4.9
(100) cut,
Method B

Fig. 4.10
(100) cut,
Method C

Fig. 4.11
(100) cut,
Method D

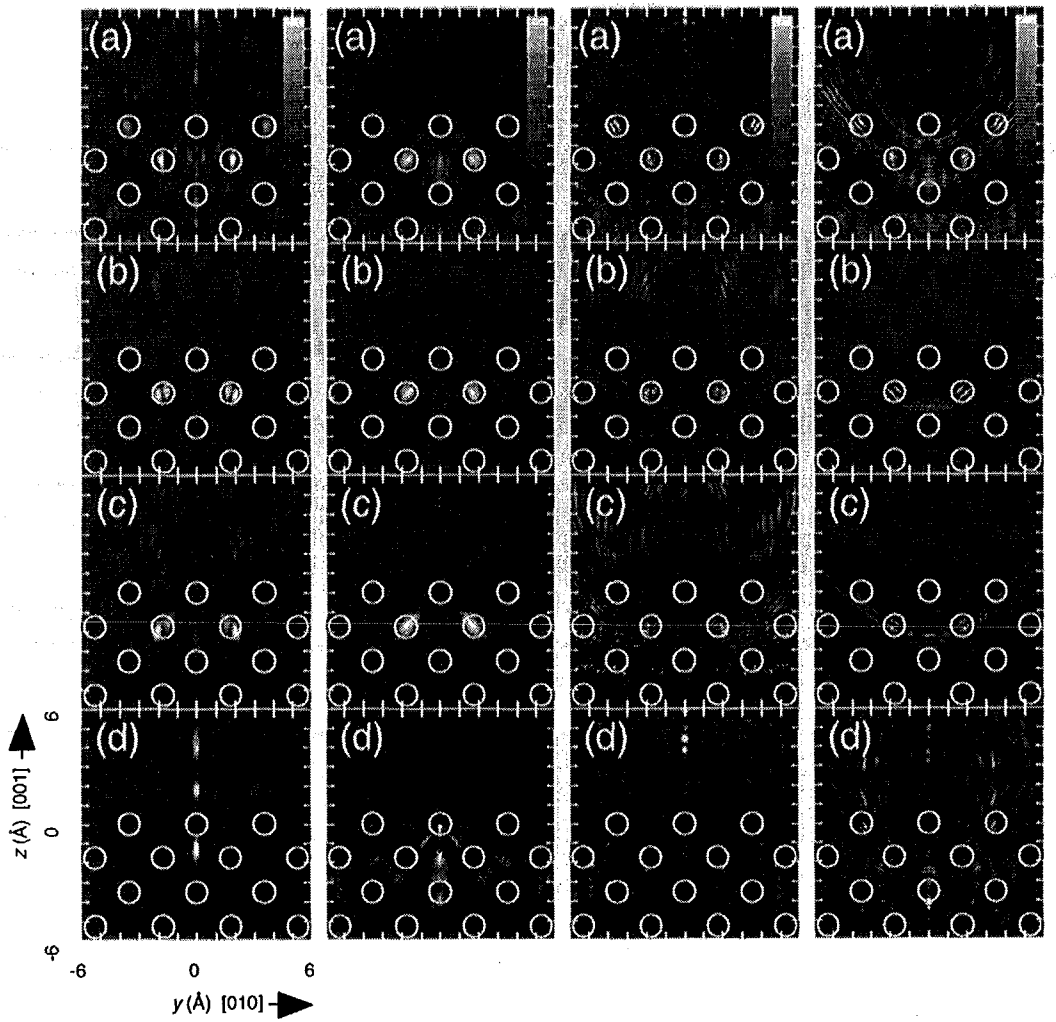

Cu/Ni(001)
(100) plane
$R \leq 4$Å
$N_E = 5$ wavenumbers
$N_D = 1{,}296$ directions
$(5° \times 5°)$
$N_{total} = 6{,}480$ data points

Cu/Ni(001)
(100) plane
$R \leq 4$Å
$N_E = 11$ wavenumbers
$N_D = 576$ directions
$(7.5° \times 7.5°)$
$N_{total} = 6{,}336$ data points

Cu/Ni(001)
(100) plane
$R \leq 4$Å
$N_E = 20$ wavenumbers
$N_D = 324$ directions
$(10° \times 10°)$
$N_{total} = 6{,}480$ data points

Cu/Ni(001)
(100) plane
$R \leq 4$Å
$N_E = 45$ wavenumbers
$N_D = 144$ directions
$(15° \times 15°)$
$N_{total} = 6{,}480$ data points

Figs. 4.8-4.11

Chapter 5

Holographic Atomic Images from Surface and Bulk W(110) Photoelectron Diffraction Data

Abstract

Photoelectron diffraction data can in principle be regarded as enabling the experimental recording of electron diffraction phases (relative to a direct reference wave), as well as intensities, thus also permitting the holographic reconstruction of atomic positions. Such holographic photoelectron diffraction patterns have been measured for surface and bulk core-level-shifted W 4*f* photoemission from W(110), yielding a data set of unprecedented size and quality. Corresponding theoretical calculations at both the single scattering and multiple scattering levels have also been performed. The surface and bulk holograms so obtained have been analyzed so as to provide the first parallel comparison of the three-dimensional atomic images that can be directly obtained via the five principal reconstruction algorithms proposed to date. The advantages and disadvantages of each of these methods are discussed. The prospects and limitations of atomic photoelectron holography as an *ab initio* technique for determining local surface structures are also explored.

5.0 Outline

5.1 Introduction

Gabor originally proposed holography with electron beams as an experimental scheme to directly record the phases and intensities of diffraction patterns relative to a reference wavefront [5.1]. Later, Szöke observed that far-field photoelectron and fluorescent x-ray diffraction patterns created by the interference between a direct unscattered wavefront and wavefronts scattered by atoms neighboring the photoemitter are also holographic in nature [5.2]. As both diffraction intensities and phases can thus be determined experimentally, three-dimensional images of the superpositions of the atomic neighborhoods of each photoemitting site can then be directly obtained using various reconstruction algorithms [5.3-5.8], as experimentally demonstrated by now in photoelectron diffraction [5.9], Auger electron diffraction [5.10], Kikuchi-electron backscattering [5.11], low-energy electron diffraction [5.12] and positron diffraction [5.13]. More recently, similar holographic imaging has been demonstrated experimentally in x-ray fluorescence as well [5.14,5.15]. Some of the notable successes of photoelectron holography to date involve the determination of the structures of adsorbate overlayers [5.6b,5.9c,5.11a,5.12a], and reconstructed surfaces [5.6d,5.9e,5.11b]. A significant advantage of photoelectron holography is in being able, via core-level binding energy shifts, to study the local structure around each type of emitter separately, and we take special advantage of that here.

However, due to the non-ideal nature of electron emission and scattering, atomic images obtained from all electron holograms suffer from aberrations, artifacts, and position shifts [5.16-5.18] relative to *e.g.* the more accurate atomic images obtained from x-ray holograms; this is due to the more ideal nature of the x-ray emission and scattering processes [5.19]. In this work, we will compare the most often used reconstruction algorithms for photoelectron holography that attempt to increase atomic image fidelity by in some way suppressing and/or directly accounting for the non-ideal nature of electron

scattering processes. Preliminary theoretical comparisons have been made earlier between these different reconstruction algorithms [5.20]; this work represents the first such comprehensive comparison of these imaging methods as applied to a very large and high-quality *experimental* data set involving photoelectrons from both surface and bulk atoms, as distinguished via their core level shifts on the W(110) surface.

The W(110) surface represents an excellent test system for photoelectron holography (PH), as it has been studied previously by various surface structure probes, including low energy electron diffraction (LEED) [5.21a] and both scanned-wavenumber [5.21b] and scanned-angle [5.21c] photoelectron diffraction (PD). The surface is known to be unreconstructed, and to have a surface-layer-to-second-layer distance that is very little relaxed from the bulk distance, with a very recent LEED study yielding only a 0.069Å inward relaxation of the surface layer relative to the bulk distance [5.21a], a similar analysis of scanned-wavenumber PD data yielding a 0.03Å outward relaxation [5.21b], and a more recent analysis of full-hemisphere scanned-angle PD data yielding a 0.12Å outward relaxation [5.21c.]. To a sufficient accuracy for modeling the photoelectron holograms for this surface, we can thus assume no interlayer relaxation. A further advantage of this surface for PD studies is that it exhibits a very large surface core-level shift relative to the bulk of 320meV. Thus, the emission from both the outermost surface layer (an "adsorbate" layer in which back scattering and side scattering are dominant) and the underlying bulk layers (a 3D lattice in which forward scattering is dominant) can be distinguished in a high-resolution spectrum, and the resulting holograms used to generate separate images of their near-neighbor atoms.

5.1 Experimental details

Photoelectron diffraction data from clean W(110) were collected at Beamline 7.0 of the Advanced Light Source at the Lawrence Berkeley National Laboratory. The experimental geometry is shown in Fig. 5.1(a); the incidence direction, the outgoing

photoelectron **k** vector, and the surface normal are co-planar in the plane of the figure. The W 4*f* photoelectron peak can be resolved into surface and bulk core-level-shifted components, as shown in Fig. 5.1(b). For each energy and direction studied, the W 4*f* peak was resolved into surface and bulk emission components by integrating the areas under the higher and lower flanks of the photoemission surface and bulk W 4*f* peaks, respectively, as shown by the shaded areas in Fig. 5.1(b). Such photoelectron spectra were measured for kinetic energies of $E = 41$eV to 197eV (wavenumbers $k = 3.3\text{Å}^{-1}$ to 7.2Å^{-1}), and collected over a polar angle range of $14° \leq \theta \leq 90° \equiv$ normal emission. These data points were measured at wavenumber intervals corresponding to $\delta k = 0.1\text{Å}^{-1}$, and angular intervals of $(\delta\theta, \delta\phi) = (3°, 3°\cos\theta)$ corresponding to roughly equal solid angle elements, making a total of 12,280 unique measurements in a symmetry-reduced 1/4th of the total solid-angle above the sample.

Figures 5.2(a) and 5.3(a) show the surface and bulk $I(\mathbf{k})$ data sets in **k**-space, respectively, as viewed down along $[\bar{1}\,\bar{1}\,0]$. Each pixel represents a single data point, with no smoothing being done. Data points in the lower right quadrant have been cut away to reveal the intensities $I(\mathbf{k})$ for the minimum $k = 3.3\text{Å}^{-1}$; the other quadrants show the intensities $I(\mathbf{k})$ for the maximum $k = 7.2\text{Å}^{-1}$. The dark bands at the perimeter indicate the locations in **k**-space on these equal-wavenumber surfaces where data was not collected. Also, data was omitted for the lower polar angles that would lie below the lowest common polar angle of $\theta = 90°$ *after* a subsequent inner potential correction. Due to the strong atomic scattering of electrons (as compared *e.g.* to fluorescent x-rays), the anisotropy of the raw $I(\mathbf{k})$ data (defined as $\Delta I / I_0 = (I_{max} - I_{min}) / I_0 \approx 30\%$) is easily discernible with this gray scale. This can be compared to raw x-ray $I(\mathbf{k})$ data, which has anisotropies about two orders of magnitude less [5.22].

Before atomic images can be reconstructed from these $I(\mathbf{k})$ data sets, the normalized holographic intensities $\chi(\mathbf{k})$ must be obtained via $\chi(\mathbf{k}) \equiv [I(\mathbf{k}) - I_0(\mathbf{k})] / \sqrt{I_0(\mathbf{k})}$, where $I_0(\mathbf{k})$ is the intensity that would be measured in the

absence of atomic scattering (*i.e.*, the intensity of the reference wave, including any modulations due to geometrical excitation or detection effects). Dividing by $I_0(\mathbf{k})$ in deriving $\chi(\mathbf{k})$ has also been done in some studies [5.6c,5.9d,5.11b], but in practice, we find there is little difference in the final holographic images between this choice and dividing by $\sqrt{I_0(\mathbf{k})}$. In practice, this $I_0(\mathbf{k})$ background must be deduced analytically from experimental $I(\mathbf{k})$ intensities, which is done here by fitting a low-order polynomial in wavenumber k and polar angle θ to the full $I(\mathbf{k})$ data set:

$$I_0(\mathbf{k}) = a_{00} + \sum_{m=1}^{3}\sum_{n=1}^{3} a_{mn} k^m \cos[(2n-1)\theta]. \qquad (5.1)$$

Here, the coefficients a_{mn} are determined by a least-squares fit to $I(\mathbf{k})$. This is qualitatively similar to some prior normalization schemes that subtract $I_0(\mathbf{k})$ as the low-frequency Fourier components of raw $I(\mathbf{k})$ data sets [5.9c,5.15a,5.15d,5.23]. But this three-dimensional determination of $I_0(\mathbf{k})$ is distinctly different from previous methods for determining $I_0(\mathbf{k})$ in which simple linear, low-order polynomial, or spline fits were separately made for each set of different wavenumbers along a given direction: $I_{\hat{\mathbf{k}}}(k)$ [5.9a.5.9c,5.9d], or each set of different directions at a given wavenumber: $I_k(\hat{\mathbf{k}})$ [5.9b,5.9e,]. Such separate normalizations within each scanned-wavenumber or scanned-angle set of data points in $I(\mathbf{k})$ arose from the historical development of photoelectron holography, in which data tended to be collected with **k**-space resolution that was either fine-in-direction/coarse-in-wavenumber or coarse-in-direction/fine-in-wavenumber [5.24]. There has in fact been a recent proposal to consider these **k**-space sampling choices as distinct atomic structure probes [5.9e], but these choices simply represent extremes of a continuous range of **k**-space sampling, of which the optimal choice has been shown to be in the intermediate range of roughly equally resolved direction and wavenumber data steps [5.20,5.24]. Thus, this distinction [5.9e] seems artificial, and not consistent with the optimal use of the holographic methodology. As a consequence, the normalization of $I(\mathbf{k})$

intensities should ideally be made via the determination of a general $I_0(\mathbf{k})$ background that depends on wavenumber and direction dependent (such as that in Eq. 5.1), rather than determined separately for each wavenumber or direction in the $I(\mathbf{k})$ data set.

Figures 5.2(b) and 5.3(b) show the surface and bulk $I_0(\mathbf{k})$ functions as determined by applying the wavenumber and polar angle fit of Eq. (5.1) to the raw surface and bulk photoelectron diffraction $I(\mathbf{k})$ data sets of Figs. 5.2(a) and 5.3(a), respectively. Figures 5.2(c) and 5.3(c) then show the $\chi(\mathbf{k})$ functions obtained from the raw $I(\mathbf{k})$ intensities of Figs. 5.2(a) and 5.3(a), using the wavenumber and angle fit $I_0(\mathbf{k})$ of Figs. 5.2(b) and 5.3(b), and after correcting for an inner potential of $V_0 = 14$ V [5.25] to yield electron directions *and* wavenumbers beneath the surface of the sample. These data points were then remapped onto a more regular grid of $\delta k = 0.1\text{Å}^{-1}$ and $(\delta\theta, \delta\phi) = (5°, 5°)$ over the ranges $k = 3.85\text{Å}^{-1}$ to 7.45Å^{-1} ($E = 56$eV to 211eV) and $40° \leq \theta \leq 90°$, for a final total of 6,697 unique intensities in the symmetry-reduced 1/4th of the solid angle above the sample. These $\chi(\mathbf{k})$ data steps, while coarser than the data steps of the raw $I(\mathbf{k})$ data sets, are still sufficiently fine enough to ensure images free of coarse-sampling aliases and aberrations to within ≈ 6Å from the emitting sites [5.24].

5.2 Generation of theoretical diffraction patterns

For comparison with experiment, single-scattering and multiple-scattering theoretical models were used to calculate surface and bulk emission $I(\mathbf{k})$'s from W(110) clusters. The Rehr-Albers separable Green's function approach was used to describe the scattering [5.26]. This was first implemented in photoelectron diffraction calculations by Kaduwela *et al.* [5.27], and a faster algorithm employing it (SCAT) has recently been developed by Chen *et al.* [5.28]. The calculations reported here made use of this newer program. The radial matrix elements and phase shifts necessary for describing the primary excitation, as well as the scattering phase shifts were calculated using SCAT. Figure 5.4 shows several of the key physical ingredients of such theoretical calculations, as evaluated

at the two extreme energies studied here of $k_{min} = 3.85\text{Å}^{-1}$ ($E = 56$ eV) and $k_{max} = 7.45\text{Å}^{-1}$ ($E = 211$ eV): (a) the W $4f$ differential photoelectric cross sections $\frac{d\sigma}{d\Omega}$, and W-atom scattering factor (b) magnitudes $|f(\Theta_r^k)|$ and (c) phases $\psi(\Theta_r^k)$. As a first point, the cross section is reasonably isotropic over this energy range, suggesting that photoelectron *source-wave* anisotropies should not affect holographic images too seriously. However, a correct allowance for such source wave effects would also deal with the amplitudes and phases of the *d* and *g* final-state channels involved [5.29], leading to more complex effects on holographic images that we will not consider here. As far as *scattered-wave* effects are concerned, it is clear that both the W scattering factor magnitudes and phases of Fig. 5.4(b)-(c) are strongly anisotropic compared to the more ideal scattering nature of x-rays [5.19,5.22], and that these anistropies could adversely affect the resulting reconstructed atomic images, introducing aberrations and position shifts [5.16-5.18]. We will consider correcting for such scattered-wave effects below.

The clusters used for simulating surface and bulk emission considered here consisted of 72 atoms and 64 atoms, respectively, and were chosen in order to include all events down to a 2% cutoff of all multiply scattered wavefront contributions to the detected intensity in the far-field. Debye-Waller vibration effects corresponding to a sample temperature of 300K were included, as well as inelastic attenuation effects, with the inelastic attenuation lengths ranging from 1.71Å at $k_{min} = 3.85\text{Å}^{-1}$ to 4.42Å at $k_{max} = 7.45\text{Å}^{-1}$. The detector full angle of acceptance was taken to be 3°, and the geometry between the incident radiation polarization, sample, and detector was identical to the experimental setup of Fig. 5.1(a). These theoretical photoemission intensities were then also normalized using the wavenumber and direction dependent normalization scheme of Eq. (5.1).

5.3. Atomic images from experimental and theoretical χ(k) data sets

Once the normalized holographic $\chi(\mathbf{k})$ intensities have been obtained from either experiment or theory, atomic images $U(\mathbf{r}')$ can then be reconstructed via several methods that we now review below. The simplest of these is denoted here as Method A [5.3]:

$$U_A(\mathbf{r}') \equiv \iiint_K d^3\mathbf{k} \cdot e^{-i(\mathbf{k}\cdot\mathbf{r}'-kr')}\chi(\mathbf{k}), \tag{5.2}$$

and it is a deconvolution transform with a path-length-difference kernel $e^{i(\mathbf{k}\cdot\mathbf{r}'-kr')}$. This kernel assumes an outgoing source wave of s character, weak s-wave electron-atom scattering, and a negligible, or at least small, scattering phase shift, and can be thought of as an "optical" limit. In this limit, this transform should reconstruct the atomic scattering field at relative positions $\mathbf{r}'$ surrounding the emitter [5.3,5.22]. An additional important property of this method is that, in being a transform over a volume in $\mathbf{k}$ space (*i.e.*, over both direction and wavenumber), it suppresses both twin-image and multiple scattering effects, as first pointed out by Barton [5.3a,5.3b], and subsequently by Tong *et al.* [5.3c]. However, due to the non-ideal nature of electron emission and scattering, atomic images obtained via Method A have still been found to suffer from aberrations, artifacts, and position shifts [5.16-5.18]. Nonetheless, such images can be of good enough quality to allow an initial and useful determination of atomic structure [5.9-5.13].

Figure 5.5 shows the reconstructed images in the vertical $(\bar{1}\,1\bar{2})$ plane obtained from applying Method A (Eq. (5.2)) to: (a) the experimental surface emission $\chi(\mathbf{k})$ of Fig. 5.2(c); (b) a theoretical single-scattering surface emission $\chi(\mathbf{k})$; and (c) a theoretical multiple-scattering surface emission $\chi(\mathbf{k})$. The $(\bar{1}\,1\bar{2})$ plane was chosen to pass through the nearest-neighbor atoms to a given emitter that lie in the surface plane, as these would presumably also be the strongest atoms in the holographic images. The emitter position is indicated by a dashed square, and the ideal positions of the neighboring atoms are indicated by circles. The expected atomic image resolution for this wavenumber and

angular range of $\chi(\mathbf{k})$ in the horizontal $[\bar{1}11]$ direction is given by $\delta x \approx \pi / \Delta k_x \equiv \pi / (2k_{max} sin(\theta_{max} - \theta_{min})) \approx 0.3$Å, and in the vertical [110] direction is given by $\delta z \approx \pi / \Delta k_z \equiv \pi / (k_{max} - k_{min} \cos(\theta_{max} - \theta_{min})) \approx 0.6$Å [5.23], and these numbers are comparable to the actual atomic image dimensions in Fig. 5.5. As noted above, Eq. (5.2) makes no special effort to suppress aberrations due to the non-optical nature of the electron scattering process. In all of the images in Fig. 5.5, the backscattering atom along $\bar{1}\,\bar{1}\,0$ and the $\frac{1}{2}\frac{\bar{1}}{2}\frac{\bar{1}}{2}$ and $\frac{\bar{1}}{2}\frac{1}{2}\frac{1}{2}$ side scattering atoms are reasonably well-resolved, with experiment and the more accurate multiple-scattering theory showing the sharpest features for the backscattering atoms, and agreeing very well with one another. In the experimental image of Fig. 5.5(a), the $\frac{1}{2}\frac{\bar{1}}{2}\frac{\bar{1}}{2}$ and $\frac{\bar{1}}{2}\frac{1}{2}\frac{1}{2}$ atoms are shifted in toward the emitter (by ≈ 0.7Å), and downward from the $z = 0$Å surface (by ≈ 0.2Å); this is perhaps due to the strong anisotropies of the atomic scattering factor and its phase shift for such side-scattering directions (*cf.* Fig. 5.4(b),(c)). As expected, the backscattering $\bar{1}\,\bar{1}\,0$ atom is better resolved due to the more ideal nature of electron backscattering (approximately constant amplitude and phase shift, as shown also in Figs. 5.5(b)-(c)), with no significant position shift [5.22]. The experimental backscattering image is also less intense (≈50%) than the side scattering atomic images; and image intensities above and below $z = -3.5$Å have been scaled accordingly (with scale factors indicated directly on each panel). This difference in relative image intensity is qualitatively expected due to the longer inelastic attenuation path of the wavefront that illuminates, and is subsequently scattered by, the backscattering atom, as compared to the wavefront paths that involve the side scattering atoms. Despite these position shifts and aberrations, this experimental atomic image overall gives good *ab initio* estimates of the positions of the atoms surrounding the surface W(110) emitter, which could in principle then be refined *e.g.*, using *R*-factor comparisons of experiment with model diffraction calculations for various structures [5.9c,5.21,5.30].

The single and multiple scattering images of Figs. 5.5(b)-(c) are similar to experiment in that the $\frac{1}{2}\frac{\bar{1}}{2}\frac{\bar{1}}{2}$ and $\frac{\bar{1}}{2}\frac{1}{2}\frac{1}{2}$ side scatterers exhibit side lobes which are shifted in

towards the emitter, and downward from the surface. However, the theoretical side-scattering atomic images of Figs. 5.5(b)-(c) differ from those of Fig. 5.5(a) in that the theoretical image peaks are split. This splitting may be due to a number of reasons, among them the differences between the theoretical and actual photoemitted source-wave angular distributions and atomic scattering factors. Yet, these single- and multiple-scattering models produce other image features that rather closely match the experimental image of Fig. 5.5(a) in the side scattering region, even including the faint aberrations seen at (x,z) $\approx (\pm 4\text{Å}, 0\text{Å})$. The most marked difference between the experimental image of Fig. 5.5(a) and the single-scattering image of Fig. 5.5(b) is the triply-split backscattering $\bar{1}\,\bar{1}\,0$ atom in the latter, which is also very much weaker in intensity ($\approx 1\%$) relative to the side scattering $\frac{1}{2}\frac{\bar{1}}{2}\frac{\bar{1}}{2}$ and $\frac{\bar{1}}{2}\frac{1}{2}\frac{1}{2}$ peaks. This must be primarily due to the oversimplification of the single-scattering model, as seen by comparing Figs. 5.5(b) and (c), for which the agreement is excellent. For example, in the multiple-scattering image of Fig. 5.5(c), the backscattering $\bar{1}\,\bar{1}\,0$ peak intensity relative to the side scattering $\frac{1}{2}\frac{\bar{1}}{2}\frac{\bar{1}}{2}$ and $\frac{\bar{1}}{2}\frac{1}{2}\frac{1}{2}$ peaks ($\approx 33\%$) is very close to that of Fig. 5.5(a) ($\approx 50\%$). This dramatic difference between single and multiple scattering can arise because each of the atoms in the multiple-scattering model becomes an emitter which can then illuminate the atoms surrounding it, especially the atom located at the $\bar{1}\,\bar{1}\,0$ relative position. In this way more scattering events contribute to the backscattering signal in the resulting holographic $\chi(\mathbf{k})$ intensities, and as such the reconstructed $\bar{1}\,\bar{1}\,0$ atomic intensity can be much stronger for the image reconstructed from the multiple-scattering model than that from the single-scattering model. Thus, the closer match between Fig. 5.5(c) and the experimental image of Fig. 5.5(a) graphically illustrates that multiple-scattering more accurately describes the nature of the creation of the experimental holographic photoelectron intensities $I(\mathbf{k})$. This is all the more noteworthy in view of the fact that such a multiple wavenumber volume transform is known to suppress multiple scattering effects [5.3b]; obviously there is not a complete suppression, even with this large data set.

Atomic images were also reconstructed from the experimental bulk emission $\chi(\mathbf{k})$ of Fig. 5.3(c), as well as from theoretical single-scattering and multiple-scattering bulk emission $\chi(\mathbf{k})$'s. Figures 5.6-5.8 show these experimental and theoretical images reconstructed via Method A (Eq. (5.2)) in the vertical $(\bar{1}\,1\,\bar{2})$, $(\bar{1}\,1\,0)$, and (001) planes, respectively. Immediately apparent in all of the experimental and theoretical images of Figs. 5.6-5.8(a) is the lack of a clear backscattering $\bar{1}\,\bar{1}\,0$ atomic image. The faint features spaced at ≈ 0.9Å intervals along the $[\bar{1}\,\bar{1}\,0]$ direction are in fact alias peaks that arise from the Fourier transform-like properties of Eq. (5.2) [5.24]. Because of the finite amount of volume enclosed by the $\chi(\mathbf{k})$ data set in **k**-space, these spurious peaks are expected at $\pi/(k_{max}-k_{min}) = \pi/(7.45\text{Å}^{-1}-3.85\text{Å}^{-1}) = 0.871$Å intervals along low-index backscattering directions (*i.e.*, $[\bar{1}\,\bar{1}\,0]$). These alias peaks are also faintly evident along the $[0\bar{1}\,0]$ and $[\bar{1}\,00]$ directions in the experimental (001) plane image of Fig. 5.8(a). Aside from these alias backscattering peaks, no appreciable backscattering or side scattering atomic images are seen in the experimental images of Figs. 5.6-5.8(a), as well as the theoretical images of Figs. 5.6-5.8(b)-(c). This is simply due to much stronger forward scattering amplitudes causing the contribution of the forward scattering atoms to dominate the $\chi(\mathbf{k})$ data set intensities, thus subsequently causing them to be preferentially imaged, as seen in previous studies of bulk Cu(001) [5.31]. The form of the scattering factor amplitudes in Fig. 5.4(b) makes it clear why this is true as well: forward scattering is ~6-8 times stronger than back scattering over the energy interval involved here. As expected from the comparison of the experimental and theoretical surface emission images above, the relative intensities of the experimental backscattering images for the bulk emission case (even though for the most part merely artifactual) are better reproduced in the multiple-scattering model images of Figs. 5.6(c)-5.8(c), as the relative backscattering intensities in the single-scattering images of Figs. 5.6(b)-5.8(b) are much weaker.

Considering now the image features in the forward scattering directions, we note that, for the $(\bar{1}\,1\,\bar{2})$ plane images of Fig. 5.6, there are three forward scattering artifacts in

the experimental image of Fig. 5.6(a), approximately 3Å from the emitter and along the [131], [110], and [31$\bar{1}$] directions, which do not correspond to actual atomic locations. These artifacts are weak compared to the features seen in the other ($\bar{1}$10) and (001) plane images of Figs. 5.7-5.8. That is, these artifacts in the ($\bar{1}$1$\bar{2}$) plane are only ≈3× more intense than the backscattering alias peaks discussed above, compared to the forward scattering features in the ($\bar{1}$10) and (001) planes, which are respectively ≈6× and ≈10× more intense than the backscattering alias peaks. The artifact along the [110] direction can be seen in the single-scattering image of Fig. 5.6(b), as well as faint indications of the [131] and [31$\bar{1}$] artifacts. The artifacts along the [131] and [31$\bar{1}$] directions dominate the multiple-scattering image of Fig. 5.6(c), but the artifact along the [110] direction is now only faintly discernible. Thus the single-scattering and multiple-scattering images are reasonably similar to the experimental image of Fig. 5.6(a), differing only in the relative intensities of the artifacts along the [110] and [131], [31$\bar{1}$] directions.

The differences between the experimental, single-scattering and multiple-scattering forward scattering atomic images in the ($\bar{1}$10) and (001) planes (Figs. 5.7-5.8) are less apparent than for the case of the ($\bar{1}$1$\bar{2}$) plane images of Fig. 5.6. Note here that the ($\bar{1}$10) plane is special for a bulk emitter in that it contains the nearest-neighbor forward scattering atoms that are expected to be the strongest features in the holographic images. Previous studies have demonstrated that single-scattering models can adequately reproduce the features seen in forward scattering atomic images reconstructed from bulk systems, even though they often exhibit elongation roughly parallel to the scattering direction [5.9a], but we see here that the bulk atomic images reconstructed from multiple-scattering models do not differ greatly from images obtained from experiment and single-scattering models. This could be due to both inelastic attenuation and elastic scattering of the photoelectron wavefronts, such that higher-order multiple-scattering events deep in the bulk do not contribute much to the $I(\mathbf{k})$ intensities measured above the sample;

instead, the majority of the $I(\mathbf{k})$ signal that originates from deeply-buried emitters comes from lower-order multiple-scattering events [5.32].

Note also that the only nearest-neighboring forward scattering atoms imaged in *any* of these experimental or theoretical bulk emission images are the $\frac{\bar{1}}{2}\frac{1}{2}\frac{1}{2}$ and $\frac{1}{2}\frac{1}{2}\frac{1}{2}$ atoms, as seen in the $(\bar{1}10)$ plane images of Fig. 5.7. Neither the 100 or the symmetry-equivalent 010 forward scattering atoms are visible in the experimental or theoretical (001) plane images of Fig. 5.8. The cause of this preferential imaging of the $(\bar{1}10)$ plane atoms; as well as the strong double-peak artifacts near the origin in the $(\bar{1}10)$ and (001) planes, located in the horizontal (110) plane of the emitter and approximately 0.7Å away from the emitter, is discussed below.

As noted before, Figure 5.4(b) shows the W scattering factor magnitudes for $k_{min} = 3.85\text{Å}^{-1}$ and $k_{max} = 7.45\text{Å}^{-1}$ photoelectrons. Note that the forward scattering peak is quite narrow, having a half angle at half-maximum amplitude of approximately 30° for $k_{min} = 3.85\text{Å}^{-1}$ photoelectrons; and approximately 15° for $k_{max} = 7.45\text{Å}^{-1}$ photoelectrons. While it is the presence of these forward scattering peaks that causes the preferential scattering from, and subsequent imaging of, forward scattering atoms, we demonstrate more quantitatively in Figs. 5.9-5.10 how this narrow angular width of the forward scattering peak also causes the preferential imaging of forward scattering atoms nearest to the azimuthal axis (*i.e.*, the surface normal) of the $\chi(\mathbf{k})$ data set.

The panels to the left of Figs. 5.9(a) and 5.10(a) show the geometry of two small W clusters. The geometry for Figure 5.9 is a single W photoemitter, with only $\frac{\bar{1}}{2}\frac{1}{2}\frac{1}{2}$ and $\frac{1}{2}\frac{1}{2}\frac{1}{2}$ W scatterers in the $(\bar{1}10)$ plane. That for Figure 5.10 is a single W photoemitter, with only 100 and 010 forward scattering atoms in the (001) plane. Single-scattering $\chi(\mathbf{k})$ intensities were calculated for both of these simple W clusters, and images reconstructed from these theoretical $\chi(\mathbf{k})$ data sets using Method A in the $(\bar{1}10)$ and (001) planes are shown in Figs. 5.9(a)-(b) and 5.10(a)-(b), respectively. The intensities of all the images of Figs. 5.9(a)-(b) and 5.10(a)-(b) have been rescaled relative to each other

to yield the same maximum-to-minimum gray scale; these relative scale factors are indicated on each image, with that in the most intense image of Fig. 5.9(a) being arbitrarily set to 1.0.

Figures 5.9(a)-(b) show the $(\bar{1}10)$ and (001) plane image reconstructions of the cluster with only $\frac{\bar{1}}{2}\frac{1}{2}\frac{1}{2}$ and $\frac{1}{2}\frac{1}{2}\frac{1}{2}$ scatterers. Note that while the $\frac{\bar{1}}{2}\frac{1}{2}\frac{1}{2}$ and $\frac{1}{2}\frac{1}{2}\frac{1}{2}$ atomic images are clearly and strongly visible in the $(\bar{1}10)$ plane containing these atoms, these atoms produce spurious images in the (001) plane, notably the strong features located approximately 0.7Å to either side of the emitter along the horizontal (110) plane. Figures 5.10(a)-(b) show the $(\bar{1}10)$ and (001) plane image reconstructions of the cluster with only 100 and 010 scatterers. The 100 and 010 atomic images are again clearly visible in the (100) plane containing these atoms, and these atoms also produce similar near-emitter artifacts in the $(\bar{1}10)$ plane. These near-emitter artifacts are also similar to those that appear in the experimental and theoretical bulk emitter images of Figs. 5.6-5.8. These near-emitter artifacts are thus not caused by incomplete $I(\mathbf{k})$ background subtraction, but are simply extraneous reconstructed features of the forward scattering $\frac{\bar{1}}{2}\frac{1}{2}\frac{1}{2}$, $\frac{1}{2}\frac{\bar{1}}{2}\frac{1}{2}$, 100, and 010 atoms.

Note also that the 100 and 010 atomic images in the (001) plane (Fig. 5.10(b)), are ~1.8× less intense than those of the $\frac{\bar{1}}{2}\frac{1}{2}\frac{1}{2}$ and $\frac{1}{2}\frac{1}{2}\frac{1}{2}$ atomic images in the $(\bar{1}10)$ plane (Fig. 5.9(a)). This can be understood from the narrowness of the forward scattering maxima of the W scattering factor, as shown in Fig. 5.4(b). Since the $\chi(\mathbf{k})$ data set spans a polar-angle range of $40° \le \theta \le 90°$ as measured within the surface, this means that the strong forward scattering diffraction features of the $\frac{\bar{1}}{2}\frac{1}{2}\frac{1}{2}$ and $\frac{1}{2}\frac{1}{2}\frac{1}{2}$ atoms (which lie along the $[\bar{1}11]$ and [111] directions) will be well within this polar angle range, as the angle between $[\bar{1}11]$ (or [111]) and the normal [110] direction is $\theta^{[110]}_{[\bar{1}11]} \approx 35.3°$. In contrast, nearly half of the forward scattering diffraction features of the 100 and 010 atoms (which lie along the [100] and [010] directions) will be outside of this polar angle range, as the angle between [100] (or [010]) and the normal [110] direction is $\theta^{[110]}_{[100]} = 45°$.

Thus the preferential imaging of the nearest-neighbor $\frac{\bar{1}}{2}\frac{1}{2}\frac{1}{2}$ and $\frac{1}{2}\frac{1}{2}\frac{1}{2}$ forward scatterers can be understood by the localization of their strongest forward scattering diffraction features within the polar angle range of this $\chi(\mathbf{k})$ data set. The absence of the atomic images of the 100 and 010 forward scattering atoms is merely due to a portion of their forward scattering diffraction features lying outside the polar angle range of this $\chi(\mathbf{k})$ data set. This also explains the total absence of any side scattering atomic image features, as their forward scattering diffraction features lie well outside of the polar angle range of the $\chi(\mathbf{k})$ data set. Any low-energy photoelectron diffraction data set is thus expected to exhibit qualitatively similar effects due to electron refraction at the inner-potential surface barrier, even if the experimental data is initially taken down to very low takeoff angles with respect to the surface.

Thus imaging forward scattering atoms is dependent on whether their strong forward scattering diffraction features lie within the $\chi(\mathbf{k})$ data set polar angle range. In addition, due to the strong, non-optical nature of forward scattering (non-constant amplitude and phase shift, as shown in Figs. 5.4(b)-(c)), these forward scattering atomic images are expected to be less ideal than those of backscattering atoms. For imaging backscattering atoms from overlayer and surface systems, it has thus been shown to be of benefit to exclude the forward scattering regions of the surface and near-surface plane atoms, in order to retrieve only the more ideal optical backscattering information of atoms that lie more nearly below emitter sites [5.5]. More recently, there has also been a proposal to image even forward scattering atoms by means of their more ideal side scattering contributions, by experimentally keeping the angle between the incident polarized radiation and the photoelectron detector small, such that the detector is kept near the photoexcitation cross-section node that exists for emission from *s* subshells, and to a lesser degree for emission from non-*s* subshells [5.33]. This has the effect of suppressing the strong contribution of forward scattering, and putting more emphasis on the side scattering contributions from these forward scattering atoms. However, it is clear

that this effect does not work for all levels at all wavenumbers, as the photoelectric cross sections in Fig. 5.4(a) are very nearly uniform in amplitude.

5.5. Comparison of atomic images obtained from different reconstruction algorithms

There have been various modifications to the basic optical reconstruction algorithm of Method A (Eq. (5.2)), and to the definition of the reconstruction integral itself, in order to account for the non-optical nature of electron scattering, of which four methods will be discussed here. The first of these, which we will call Method $\tilde{\mathrm{A}}$, is a straightforward attempt to remove the effects of the complex electron scattering factor $f(\Theta^{\mathbf{k}}_{\mathbf{r}'})$ by dividing it out in the transform kernel. This has been termed the "Scattered-Wave Included Fourier Transform" (SWIFT) by Tonner *et al.* [5.4], and it can be written as:

$$U_A(\mathbf{r}') \equiv \iiint_K d^3\mathbf{k} \cdot \frac{e^{-i(\mathbf{k}\cdot\mathbf{r}'-kr')}}{f(\Theta^{\mathbf{k}}_{\mathbf{r}'})} \chi(\mathbf{k}). \tag{5.3}$$

Carrying out this transform implies knowing the identity of the scatterer to be imaged in each region of space, so that $f(\Theta^{\mathbf{k}}_{\mathbf{r}'})$ can be uniquely defined. For the present case, this is trivial, since all scatterers are W atoms and can be assumed to be identical. (A more refined treatment might consider surface atoms to have a different scattering factor, since they are not uniformly surrounded by neighbors, but this type of correction is not necessary in the analysis of LEED data at similar wavenumbers [5.21a].

A second method (Method B) for improving atomic image fidelity is to utilize only the **k**-space regions in $\chi(\mathbf{k})$ where the photoemitted source wave is most stationary, and the electron $f(\Theta^{\mathbf{k}}_{\mathbf{r}'})$ is most optical-like for specific atomic positions. This general approach was first used in high-energy photoelectron holography of near-forward scattering atoms by Thevuthasan *et al.* [5.5], but it has more recently been applied to low-

energy studies of back-scattering atoms by Wu and Lapeyre [5.6a], and Tong *et al.* [5.6b]. Since the electron scattering factor magnitude and phase are roughly constant for backscattering directions ($\Theta^{\mathbf{k}}_{\mathbf{r}'} \approx 180°$) [5.6,5.22], $\chi(\mathbf{k})$ regions in a cone of half-angle $\alpha \approx 30°$ centered on $\hat{\mathbf{k}} = -\hat{\mathbf{r}}'$ directions are used in reconstructing atoms directly beneath the photoemitter site. For the present case, , as illustrated in Figs. 5.4(b)-(c) ,these simplifying assumptions are at least partly true: the magnitude of f is actually fairly strongly varying in the backscattering direction, but the phase Ψ is quite constant. Thus, this "small-cone" algorithm uses the usual optical reconstruction kernel $e^{i(\mathbf{k}\cdot\mathbf{r}'-kr')}$, but as multiplied by a window function $w(\Theta^{\mathbf{k}}_{-\mathbf{r}'})$ which is equal to unity when $\Theta^{\mathbf{k}}_{-\mathbf{r}'} \leq \alpha$, and is zero elsewhere in **k**-space:

$$U_B(\mathbf{r}') \equiv \iiint_K d^3\mathbf{k} \cdot e^{-i(\mathbf{k}\cdot\mathbf{r}'-kr')} w(\Theta^{\mathbf{k}}_{-\mathbf{r}'})\chi(\mathbf{k}) . \tag{5.4}$$

A Hanning window function of the form $w_{Hanning}(\Theta^{\mathbf{k}}_{-\mathbf{r}'}) \equiv \cos^2(\pi \cdot \Theta^{\mathbf{k}}_{-\mathbf{r}'} / \alpha)$ has been used in some implementations of Eq. (5.4) [5.6c,5.6d], but here, as in the first uses of Method B [5.8a,5.8b], the step function $w(\Theta^{\mathbf{k}}_{-\mathbf{r}'})$ window function was used.

A third algorithm (Method C) due to Rous and Rubin [5.7] recognizes the quantum mechanical nature of the electron wavefront propagating in the bulk, and describes it in terms of the Lippman-Schwinger equation and the first Born Approximation. In the form that can be most directly related to Eq. (5.2), this quantum mechanically-based reconstruction algorithm is given by:

$$U_C(\mathbf{r}') \equiv \frac{d}{dr'}\left[r' \cdot \mathrm{Re}\left[\iiint_K d^3\mathbf{k} \cdot e^{-i(\mathbf{k}\cdot\mathbf{r}'-kr')}\chi(\mathbf{k})\right]\right]. \tag{5.5}$$

The final reconstruction algorithm (Method D) considered here is due to Hoffman and Schindler [5.8a], and is not strictly speaking holographic in nature. But it is a so-

called "direct method" for analyzing photoelectron diffraction data so as to estimate atomic positions, usually of backscattering atoms under adsorbates [5.8b] Its form is given by:

$$U_D(\mathbf{r}') = \sum_{\hat{\mathbf{k}}} \Delta\sigma_{\hat{\mathbf{k}}} \exp\left[r' \cdot \int_k dk \cdot \chi_{theory}(\mathbf{k},\mathbf{r}')\chi(\mathbf{k}) \right], \tag{5.6}$$

where $\Delta\sigma_{\mathbf{k}}$ is a weighting factor for data taken along each direction that is usually treated as a constant, and $\chi_{theory}(\mathbf{k},\mathbf{r}')$ is calculated via a single-scattering model from:

$$\chi_{theory}(\mathbf{k},\mathbf{r}') = \mathrm{Re}\left[\frac{e^{j(kr'-\mathbf{k}\cdot\mathbf{r}')}}{kr'} f(\Theta^{\hat{\mathbf{k}}}_{\hat{\mathbf{r}}'}) \right]. \tag{5.7}$$

Calculating $\chi_{theory}(\mathbf{k},\mathbf{r}')$ thus again requires a knowledge of the atomic identity of each scatterer in order for the scattering factor to be uniquely specified. Thus Eq. (5.7) is a redefinition of the reconstruction integral of Eq. (5.2), but it still relies on the orthogonality of a theoretically calculated single-scattering model $\chi_{theory}(\mathbf{k},\mathbf{r}')$ with the experimental $\chi(\mathbf{k})$, whose exponentiated dot product over **k**-space as defined above will tend to produce image intensity peaks at atomic positions. This method inherently assumes individual fine-step scans of intensity with photon wavenumber over the range *k* of the integral, and then a coarse sum over directions $\hat{\mathbf{k}}$, as weighted ideally by the solid angle $\Delta\sigma_{\hat{\mathbf{k}}}$ each subtends.

Figures 5.11(a)-(d) show the reconstructed atomic images in the vertical $(\bar{1}\,1\bar{2})$ plane obtained from applying the reconstruction algorithms of Eqs. (5.3)-(5.6) (Methods Ã-D, respectively) to the experimental *surface* emission $\chi(\mathbf{k})$ of Fig. 5.2(c), and these can be compared to Fig. 5.5(a) (Method A). As discussed earlier, the first four methods

differ from Method A in some way in order to correct for the non-optical emission, propagation, and/or scattering of electrons.

Figure 5.11(a) shows the reconstructed atomic images obtained via Method $\tilde{A}$ (Eq. (5.3)), where the effect of the anisotropy in the scattering factor magnitude and phase is divided out of the holographic $\chi(\mathbf{k})$ intensities during the imaging deconvolution process. The backscattering $\bar{1}\,\bar{1}\,0$ image is still less intense than the $\frac{1}{2}\,\frac{\bar{1}}{2}\,\frac{\bar{1}}{2}$ and $\frac{\bar{1}}{2}\,\frac{1}{2}\,\frac{1}{2}$ side scatterers, and is surprisingly even more different ($\approx$1/3) compared to the case in Fig. 5.5(a) ($\approx$1/2) with no correction for scattering factor. This remaining difference in relative intensity can be explained from the fact that Eq. (5.3) still does not correct for the difference in the attenuation paths of the wavefronts involving these atomic sites, nor intensity changes due to multiple scattering, as discussed above. Also, the $\frac{1}{2}\,\frac{\bar{1}}{2}\,\frac{\bar{1}}{2}$ and $\frac{\bar{1}}{2}\,\frac{1}{2}\,\frac{1}{2}$ atomic images are still shifted in towards the emitter, and downward, by essentially the same amounts as in the image derived from Method A. Thus, the theoretical scattering factor $f(\Theta_{\mathbf{r}'}^{\mathbf{k}})$ may not be sufficiently accurate to describe the actual effective scattering factor for this system (particularly in the side scattering direction), and other effects involving anisotropies of the photoemitted source wave, as well as multiple scattering, also may be involved. The potential importance of such additional effects is also illustrated by the fact that the single- and multiple-scattering images of Figs. 5.5(b)-(c), derived from model clusters containing the same theoretical scattering factor used in Eq. (5.3), do not exactly reproduce the experimental image of Fig. 5.5(a). However, some weaker image artifacts in the region enclosed by the $\frac{1}{2}\,\frac{\bar{1}}{2}\,\frac{\bar{1}}{2}$, $\frac{\bar{1}}{2}\,\frac{1}{2}\,\frac{1}{2}$, and $\bar{1}\,\bar{1}\,0$ atoms in Fig. 5.5(a) have been somewhat suppressed in Fig. 5.11(a), thus suggesting that the theoretical scattering factor used in Eq. (5.3) does beneficially account for some of the scattering anisotropy in this system. Further development in the application of Method $\tilde{A}$ would involve refining the treatment of the theoretical scattering factors (perhaps they are different at the surface for example), as well as better accounting for the inelastic attenuation of direct and scattered wavefronts (*e.g.* by using complex phase shifts), and

explicitly correcting for the wavenumber and angular dependence of the photoemitted source-wave, including its *d* and *g* wave components.

Figure 5.11(b) shows the reconstructed atomic images obtained via Method B (Eq. (5.4)), where only the holographic surface-atom $\chi(\mathbf{k})$ intensities in a localized angular region of the source wave and images corresponding to more nearly ideal backscattering regions are used in the imaging deconvolution process. Here, the backscattering $\bar{1}\,\bar{1}\,0$ image peak does appear to be sharper, but it also has more extended and diffuse wings in this image compared to that of Method A in Fig. 5.5(a).The side scattering $\frac{1}{2}\frac{\bar{1}}{2}\frac{\bar{1}}{2}$ and $\frac{\bar{1}}{2}\frac{1}{2}\frac{1}{2}$ atomic images in Fig. 5.11(b) are completely absent, and this is simply due to the fact that the window function $w(\Theta^{\mathbf{k}}_{-\mathbf{r}_i})$ with half-angle $\alpha = 30°$ lies outside the angular range of the $\chi(\mathbf{k})$ data set, which spans only $40° \le \theta \le 90°$. Thus, atoms along the side scattering directions ($\theta = 0°$) simply cannot be imaged from this data set via this method. Nor was this method proposed for imaging side scattering atoms. The position of the $\bar{1}\,\bar{1}\,0$ atom is also essentially unchanged from Fig. 5.5(a), so there is no apparent advantage in Method B for this case as far as locating this atom accurately, even though the method was proposed for more accurately imaging backscattering atoms. The limited size of the window function used in this method also must inherently reduce the resolution of the atomic images, and it is seen to create image aberrations along the low-index directions $[\bar{1}\,\bar{1}\,0]$, $[\bar{1}\,\bar{3}\,\bar{1}]$ and $[\bar{3}\,\bar{1}\,1]$ [5.34]; these aberrations include an expected broadening of the $\bar{1}\,\bar{1}\,0$ atomic image along the $[\bar{1}\,1\,1]$ direction. However, a positive feature of Method B is that it does manage to reconstruct faintly discernible images for the $\frac{\bar{1}}{2}\frac{\bar{3}}{2}\frac{\bar{1}}{2}$ and $\frac{\bar{3}}{2}\frac{\bar{1}}{2}\frac{1}{2}$ backscattering atoms that are barely visible on this gray scale. Thus Method B may be slightly better suited for the refinement of backscattering atomic images, but some loss of image resolution and the appearance of additional artifacts along low-index directions are inherent disadvantages in this approach.

Figure 5.11(c) shows the reconstructed atomic images obtained via Method C (Eq. (5.5)), where the quantum mechanical nature of the propagation of electron wavefronts is

accounted for in the imaging deconvolution process. The backscattering $\bar{1}\,\bar{1}\,0$ atom is a little more sharply defined in this image, but has a position essentially identical to that in Fig. 5.5(a). The side scattering $\frac{1}{2}\frac{\bar{1}}{2}\frac{\bar{1}}{2}$ and $\frac{\bar{1}}{2}\frac{1}{2}\frac{1}{2}$ atomic images are a little less shifted in towards the emitter (by only 0.3Å), as compared to either Fig. 5.5(a) or Fig. 5.11(a). These slight image improvements suggest that not correctly allowing for the propagation of electron wavefronts may account for some of the atomic peak positions shifts seen in Figs. 5.4(a) and 5.11(a). However, these slight advantages do not compensate the fact that the background level of image artifacts, especially around the forward scattering atoms, is significantly higher with Method C. Thus, although this method certainly deserves further testing with experimental data, it does not appear to have significant advantages over the simple optical transform.

Figure 5.11(d) shows the reconstructed atomic images obtained via Method D (Eq. (5.6)), which is similar to Eq. (5.2) in attempting to retrieve the object field $u(\mathbf{r}')$ via an orthogonality relation, but this time between experimental $\chi(\mathbf{k})$ intensities and single-scattering model $\chi_{theory}(\mathbf{k},\mathbf{r}')$ intensities. The backscattering $\bar{1}\,\bar{1}\,0$ atom is located very well in this image, but with no better accuracy than for the other methods discussed previously. The side scattering $\frac{1}{2}\frac{\bar{1}}{2}\frac{\bar{1}}{2}$ and $\frac{\bar{1}}{2}\frac{1}{2}\frac{1}{2}$ atoms cannot be seen in this image, as in the reconstruction algorithm of Eq. (5.6) best describes the correlation between backscattering $\chi_{theory}(\mathbf{k},\mathbf{r}')$ and $\chi(\mathbf{k})$ contributions. Because the same atomic electron scattering factors were used for both Methods Ã and Method D, the corresponding atomic images of Figs. 5.11(a) and 5.11(d) show corrections for image aberrations and position shifts that are of a comparable degree. Note for Method D that the backscattering image peak in Fig. 5.11(d) is approximately the same intensity as the side scattering image peaks, and no multiplication factor is present between the upper and lower regions of the image. It should be noted that Method D has been used most successfully in imaging molecular adsorbates on surfaces [5.8], where the conditions are probably better described by single-scattering than is the case for the clean W(110) surface

considered here. The slight position shift of the $\bar{1}\,\bar{1}\,0$ atomic peak can be explained by the W scattering factors used in Eq. (5.7) and elsewhere in this study (*cf.* comparable $\bar{1}\,\bar{1}\,0$ position shift for the theoretical image in Fig. 5.5(c)).

Figures 5.12(a)-(d) now show the reconstructed atomic images in the same vertical $(\bar{1}\,10)$ plane obtained from applying the reconstruction algorithms of Eqs. (3)-(6) (Methods $\tilde{\text{A}}$-D) to the experimental *bulk* emission $\chi(\mathbf{k})$ of Fig. 5.3(c). These can be compared to Fig. 5.8(a) (Method A). Because Methods B and D have been developed specifically to treat backscattering atoms, we do not expect them to perform particularly well for this forward-scattering-dominated case, but they are included for completeness and to see whether they are able in any case to resolve something from the backscattering atoms. In Figs. 5.12(a)-(d), there are no convincingly strong $\frac{\bar{1}}{2}\frac{\bar{1}}{2}\frac{\bar{1}}{2}$ and $\frac{\bar{1}}{2}\frac{\bar{1}}{2}\frac{1}{2}$ backscattering atomic images visible (except for things which coincide with alias peaks along the $[\,\bar{1}\,\bar{1}\,0\,]$ direction, as discussed earlier in Figs. 5.6-5.8), especially as compared to the stronger forward scattering image features. Figure 5.12(c)-(d) seems to show no resolvable images for the $\frac{\bar{1}}{2}\frac{\bar{1}}{2}\frac{\bar{1}}{2}$ and $\frac{\bar{1}}{2}\frac{\bar{1}}{2}\frac{1}{2}$ atoms.

Figure 5.12(a) shows the reconstructed atomic images obtained via Method $\tilde{\text{A}}$ (Eq. (5.3)). The forward scattering features here are not noticeably shifted closer towards their actual locations ($\frac{\bar{1}}{2}\frac{1}{2}\frac{1}{2}$ and $\frac{1}{2}\frac{1}{2}\frac{1}{2}$) as compared to Fig. 5.8(a). This suggests that either the forward scattering features in this plane are purely artifactual and not associated with an actual atomic image, or that these features are shifted from their actual locations due to additional effects (*e.g.*, source wave anisotropy, multiple scattering, *etc.*) that cannot be accounted for by a correction procedure involving single-scattering events. Figure 5.12(b) shows the reconstructed atomic images obtained via Method B (Eq. (5.4)). Note that the forward scattering features are now greatly elongated along the $[\bar{1}\,11]$ and [111] directions. This is to be expected, as forward scattering atomic images are much more susceptible than backscattering images to such loss of radial resolution when the solid-angle range of $\chi(\mathbf{k})$ data is limited by the cone defined by $w(\Theta^{\mathbf{k}}_{\mathbf{r}'})$ (here only 0.27π

in width) in reconstructing images using this technique [5.3c,5.20]. This can be contrasted to the larger solid-angle range of the full $\chi(\mathbf{k})$ data set (0.71π) used with Methods A, $\tilde{\text{A}}$, C, and D. Thus the radial elongation of the forward scattering features in Fig. 5.12(b) suggests that these features are not purely artifactual in origin, but are rather strongly shifted and elongated images of the $\frac{\bar{1}}{2}\frac{1}{2}\frac{1}{2}$ and $\frac{1}{2}\frac{1}{2}\frac{1}{2}$ atoms. One might even propose that they could be useful in locating these atoms in *direction* relative to the emitter, even though they yield no information on *distance* from the emitter. Figure 5.12(c) shows the reconstructed atomic images obtained via Method C (Eq. (5.5)). As seen here, Method C seems to shift the $\frac{\bar{1}}{2}\frac{1}{2}\frac{1}{2}$ and $\frac{1}{2}\frac{1}{2}\frac{1}{2}$ forward-scattering atomic images away from their actual locations of the atoms, as judged relative to Methods A or $\tilde{\text{A}}$. These forward scattering atomic peak position shifts must arise in some part from over-accounting for the quantum mechanical propagation of electron wavefronts. For example, using the first Born approximation in describing the scattering [5.7] is quasi-optical in its approach.

In contrast to the images obtained from Methods $\tilde{\text{A}}$-C (Figs. 5.12(a)-(c)), the reconstructed atomic image obtained via Method D (Fig. 5.12(d)) shows no forward scattering features, but instead chiefly manages to retrieve the near-origin artifacts seen in Figs. 5.8(a) and 5.12(a). The backscattering image at $z \approx -4.6$Å is actually related to the alias peak features seen in Figs. 5.6-5.8, and Figs. 5.12(a)-(b). The lack of forward scattering atomic images in Fig. 5.12(d) can be understood by the fact that the integral in Eq. (5.6) is evaluated over a range of wavenumbers, but separately for each different direction. The path-length difference kernel $e^{i(\mathbf{k}\cdot\mathbf{r}'-kr')}$ in Eq. (5.7) can be seen to be identical to unity for forward scatterers (*i.e.*, $\hat{\mathbf{k}} = \hat{\mathbf{r}}'$) along forward scattering directions, and have less modulations relative to backscatterers for other scattering directions. Thus the result of Eqs (5.6) and (5.7) is to emphasize backscattering atomic images more so than forward scattering images. This is what this method was originally formulated to do [5.8], and it is evidenced by its success in retrieving the $\bar{1}\,\bar{1}\,0$ backscattering atomic peak in Fig. 5.11(d). It appears that the failure of Method D in retrieving a backscattering

image here suggests the fact that the backscattering signal in the bulk emission $\chi(\mathbf{k})$ data set of Fig. 5.3(c) is far too weak to reconstruct a backscattering atomic image, compared to the stronger forward scattering $\chi(\mathbf{k})$ components.

5.6 Concluding remarks

We have applied five of the currently proposed direct-imaging algorithms for photoelectron holography to a large high-quality experimental data set from W(110), and to corresponding theoretical simulations of this data set at both the single scattering and multiple scattering levels. Separate holograms were measured for both the surface and bulk atoms by making use of the surface core-level shift. The five methods are: an "optical" transform over the volume in **k**-space spanned by the data (Method A), the transform of A but with the kernel modified to divide out the electron-atom scattering factor (Method $\tilde{A}$), the so-called "small-cone" transform which focuses on imaging back scattering atoms (Method B), a quantum-mechanically motivated transform (Method C), and a non-holographic projection method that also focuses on backscattering atoms (Method D). In analyzing the experimental data, we have introduced a general three-dimensional $I_0(\mathbf{k})$ background subtraction scheme in **k**-space to better normalize raw $I(\mathbf{k})$ intensities, and compared the three dimensional atomic images that can be obtained via Method A from experiment and theory, and via the five reconstruction algorithms from experiment. The inclusion of multiple scattering in theory is needed with Method A to adequately predict the image of the nearest-neighbor backscattering atom. For a surface-atom emitter, Methods A, $\tilde{A}$, C, and D produce comparable atomic images of backscattering and side scattering atoms that could then in principle be refined for an unknown structure using conventional comparison to theory via *R*-factor analysis. However, Method C exhibits somewhat more background noise that could hinder image interpretation. In contrast, Method B as applied to a surface-atom emitter is somewhat more successful in retrieving backscattering atomic images, but these peaks also suffer

from some loss of image resolution which is inherent for this algorithm, and it is also not possible to image the side scattering atoms. Thus, it is not clear that Method B has a significant advantage in treating this data. Method D produces backscattering images for a surface emitter that are reasonably well defined. As applied to a bulk emitter for which back scattering, side scattering, and stronger forward scattering can all play a role, all of these methods are found to produce poorly resolved forward scattering images. The peaks in this region of image space are found to be elongated along the z direction and/or the radial direction leading away from the emitter, and to be significantly shifted away from the known atomic positions. Methods A and $\tilde{A}$ may have some success with one forward scattering image (the 110 atom), and Method B may be able to determine the *direction* of forward scatterers, but not their distance from the emitter. Method B is notable in retrieving faint *backscattering* images from the forward scattering-dominated bulk emission $\chi(\mathbf{k})$ data set. Overall, we thus find Methods A and $\tilde{A}$, to be the most robust overall for analyzing both surface and bulk $\chi(\mathbf{k})$ data sets from W(110), but with D being best for reconstructing only surface emission atomic images. Imaging back scattering and side scattering atoms is clearly the most promising aspect of photoelectron holography, with the amount of new structural information that can be derived from images of forward scattering atoms being very limited (at least with the presently available imaging methods). The photoelectron holographic images derived here at least provide an approximate determination of the structure surrounding both the surface and bulk emission sites of W(110), and suggest the broader applicability of this approach for surface structure studies. Thus photoelectron holography, along with other related forms of electron emission holography (*e.g.*, Auger [5.10], Kikuchi scattering [5.11], and diffuse LEED [5.12]) and x-ray fluorescence holography [5.14-5.15], holds much promise of at least providing approximate starting structures to be followed by more conventional structure refinements via multiple scattering calculations and R-factor analysis.

References

[5.1] D. Gabor, Nature (London) **161** (1948) 777.

[5.2] A. Szöke, in *Short Wavelength Coherent Radiation: Generation and Applications*, T. Attwood, J. Boker (eds.), AIP Conference Proceedings No. 147, (AIP, New York, 1986) 361.

[5.3] (a) J. J. Barton, Phys. Rev. Lett. **61** (1988) 1356 , and Phys. Rev. Lett. **67** (1991) 3106. (b) J. J. Barton and L. J. Terminello, paper presented at the Third International Conference on the Structure of Surfaces, Milwaukee, July 1990, and in *Structure of Surfaces III,* S. Y. Tong, M. A. Van Hove, X. Xide, and K. Takanayagi, eds., (Springer Verlag, Berlin, 1991) p. 107. (c) S. Y. Tong, H. Huang, and C. M. Wei, Phys. Rev. B **46** (1992) 2452, and references therein. (d) L. Fonda, Phys. Stat. Sol. B **188** (1995) 599.

[5.4] (a) B. P. Tonner, Z.-L. Han, G. R. Harp, and D. K. Saldin, Phys. Rev. B **43** (1991) 14423. (b) D. K. Saldin, K. Reuter, P. L. De Andres, H. Wedler, X. Chen, J. B. Pendry, and K. Heinz, Phys. Rev. B **54** (1996) 8172.

[5.5] S. Thevuthasan, R. X. Ynzunza, E. D. Tober, C. S. Fadley, A. P. Kaduwela, and M. A. Van Hove, Phys. Rev. Lett. **70** (1993) 595.

[5.6] (a) S. Y. Tong, H. Li, and H. Huang, Phys. Rev. B **51** (1995) 1850. (b) H. Wu and G. J. Lapeyre, Phys. Rev. B **51** (1995) 14549. (c) J. M. Roesler, M. T. Sieger, T.-C. Chiang, Surf. Sci. **329** (1995) L588. (d) M. T. Sieger, J. M. Roesler, D. S. Lin, T. Miller, and T.-C. Chiang, Phys. Rev. Lett. **73** (1994) 3117.

[5.7] P. J. Rous and M. H. Rubin, Surf. Sci. **316** (1994) L1068.

[5.8] (a) P. Hofmann, K.-M. Schindler, V. Fritzsche, S. Bao, A. M. Bradshaw, and D. P. Woodruff, J. Vac. Sci. Technol. A **12** (1994) 2045, Surf. Sci. **337** (1995) 169, and references therein. (b) D. P. Woodruff, R. Davis, N. A. Booth, A. M. Bradshaw, C. J. Hirschmugl, K.-M. Schindler, O. Schaff,

V. Fernandez, A. Theobald, P. Hofmann, and V. Fritzsche, Surf. Sci. **357-358** (1996) 19, and references therein.

[5.9] (a) L. J. Terminello, B. L. Petersen, and J. J. Barton, J. Electron Spec. Relat. Phenom. **75** (1995) 229, and references therein. (b) H. Wu, G. J. Lapeyre, H. Huang, and S. Y. Tong, Phys. Rev. Lett. **71** (1993) 251, and references therein. (c) M. Zharnikov, M. Weinelt, P. Zebisch, M. Stichler, and H.-P. Steinrück, Thin Sol. Films **275** (1996) 266, and references therein. (d) R. Denecke, R. Eckstein, L. Ley, A. E. Bocquet, J. D. Riley, R. C. G. Leckey, Surf. Sci. **331-333** (1995) 1085. (e) J. G. Tobin, G. D. Waddill, H. Li, S. Y. Tong, Surf. Sci. **334** (1995) 263, and references therein.

[5.10] (a) H. Li, S. Y. Tong, D. Naumovic, A. Stuck, and J. Osterwalder, Phys. Rev. B **47** (1993) 10036. (b) D. K. Saldin, G. R. Harp, and X. Chen, Phys. Rev. B **48** (1993) 8234, and references therein.

[5.11] (a) Z.-L. Han, S. Hardcastle, G. R. Harp, H. Li, X.-D. Wang, J. Zhang, and B. P. Tonner, Surf. Sci. **258** (1991) 313, and references therein. (b) I. H. Hong, S. C. Shyu, Y. C. Chou, and C. M. Wei, Phys. Rev. B **52** (1995) 16884, and references therein.

[5.12] (a) M. A. Mendez, C. Glück, J. Guerrero. P. L. de Andres, K. Heinz, D. K. Saldin, and J. B. Pendry, Phys. Rev. B **45** (1992) 9402, and references therein. (b) C. M. Wei, S. Y. Tong, H. Wedler, M. A. Mendez, and K. Heinz, Phys. Rev. Lett. **72** (1994) 2434, and references therein.

[5.13] S. Y. Tong, H. Huang, and X. Q. Guo, Phys. Rev. Lett. **69** (1992) 3654.

[5.14] (a) M. Tegze, G. Faigel, Europhys. Lett **16** (1991) 41, and Nature **380** (1996) 49.

[5.15] (a) T. Gog, P. M. Len, G. Materlik, D. Bahr, C. Sanchez-Hanke, and C. S. Fadley, Phys. Rev. Lett. **76** (1996) 3132. (b) T. Gog, R.-H. Menke, F.

Arfelli, P. M. Len, C. S. Fadley, G. Materlik, Synch. Rad. News **9** (1996) 30. (c) P. M. Len, T. Gog, G. Materlik, and C. S. Fadley, Phys. Rev. B. **51** (1997) 3323. (d) P. M. Len, T. Gog, D. Novikov, R. A. Eisenhower, G. Materlik, and C. S. Fadley, submitted to Phys. Rev. B.

[5.16] D. K. Saldin, G. R. Harp, B. L. Chen, and B. P. Tonner, Phys. Rev. B **44** (1991) 2480.

[5.17] S. Thevuthasan, G. S. Herman, A. P. Kaduwela, T. T. Tran, Y. J. Kim, R. S. Saiki, and C. S. Fadley, J. Vac. Sci. Technol. A **10** (1992) 2261.

[5.18] P. Hu and D. A. King, Phys. Rev. B **46** (1992) 13615.

[5.19] P. M. Len, S. Thevuthasan, C. S. Fadley, A. P. Kaduwela, and M. A. Van Hove, Phys. Rev. B **50** (1994) 11275.

[5.20] P. M. Len, F. Zhang, S. Thevuthasan, A. P. Kaduwela, M. A. Van Hove, and C. S. Fadley, (a) J. Electron Spec. and Relat. Phenom. **76** (1995) 351, and (b) to appear in Surf. Sci.

[5.21] (a) M. Arnold, S. Sologub, G. Hupfauer, P. Bayer, W. Frie, L. Hammer, and K. Heinz, to be published. (b) B. Kim, J. Chen, J. L. Erskine, W. N. Mei, C. M. Wei, Phys. Rev. B **48** (1993) 4735. (c) R. X. Ynzunza, in preparation.

[5.22] P. M. Len, C. S. Fadley, and G. Materlik, to appear in *X-ray and Inner Shell Processes: 17th International Conference*, R. L. Johnson, H. Schmidt-Boeckering, and B. F. Sonntag, eds., AIP Conference Proceedings No. 389 (AIP, New York, 1997).

[5.23] G. R. Harp, D. K. Saldin, X. Chen, Z.-L. Han, and B. P. Tonner, J. of Electron Spec. and Relat. Phenom. **57** (1991) 331.

[5.24] P. M. Len, S. Thevuthasan, A. P. Kaduwela, M. A. Van Hove, and C. S. Fadley, Surf. Sci. **365** (1996) 535.

[5.25] R. X. Ynzunza, private communication.

[5.26] J. J. Rehr and R. C. Albers, Phys. Rev. B **41** (1990) 8139.

[5.27] A. P. Kaduwela, D. J. Friedman, and C. S. Fadley, J. Electron Spec. Relat. Phenom. **57** (1991) 223.

[5.28] SCAT photoelectron diffraction program package, Y. Chen, H. Wu, and D. A. Shirley, private communication.

[5.29] (a) T. Greber, J. Osterwalder, D. Naumovic, A. Stuck, S. Hüfner, L. Schlapbach, Phys. Rev. Lett. **69** (1992) 1947. (b) D. K. Saldin, G. R. Harp, B. P. Tonner, Phys. Rev. B **45** (1992) 9629. (c) J. J. Barton, L. J. Terminello, Phys. Rev. B **46** (1992) 13548.

[5.30] M. A. Van Hove and S. Y. Tong, Eds., *Surface Crystallography by LEED* (Springer-Verlag, New York, 1979).

[5.31] L. J. Terminello, J. J. Barton, and D. A. Lapiano-Smith, J. Vac. Sci. Technol. B **10** (1992) 2088.

[5.32] S. D. Ruebush, R. X. Ynzunza, S. Thevuthasan, A. P. Kaduwela, M. A. Van Hove, and C. S. Fadley, Surf. Sci. **328** (1995) 302.

[5.33] T. Greber, J. Osterwalder, Chem. Phys. Lett. **256** (1996) 653, and private communication.

[5.34] M. T. Sieger, private communication.

Figure captions

Figure 5.1. (a) Experimental geometry, including the orientation of the sample (where $\hat{\mathbf{n}}$ is the surface normal) with respect to the horizontal polarization vector ($\hat{\mathbf{e}}$) of the incident excitation radiation $h\nu$, and the exit photoelectron direction $\mathbf{k}$. The angle between the incident photons and the emitted photoelectrons, as detected by a hemispherical analyzer, is fixed at 60°. The polar takeoff angle θ is varied by rotating the sample about an axis parallel to $\hat{\mathbf{e}}$; the azimuthal angle ϕ is varied by rotating about $\hat{\mathbf{n}}$. (b) Typical W $4f_{7/2}$ x-ray photoelectron spectrum from W(110), indicating the surface and bulk core-level-

shifted contributions used to generate the holographic $I(\mathbf{k})$ intensity data points of Figs. 5.2-5.3.

Figure 5.2. Schematic **k**-space volume representations of the intensity data sets for surface W $4f_{7/2}$ emission, as viewed down along $[\bar{1}\,\bar{1}\,0]$ (top panels), and down along $[00\,\bar{1}]$ (bottom panels). The wavenumbers and polar angles have here all been adjusted to be inside the surface, using an inner potential of 14 eV. The intensities in the lower right-hand quadrant have been removed to show the intensity surface at the constant minimum wavenumber. (a) Raw $I(\mathbf{k})$ data set. (b) $I_0(\mathbf{k})$ as determined by a least-squares fit in wavenumber and polar angle of Eq. (5.1) to the raw $I(\mathbf{k})$ intensities of (a). (c) The normalized $\chi(\mathbf{k})$ data set, as determined by the removal of the experimentally derived $I_0(\mathbf{k})$ of (b), and corrected with respect to both wavenumber and polar angle θ for an inner potential of V_0=14V to represent these quantities internal the surface.

Figure 5.3. As Fig. 5.2, but for bulk W $4f_{7/2}$ emission.

Figure 5.4. The angular dependence of important theoretical quantities, as evaluated at the two extreme internal wavevectors (kinetic energies) of the experimental data set: $k_{min} = 3.85\text{Å}^{-1}$ ($E = 56$ eV) and $k_{max} = 7.45\text{Å}^{-1}$ ($E = 211$ eV). (a) The W $4f$ differential photoelectric cross section $\frac{d\sigma}{d\Omega}$, as a function of emission angle with respect to the radiation polarization direction. (b) The W scattering factor magnitude ($|f(\Theta_r^k)|$), as a function of the photoelectron scattering angle Θ_r^k. Here, $\Theta_r^k = 0°$ is the forward scattering direction, and $\Theta_r^k = 180°$ is the backscattering direction. (c) The scattering phase shift $\psi(\Theta_r^k)$, again as a function of scattering angle.

Figure 5.5. W(110) atomic images obtained from experimental and theoretical W $4f$ surface-emission $\chi(\mathbf{k})$ data sets, in the vertical $(\bar{1}\,1\bar{2})$ plane, via Method A. The surface

emitter site at the origin is indicated by dashed squares, and the positions of the scatterers (assuming no surface relaxation) are indicated by circles. The nearest and next-nearest scattering positions have been labeled in panel (a). Axes are marked off in 1Å units. Image intensities for $z \leq -3.5$Å have been rescaled, with the scale factors indicated on the figures. (a) Image reconstructed from the experimental $\chi(\mathbf{k})$ data set of Fig. 5.2(c). (b) Image reconstructed from a theoretical single scattering $\chi(\mathbf{k})$ data set. (c) Image reconstructed from a theoretical multiple scattering $\chi(\mathbf{k})$ data set.

Figure 5.6. W(110) atomic images obtained from experimental and theoretical W 4*f* bulk emission $\chi(\mathbf{k})$ data sets, in the vertical $(\bar{1}1\bar{2})$ plane, via Method A. The bulk emitter site at the origin is indicated by dashed squares, and the positions of the scatterers are indicated by circles. The nearest and next-nearest scattering positions have been labeled in panel (a). Axes are marked off in 1Å units. Image intensities for $z \leq -1.5$Å have been rescaled, with the scale factors indicated on the figures. (a) Image reconstructed from the experimental $\chi(\mathbf{k})$ data set of Fig. 5.3(c). (b) Image reconstructed from a theoretical single scattering $\chi(\mathbf{k})$ data set. (c) Image reconstructed from a theoretical multiple scattering $\chi(\mathbf{k})$ data set.

Figure 5.7. As Fig. 5.6, but for the vertical $(\bar{1}10)$ plane.

Figure 5.8. As Fig. 5.6, but for the vertical (001) plane.

Figure 5.9. Simple $\frac{\bar{1}}{2}\frac{1}{2}\frac{1}{2}$ and $\frac{1}{2}\frac{1}{2}\frac{1}{2}$ forward-scattering W cluster, for which images have been derived as: (a) Atomic image obtained from a theoretical single scattering W 4*f* $\chi(\mathbf{k})$ data set calculated for this cluster, in the vertical $(\bar{1}10)$ plane, via Method A. The emitter site at the origin is indicated by dashed squares, and the positions of the scatterers are indicated by circles. Axes are marked off in 1Å units. Image intensities have been

rescaled relative to the same standard maximum in this panel (=1.0) for both Figs. 5.9 and 5.10, with the scale factors indicated. (b) As (a), but in the (001) plane and with a scale factor of 1.7.

Figure 5.10. As Fig. 5.9, but for a 100 and 010 forward-scattering W cluster. (a) Image in the vertical $(\bar{1}10)$ plane, with a scale factor of 3.0. (b) Image in the vertical (001) plane, with a scale factor of 1.8.

Figure 5.11. W(110) atomic images obtained in the vertical $(\bar{1}1\bar{2})$ plane from the experimental W 4*f* surface emission $\chi(\mathbf{k})$ data set of Fig. 5.2(c), via Methods $\tilde{A}$-D, as defined in the text. (a) Method $\tilde{A}$. (b) Method B. (c) Method C. (d) Method D. The surface emitter site at the origin is indicated by dashed squares, and the positions of the scatterers (assuming no surface relaxation) are indicated by circles. The nearest and next-nearest scattering positions have been labeled in panel (a). Axes are marked off in 1Å units. Image intensities for $z \leq -3.5$Å have been rescaled (with the exception of (d)), with the scale factors indicated on the figures.

Figure 5.12. W(110) atomic images obtained in the vertical $(\bar{1}10)$ plane from the experimental W 4*f* bulk emission $\chi(\mathbf{k})$ data set of Fig. 5.3(c), via Methods $\tilde{A}$-D. (a) Method $\tilde{A}$. (b) Method B. (c) Method C. (d) Method D. The bulk emitter site at the origin is indicated by dashed squares, and the positions of the scatterers are indicated by circles. The nearest and next-nearest scattering positions have been labeled in panel (a). Axes are marked off in 1Å units. Image intensities for $z \leq -1.5$Å have been rescaled, with the scale factors indicated on the figures.

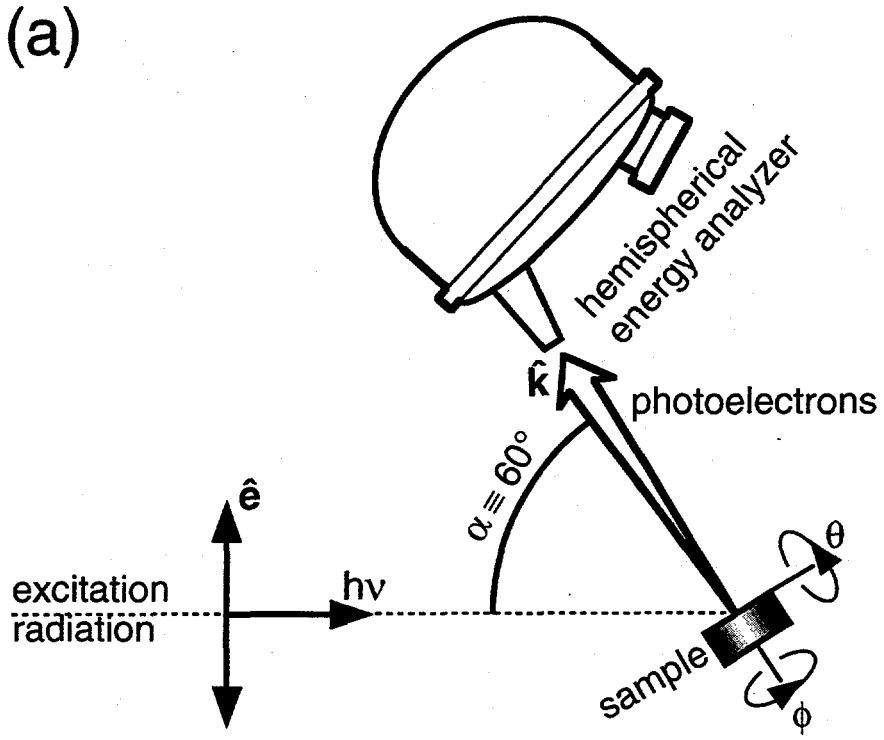

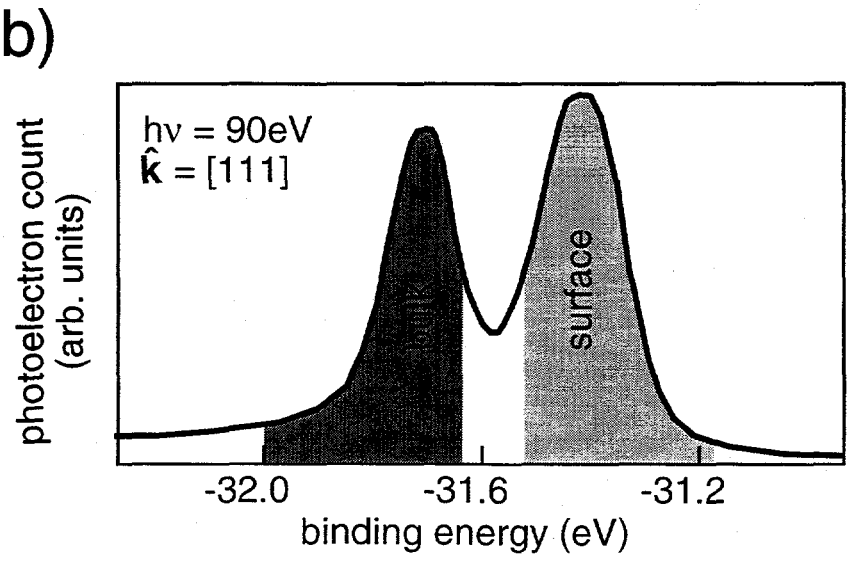

Fig. 5.1

5.2. Surface W$f_{7/2}$ photoelectron diffraction patterns

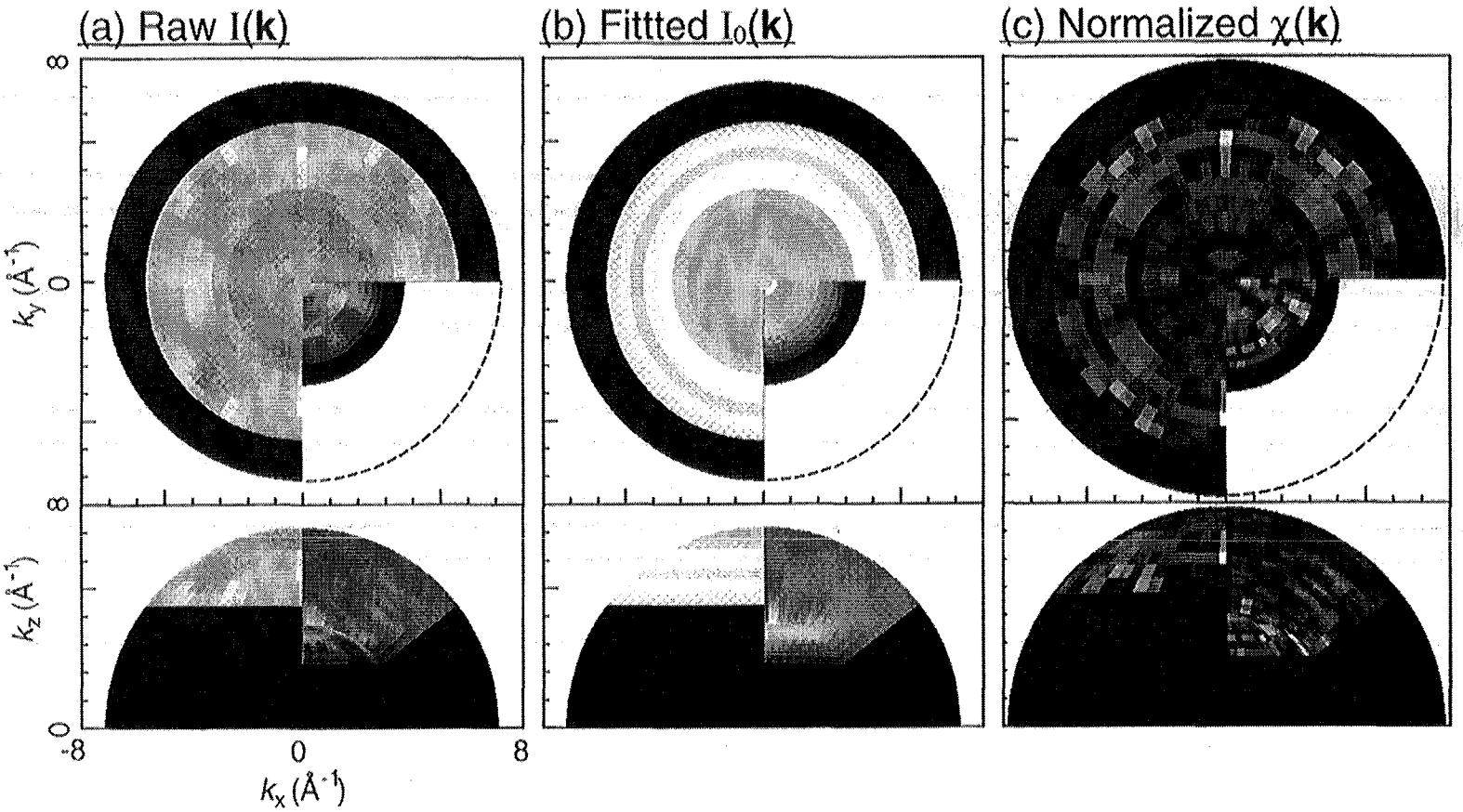

Fig. 5.2

5.3. Bulk W$f_{7/2}$ photoelectron diffraction patterns

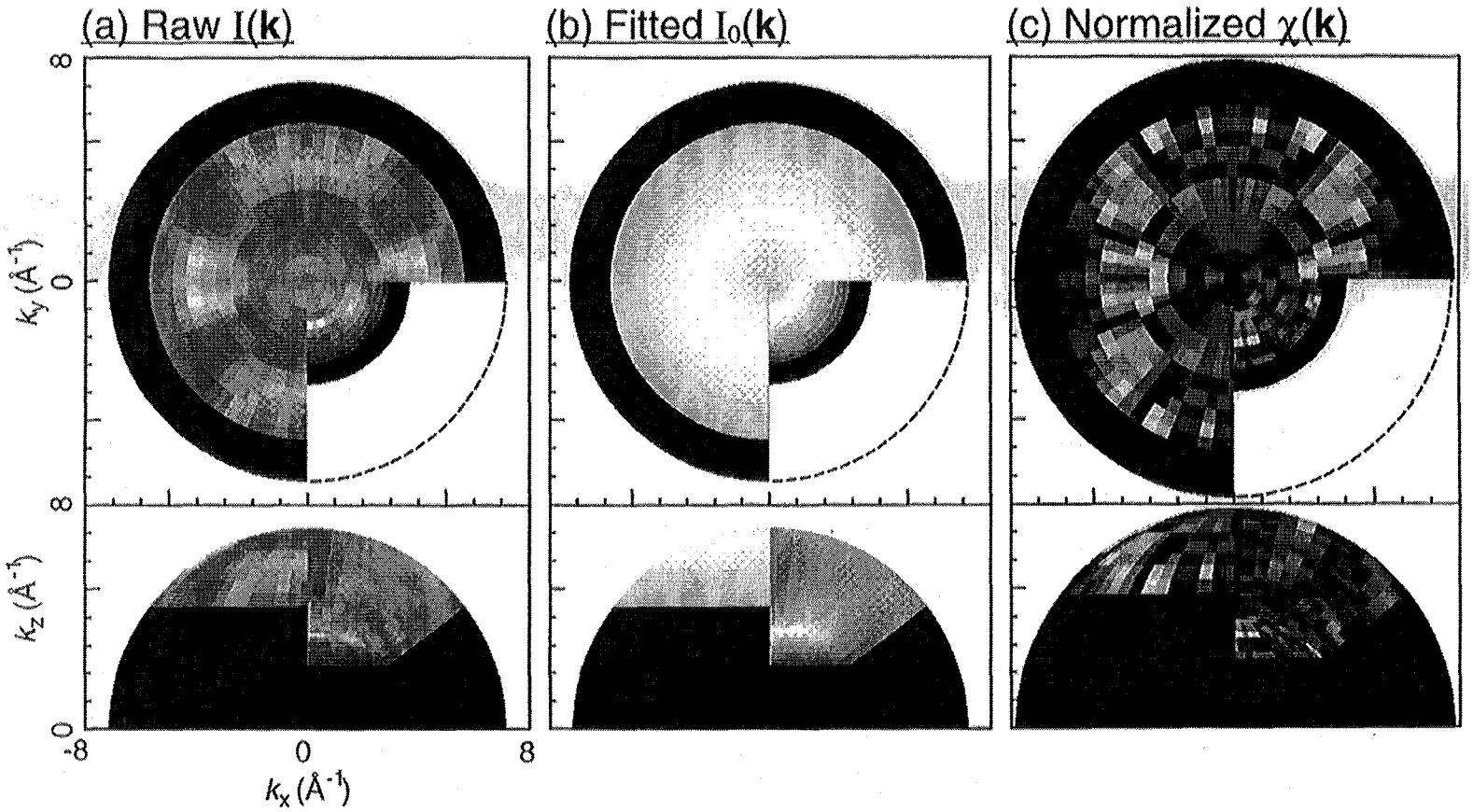

Fig. 5.3

(a) photoelectric cross sections $\frac{d\sigma(\alpha)}{d\Omega}$

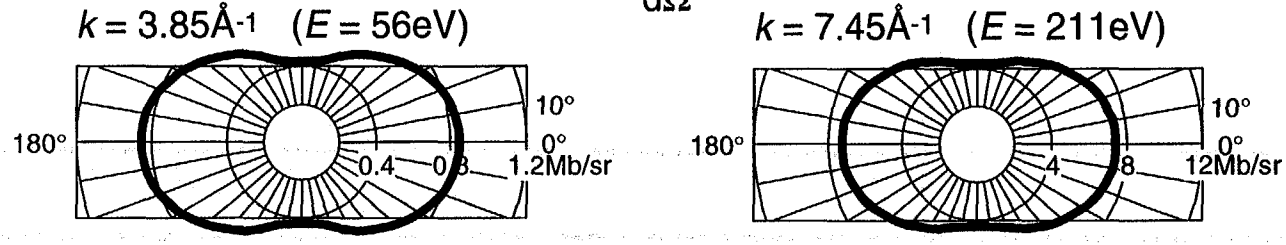

(b) scattering factor magnitudes $|f(\Theta)|$

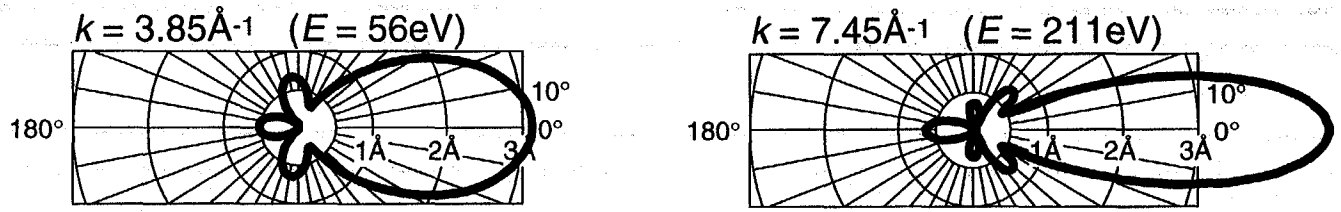

(c) scattering factor phases $\psi(\Theta)$

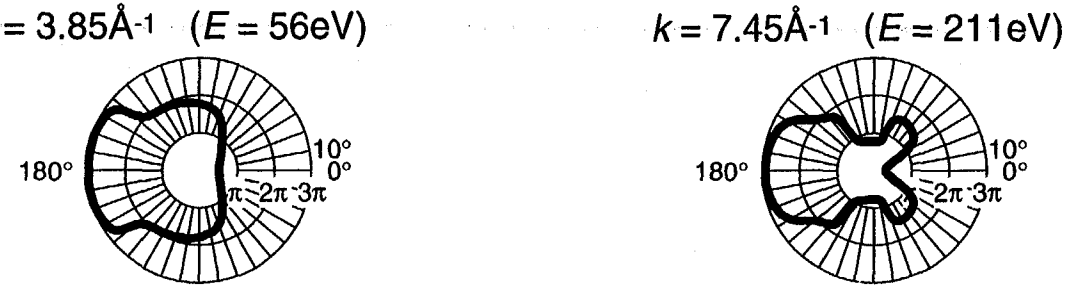

Fig. 5.4

5.5. Method A, $(\bar{1}1\bar{2})$ cut, surface emitter site

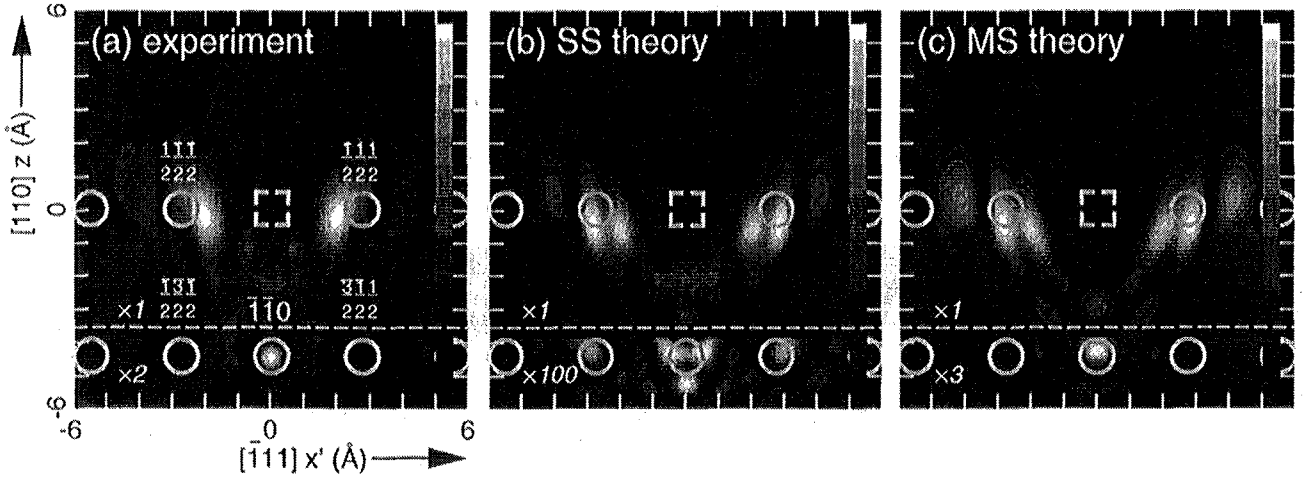

5.6. Method A, $(\bar{1}1\bar{2})$ cut, bulk emitter site

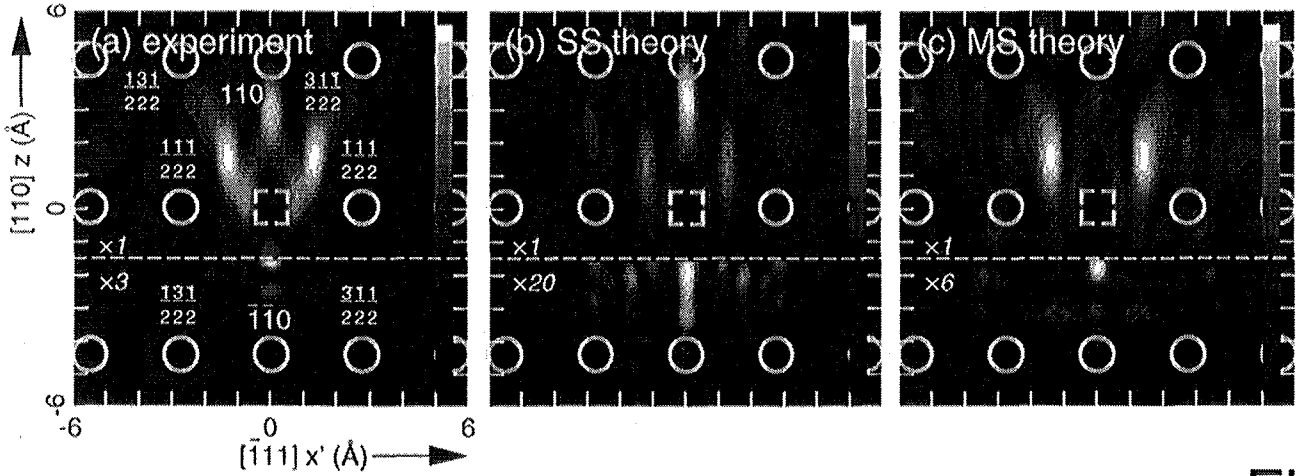

Figs. 5.5-5.6

5.7. Method A, ($\bar{1}10$) cut, bulk emitter site

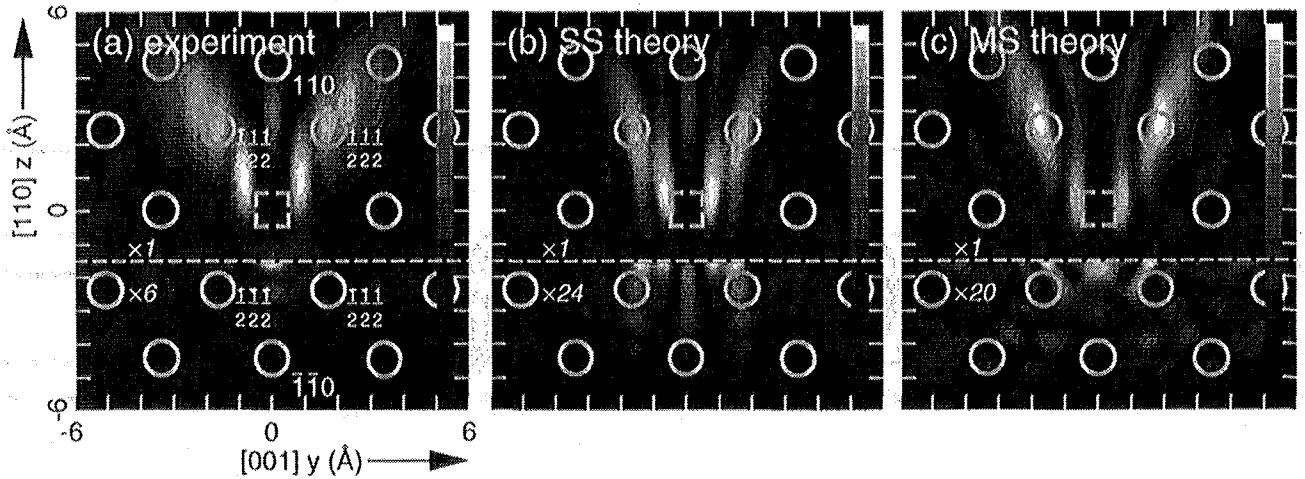

5.8. Method A, (001) cut, bulk emitter site

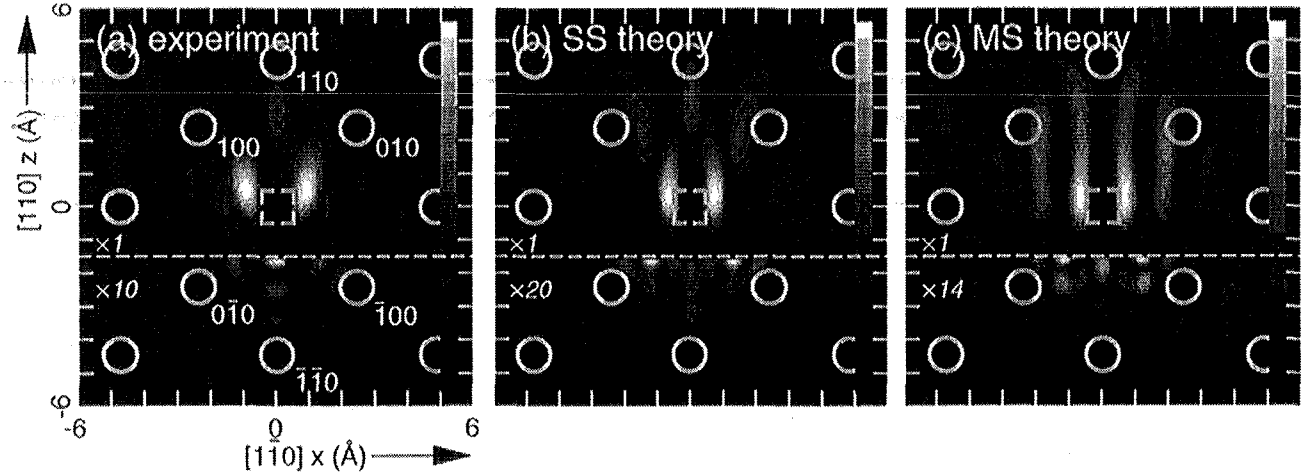

Figs. 5.7-5.8

5.9. Method A, ($\bar{1}10$) plane FS, SS theory

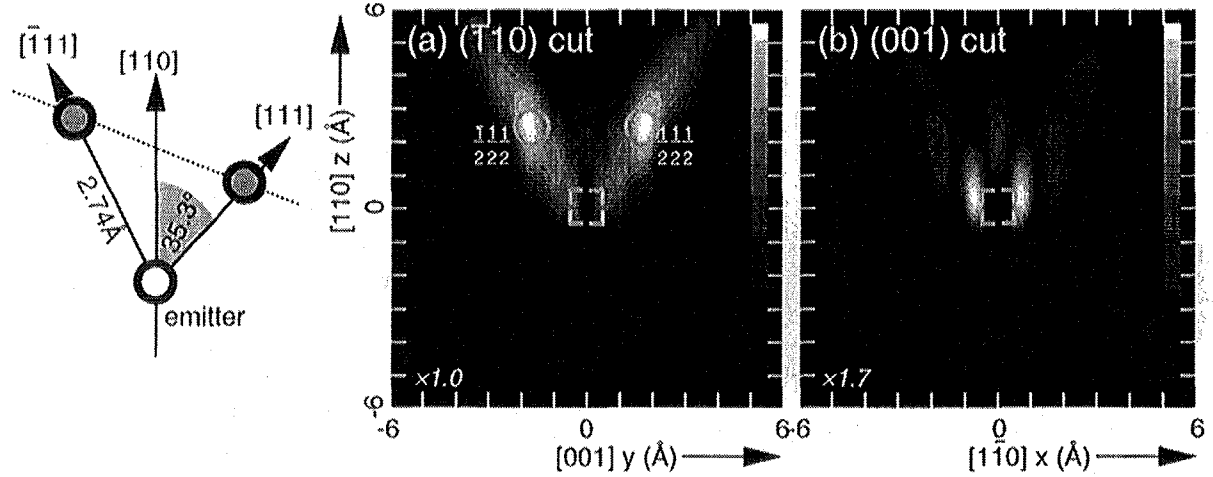

5.10. Method A, (001) plane FS, SS theory

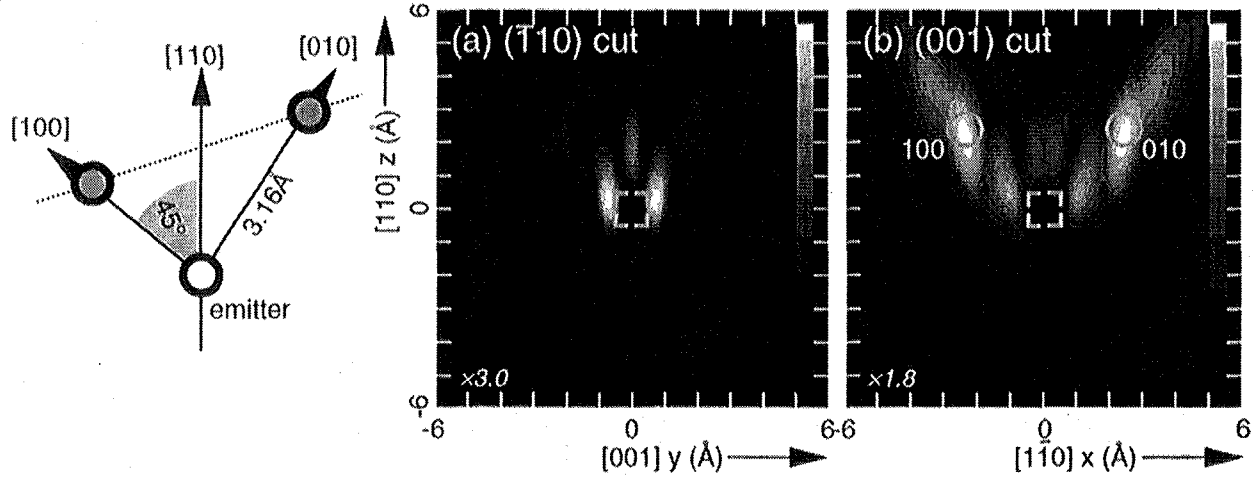

Figs. 5.9-5.10

5.11. Experiment, $(\bar{1}12)$ cut, surface emitter site

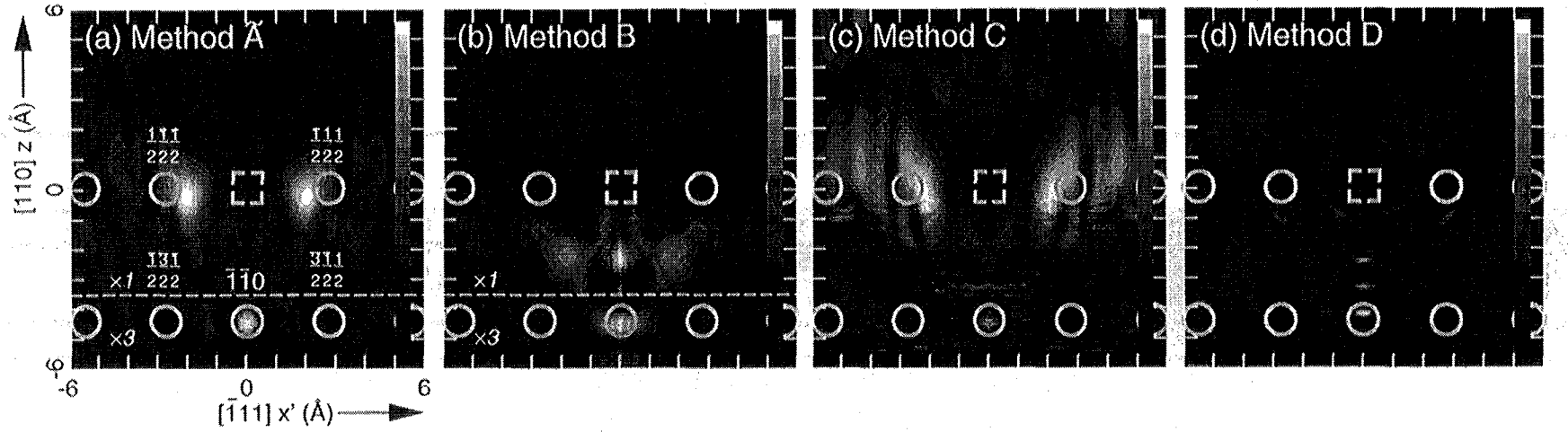

5.12. Experiment, $(\bar{1}10)$ cut, bulk emitter site

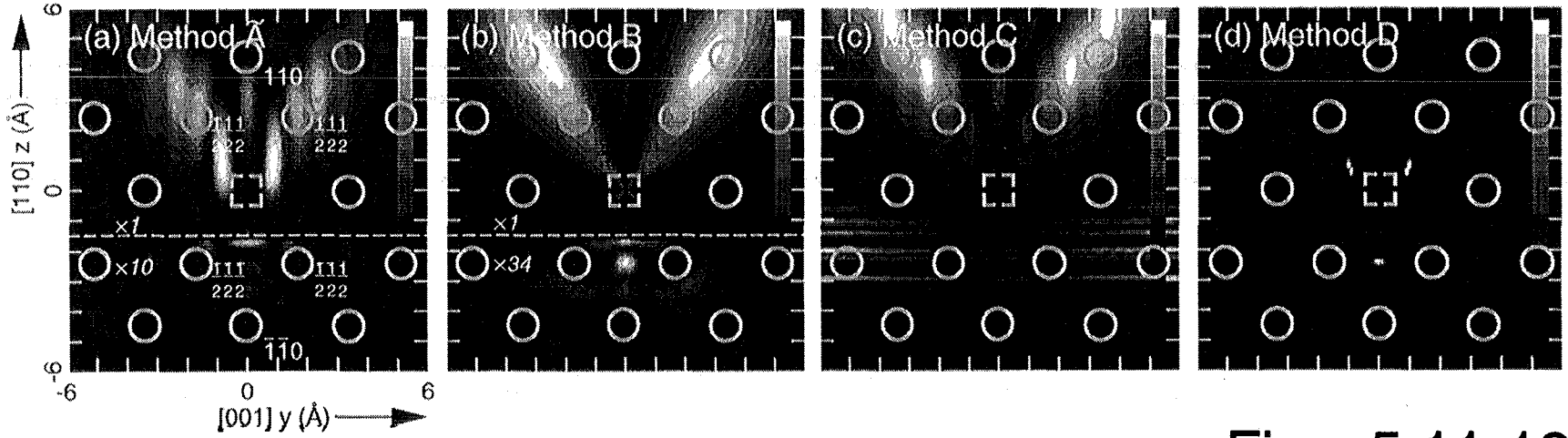

Figs. 5.11-12

Chapter 6

Atomic Imaging by X-Ray Fluorescence Holography: A Theoretical Study

Abstract

We consider from a theoretical viewpoint the direct imaging of atoms by x-ray fluorescence holography (XFH) and compare it to its close relative photoelectron holography (PH). We review the relationship of XFH, ideally a probe of *short-range* atomic structure, with other types of elastic/inelastic and/or incident/fluorescent x-ray scattering probes of *long-range* ordered atomic structure. The more ideal nature of x-ray scattering makes XFH atomic images superior to single-wavenumber PH atomic images. The overlap of real and twin features for pairs of atoms at certain inversion related positions $\pm\mathbf{a}$ can cause their XFH or PH atomic images to cancel for certain combinations of wavenumbers k and emitter-scatterer distances $|\mathbf{a}|$, but using multiple wavenumber holography is found to solve this problem. The relative merits of photoelectron and fluorescent x-ray holography for structure studies are considered.

Outline

6.1 Introduction

In 1948 Gabor proposed holography as a means to circumvent the current limitations of electron microscopy [6.1], where not only intensities but the phases of diffracted wavefronts can be recorded as referenced to an unscattered direct wavefront. Szöke in 1985 then observed that the interference patterns produced in the emission of photoelectrons or characteristic x-rays from localized core levels could be thought of as holograms [6.2]. The unscattered photoelectron or x-ray component from an emitting atom that reaches a distant detector is in this case considered to be the holographic reference wave, while the components that scatter from neighboring atoms before reaching the detector are the object waves. The interference pattern created by the reference and object waves is then a photoelectron hologram (PH), or an x-ray fluorescence hologram (XFH) [6.3, 6.4]. The first experiments to record such single-wavenumber holographic photoelectron [6.5-6.7], or fluorescent x-ray [6.8] intensities, and reconstruct images of the immediate atomic environment surrounding each (equivalent) emitting site have made use of a simple numerical algorithm derived from the Helmholtz-Kirchhoff theorem, as first discussed by Barton [6.9]:

$$U_A^k(\mathbf{r}') = \iint_S d\sigma_{\hat{\mathbf{k}}} e^{-i\mathbf{k}\cdot\mathbf{r}} \chi(\mathbf{k}), \tag{6.1}$$

where $U_A^k(\mathbf{r}')$ is the image of the atomic scatterers as evaluated at position $\mathbf{r}'$, $d\sigma_{\hat{\mathbf{k}}} \equiv \cos\theta d\theta d\phi$ is the solid-angle integration increment, $\chi(\mathbf{k})$ is the normalized interference pattern $= [I(\mathbf{k}) - I_0(\mathbf{k})]/\sqrt{I_0(\mathbf{k})}$. $I_0(\mathbf{k})$ is the reference wave intensity in the absence of any scattering, $\hat{\mathbf{k}} \equiv \mathbf{k}/|\mathbf{k}|$ is the direction of the emission wavevector, and the integral is over the $\mathbf{k}$-space surface of constant wavenumber $k = |\mathbf{k}|$ for which holographic intensities have been measured. In finally representing images, it is the absolute value of $U_A^k(\mathbf{r}')$ that is always used. For holographic electron diffraction, one may easily record intensities at many different wavenumbers k, such that the $\chi(\mathbf{k})$ data set

will span a volume in **k**-space. The imaging from such a **k**-space volume $\chi(\mathbf{k})$ is then a phased summation of images reconstructed from different wavenumber $\chi(\mathbf{k})$ holograms, as first suggested by Barton [6.9b] and in a slightly different form by Tong *et al.* [6.9c]. This imaging algorithm is then identical to Eq. (1.9) [6.9b, 6.9c]:

$$\begin{aligned} U_A(\mathbf{r}') &= \int_k k^2 dk \cdot e^{ikr'} U_A^k(\mathbf{r}') \\ &= \iiint_K d^3\mathbf{k} \cdot e^{-i(\mathbf{k}\cdot\mathbf{r}'-kr')} \chi(\mathbf{k}). \end{aligned} \tag{6.2}$$

In this study, we first compare XFH to other structural methods making use of x-ray scattering, and then carry out theoretical calculations of both XFH and PH diffraction patterns and their resulting images. This work represents an expansion of a shorter study that has already been published [6.4].

6.2 Relationship of XFH to other x-ray structural probes

XFH is related to several previously implemented probes of atomic structure that use elastically or inelastically scattered incident and/or fluorescent x-rays [6.3, 6.10]. The earliest use of x-rays to probe atomic structure is the recording of the intensities of x-rays elastically scattered from Bragg planes of crystals with *long-range* order [6.11] (Fig. 6.1(a)). However, the atomic structure of non-trivial unit cells cannot be unambiguously determined unless the phase of the reference wave compared to the scattered waves is known, such that in this method the phase must be deduced analytically [6.12], or the interference effect of multiple incident x-ray beams must be exploited [6.13, 6.14].

Bragg-plane scattering of atomic fluorescence results in Kossel line patterns [6.15] (Fig. 6.1(b)). Since an unscattered wavefront interferes with the Bragg-plane scattered wavefronts in the far-field, the diffracted wavefront phases are then referenced to the direct wavefront, and atomic structure in an equivalent unit cell can subsequently be determined [6.16]. The method of x-ray standing waves (XSW) has also been used to

determine atomic structure [6.17], and this method is closely related to Kossel lines in a time-reversed sense in that x-rays of arbitrary energy Bragg scatter from planes so as to create a standing wave (Fig. 6.1(c)). Fluorescence radiation is used to detect the maxima and minima in the standing wave, and thus determine atomic positions. Due to the long attenuation lengths of x-rays, the use of Kossel lines or XSW are probes of *long-range* ordered samples, as manifested by sharp Bragg-like interference effects in the outgoing fluorescence x-ray pattern, or sharp rocking curve profiles in XSW.

Figure 6.1(d) illustrates another method of x-ray resonant inelastic scattering (XRIS), where an incident x-ray beam whose energy is just above the absorption edge of the atomic species of the sample coherently excites Bragg planes of fluorescing atoms, with the intermediate electronic state having delocalized valence character [6.18]. The interference between the fluorescence from each emitting site is coherent due to the short lifetime of the core hole for excitation energies just above the fluorescence edge and the delocalized nature of the intermediate state. Thus no phase information is easily gained in this method, although valuable band structure information can be deduced from the momentum transfer equation involving both Bragg and energy excitation conditions.

Figure 6.1(e) illustrates yet another method for using x-rays to probe atomic structure: the interference of unscattered fluorescent or radioactive electron-capture x-rays from an ordered molecular film (*e.g.* a Langmuir-Blodgett film) with a wavefront that is totally externally reflected from a bulk substrate in a so-called Lloyd's Mirror configuration [6.19]. A standing wave is also created in this sort of experiment, but the direct or reference wave is now directly involved. However, while this interference is holographic in that phase information of the totally externally reflected wavefront is referenced to the direct wavefront, only macroscopic structural information regarding the film-substrate spacing ($10^2 - 10^3$ Å) is obtained in this method.

For nearly perfect crystals, XFH (Fig. 6.1(f)) is merely the equivalent of imaging Kossel line intensities using Eq. (6.1). However, as seen in the atomic imaging of

holographic electron intensities, due to the short attenuation length of electrons, Eqs. (6.1) and (6.2) are ideally suited for probing *short-range* atomic order surrounding each emitter species. Thus *long-range atomic order is not a condition necessary* for the implementation of atomic imaging via XFH. *Short-range* atomic order in XFH can be imaged by either recording holographic fluorescent $\chi(\mathbf{k})$ intensities from mosaic and dilute samples (*i.e.*, structures with no long-range order) as shown in Fig. 6.1(f), or by applying Eq. (6.1) to only the lower-frequency **k**-space components in $\chi(\mathbf{k})$ intensities measured from long-range ordered samples [6.3].

6.3 Comparison of atomic images

We first carry out a comparison of theoretical single-wavenumber photoelectron holography [6.20] and XFH atomic images in the same short-range-order domain.

Figure 6.2 schematically shows the clusters considered in this work. A planar cluster of 49 Mo atoms with an emitter at its 2D center simulates a domain of short-range order on a Mo(001) surface (Fig. 6.2(a)), and a much larger 68,705 atom Mo(001) bcc cluster with an emitter at its 3D center simulates a bulk domain of more long-range order (Fig. 6.2(b)). Ideally, due to the long attenuation length of x-rays ($\approx \mu m$), a cluster several orders of magnitude larger than that of Fig. 6.2(b) should be considered, but as discussed previously [6.3] and further below, a $10^4 - 10^5$ atom cluster will already give a good indication of the concerns involved in the case of nearly perfect or mosaic crystals (or other systems without long-range order), without making the calculation of holographic $\chi(\mathbf{k})$ intensities prohibitively time-consuming.

Figure 6.3 compares the magnitudes ($|f(\Theta)|$) and phases ($\psi(\Theta)$) of the complex scattering factors $f(\Theta) \equiv |f(\Theta)|e^{i\psi(\Theta)}$ for electrons and x-rays of the same wavenumber ($k = 10.1\text{Å}^{-1}$), corresponding to electrons with a kinetic energy of 391eV, and x-rays at an energy of 20keV (very near the Mo Kβ energy of 19.6keV). The scattering factor for electrons was computed from muffin-tin partial-wave phase shifts using a spherical-wave

method [6.20]; that for x-rays was calculated from standard tables of the quantity $f(\Theta) \equiv f_0(\Theta) + \Delta f_1 + i\Delta f_2$ as a function of scattering angle Θ and wavelength λ through $(\sin\Theta / \lambda)$ [6.21] to yield both a magnitude $|f(\Theta)|$ and phase $\psi(\Theta)$. Figure 6.3(a) shows that both electron and x-ray scattering factors have maximum magnitudes in the forward direction, but x-ray scattering is relatively more isotropic in that there are no nodes, and is for this case about $10^3 \times$ lower in magnitude than that for electrons. Figure 6.3(b) shows that the x-ray scattering phase shift is negligible when compared to that for electrons, however both depend strongly on the scattering direction. The only expected disadvantage of using x-rays is therefore that the magnitude of the scattering factor will be about 10^3 to 10^4 times lower for a given wavenumber, leading to similarly reduced fractional diffraction anisotropies $\Delta I / I_0 \equiv (I_{max} - I_{min}) / I_0$, where I_0 is the intensity that would be measured in the absence of atomic scattering (*i.e.*, the reference wave).

Holographic photoelectron (Fig. 6.4(a)) and fluorescent x-ray $\chi(\mathbf{k})$ intensities (Fig. 6.5(a)) were first calculated on a $1° \times 1°$ grid in polar and azimuthal angles for emission from the 49-atom Mo(001) planar cluster of Fig. 6.2(a). To permit direct comparison of image quality and resolution, the electron and x-ray emission processes have both been assumed to generate reference waves with *s*-character outgoing from the emitter, and have also been chosen to have the same wavenumber of $k = 10.1 Å^{-1}$. Exponential attenuation due to inelastic scattering of electrons or absorption of x-rays for propagation within the cluster has also been incorporated, with decay lengths of 7.6Å for electrons and 5×10^{-5} Å for x-rays. Attenuation is thus taken to be isotropic in space, an assumption that is expected to be fully valid in this short-range-order limit, as verified for example in prior studies of photoelectron and low-energy electron diffraction studies [6.20, 6.22], and of the absorption and transmission of x-rays in samples without long-range order [6.23]. The $\chi(\mathbf{k})$ intensities of Figs. 6.4(a) and 6.5(a) contain similar **k**-space frequency components, due to the same wavenumber of the respective direct and scattered wavefronts. But due to the greater angular anisotropy of the scattering factor magnitude

and phase of electrons, the pattern in the holographic photoelectron $\chi(\mathbf{k})$ intensities of Fig. 6.4(a) is not as isotropic as in the holographic fluorescent $\chi(\mathbf{k})$ intensities of Fig. 6.5(a). Also, as expected from the relative scattering strengths of electrons and x-rays (Fig. 6.3(a)), the anisotropy $\Delta I / I_0$ is 28% for the photoelectron $\chi(\mathbf{k})$ hologram of Fig. 6.4(a), and 0.28% for the fluorescent x-ray $\chi(\mathbf{k})$ hologram of Fig. 6.5(a).

Atomic images reconstructed from these calculated $\chi(\mathbf{k})$ intensities using Eq. (6.1) are shown in Figs. 6.4(b) and 6.5(b). As expected from prior studies [6.5-6.7], the photoelectron atomic image peaks in (Fig. 6.4(b)) are within 0.5Å of their true atomic positions; however, the XFH image peaks (Figs. 6.5(b)) are much more accurately located, to within 0.1Å or less. Also, the XFH images do not have the characteristic elongations and satellite features that are present in those of Fig. 6.4(b) and other single-wavenumber photoelectron images [6.5-6.7]. These differences in image quality are expected in view of the much more ideal nature of x-ray scattering from atoms, where the absence of nodes in the scattering factor magnitude, together with the absence of an appreciable phase shift (*cf.* Fig. 6.3). Thus in the same short-range order domain, XFH atomic images are much more accurate than photoelectron holographic atomic images.

In order to illustrate what can be expected in more realistic simulations of XFH experiments, we now consider the atomic images obtained from the larger Mo cluster with more long-range order. Figure 6.6(a) shows the fluorescent x-ray $\chi(\mathbf{k})$ intensities calculated on a $1° \times 1°$ grid in polar and azimuthal angles for emission from the 68,705-atom Mo(001) bcc cluster of Fig. 6.2(b). As expected, the angular features of the $\chi(\mathbf{k})$ intensities begin to sharpen as a result of the larger size of the cluster; these features would result in Kossel lines if the size of the cluster were to approach the volume of a nearly perfect crystal that would be probed without appreciable attenuation ($\approx \mu m^3$) [6.3], and such features in fact are beginning to appear as fine regular arcs and lines in Fig. 6.6(a). Such fine angular features from long-range ordered samples could make it difficult to determine via Eq. (6.1) the short-range order atomic structure surrounding each

(equivalent) emitter site, as the data density of the $\chi(\mathbf{k})$ hologram would increase beyond reasonable sampling densities of the 2π solid angle above the sample [6.3].

Figure 6.6(b) shows the atomic image reconstructed from the $\chi(\mathbf{k})$ intensities of Fig. 6.6(a) using Eq. (6.1). The nearest neighbor atoms at $(x,y) = (0.0\text{Å}, \pm 3.15\text{Å})$ and $(\pm 3.15\text{Å}, 0.0\text{Å})$ are distinct, although coarse-sampling noise begins to wash out the image peaks of atoms farther away from the emitter [6.25]. For a larger cluster simulating a more nearly perfect crystal, this noise might overwhelm even the nearest neighbor atomic images, as their lower-frequency $\chi(\mathbf{k})$ intensities would become less visible compared to the sharp Kossel features arising from dynamical Bragg-plane scattering [6.3]. If atomic images are to be obtained for such a long-range sample, Tegze and Faigel have proposed a Gaussian convolution in **k**-space as a low-pass filter to extract the lower frequency $\chi(\mathbf{k})$ features that correspond to holographic information of the scatterers nearer to the emitter. In this approach, the higher frequency $\chi(\mathbf{k})$ features would be removed, suppressing the presence of scatterers more distant from emitter [6.3]:

$$\tilde{\chi}(\mathbf{k}) = \frac{\iint_S d\sigma_{\hat{\mathbf{k}}'} e^{-\sigma^2(\mathbf{k}-\mathbf{k}')^2} \chi(\mathbf{k}')}{\iint_S d\sigma_{\hat{\mathbf{k}}'}}, \tag{6.3}$$

where $\tilde{\chi}(\mathbf{k})$ is the resulting low-pass filtered holographic intensity data set.

Figure 6.7(a) shows the low-pass filtered $\tilde{\chi}(\mathbf{k})$ intensities obtained from the $\chi(\mathbf{k})$ intensities of Fig. 6.6(a) using the Gaussian convolution of Eq. (6.3), but with allowance also for the expected degree of statistical scatter in intensities in a real experiment. In order to realistically simulate conditions in an XFH experiment, the smoothed $\tilde{\chi}(\mathbf{k})$ intensities of Fig. 6.7(a) have been mapped from the density of Fig. 6.6(a) onto a $3° \times 3°$ grid to reduce the number of measurements (3600 total), and statistical noise corresponding to 10^9 counts per data point (*i.e.*, a standard deviation of $1{:}10^{4.5}$) was

added. This simulated experimental uncertainty accounts for the lack of symmetry in the $\tilde{\chi}(\mathbf{k})$ intensities of Fig. 6.7(a), as no symmetry mapping or reflections were used.

The atomic image obtained from these $\tilde{\chi}(\mathbf{k})$ intensities via Eq. (6.1) is shown in Fig. 6.7(b). The nearest-neighbor atomic peaks are still discriminated against the background noise, despite the coarser angular steps and statistical noise included in the $\tilde{\chi}(\mathbf{k})$ data set of Fig. 6.7(a). Thus we have validated that short-range order atomic structure can be extracted and imaged from holographic fluorescent x-ray intensities measured from long-range order samples[6.4], as has now been demonstrated experimentally [6.8].

6.4 Image cancellation due to real-twin image overlap

An additional important effect in the quantitative analysis of *all* images reconstructed from single-wavenumber $\chi(\mathbf{k})$ intensities is seen in our results--for certain choices of wavelength and atomic positions, the images of certain symmetry-related pairs of scattering atoms are strongly suppressed. An example of this effect can be seen in Fig. 6.4(b) by comparing the relative strengths of features due to different scatterers near the emitter: note the missing atomic images in XFH at $(x,y) = (0.0\text{Å}, \pm 9.45\text{Å})$ and $(\pm 9.45\text{Å}, 0.0\text{Å})$. This image cancellation was first qualitatively discussed by Tegze and Faigel [6.3] for XFH, and more quantitatively considered by the author and collaborators [6.4], and is due to the overlap of the complex conjugate real and twin images for atomic pairs located at $\mathbf{r} = \pm\mathbf{a}$.

This image cancellation can be quantitatively understood in general for both photoelectron and fluorescent x-ray holograms by applying the algorithm of Eq. (6.1) to a pair of scattering atoms situated at $\mathbf{r} = \pm\mathbf{a}$ in the (001) plane. We also assume that these two atoms are illuminated equally by the reference wave (as is the case with our previous assumption of *s*-character). The reconstructed image at $\mathbf{r}'$ of a *single* atomic scatterer located at $\mathbf{r} = +\mathbf{a}$ can then be written in a single scattering picture as [6.20]:

$$U_A^k(\mathbf{r}') \propto \iint_S d\sigma_{\hat{\mathbf{k}}} \left[f_k^*(\Theta_{+\mathbf{a}}^{\mathbf{k}}) e^{-ika} e^{i\mathbf{k}\cdot(\mathbf{a}-\mathbf{r}')} + f_k(\Theta_{+\mathbf{a}}^{\mathbf{k}}) e^{ika} e^{i\mathbf{k}\cdot(-\mathbf{a}-\mathbf{r}')} \right], \tag{6.4}$$

where the f_k's are atomic scattering factors for the wavenumber k, and $\Theta_{+\mathbf{a}}^{\mathbf{k}}$ is the scattering angle between $+\mathbf{a}$ and $\mathbf{k}$. The first term contributes to the real image at $\mathbf{r}' = +\mathbf{a}$, and the second term to the twin image at $\mathbf{r}' = -\mathbf{a}$. As |a| varies for a given k, the image function $U_A^k(\mathbf{r}')$ thus oscillates between being pure real and pure imaginary due to the phase factors $e^{\pm ika}$ associated with path length differences. For a *pair* of scattering atoms at $\pm\mathbf{a}$ (Fig. 6.8(a)), the atomic image at the special point $\mathbf{r}' = +\mathbf{a}$ is thus the superposition of the actual image from the $+\mathbf{a}$ atom and the twin image from the $-\mathbf{a}$ atom:

$$U_A^k(\mathbf{r}') \propto e^{-ika} \iint_S d\sigma_{\hat{\mathbf{k}}} f_k^*(\Theta_{+\mathbf{a}}^{\mathbf{k}}) + e^{ika} \iint_S d\sigma_{\hat{\mathbf{k}}} f_k(\Theta_{-\mathbf{a}}^{\mathbf{k}}), \tag{6.5}$$

where $\Theta_{-\mathbf{a}}^{\mathbf{k}}$ $(= \pi - \Theta_{+\mathbf{a}}^{\mathbf{k}})$ is the angle between $-\mathbf{a}$ and $\mathbf{k}$. For such a pair of equally-illuminated scatterers in a plane perpendicular to the symmetry axis of the hologram, we further note that

$$\iint_S d\sigma_{\hat{\mathbf{k}}} f_k(\Theta_{+\mathbf{a}}^{\mathbf{k}}) = \iint_S d\sigma_{\hat{\mathbf{k}}} f_k(\Theta_{-\mathbf{a}}^{\mathbf{k}}). \tag{6.6}$$

Then the image at $\mathbf{r}' = +\mathbf{a}$ of the $\pm\mathbf{a}$ pair becomes

$$U_A^k(\mathbf{r}' = +\mathbf{a}) \propto \cos(ka) \iint_S d\sigma_{\hat{\mathbf{k}}} \operatorname{Re}\left[f_k(\Theta_{+\mathbf{a}}^{\mathbf{k}}) \right] - \sin(ka) \iint_S d\sigma_{\hat{\mathbf{k}}} \operatorname{Im}\left[f_k(\Theta_{+\mathbf{a}}^{\mathbf{k}}) \right]. \tag{6.7}$$

There can thus be values of ka such that the image at $\mathbf{r}' = +\mathbf{a}$ disappears, with the general condition for image cancellation being:

$$\tan(ka) = \frac{\iint_S d\sigma_{\hat{\mathbf{k}}} \, \mathrm{Re}\left[f_k(\Theta^{\mathbf{k}}_{+\mathbf{a}})\right]}{\iint_S d\sigma_{\hat{\mathbf{k}}} \, \mathrm{Im}\left[f_k(\Theta^{\mathbf{k}}_{+\mathbf{a}})\right]} \tag{6.8}$$

In the case of x-ray scattering, $\mathrm{Im}\left[f_k(\Theta^{\mathbf{k}}_{+\mathbf{a}})\right] \approx 0$ (*cf.* Fig. 6.3(b)), so the cancellation condition (Eq. (6.7)) can be simplified to $ka = \pi(2m+1)/2$, with m equal to some non-zero integer. So when $|\mathbf{a}| = \lambda(2m+1)/4$, pairs of atoms at $\pm\mathbf{a}$ cannot be imaged. The missing atomic images in Figs. 6.5(b) are in fact found to correspond to the cancellation condition for $m = 30$.

Figures 6.8(b)-(d) shows image intensities $\left|U^k_A(\mathbf{r}' = +\mathbf{a})\right|$ as a function of $|\mathbf{a}|$ for the three-atom cluster in Fig. 6.8(a). The expected sinusoidal dependence of the XFH image intensities is apparent in Fig. 6.8(c), for which the minima can be well predicted from $ka = \pi(2m+1)/2$. For electrons (Fig. 6.8(b)) emitted at the same wavelength from the same cluster, the same effects are clearly seen also, although the cancellation minima of the atomic peaks are masked by the broad satellite images that surround them (*cf.* Fig. 6.4(b)).

Such suppression of certain peaks could make the relative intensities in holographic images difficult to interpret for high-symmetry experimental geometries such as that considered here. However, this undesirable real-twin interference may be partially remedied by breaking the symmetry conditions leading to Eq. (6.5), for example, by using only a selected part of the full 2π hologram solid angle above the bulk surface [6.6], or by orienting the exciting polarization vector in photoelectron holography so that the atoms at $\pm\mathbf{a}$ are inequivalent in their illumination by the outgoing reference wave. A more general and complete solution is to remove twin images by using a phased summation of different wavenumber image reconstructions [6.9(b)], as in Eq. (6.2). To illustrate how the latter would function, we insert Eq. (6.5) into Eq. (6.2) and find in the limit of an integral over continuously-distributed k values:

$$U_A(\mathbf{r}' = +\mathbf{a}) = \int_k k^2 dk \iint_S d\sigma_{\hat{\mathbf{k}}} f^*_k(\Theta^{\mathbf{k}}_{+\mathbf{a}}). \tag{6.9}$$

Here, image cancellation is seen to be eliminated, as the twin image term proportional to $f_k(\Theta^{\mathbf{k}}_{-\mathbf{a}})$ in Eq. (6.5) does not survive the integration on wavenumber k. To assess the behavior of such images for the practical case of summations over a finite k range and finite n, we show in Fig. 6.8(d) a series of calculations. The solid curve represents the photoelectron holography image magnitude $\left|U^k_A(\mathbf{r}'=+\mathbf{a})\right|$ as a function of $|\mathbf{a}|$, as obtained from Eq. (6.7), which idealizes the cancellation of photoelectron holography atomic images, and thus does not include the presence of satellite features. Also shown are broken curves representing phased summations $\left|U_A(\mathbf{r}'=+\mathbf{a})\right|$ from Eq. (6.2) of various numbers n of different wavenumber reconstructions, all with $k_{min} = 10.1\text{Å}^{-1}$, and a numerical integration increment $\delta k = 0.3\text{Å}^{-1}$. After phase-summing just two different wavenumber reconstructions, there is no longer complete suppression of image peaks. Increasing the number of reconstructions in the sum gradually removes the modulation of the image intensity, and by n = 10-15 wavenumber images, the image suppression is reduced to an acceptable level.

Note that while phased summing would also in principle remove the cancellation effect in XFH images (as well as other image aberrations due to twins and multiple scattering [6.9(b)]), it would not be experimentally feasible to carry out using only the scattering of fluorescence radiation. That is, the number and spacing of different wavenumber reconstructions available would be severely limited by the characteristic fluorescence energies of the emitting atom. In Auger electron holography, a similar limitation would apply. But in photoelectron holography [6.26-6.31], back-scattered Kikuchi electron holography [6.32], or the holographic analysis of elastic diffuse low energy electron diffraction [6.33], simply varying photon energy or incident electron energy should permit such summations over a sufficient number of different wavenumber holograms. And in another more recently suggested variant of x-ray holography which is the time-reversed version of XFH shown in Fig. 6.1(f), it should also be possible to

continuously vary the exciting x-ray energy so as to achieve multiple wavenumber holographic images with minimal image cancellation effects [6.34]. This method has been termed multiple-energy x-ray holography (MEXH) and it is discussed in detail in Chapters 7-8.

6.5 Concluding Remarks

In conclusion, the weaker, more isotropic scattering of x-rays causes XFH reconstructions to yield significantly better atomic images than those of holographic photoelectron reconstructions. At comparable wavelengths, XFH images should be approximately an order of magnitude more accurate than those of photoelectrons, yielding atomic positions to within 0.1Å or less, and they should be much less troubled by image distortions and satellites. The much greater attenuation lengths of x-rays (5×10^5 Å, compared to 7.6Å for electrons in the Mo case considered here) would in general make XFH more of a bulk and long-range-order probe. However, probing short-range order should be possible by using some sort of low-frequency filter such as the Gaussian deconvolution of Eq. (6.3), or applying XFH to atoms in a mosaic crystal or a thin adsorbed or epitaxial overlayer with limited domain sizes, and/or carrying out measurements in a grazing emergence condition. Although the much weaker scattering of x-rays will reduce relative effects by 10^3-10^4 times, it is nonetheless of interest to further explore XFH experimentally in the future, combining high-brightness synchrotron radiation (SR), or a free-electron laser (FEL) for excitation with some form of multichannel detection to shorten data acquisition times relative to the first experimental implementation of XFH, which was performed with a standard x-ray tube and a single solid-state detector [6.8]. The 10^9 statistics used in arriving at Fig. 1(d) also make it appear that such data is feasible to obtain in a reasonable time of several days with parallel detection and an x-ray wiggler or undulator for excitation. For example, it should be possible to achieve *at least* a count rate per 3° × 3° channel of about $150,000s^{-1}$ (the

maximum that can be handled by current semiconductor detectors) and this yields ≈ 1.9 hrs/emission direction. With ≈ 450 emission directions in the symmetry-reduced 1/8th of the hologram that would need to be covered for the case considered here, this yields a total time of 833 hrs = 35 days. However, using multichannel semiconductor detection could reduce this by 5-20 times, if not more. The energy tunability of SR would also permit measuring interference patterns just above and just below the fluorescence threshold in question, leading to more accurate methods of background subtraction. SR will also permits fully exploiting the multi-energy (inverse) x-ray holography method [6.34]. Due to the path-length dependent phase factors present in the reconstruction algorithm, both XFH and PH can in single-wavenumber images and for high-symmetry geometries suffer from image cancellations due to the overlap of real and twin images when two scattering atoms are related by inversion symmetry. Using an experimental geometry of reduced symmetry or phased summations of reconstructions at different wavenumbers will suppress these cancellation effects. The latter procedure would not be possible for XFH, but is possible in MEXH.

References

[6.1] D. Gabor, Nature (London) **161** (1948) 777.

[6.2] A. Szöke, in *Short Wavelength Coherent Radiation: Generation and Applications*, edited by D. T. Atwood and J. Boker, AIP Conf. Proc. No. 147 (AIP, New York, 1986).

[6.3] M. Tegze and G. Faigel, Europhys. Lett. **16** (1991) 41.

[6.4] P. M. Len, S. Thevuthasan, C. S. Fadley, A. P. Kaduwela, and M. A. Van Hove, Phys. Rev. B **50** (1994) 11275.

[6.5] D. K. Saldin, G. R. Harp, B. L. Chen, and B. P. Tonner, Phys. Rev. B **44** (1991) 2480; D.K. Saldin, G.R. Harp, and B. P. Tonner, Phys. Rev B **45** (1992) 9629, and references therein.

[6.6] S. Thevuthasan, R. X. Ynzunza, E. D. Tober, C. S. Fadley, A. P. Kaduwela and M. A. Van Hove, Phys. Rev. Lett. **70** (1993) 595, and references therein.

[6.7] L. J. Terminello, J. J. Barton, and D. A. Lapiano-Smith, J. Vac. Sci. Tech. B **10** (1992) 2088; Phys. Rev. Lett. **70** (1993) 599, and references therein.

[6.8] M. Tegze and G. Faigel, Nature **380** (1996) 49.

[6.9] (a) J. J. Barton, Phys. Rev. Lett. **61** (1988) 1356, and Phys. Rev. Lett. **67** (1991) 3106. (b) J. J. Barton and L. J. Terminello, paper presented at the Third International Conference on the Structure of Surfaces, Milwaukee, July 1990, and in *Structure of Surfaces III,* eds. S. Y. Tong, M. A. Van Hove, X. Xide, and K. Takayanagi (Springer Verlag, Berlin, 1991), 107. (c) S. Y. Tong, H. Huang, and C. M. Wei, Phys. Rev. B **46** (1992) 2452, and references therein.

[6.10] C. S. Fadley and P. M. Len, Nature **380** (1996) 27.

[6.11] W. H. Bragg and W. L. Bragg, Proc. R. Soc. London Ser. A **88** (1913) 428.

[6.12] J. Karla and H. Hauptmann, Acta Cryst. **3** (1950) 18.

[6.13] W. N. Lipscomb, Acta Cryst. A **30** (1982) 841.

[6.14] S. L. Chang, Phys. Rev. Lett. **48** (1982) 163.

[6.15] W. Kossel, V. Loeck, and H. Voges, Z. Phys. **94** (1935) 139.

[6.16] J. T. Hutton, G. T. Trammell, and J. P. Hannon, Phys. Rev. B **31** (1985) 743; and Phys. Rev. B **31** (1985) 6420.

[6.17] M. J. Bedyzk and G. Materlik, Phys. Rev. B **32** (1985) 6456.

[6.18] Y. Ma, K. E. Miyano, P. L. Cowan, Y. Aglitzkiy, and B. A. Karlin, Phys. Rev. Lett. **74** (1995) 478.

[6.19] (a) T. Noma, A. Iida, K. Sakurai, Phys. Rev. B **48** (1993) 17524. (b) Y. C. Sasaki, Y. Suzuki, Y. Tomioka, T. Ishibashi, I. Satoh, and K. Hirokawa, Phys. Rev. B **50** (1994) 15516. (c) Y. C. Sasaki, Y. Suzuki, and T. Ishibashi, Science **263** (1994) 62. (d) Y. C. Sasaki, Y. Suzuki, Y. Tomioka, and A. Fukuhara, Phys. Rev. B **48** (1993) 7724.

[6.20] C.S. Fadley, (a) in *Synchrotron Radiation Research: Advances in Surface and Interface Science*, R. Z. Bachrach, ed. (Plenum Press, New York, 1992). (b) Surf. Sci. Repts. **19** (1993) 231. (c) Mat. Sci. Soc. Symp. Proc. **307** (1993) 261.

[6.21] *International Tables for X-ray Crystallography, Vol. III*, K. Lonsdale, Gen. Ed. (D. Reidel Publishing, Dordrecht, Holland, 1968).

[6.22] M.A. Van Hove and S.Y. Tong, eds., *Surface Crystallography by LEED* (Springer-Verlag, New York, 1979).

[6.23] B.W. Batterman and H. Cole, Rev. Mod. Phys. **36** (1964) 681.

[6.24] D.K. Saldin, G. R. Harp, B. L. Chen, and B. P. Tonner, Phys. Rev. B **44** (1991) 2480.

[6.25] P. M. Len, S. Thevuthasan, A. P. Kaduwela, M. A. Van Hove, and C. S. Fadley, to appear in Surf. Sci. **365** (1996) 535.

[6.26] (a) B. L. Petersen, L. J. Terminello, J. J. Barton, and D. A. Shirley, Chem. Phys. Lett. **220** (1994) 46. (b) L. J. Terminello, J. J. Barton, and D. A. Lapiano-Smith, J. Vac. Sci. Technol. B **10** (1992) 2088, and Phys. Rev. Lett. **70** (1993) 599.

[6.27] H. Wu, G. J. Lapeyre, H. Huang, and S. Y. Tong, Phys. Rev. Lett. **71** (1993) 251.

[6.29] M. Zharnikov, M. Weinelt, P. Zebisch, M. Stichler, and H.-P. Steinrück, Surf. Sci. **334** (1995) 114, and references therein.

[6.30] J. G. Tobin, G. D. Waddill, H. Li, and S. Y. Tong, Surf. Sci. **334** (1995) 263, and references therein.

[6.31] (a) R. Denecke, R. Eckstein, L. Ley, A. E. Bocquet, J. D. Riley, and R. C. G. Leckey, Surf. Sci. **331-333** (1995) 1085.

[6.32] (a) Z.-L. Han, S. Hardcastle, G. R. Harp, H. Li, X.-D. Wang, J. Zhang, and B. P. Tonner, Surf. Sci. **258** (1991) 313, and references therein. (b) P. R. Jeng, I. H. Hong, Y. C. Chou, and C. M. Wei, Phys. Rev. B **51** (1995) 13645, and references therein.

[6.33] (a) M. A. Mendez, C. Glück, J. Guerrero, P. L. de Andres, K. Heinz, D. K. Saldin, and J. B. Pendry, Phys. Rev. B **45** (1992) 9402, and references therein. (b) C. M. Wei, S. Y. Tong, H. Wedler, M. A. Mendez, and K. Heinz, Phys. Rev. Lett. **72** (1994) 2434, and references therein.

[6.34] T. Gog, P. M. Len, G. Materlik, D. Bahr, C. Sanchez-Hanke, and C. S. Fadley, Phys. Rev. Lett. **76** (1996) 3132.

Figure Captions

Figure 6.1. X-ray diffraction probes of atomic structure. (a) Conventional x-ray crystallography, where x-rays are diffracted by Bragg planes of atoms. Diffraction phases are determined by analysis of peakrelative intensities. (b) Kossel line patterns. Fluorescent x-rays from a photoexcited emitter are diffracted by Bragg planes of atoms. Diffraction phases are thus here directly referenced to the unscattered portion of the fluorescence. (c) Standing wave method. This is the optical reciprocal of (b), where a coherent plane wave with some energy above the fluorescent threshold illuminates a fluorescing atom either directly, or after being scattered by Bragg planes of atoms. The interference between these wavefronts determines the amount of fluorescence from the emitter. (d) X-ray resonant interference scattering (XRIS). An incident x-ray beam energetically just above the absorption edge of the atomic species of the sample coherently excites Bragg planes of fluorescing atoms. (e) Total external reflection of fluorescent x-rays. Here, the vertical spacing of a Langmuir-Blodgett layer of emitters from the bulk substrate is determined by the Lloyd's Mirror interference between the direct and totally externally reflected wavefronts. (f) X-ray fluorescence holography (XFH). Fluorescent x-rays from a photoexcited emitter are diffracted by the immediate atomic environment surrounding the emitter. Note that in the case of long-range atomic order samples, XFH is equivalent to (b). However, in contrast to (a)-(e), XFH can also be done on samples possessing only short-range atomic order.

Figure 6.2. (a) Schematic representation of a 49-atom Mo(001) planar cluster, with a single emitter at the origin. (b) Schematic representation of a 68,705-atom Mo(001) cluster, with a single emitter at the center of the $32 \times 32 \times 32$ bcc unit cell cluster.

Figure 6.3. Mo scattering factors $f(\Theta) = |f(\Theta)|\exp(i\psi(\Theta))$ for electrons and x-rays with the same wavenumber $k = 10.1\text{Å}^{-1}$; Θ is the scattering angle. (a) Polar plots of the magnitude $|f(\Theta)|$ in Å for electrons and x-rays. (b) Polar plots of the phase shift $\psi(\Theta)$ in radians for electrons and x-rays.

Figure 6.4. (a) Theoretically generated $\chi(\mathbf{k})$ intensities for $k = 10.1\text{Å}^{-1}$ (or $E =$ 391eV) photoelectrons as viewed down along $[00\bar{1}]$ in $\mathbf{k}$-space, obtained from the 49-atom Mo(001) planar cluster of Fig. 6.2(a). (b) Atomic images reconstructed from (a), in the horizontal (001) plane. The actual locations of the atoms in the fourth quadrant are indicated as circles. The location of the emitter, which is not imaged, is indicated by the dashed square at the origin.

Figure 6.5. As Fig. 6.4, but for $k = 10.1\text{Å}^{-1}$ ($E = 20.0$keV) x-rays.

Figure 6.6. As Fig. 6.4, but for $k = 10.1\text{Å}^{-1}$ (or $E = 20.0$keV) x-rays from the 68,705 atom cluster of Fig. 6.2(b).

Figure 6.7. As Fig. 6.4, but for the low-pass filtered $\tilde{\chi}(\mathbf{k})$ obtained from the $\chi(\mathbf{k})$ of Fig. 6.6(a) via the Gaussian convolution of Eq. (6.3) and a compression from a total number of 32,400 data points down to about 3,000 data points.. A statistical scatter in the data appropriate to counts of $\sim 10^9$ in each channel has also been added.

Figure 6.8. (a) Three-atom Mo cluster, with a variable emitter-scatterer separation $|\mathbf{a}|$. $\Theta^{\mathbf{k}}_{+\mathbf{a}}$ is the scattering angle between $+\mathbf{a}$ and $\mathbf{k}$, and $\Theta^{\mathbf{k}}_{-\mathbf{a}}$ is the scattering angle between $-\mathbf{a}$ and $\mathbf{k}$. Holographic reconstruction magnitudes $\left|U^{k}_{A}(\mathbf{r}'=+\mathbf{a})\right|$ and $\left|U_{A}(\mathbf{r}'=+\mathbf{a})\right|$ for the scatterer at $\mathbf{r}' = +\mathbf{a}$ as a function of $|\mathbf{a}|$ for: (b) single-wavenumber photoelectron holography (PH) images, (c) single-wavenumber XFH images, (d) idealized phase-summed photoelectron holography images using reconstructions with different numbers n of wavenumbers.

(a)

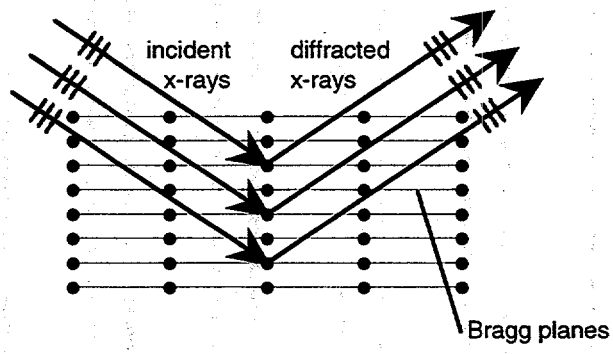

(b)

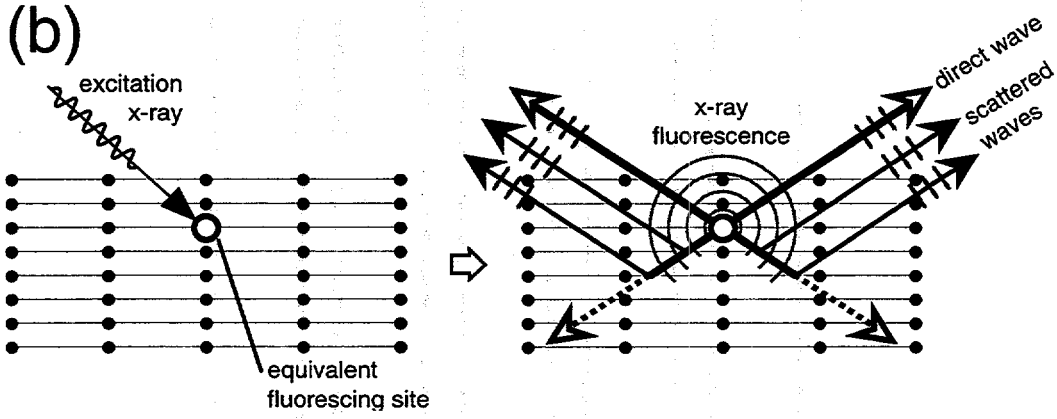

(c)

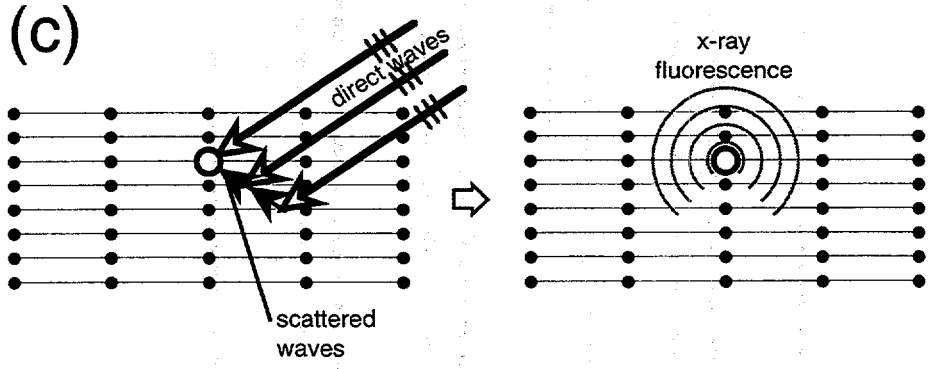

Figs. 6.1(a)-(c)

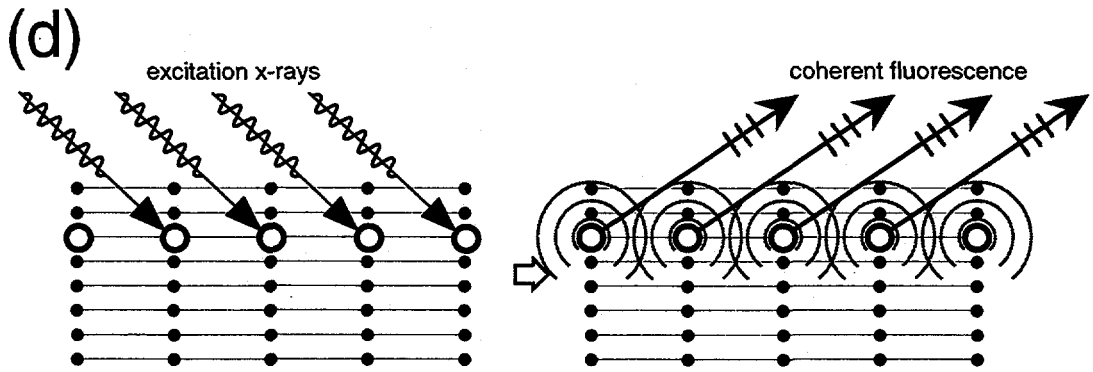

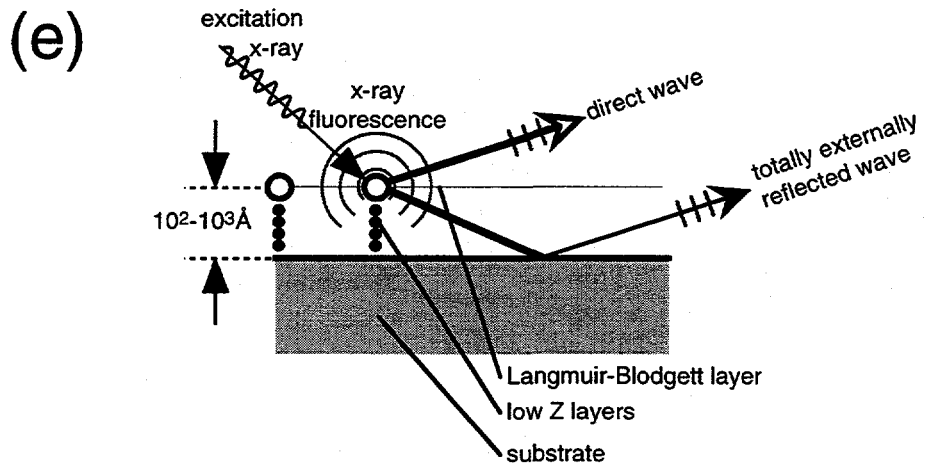

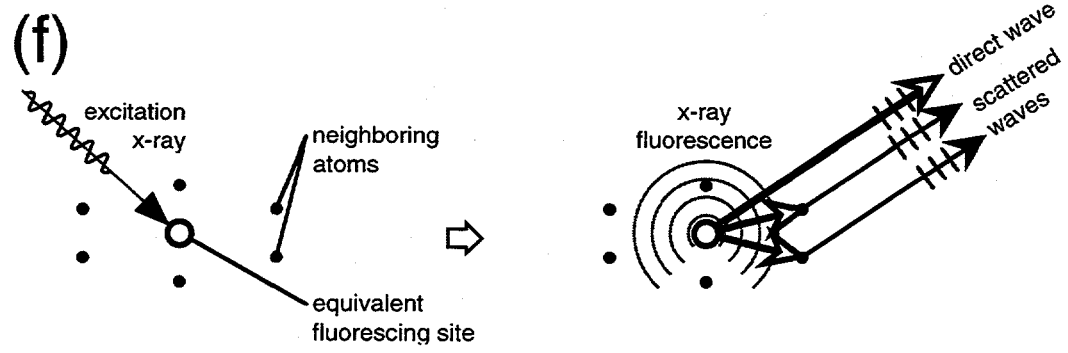

Figs. 6.1(d)-(f)

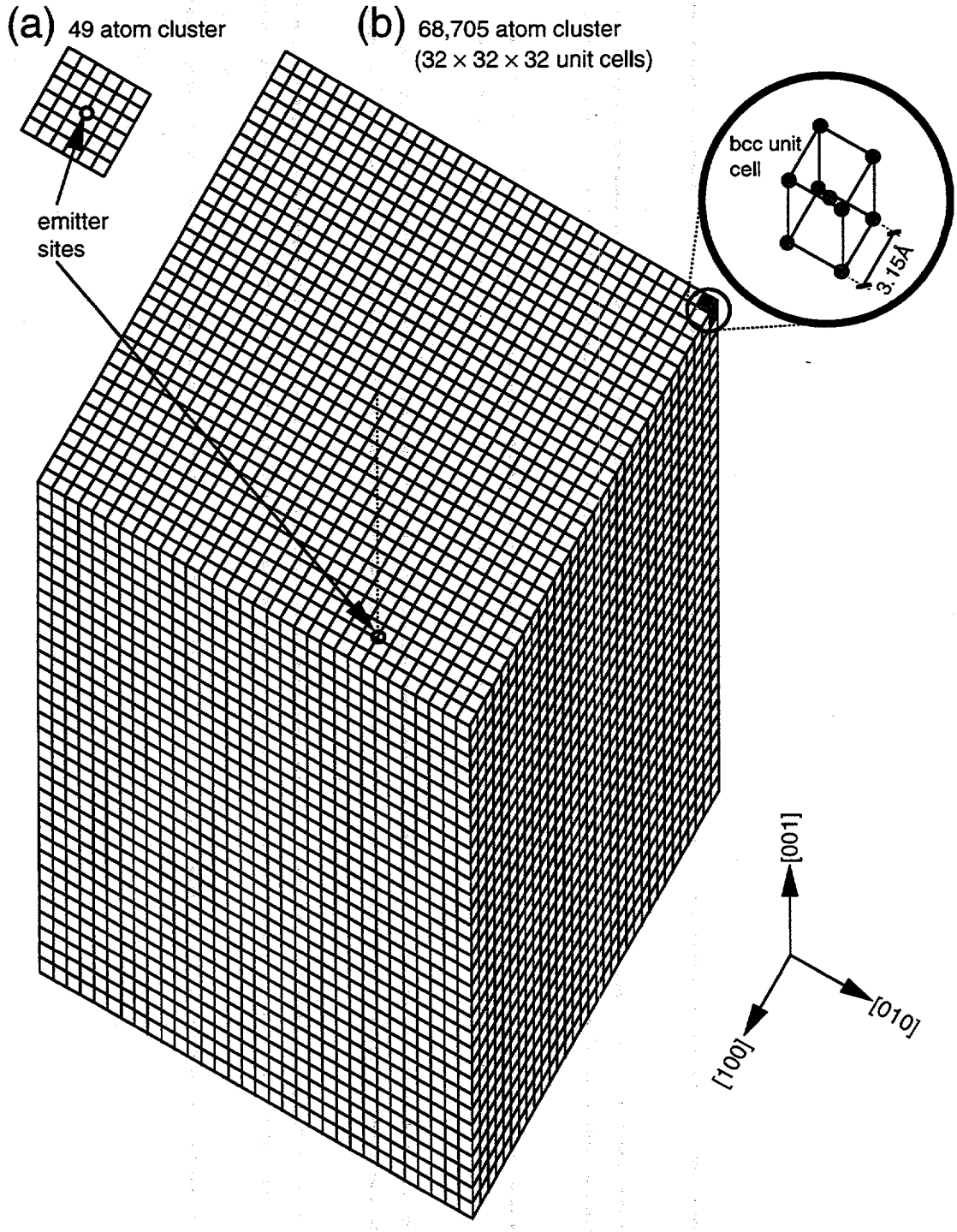

Fig. 6.2

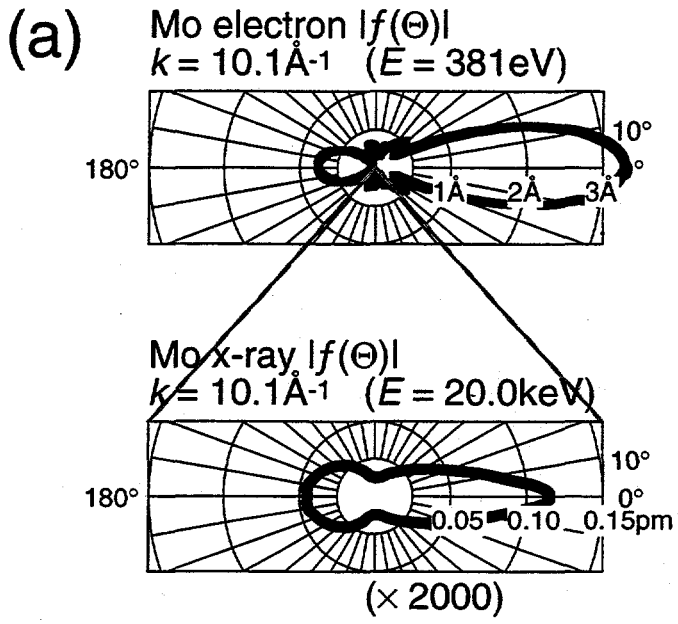

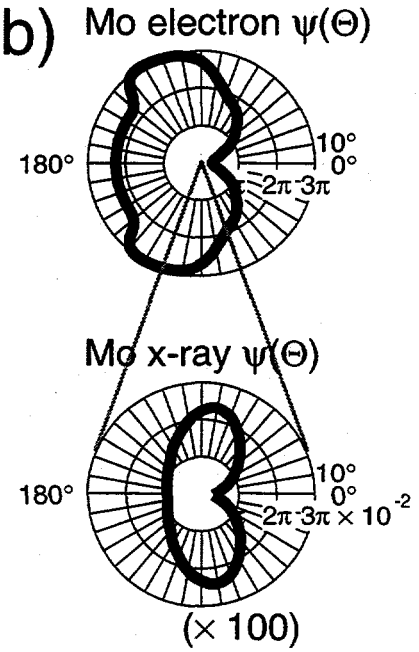

Fig. 6.3

Fig. 6.4 photoelectrons

Fig. 6.5 XFH

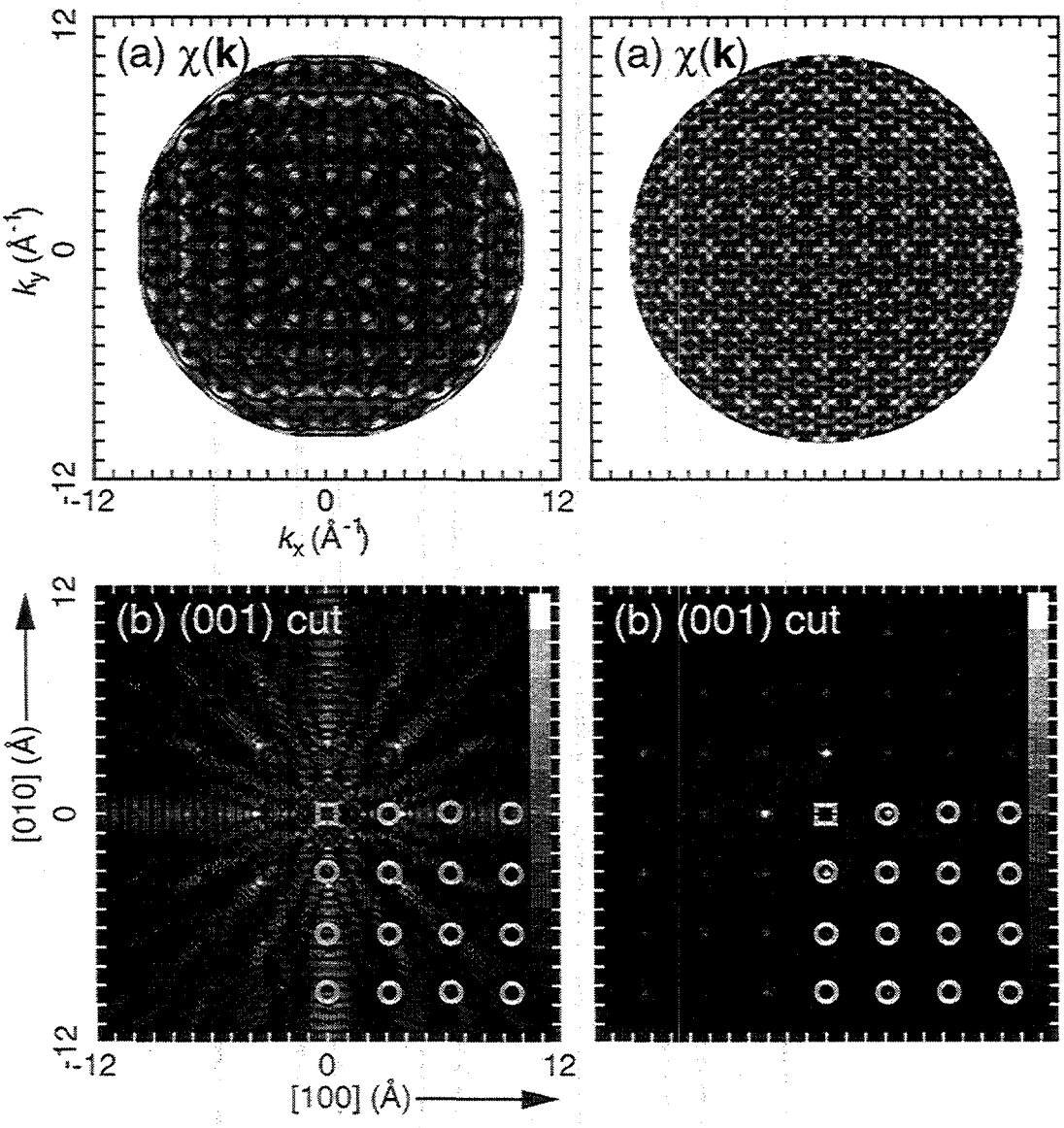

Figs. 6.4-6.5

Fig. 6.6 XFH, sim. exp. Fig. 6.7 XFH, filter. exp.

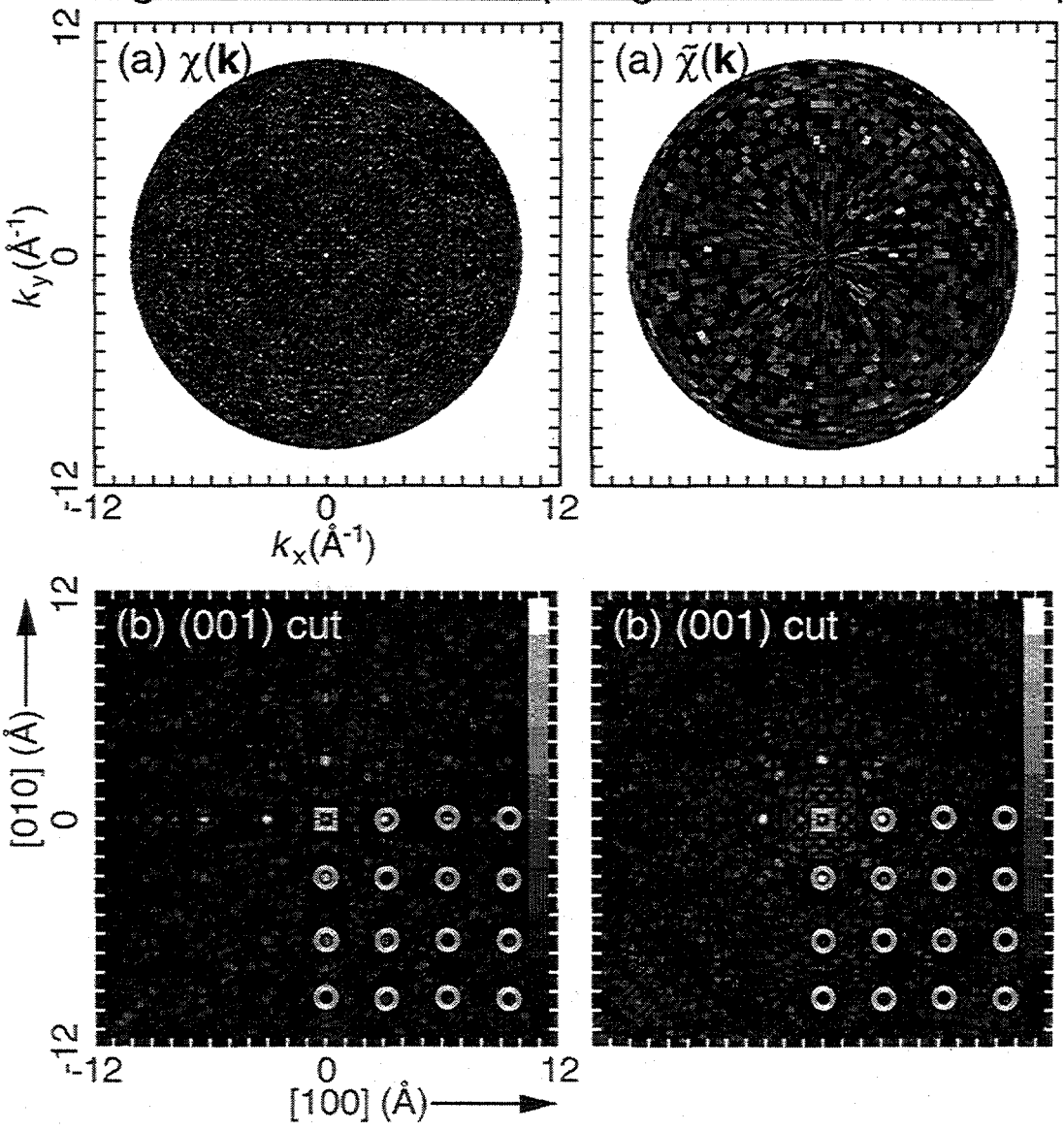

Figs. 6.6-6.7

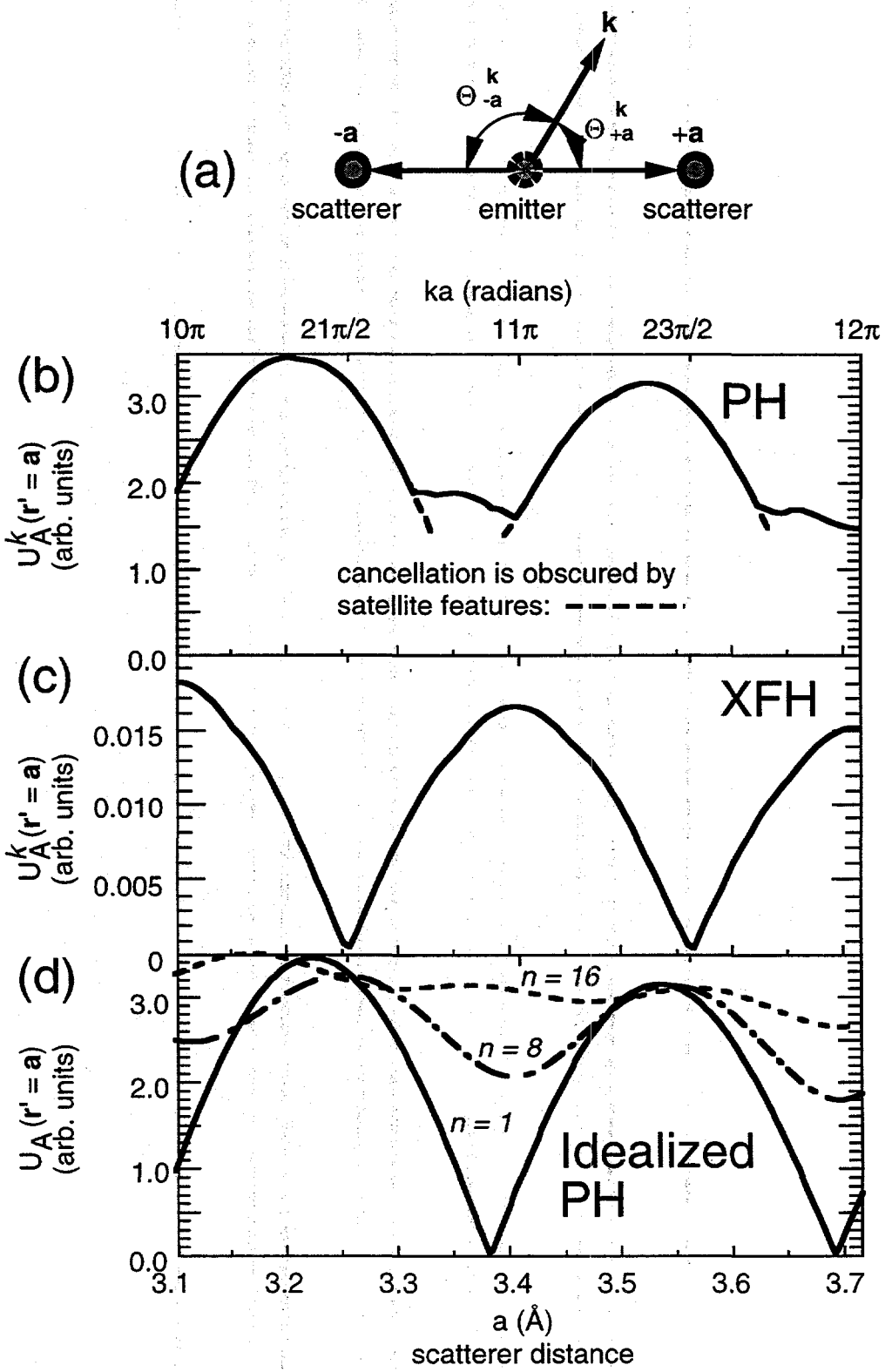

Fig. 6.8

Chapter 7

X-Ray Fluorescence Holography and Multiple Energy X-Ray Holography: A Critical Comparison of Atomic Images

Abstract

We compare *x-ray fluorescence holography* (XFH) and *multiple energy x-ray holography* (MEXH), two techniques that have recently been used for the first time to obtain experimental three-dimensional atomic images. For single-energy holograms, these methods are equivalent by virtue of the optical reciprocity theorem. However, XFH can only record holographic information at the characteristic fluorescence energies of the emitting species, while MEXH can record holographic information at any energy above the fluorescent edge of the emitter, thus enabling the suppression of real-twin overlaps and other aberrations and artifacts in atomic images.

Outline

7.1 Introduction

Nearly a half century ago, Gabor proposed a holographic solution to the classic phase problem in crystal diffraction [7.1]. Whereas only the intensity of the wavefronts scattered by atoms in a crystal are measured in a conventional diffraction experiment, Gabor suggested that the phases of these diffracted wavefronts could be referenced to a coherent source that simultaneously illuminates the detector as well as the crystal. This

technique has successfully imaged nanometer-scale structures with electrons from field-emission tips [7.2], but these sources lack the necessary source size and wavelength resolution to image atomic structure on the Ångstrom scale. However, Szöke noted about a decade ago that photoexcited atoms within the sample itself may serve as highly coherent sources of outgoing electron or fluorescent x-ray waves [7.3]. This "inner source" implementation of Gabor's holographic solution to the phase problem has by now enabled three-dimensional atomic images with sub-Ångstrom resolution to be directly obtained from photoelectron diffraction, for example [7.4-7.17]. However, it is also well recognized that electron scattering is highly non-ideal, with angular anisotropies in scattering amplitude and phase that can distort images, and multiple scattering effects that can complicate analysis. Since x-rays scatter much more ideally than electrons, inner-source x-ray holography represents a potentially promising approach as well [7.18,7.19].

Two experimental approaches have recently obtained holographic atomic images using x-rays: *x-ray fluorescence holography* (XFH) [7.18-7.20] and *multiple energy x-ray holography* (MEXH) [7.21,7.22]. For a given single energy, holographic measurements made by these methods are equivalent by virtue of the optical reciprocal theorem, and will result in equally resolved atomic images. However, MEXH is capable of recording holographic intensities at arbitrary energies, which can suppress twin image effects, as well as other aberrations and artifacts in reconstructed images, as we illustrate below in theoretical simulations for several imaging strategies.

7.2 Optical reciprocity of MEXH and XFH

We first discuss the creation of holographic diffraction patterns from atomic scattering, in Gabor's original scheme, as shown in Fig. 7.1(a) [7.1]. Here, a convergent beam is brought to a point focus near an atom, where it begins to diverge as it illuminates both the nearby atom, and a far field screen. The wavefront scattered by the atom will reach a given position on the screen and interfere with the direct, unscattered wavefront.

The intensity pattern will depend on the phase difference between the scattered and unscattered wavefronts, *which for ideal point-like scattering* is solely due to the difference between their path lengths (ℓ and ℓ_0, respectively). Thus the phase of the scattered wavefront is visible in the holographic diffraction pattern $I(\mathbf{k})$ on this screen, as it is referenced at each point to the direct wavefront.

In the simplest implementation of XFH as first suggested by Szöke [7.3], the point focus of the coherent beam is replaced by an (ideally point-like) atom that is photoexcited to emit a spherical fluorescent x-ray wavefront (Fig. 7.1(b)). Similar to Gabor's original scheme, the wavefronts scattered by atoms neighboring the emitter will reach a far field detector, where they will interfere with the direct, unscattered portion of the emitted wavefront. Moving the detector over a large solid-angle range will then generate a holographic interference pattern $I(\mathbf{k})$ over different emission directions $\mathbf{k}$, due to the changing differences in the path lengths between the scattered and direct wavefronts.

MEXH can be thought of as a time-reversed implementation of XFH [7.21,7.22], in which the directions of all the paths in the XFH case are reversed, together with the locations of the wave source and detector (Fig. 7.1(c)). A far field point source illuminates the sample with x-rays having an energy higher than a particular absorption edge of a specific emitter of interest. This emitter will then be excited by a wavefield that is a superposition of wavefronts scattered by neighboring atoms, and the direct, unscattered wavefront. The interference between the scattered and direct wavefronts at the location of the fluorescing atom depends solely on the difference between their path lengths, as traced back to the far field source, and the resulting wavefield strength at the emitter determines the amount of fluorescence generated. Now moving the *source* relative to the sample over a large range of solid-angle with the detector fixed in direction and averaging over a large solid-angle enables recording a holographic intensity pattern $I(\mathbf{k})$ over different directions, again due to the changing difference in path lengths between the scattered and direct wavefronts.

Note that we have assumed the presence of only one fluorescing atom, whether it acts as the coherent wave source, or the path length difference detector. Realistically there will be many fluorescing atomic sites, but if each photoemitter has an identical neighborhood, then this presents no problem, as the reconstructed atomic images will merely be the superposition of each identical neighborhood [7.3]. If there exist a small number of inequivalent emitter sites, then the reconstructed image intensities will be a superposition of the neighboring environments surrounding each emitter [7.22].

For all three experimental schemes, the phases of the scattered wavefronts are referenced to the differences in path length that they have relative to the direct unscattered wave $I_0(\mathbf{k})$. If the jth scatterer is at position $\mathbf{a}_j$ relative to the emitter, then these path length differences generate a phase of $\mathbf{k}\cdot\mathbf{a}_j - ka_j$, which over $\mathbf{k}$-space are unique for each $\mathbf{a}_j$ scatterer. Thus, a sufficient data set throughout $\mathbf{k}$-space and involving the resulting phase factor $e^{i(\mathbf{k}\cdot\mathbf{a}_j - ka_j)}$ will uniquely identify each scatterer at relative positions $\mathbf{r}' = \mathbf{a}_j$ from the point focus, or emitter. Holographic intensities $\chi(\mathbf{k})$ are now generated by subtracting, and then dividing out, the unscattered wave $I_0(\mathbf{k})$ from the measured holographic intensities $I(\mathbf{k})$, and these will be given by:

$$\chi(\mathbf{k}) = \frac{I(\mathbf{k}) - I_0(\mathbf{k})}{I_0(\mathbf{k})}. \tag{7.1}$$

In a simple single scattering model of the scattering process, we can also write [7.3]:

$$\chi(\mathbf{k}) \propto \sum_j \frac{f(\Theta^{\mathbf{k}}_{\mathbf{a}_j})}{ka_j} e^{i(\mathbf{k}\cdot\mathbf{a}_j - ka_j)} + c.c., \tag{7.2}$$

where $f(\Theta^{\mathbf{k}}_{\mathbf{a}_j}) \equiv |f(\Theta^{\mathbf{k}}_{\mathbf{a}_j})| e^{i\psi(\Theta^{\mathbf{k}}_{\mathbf{a}_j})}$ is the atomic scattering factor, and $\Theta^{\mathbf{k}}_{\mathbf{a}_j}$ is the angle between $\mathbf{k}$ and $\mathbf{a}_j$. Inverting such a hologram at a single energy via:

$$U(\mathbf{r}') = \iint_{\Omega} d\sigma_{\hat{\mathbf{k}}} e^{-i\mathbf{k}\cdot\mathbf{r}'} \chi(\mathbf{k}), \tag{7.3}$$

(where $d\sigma_{\hat{\mathbf{k}}} \equiv \cos\theta d\theta d\phi$) shows that the first term in $\chi(\mathbf{k})$ will reconstruct holographic real images at $\mathbf{r}' = \mathbf{a}_j$, while the complex conjugate term will result in holographic twin images at $\mathbf{r}' = -\mathbf{a}_j$. Extending Eq. (7.3) so as to simultaneously invert images at multiple energies produces intensity peaks only at the real locations of the atoms ($\mathbf{r}' = \mathbf{a}_j$) [7.4]. This is a transform over some volume in $\mathbf{k}$-space with a kernel ($e^{-i(\mathbf{k}\cdot\mathbf{r}' - kr')}$) which produces a stationary phase with the path length difference factor and yields image intensities located at relative positions $\mathbf{r}'$ via:

$$U(\mathbf{r}') = \int_k k^2 dk \iint_{\Omega} d\sigma_{\hat{\mathbf{k}}} e^{-i(\mathbf{k}\cdot\mathbf{r}' - kr')} \chi(\mathbf{k}). \tag{7.4}$$

If the scattering factor in Eq. (7.1) is weak and fairly isotropic (as is the case with x-rays), then the resulting holographic images will be located very close to the actual atomic positions, and will be much freer from undesirable aberrations and artifacts [7.10-7.12,7.19]. Various modifications to the basic reconstruction transforms of Eqs. (7.3) and (7.4) [7.13-7.15], as well as entirely different reconstruction algorithms [7.16,7.17] have been proposed to account for the anisotropic emission and scattering processes inherent in electron holography.

The above discussion has emphasized the equivalence of XFH and MEXH due to the optical reciprocity theorem, where the two methods can be thought of as time-reversed cases of each other. However, this symmetry is broken when the manner in which atomic fluorescence is used to measure the path length differences between scattered and unscattered wavefronts is considered. Thus, in XFH the fluorescent x-ray of a definite energy is used as the source of the direct and scattered waves, whereas in MEXH the same fluorescent x-ray is used as a detector of the exciting x-ray wave field, *which can be at any energy above the fluorescence threshold.* Thus, despite the

reciprocal equivalence of XFH and MEXH, as discussed in the previous section above, there are significant differences between them, including the fact that *XFH and MEXH holograms cannot be recorded at the same energy.*

7.3 Theoretical holographic images for Fe bcc

This section discusses theoretical images for XFH and MEXH, derived for choices of photon energies that would be accessible and/or selected for optimum image formation in experiments on a real system (bcc Fe).

Figures 7.2(a)-(c) show the XFH, single-energy MEXH, and multiple-energy MEXH $\chi(\mathbf{k})$ holograms, respectively, that were calculated from a model 189-atom Fe(001) bcc cluster, using a single scattering model that includes the full complex atomic scattering factor for x-rays [7.19,7.23]. These holograms were calculated on a 5°×5° grid in polar and azimuthal angles.

In XFH, because a fluorescing atom is used as the wave source, one may only record holograms at the characteristic fluorescent energies of the emitting atom species. Figures 7.3(a)-(b) show the expected atomic images reconstructed via Eq. (7.3) from the theoretical XFH $\chi(\mathbf{k})$ calculated for Fe Kα emission ($k = 3.245$Å^{-1}, or $E = 6.40$keV) of Fig. 7.2(a). Some of the Fe atoms in the reconstructed images of Figs. 7.3(a)-(b) are clearly imaged, but they are only modestly resolved, with a major reason being the long wavelength of the x-rays at this energy ($\lambda = 1.937$Å). While higher Z atoms in general have more energetic fluorescence energies, and thus could produce higher resolution atomic images, reconstructions from XFH holograms from low Z emitters will be much less practical. Of note here is that of the neighboring sites immediately surrounding the emitter, only the 001 and 100 atoms (and their symmetry-related sites) are visible, while the 200 and 110 atoms are missing) see Fig. 7.4 for the locations of the latter atoms). This is due to a well-recognized problem with single-energy holography [7.18,7.19]: at this 6.40keV energy the real and twin images of both the 200 and 110 atoms overlap out

of phase, suppressing the image intensity at these locations. These real-twin image overlaps are an inherent problem in reconstructing centrosymmetric atomic structure images from single-energy holograms, but using more than one energy promises to solve this problem [7.19]. The 001 and 100 atoms in Fig. 7.3 are also shifted slightly outwards (by $\approx 0.05\text{Å}$) from their actual locations due to the angular dependence of the small scattering phase shift at this energy. This is found to be of the form $\psi(\Theta^{k}_{a_j}) \propto \beta(1-\cos\Theta^{k}_{a_j})+\gamma$, with $\beta \approx 0.09$ and $\gamma \approx 0.19$, which is expected to cause position shifts of $\Delta r \approx \beta / k \approx 0.03\text{Å}$ in the reconstructed images [7.10].

In MEXH, the unscattered and direct wavefronts are generated by a coherent far field source, which can be tuned to *any* desirable x-ray energy above an absorption edge (7.11keV, for Fe K), with the fluorescence serving only as a detector for the resulting path length differences between the scattered and direct wavefronts. Figures 7.4(a)-(b) show the expected Fe atomic images reconstructed via Eq. (7.3) from the theoretical *single-energy* MEXH hologram at $k = 3.902\text{Å}^{-1}$ ($E = 7.70$keV, chosen to be just above various near-edge effects), of Fig. 7.2(b). The resolution of the Fe images in Figs. 7.4(a)-(b) is slightly improved, due to the slightly shorter wavelength of x-rays used ($\lambda = 1.610\text{Å}$). But note that the 111 and 110 atoms are now visible, while the 001 and 100 atoms are suppressed due to changes in the real-twin overlap at this choice of hologram energy. The relative brightness in intensity of the 111 atomic image, compared to the 110, 001, and 200 atomic image in Figs. 7.4(a)-(b) indicates that these latter atomic images are almost real-twin image suppressed. The 111 image intensities are also shifted outwards by 0.04Å, again due to the phase ($\beta \approx 0.12$ and $\gamma \approx 0.19$, making $\Delta r \approx \beta / k \approx 0.03\text{Å}$) of the complex atomic scattering factor at this hologram energy [7.10].

Ideally, one could record single-energy holograms for various energies, and simply superpose their reconstructed images in order to override the real-twin image suppression conditions for different centrosymmetric atomic pairs at different energies. However, it is much more advantageous to reconstruct images from a single data set of multiple

hologram energies via Eq. (7.4), such that the holographic data points used in the image reconstruction span a **k**-space volume. This improves the resulting atomic images, as the transform of Eq. (7.4) breaks the symmetry between the real and twin terms in Eq. (7.2) when extended over a finite energy (or k) range [7.4,7.19]. The use of multiple-energy holograms in reconstructing atomic images is in fact commonplace in electron emission holography (*e.g.*, due to the tunability of the photoelectron energy of the source atom), where it has been shown to suppress the presence of undesirable twin images, and to increase image fidelity [7.5-7.9,7.14-7.17].

Figures 7.5(a)-(b) now show the expected Fe atomic images reconstructed from the theoretical seven-energy MEXH data set of Fig. 7.2(c), which spans $k = 6.081\text{Å}^{-1}$ to 9.122Å^{-1} ($E = 12.00\text{keV}$ to 18.00keV), with $\delta k = 0.507\text{Å}^{-1}$ (corresponding to an energy interval of $\delta E = 1.00\text{keV}$). The atomic images of Figs. 7.5(a)-(b) are better resolved than Figs. 7.3-7.4, due to the shorter range x-ray wavelengths used ($\lambda = 1.033\text{Å}$ to 0.689Å), and are more resolved than any single-energy holographic image within this range of energies [7.4]. *All* near-neighboring atoms surrounding the emitter are furthermore clearly imaged with no real-twin cancellations present. The presence of faint aberrations and artifacts visible in the single-energy holographic images of Figs. 7.3-7.4 have also been further suppressed. In XFH it would also be possible in principle to measure holograms at the different fluorescence energies of a specific emitter type in order to suppress real-twin image overlaps. However, the limited number, and varying intensities and spacings of these characteristic energies would present severe constraints on the reconstruction of multiple-energy holograms in XFH [7.19].

7.4 Concluding remarks

The evolution of Gabor in-line holography into XFH and MEXH has been discussed, as well as the equivalence of XFH and MEXH for single-energy holograms by virtue of the optical reciprocity theorem. However, XFH and MEXH holograms cannot

be recorded at the same energy. XFH data can only be recorded at the characteristic fluorescence energies of an emitting atom, and thus XFH images may suffer from the unavoidable effects of real and twin images overlapping (including out of phase overlap, producing image cancellations), as well as undesirable aberrations and artifacts inherent in single-energy holographic images. In XFH, however, a whole single-energy hologram can in principle be instantaneously imaged by a large parallel detector array. This can be advantageous if time-resolved XFH using x-ray laser excitation sources will be attempted. MEXH data can be recorded at any wavenumber *above* the absorption edge of an emitter. Thus, single-energy MEXH data can be taken at those energies where real and twin images will interfere in phase at atomic locations of interest (*cf.* Fig. 7.4). More importantly, multiple-energy MEXH data sets can be used to suppress real-twin image overlaps, and thus generate atomic images with better resolution and higher fidelity than any single-energy hologram within the same energy range (*cf.* Fig. 7.5).

References

[7.1] D. Gabor, Nature (London) **161** (1948) 777.

[7.2] H. Schmid, H.-W. Fink, and J. Kreuzer, J. Vac. Sci. Technol. B **13** (1995) 2428, and references therein.

[7.3] A. Szöke, in *Short Wavelength Coherent Radiation: Generation and Applications*, T. Attwood, J. Boker (eds.), AIP Conference Proceedings No. 147, (AIP, New York, 1986) 361.

[7.4] (a) J. J. Barton, Phys. Rev. Lett. **61** 1356 (1988), and Phys. Rev. Lett. **67** (1991) 3106. (b) S. Y. Tong, H. Huang, and C. M. Wei, Phys. Rev. B **46** (1992) 2452, and references therein.

[7.5] (a) B. L. Petersen, L. J. Terminello, J. J. Barton, and D. A. Shirley, Chem. Phys. Rev. Lett. **220** (1994) 46, and references therein. (b) H. Wu, G. J. Lapeyre, H. Huang, and S. Y. Tong, Phys. Rev. Lett. **71** (1993) 251 and references therein.

(c) M. Zharnikov, M. Weinelt, P. Zebisch, M. Stichler, H.-P. Steinrück, Surf. Sci. **334** (1995) 114, and references therein. (d) R. Denecke, R. Eckstein, L. Ley, A. E. Bocquet, J. D. Riley, R. C. G. Leckey, Surf. Sci. **331-333** (1995) 1085. (e) J. G. Tobin, G. D. Waddill, H. Hi, S. Y. Tong, Surf Sci **334** (1995) 263, and references therein.

[7.6] (a) H. Li, S. Y. Tong, D. Naumovic, A. Stuck, and J. Osterwalder, Phys. Rev. B **47** (1993) 10036. (b) D. K. Saldin, G. R. Harp, and X. Chen, Phys. Rev. B **48** (1993) 8234, and references therein.

[7.7] (a) Z.-L. Han, S. Hardcastle, G. R. Harp, H. Li, X.-D. Wang, J. Zhang, and B. P. Tonner, Surf. Sci. **258** (1991) 313, and references therein. (b) I. H. Hong, S. C. Shyu, Y. C. Chou, and C. M. Wei, Phys. Rev. B **52** (1995) 16884, and references therein.

[7.8] (a) M. A. Mendez, C. Glück, J. Guerrero. P. L. de Andres, K. Heinz, D. K. Saldin, and J. B. Pendry, Phys. Rev. B **45** (1992) 9402, and references therein. (b) C. M. Wei, S. Y. Tong, H. Wedler, M. A. Mendez, and K. Heinz, Phys. Rev. Lett. **72** (1994) 2434, and references therein.

[7.9] S. Y. Tong, H. Huang, and X. Q. Guo, Phys. Rev. Lett. **69** (1992) 3654.

[7.10] D. K. Saldin, G. R. Harp, B. L. Chen, and B. P. Tonner, Phys. Rev. B **44** (1991) 2480.

[7.11] S. Thevuthasan, G. S. Herman, A. P. Kaduwela, T. T. Tran, Y. J. Kim, R. S. Saiki, and C. S. Fadley, J. Vac. Sci. Technol. A **10** (1992) 2261.

[7.12] P. Hu and D. A. King, Phys. Rev. B **46** (1992) 13615.

[7.13] (a) B. P. Tonner, Z.-L. Han, G. R. Harp, and D. K. Saldin, Phys. Rev. B **43** (1991) 14423. (b) D. K. Saldin, K. Reuter, P. L. De Andres, H. Wedler, X. Chen, J. B. Pendry, and K. Heinz, Phys. Rev. B **54** (1996) 8172.

[7.14] (a) S. Y. Tong, H. Li, and H. Huang, Phys. Rev. B **51** (1995) 1850. (b) H. Wu and G. J. Lapeyre, Phys. Rev B **51** (1995) 14549. (c) J. M. Roesler, M. T. Sieger,

T.-C. Chiang, Surf. Sci. **329** (1995) L588, and references therein.

[7.15] P. J. Rous and M. H. Rubin, Surf. Sci. **316** (1994) L1068.

[7.16] P. Hofmann, K.-M. Schindler, V. Fritzsche, S. Bao, A. M. Bradshaw, and D. P. Woodruff, J. Vac. Sci. Tech. A. **12** (1994) 2045, Surf. Sci. **337** (1995) 169, and references therein.

[7.17] X. Chen and D. K. Saldin, Phys. Rev. B **50** (1994) 17463.

[7.18] M. Tegze, G. Faigel, Europhys. Lett. **16** (1991) 41.

[7.19] P. M. Len, S. Thevuthasan, C. S. Fadley, A. P. Kaduwela, and M. A. Van Hove, Phys. Rev. B **50** (1994) 11275.

[7.20] M. Tegze, G. Faigel, Nature **380** (1996) 49.

[7.21] T. Gog, P. M. Len, G. Materlik, D. Bahr, C. Sanchez-Hanke, and C. S. Fadley, Phys. Rev. Lett. **76** (1996) 3132.

[7.22] T. Gog, R.-H. Menke, F. Arfelli, P. M. Len, C. S. Fadley, G. Materlik, Synch. Rad. News **9** (1996) 30.

[7.23] *International Tables for X-ray Crystallography*, edited by K. Lonsdale (Reidel, Dordrecht, 1968), Vol. III.

Figure captions

Figure 7.1. Three experimental holographic schemes for recording the phases of atomically scattered wavefronts by referencing them to a direct, unscattered wavefront. (a) Gabor's original proposal, where an external coherent beam is brought to a point focus near the scattering atoms, and the resulting scattered and unscattered wavefronts are collected on a far field screen. (b) *X-ray fluorescence holography* (XFH). The point focus of the coherent beam in (a) is replaced by a fluorescing atom, while a far field detector is moved so as to collect the scattered and unscattered wavefronts over a range of different directions. (c) *Multi-energy x-ray holography* (MEXH). The time-reversed version of XFH, in which a far field coherent plane wave source is moved over a range of different directions, while the fluorescing atom senses the superposition of the scattered and unscattered wavefronts, and a remote *stationary* detector collects the amount of fluorescence from the emitter. The incident waves in MEXH can be of any energy above the absorption edge of the emitter.

Figure 7.2. Theoretically generated $\chi(\mathbf{k})$ holograms calculated from a 189-atom Fe(001) bcc single scattering cluster, as viewed down along $[00\bar{1}]$ in **k**-space. (a) Fe Kα fluorescent radiation ($k = 3.245\text{Å}^{-1}$, or $E = 6.40\text{keV}$) XFH $\chi(\mathbf{k})$ hologram. (b) Single-energy ($k = 3.902\text{Å}^{-1}$, or $E = 7.70\text{keV}$) MEXH $\chi(\mathbf{k})$ hologram. (c) Multiple-energy (seven energies spanning $k = 6.081\text{Å}^{-1}$ to 9.122Å^{-1}, or $E = 12.00\text{keV}$ to 18.00keV) MEXH $\chi(\mathbf{k})$ hologram. The intensities in the fourth quadrant have been cut away to reveal the $k = 6.081\text{Å}^{-1}$ ($E = 12.00\text{keV}$) iso-energy surface.

Figure 7.3. Theoretically generated atomic images reconstructed from the single-energy XFH with Fe Kα fluorescent radiation ($k = 3.245\text{Å}^{-1}$, or $E = 6.40\text{keV}$) $\chi(\mathbf{k})$ hologram of Fig. 7.2(a). Cross-section cuts are shown for (a) a vertical (110) plane, and (b) a horizontal (001) plane. The actual locations of the atoms are indicated as circles. The

location of the emitter, which is not imaged, is indicated by the dashed square at the origin. The bcc unit cell is indicated by the dashed lines.

Figure 7.4. As Fig. 7.3, but for images reconstructed from the single-energy MEXH (k = 3.902Å^{-1}, or E = 7.70keV) $\chi(\mathbf{k})$ hologram of Fig. 7.2(b).

Figure 7.5. As Fig. 7.3, but for image reconstructed from the multiple-energy MEXH (seven energies spanning k = 6.081Å^{-1} to 9.122Å^{-1}, or E = 12.00keV to 18.00keV) $\chi(\mathbf{k})$ hologram of Fig. 7.2(c). Note the image cancellations for different atoms in Figs. 7.3 and 7.4, while all near-neighbor atoms surrounding the emitter in Fig. 7.5 are visible.

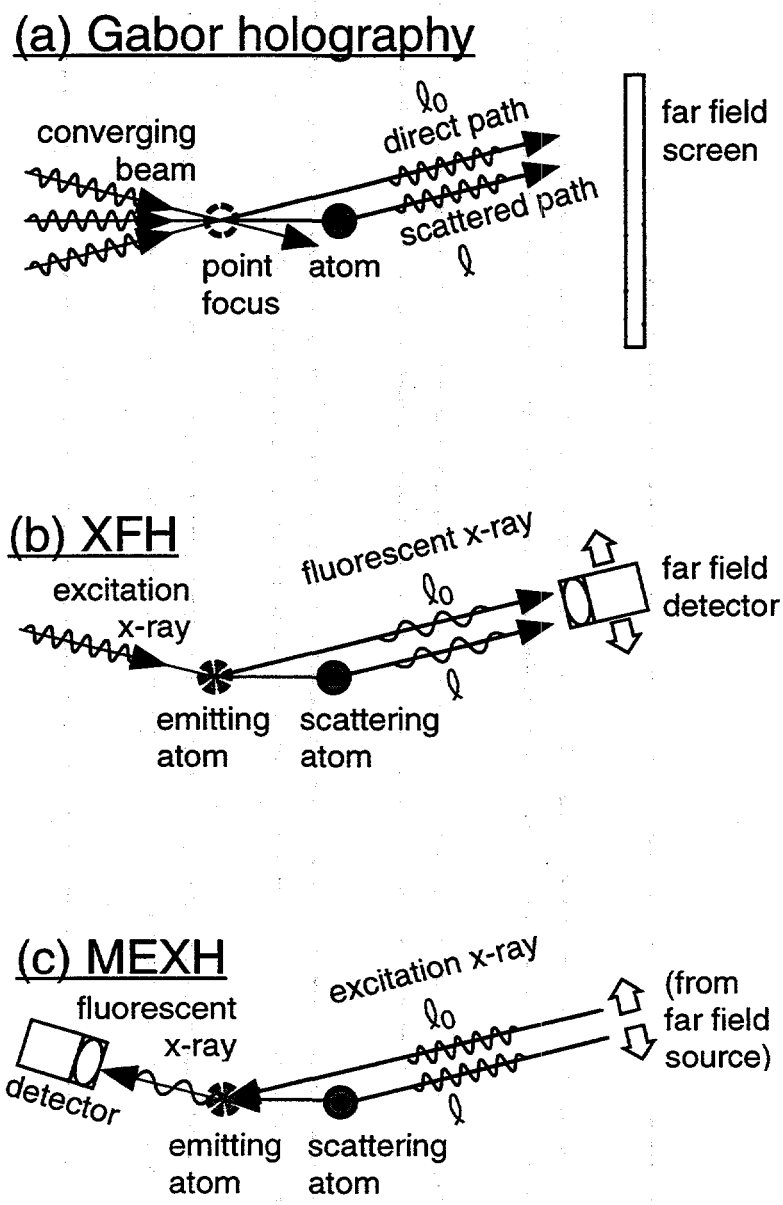

Fig. 7.1

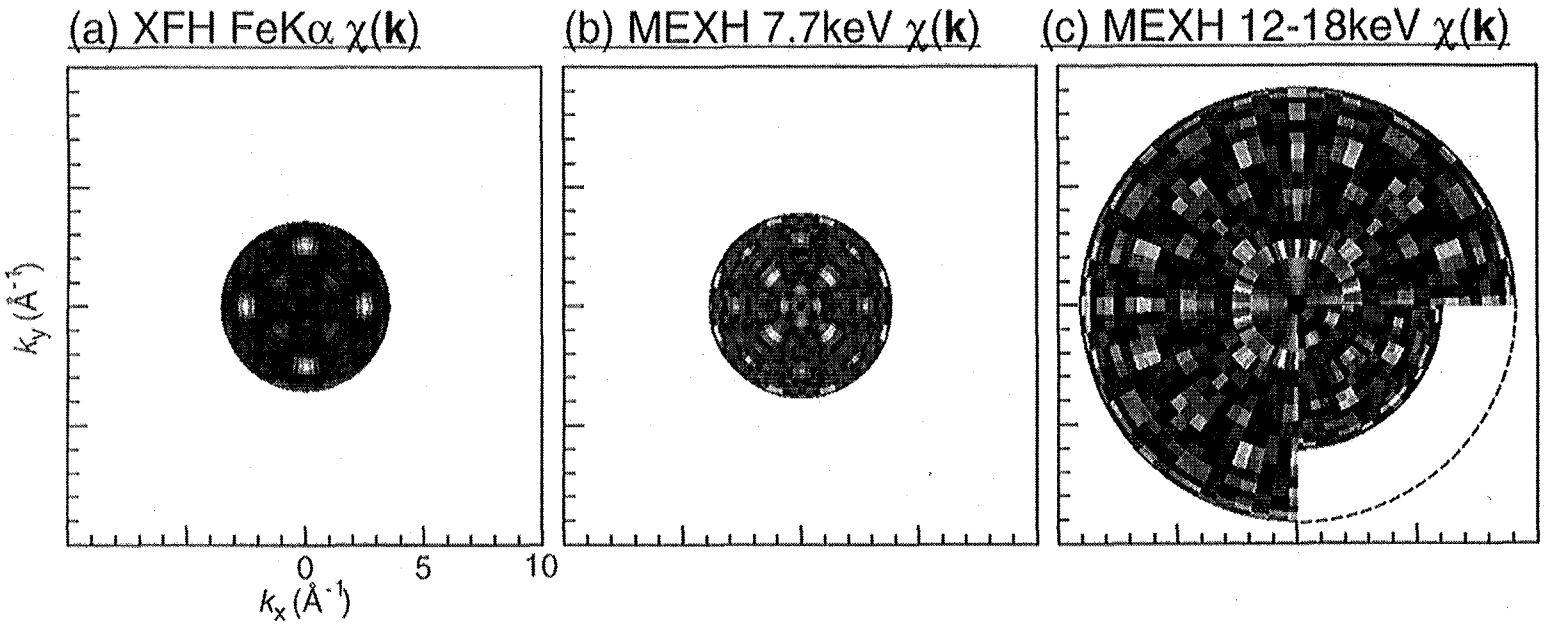

Fig. 7.2

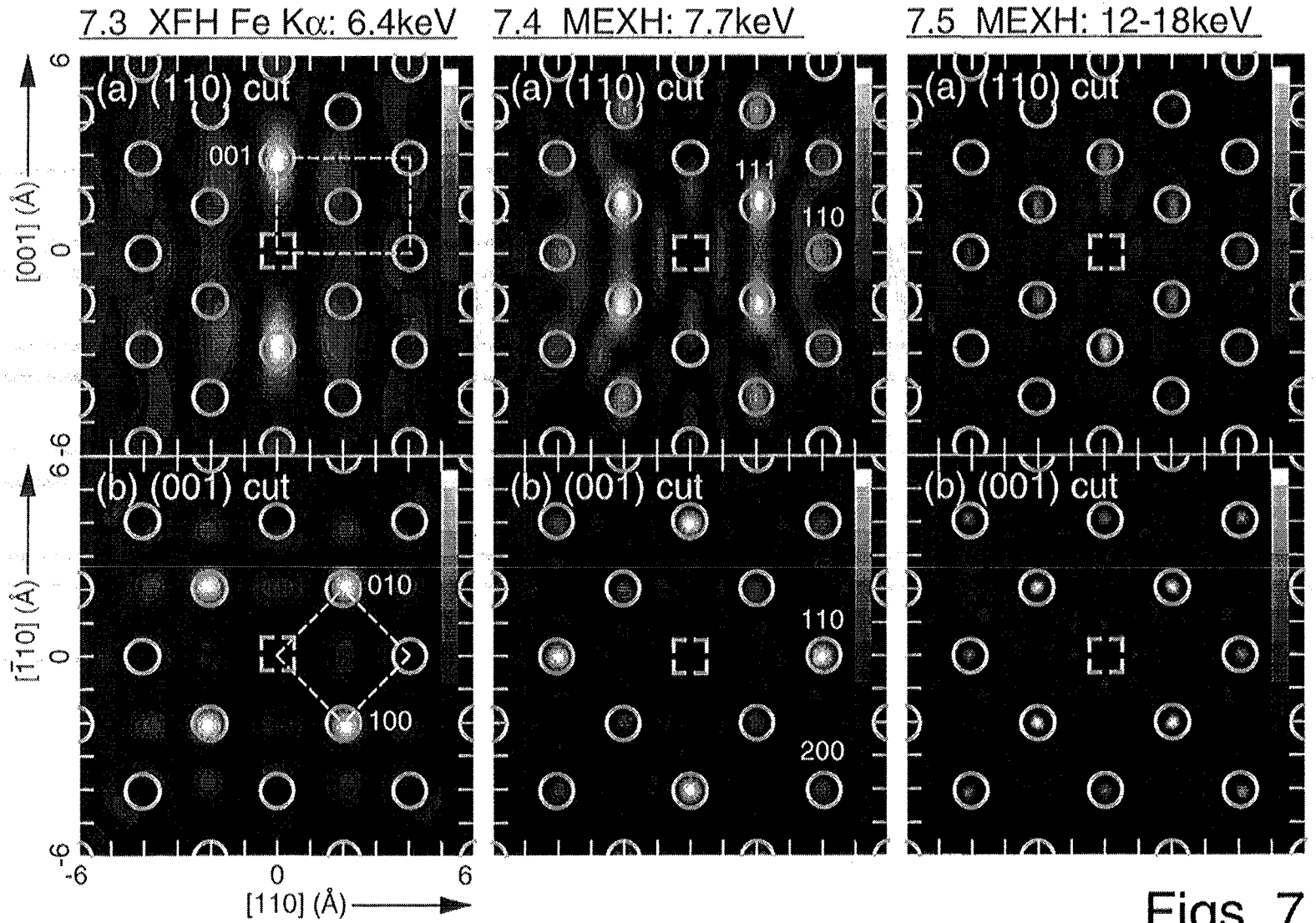

Figs. 7.3-7.5

Chapter 8

Multiple Energy X-Ray Holography: Incident Radiation Polarization Effects

Abstract

Multiple Energy X-ray Holography (MEXH) measures both phase and amplitude information for x-rays scattered from an incident reference beam, from which three-dimensional atomic images can be directly reconstructed. The angular distribution of the x-ray scattering is highly dependent on the polarization direction, via the Thomson scattering cross section. We here consider the effect of incident x-ray polarization on images of Fe atoms reconstructed from theoretical and experimental MEXH data for α-Fe_2O_3(001) (hematite). We also illustrate such polarization effects theoretically in the enhancement of specific atomic structural information of ideal Fe trimers, and a Ge δ-layer buried in Si(001), where the use of different polarization modes and experimental geometries is found to strongly influence atomic images.

8.0 Outline

8.1. Introduction

Gabor first proposed holography in 1948 as a means of surpassing the current limitations of electron microscopy, specifically by experimentally recording the amplitude and phase of scattered wavefronts relative to a direct unscattered reference wave [8.1]. Later, Szöke observed that the phases of atomically-scattered photoelectron or fluorescent x-ray wavefronts can be referenced to the direct or unscattered wavefront [8.2]. This assumes that the electron or x-ray emission is from a highly localized core excitation. Thus, structural information on the atomic environment surrounding each emitting atom is uniquely encoded in the holographic photoelectron or fluorescence intensities, as detected in the far field outside the sample. Algorithms to retrieve direct three-dimensional atomic images from these holograms have subsequently been developed [8.3-8.7] and successfully implemented in applications to *e.g.* photoelectron diffraction data [8.8-8.12].

These holographic principles have also been demonstrated theoretically for x-rays [8.13,8.14], and more recently experimentally implemented in two distinct forms: single energy *x-ray fluorescence holography* (XFH) [8.15], and *multiple energy x-ray holography* (MEXH) [8.16,8.17]. MEXH is the time-reversed reciprocal method of XFH, and the relationship between these two methods has been discussed in detail in an earlier study [8.18]. MEXH is found to be more versatile in that aberrations and twin-image overlaps can be suppressed by reconstructing images from holograms covering a range of different energies [8.3,8.14], but it is also more strongly influenced in both positive and negative ways by the polarization of the incident radiation, and this is the topic of the present paper.

While preliminary MEXH images of Fe atoms in hematite (α-Fe_2O_3(001)) have been reported in a previous study [8.16], we here present additional experimental and theoretical atomic images in order to illustrate the effects of the polarization of the incident radiation used, which can enhance or suppress the images at specific atomic locations. These effects are also theoretically demonstrated through the imaging of simple

Fe trimers and a Ge δ-layer buried in Si(001), a dilute species-specific structure that is ideally suited for MEXH studies. The limitations and future prospects of this new method, specifically as related to polarization effects, are also discussed.

8.2. Image reconstruction of MEXH data

As illustrated in Fig. 8.1(a), raw MEXH $I(\mathbf{k})$ intensities are measured by detecting the net fluorescence from a sample that is illuminated with coherent radiation incident over different directions and energies. The fluorescing emitter detects the overall radiation field strength resulting from a superposition of wavefronts elastically scattered by neighboring atoms and the direct, unscattered wavefront (*i.e.*, the direct or reference wave). The amount of fluorescence is thus determined by the interference of the scattered and direct wavefronts at the emitting atomic site [8.16-8.18]. Normalized $\chi(\mathbf{k})$ intensities are obtained via $\chi(\mathbf{k}) = [I(\mathbf{k}) - I_0(\mathbf{k})]/\sqrt{I_0(\mathbf{k})}$, where $I(\mathbf{k})$ is the raw measured fluorescence, and $I_0(\mathbf{k})$ is the fluorescence due specifically to the unscattered, direct wavefront excitation of the emitter. These normalized $\chi(\mathbf{k})$ intensities in **k**-space can be considered an **r**-space convolution of the object field $u(\mathbf{r})$ of the scattering atoms surrounding the emitter at the origin, with the convolution kernel describing all of the physics of the x-ray scattering [8.19]. This object field can in principle be recovered as an image intensity $U(\mathbf{r}')$, via a **k**-space deconvolution of the $\chi(\mathbf{k})$ data set that is in its simplest "optical" form given by:

$$U(\mathbf{r}') \equiv \iiint_K d^3\mathbf{k} \cdot e^{-i(\mathbf{k}\cdot\mathbf{r}' - kr')}\chi(\mathbf{k}). \tag{8.1}$$

This multiple energy imaging algorithm, and its positive aspects in suppressing twin images and other sources of image aberrations, was first pointed out by Barton [8.3a,8.3b], and subsequently proposed in a slightly different form by Tong *et al.* [8.3c]. The kernel $e^{-i(\mathbf{k}\cdot\mathbf{r}' - kr')}$ implies that the scattered x-rays are isotropic in amplitude, and that

the scattering phase shift is zero, or at least constant, both of which conditions are reasonably well met for the scattering of *unpolarized* x-rays [8.14]. However, since MEXH is most easily done on synchrotron radiation beamlines whose most intense radiation has very strong linear polarization, we here explore the consequences of the highly anisotropic scattering amplitudes which result largely due to Thomson scattering.

8.3. Theoretical and experimental images of α-Fe_2O_3(001)

We now show results of applying the reconstruction algorithm of Eq. (8.1) to experimental and theoretical α-Fe_2O_3(001) (hematite) MEXH $\chi(\mathbf{k})$ data sets, with the radiation polarization being explicitly included in the calculations. The experimental MEXH data was measured by Gog and co-workers at beamline X-14A of the National Synchrotron Light Source at the Brookhaven National Laboratory [8.16]. Fe Kα fluorescence was collected for horizontally polarized incident radiation spanning three energies from $k = 4.561\text{Å}^{-1}$ to 5.220Å^{-1} ($E = 9.00$keV to 10.30keV) and incident on the α-Fe_2O_3(001) sample over a polar range of $60° \le \theta \le 90°$. The experimental geometry is illustrated in Fig. 8.1(b), with the relationship between the horizontal polarization and the rotation axes of the sample being indicated. The polarization is here parallel to the polar rotation axis ($\hat{\theta}$) of the sample, with the azimuthal rotation axis ($\hat{\phi}$) being parallel to the surface normal. These data points were measured at $\delta k = 0.329\text{Å}^{-1}$ ($\delta E = 650$eV) energy intervals, and at $(\delta\theta,\delta\phi) = (5°,5°)$ angular intervals, making a total of 435 unique measurements in a symmetry-reduced 1/3rd of the total solid-angle above the sample. Fig. 8.1(c) shows the raw measured $I(\mathbf{k})$ intensities in **k**-space, as viewed down along $[00\bar{1}]$. Data points in the fourth quadrant have been cut away to reveal the $k = 4.561\text{Å}^{-1}$ $I(\mathbf{k})$ intensities. The dark bands at the perimeter indicate the locations in **k**-space on these iso-energy surfaces where data was not collected. Note that the weak atomic scattering of x-rays renders the anisotropy of the raw $I(\mathbf{k})$ data ($\Delta I / I_0 \approx 0.5\%$) barely discernible with this gray scale; and thus much more demanding statistical accuracy is required in x-ray

holographic measurements than in comparable atomic electron holography measurements (where $\Delta I / I_0 \approx 30\%$) [8.20]. However, the more ideal and weaker nature of the atomic scattering of x-rays also produces atomic images that are relatively free of image aberrations, artifacts, and positions shifts compared to atomic electron holography images [8.14,8.21-8.23].

Due to the limited energy range of this $I(\mathbf{k})$ data set, a separate $I_0^k(\mathbf{k})$ was determined for each of the three different hologram energies via a high-pass filter [8.24], thereby including in $I_0^k(\mathbf{k})$ the reference wave as well as any low-angular-frequency effects in the initial excitation of the x-ray and the subsequent absorption as the fluorescence exits the sample, via:

$$I_0^k(\mathbf{k}) = \frac{\iint_S k^2 d\sigma_{\hat{\mathbf{k}}} e^{-\sigma^2(\mathbf{k}-\mathbf{k}')^2} I_k(\mathbf{k}')}{\iint_S k^2 d\sigma_{\hat{\mathbf{k}}}}. \tag{8.2}$$

All of these effects need to removed from the raw $I(\mathbf{k})$ intensities before applying the imaging algorithm. Figure 8.1(d) shows the normalized $\chi(\mathbf{k})$ obtained by this method from the raw $I(\mathbf{k})$ intensities of Fig. 8.1(c), with holographic modulations more visible.

For comparison, a single-scattering model [8.14,8.25] was used to calculate a theoretical MEXH $\chi(\mathbf{k})$ data set from an ideal α-$Fe_2O_3(001)$ cluster containing only 384 Fe atoms occupying the two inequivalent Fe emitter sites appropriate to this crystal structure. The O atoms were omitted, as they will be negligibly strong in the resulting reconstructed images due to their relatively smaller scattering power [8.16]. The incident radiation in this model calculation is polarized horizontally with respect to the $\hat{\theta}$ and $\hat{\phi}$ rotations performed on this cluster, just as for the measurement of the experimental $I(\mathbf{k})$ data set discussed above (*cf.* Fig. 8.1(b)). As the sample was rotated over the $60° \leq \theta \leq 90°$ range of the experimental data, the polarization (and the resultant Thomson cross section) rotated also with respect to the crystal structure, but with an average overall

effect still of having much stronger scattering for atoms above and below a given emitter along the surface normal or [001] direction.

Figure 8.2 schematically shows the **r**-space regions in the vertical (120) and horizontal $(00\bar{2})$ planes that would have enhanced/suppressed image intensities due to the effect of using horizontally polarized incident radiation, relative to the image intensities obtained from an unpolarized incident radiation MEXH data set. The image intensity in Fig. 8.2 is thus the ratio $U_{horizontal}(\mathbf{r}')/U_{unpolarized}(\mathbf{r}')$, with white representing a value of unity, and gray, values of < 1. As can be seen in Fig. 8.2, the use of horizontally polarized incident radiation would most strongly suppress atomic images in the horizontal (001) plane containing the emitter, with this suppression being less in horizontal planes farther above and below the emitter plane. Images along the [001] axis would be least suppressed by using horizontally polarized incident radiation. Thus, using horizontally polarized radiation in the geometry of Fig. 8.1(b) would in fact be disadvantageous in the study of horizontal planar structures such as those prevalent in α-$Fe_2O_3(001)$, which is comprised of closely stacked horizontal Fe bi-layers.

We now show the reconstructed atomic images obtained from applying Eq. (8.1) to the experimental (Fig. 8.3) and theoretical (Fig. 8.4) single-scattering model MEXH $\chi(\mathbf{k})$ data sets for α-$Fe_2O_3(001)$ in (a) the vertical (120) plane, and (b) the horizontal $(00\bar{2})$ plane that is 6.89Å below the emitter. These images are the all superpositions of images for both of the inequivalent Fe emitter sites, with these emitter sites indicated by a common dashed square at the origin, and the relative positions of the Fe scatterers indicated by circles. Fe scatterers just above or below the $(00\bar{2})$ Fe bi-layer are indicated by dashed circles, and Fe scatterers in relative positions common to both inequivalent Fe emitters are indicated by bold circles. The atomic image resolutions expected from $\chi(\mathbf{k})$ data sets of this energy and angular range [8.24] are $\delta x = \delta y \approx 0.6$Å in the horizontal ([001] and [120]) directions, and $\delta z \approx 2.5$Å in the vertical ([001]) direction, and these resolutions are indicated by white error bars in the figures. The experimental and

theoretical images are in excellent agreement. In particular, both experiment and theory show that three of the Fe atoms from the neighboring upper bi-layer intrude into the $(00\bar{2})$ image plane. This is due to the limited energy and angular range of the $\chi(\mathbf{k})$ data set in **k**-space, which results in atomic images much less resolved in the vertical [001] direction [8.24]. Also, as expected from the suppression of horizontal image intensities that arises from the use of horizontally polarized incident radiation, the Fe atomic images in the (001) plane are not visible in Figs. 8.3-8.4(a), and the $(00\bar{2})$ in-plane atoms ($10\frac{\bar{1}}{2}$, $01\frac{\bar{1}}{2}$, *etc.*) are also not visible in Figs. 8.3-8.4(b), due to their horizontal distance from the [001] axis. The only Fe atomic images that have not been appreciably suppressed lie more nearly along the vertical [001] direction above and below the emitter (*cf.* Figs. 8.2(a), 8.3(a), 8.4(a)). In spite of the image suppression due to the polarization of the incident radiation, and the resolution loss due to the limited energy and angular range of these $\chi(\mathbf{k})$ data sets, the resulting images are found to exhibit a suppression of real-twin image overlaps, as they are reconstructed from a multiple energy $\chi(\mathbf{k})$ data set [8.3,8.14,8.16-8.18].

8.4. Effect of incident polarization on MEXH holographic intensities

In order to best image horizontal and vertical atomic positions simultaneously, utilizing unpolarized incident radiation would be ideal. However, because synchrotron radiation is the most practical experimental MEXH incident radiation source due to its energy tunability, high brightness, and potentially high energy resolution (*e.g.* via undulators and/or crystal monochromators), linearly polarized incident radiation must be considered. We thus now discuss in more detail the effect of incident radiation polarization on the creation of MEXH $\chi(\mathbf{k})$ intensities for two model systems.

Figure 8.5 shows the Fe atomic scattering factor magnitudes $|f_{Fe}(\Theta)|$ for x-rays at $k = 5.220\text{Å}^{-1}$ ($E = 10.30\text{keV}$), where Θ is the angle between the incident (**k**) and scattered (**k'**) wavefronts [8.25]. The raw Fe scattering factor magnitude, as given in relative electron scattering units (Fig. 8.5(a)), is converted to absolute units by multiplying by the

Thomson scattering factor for a single electron interacting with either unpolarized or linearly polarized light, as the case may be. The general form of the well-known Thomson scattering factor is $\sin\Theta_{\hat{\mathbf{e}}}^{\mathbf{k}'}$, where $\Theta_{\hat{\mathbf{e}}}^{\mathbf{k}'}$ is the angle between the polarization vector of the incident radiation $\hat{\mathbf{e}}$, and the direction $\mathbf{k}'$ of the scattered radiation. Figures 8.5(b)-(d) show the Thomson scattering factors for unpolarized, horizontally polarized, and vertically polarized light, respectively. The "peanut"-shaped unpolarized electron scattering factor (Fig. 8.5(b)) has azimuthal symmetry about the incident wavevector axis, while this symmetry is broken for the "bagel"-shaped linearly polarized scattering factors (Figs. 8.5(c)-(d)), which for horizontal and vertical polarization show preferential scattering in the vertical and horizontal directions, respectively.

The effect of polarized incident radiation in MEXH can be demonstrated by considering the ideal $\chi(\mathbf{k})$ holograms created by simple [001] and [100] linear Fe trimers oriented along the vertical or horizontal direction, respectively, as shown to the left of Figs. 8.6-8.8. In these calculations, the trimers were rotated with respect to the incident radiation polarization so as to simulate a real experimental situation with a movable sample and a fixed beamline. Figures 8.6-8.8 show the expected holographic intensities in the full upper 2π hemisphere above these Fe trimers, as viewed down along the $[00\bar{1}]$ directions, for a hologram energy of $k = 5.220\text{Å}^{-1}$ ($E = 10.30\text{keV}$). The holographic interference fringes in the case of unpolarized incident radiation are visible as azimuthal bands for the vertical [001] Fe trimer in Fig. 8.6(a), and as vertical bands centered along the [100] direction for the horizontal [100] Fe trimer in Fig. 8.6(b). Figures 8.9-8.11 show the atomic image intensities reconstructed via Eq. (8.1) along these trimers. The full-width at half-max (FWHM) of these image peaks are close to the resolutions expected from the energy and angular range of these $\chi(\mathbf{k})$ data sets ($dx \approx 0.31\text{Å}$; $dz \approx 0.61\text{Å}$) [8.24].

Figure 8.7 shows the MEXH $\chi(\mathbf{k})$ holograms from these same Fe trimers, but in the case of incident radiation polarized horizontally with respect to a stationary

synchrotron source, where the polarization vector $\hat{\mathbf{e}}_1$ is parallel to the $\hat{\theta}$ rotation axis, as shown in Fig. 8.1(b). Due to the azimuthal symmetry of the horizontal polarization with respect to the [001] Fe trimer for all incident radiation angles, the resulting hologram in Fig. 8.7(a) is virtually identical (although relatively less intense, due to the loss of one polarization mode) to the unpolarized incident radiation hologram in Fig. 8.6(a). However, the $\chi(\mathbf{k})$ hologram intensities for the [100] Fe trimer in the case of horizontally polarized light are suppressed in directions perpendicular to the [100] trimer axis (Fig. 8.7(b)). There, the Thomson scattering factor selects against scattering between the trimer atoms, such that there is much reduced holographic information in these regions. This effect is seen in the reconstructed images of Fig. 8.10, where the [001] Fe trimer image peaks (Fig. 8.10(a)) are now approximately four times higher in intensity than the [100] Fe trimer image peaks (Fig. 8.10(b)). Thus horizontal polarization emphasizes atomic images along the vertical azimuthal axis, while suppressing horizontal planar atomic images, as noted before for the more complex α-$Fe_2O_3(001)$ case.

Figure 8.8 shows the MEXH $\chi(\mathbf{k})$ holograms from the [001] and [100] Fe trimers, in the case of incident radiation polarized vertically with respect to a stationary synchrotron source, where the polarization vector $\hat{\mathbf{e}}_2$ is now always perpendicular with the $\hat{\theta}$ rotation axis. Again, due to the azimuthal symmetry of the vertical polarization with respect to the [001] Fe trimer for all incident radiation angles, the resulting hologram in Fig. 8.9(a) is nearly identical in the upper polar regions to the unpolarized incident radiation hologram in Fig. 8.7(a), but is weaker in intensity for lower polar angles, where the polarized Thomson scattering factor selects against scattering between the trimer atoms, leading to reduced holographic information in these regions. For the [100] Fe trimer hologram, the polarized Thomson scattering factor suppresses holographic intensities in the upper polar regions parallel to the [100] trimer orientation. This effect is seen in the reconstructed images of Fig. 8.11, where the [001] Fe trimer image peaks (Fig. 8.11(a)) are now approximately half the intensity of the [100] Fe trimer image peaks (Fig.

8.11(b)). Thus for horizontal polarized incident radiation, holographic intensities in specific regions are suppressed for both the [001] and [100] trimers, but the net effect for images reconstructed from the full upper 2π hemisphere is to suppress peak intensities along the vertical [001] axis more than in the horizontal plane.

Therefore compared to unpolarized incident radiation, linearly polarized incident radiation reduces the amount of spatial information corresponding to specific atomic sites available in MEXH $\chi(\mathbf{k})$ intensities. Horizontally polarized incident radiation suppresses holographic and reconstructed image intensities for atoms in the horizontal (001) plane of the emitter, while emphasizing intensities for atoms in the vertical [001] axis through the emitter. For low polar angles, vertically polarized incident radiation suppresses low take-off angle $\chi(\mathbf{k})$ intensities from atoms in the vertical [001] axis through the emitter, while emphasizing $\chi(\mathbf{k})$ intensities from atoms in the horizontal plane of the emitter; these effects are reversed when higher polar angles are considered for vertically polarized incident radiation. When taken over the entire full upper 2π hemisphere of $\chi(\mathbf{k})$ intensities, reconstructed image intensities for atoms along the vertical [001] axis are suppressed more, relative to atoms in the horizontal plane of the emitter.

8.5. Effect of incident polarization on MEXH atomic images

In order to illustrate the possible utility of linearly polarized incident radiation in obtaining MEXH atomic images, we consider a general class of structures where it should be advantageous to utilize horizontally polarized incident radiation, and for which vertical structural information can be much more desirable than horizontal structural information: surface atomic layers and buried epitaxial atomic layers. A specific case theoretically illustrated here is a Ge δ-layer buried in Si(001). The Ge atoms in the δ-layer are here assumed to lie in horizontal epitaxial sites with respect to the surrounding Si(001), such that structural information in the horizontal plane of a Ge emitter is relatively unimportant compared to the strained vertical distances between the Ge δ-layer atoms and their Si

neighbors above and below them [8.26]. Thus using horizontally polarized incident radiation to record a MEXH Ge Kα data set for this system or others like it may prove to be advantageous.

MEXH $\chi(\mathbf{k})$ intensities were calculated for unpolarized, horizontally polarized, and vertically polarized radiation incident on an ideal Ge δ-layer buried in a Si(001) cluster containing a total of 96 atoms, where for simplicity no vertical interlayer strain was considered. The incident radiation ranged in energy from $k = 6.081\text{Å}^{-1}$ to 9.122Å^{-1} ($E =$ 12.00keV to 18.00keV), which is above the Ge K absorption edge ($k = 5.625\text{Å}^{-1}$, or $E =$ 11.00keV), and enables the imaging of the equivalent atomic environment surrounding each Ge emitter. This radiation is incident over a polar range of $10° \le \theta \le 90°$, and these holograms were calculated at seven energies corresponding to $\delta k = 0.507\text{Å}^{-1}$ ($\delta E =$ 1.000keV) and $(\delta\theta, \delta\phi) = (5°, 5°)$ intervals, for a total of 1,897 unique data points in a symmetry-reduced 1/4th of the total solid-angle above the cluster. The higher energy and larger energy and angular ranges of this MEXH data ensure better resolved atomic images ($\delta x = \delta y \approx 0.2\text{Å}$; $\delta z \approx 0.4\text{Å}$) than those of Figs. 8.3-8.4 [8.24].

Figure 8.12 shows the reconstructed atomic image in the vertical $(\bar{1}10)$ plane obtained by applying Eq. (8.1) to the theoretical unpolarized incident radiation MEXH $\chi(\mathbf{k})$ data set. The typical Ge emitter site is indicated by a dashed square, Ge scatterers are indicated by squares, and the bulk Si scatterers are indicated by circles. In this image the Ge δ-layer atoms are well-defined, and the Si atoms in the layer immediately above the δ-layer are moderately resolved. Images of the Si layers further above, and below the δ-layer are faintly discernible with this gray scale.

In contrast, atomic images reconstructed from linearly polarized incident radiation MEXH $\chi(\mathbf{k})$ data sets are enhanced/suppressed in specific regions, relative to the unpolarized incident radiation atomic images of Fig. 8.12. Figures 8.13(a) and 8.14(a) show the relative image enhancement ratios $U_{horizontal}(\mathbf{r}')/U_{unpolarized}(\mathbf{r}')$ and $U_{vertical}(\mathbf{r}')/U_{unpolarized}(\mathbf{r}')$, respectively, for atomic images reconstructed in the $(\bar{1}10)$

plane from horizontally and vertically polarized incident radiation $\chi(\mathbf{k})$ data sets. As seen earlier in Fig. 8.2(a), Fig. 8.13(a) shows that atomic images along the vertical [001] axis through the emitter (*i.e.*, the 001 and $00\bar{1}$ atoms) will be most enhanced relative to images near the horizontal (001) plane (the $\frac{\bar{1}}{2}\frac{\bar{1}}{2}0$, $\frac{1}{2}\frac{1}{2}0$, $\frac{\bar{1}}{4}\frac{\bar{1}}{4}\frac{1}{4}$, and $\frac{1}{4}\frac{1}{4}\frac{1}{4}$ atoms) when reconstructed from MEXH data obtained with horizontally polarized incident radiation. The image regions specifically enhanced in Fig. 8.13(a) differ slightly from that of Fig. 8.2(a), due to the different energy and angular ranges of their respective $\chi(\mathbf{k})$ data sets. Figure 8.13(b) shows the reconstructed atomic images obtained from horizontally polarized MEXH data in the vertical $(\bar{1}10)$ plane, where as expected the Ge δ-layer atomic images are suppressed relative to the prominent Si atomic images along the [001] axis. Thus strain in the vertical interlayer distances in this system would be most easily determined in an MEXH experiment using horizontally polarized incident radiation.

Figure 8.14(a) shows that atomic images in the horizontal (001) plane (*i.e.*, the $\frac{\bar{1}}{2}\frac{\bar{1}}{2}0$ and $\frac{1}{2}\frac{1}{2}0$ atoms) will be enhanced relative to images in the vertical [001] axis (the 001 and $00\bar{1}$ atoms) when reconstructed from MEXH data obtained with vertically polarized incident radiation. Figure 8.14(b) shows the reconstructed atomic images in the vertical $(\bar{1}10)$ plane obtained from such a data set. Similar to the unpolarized images of Fig. 8.12, the most prominent features in Fig. 8.14(b) are the Ge δ-layer atoms, followed by the Si atoms in the layer immediately above them. However, the faint Si atomic images in the outlying planes of Fig. 8.12 are strongly suppressed in Fig. 8.14(b), both due to their distance from the Ge emitter, and the vertical polarization of the incident radiation. Thus, recording MEXH intensities with vertically polarized incident radiation would not be most ideal for this particular system, but would be ideal for the imaging of other structures where atomic images in the horizontal (001) plane would be of more interest.

Also of note are the presence of faint image aberrations in Figs. 8.13(b) and 8.14(b) near the emitter, as compared to Fig. 8.12. These aberrations are due to there being less holographic information overall (*i.e.*, fewer visible hologram fringes) in the

MEXH $\chi(\mathbf{k})$ data sets obtained with polarized incident radiation, relative to the set obtained with unpolarized incident radiation (*cf.* Figs. 8.6-8.11).

The relative intensities of the atomic sites that have been preferentially/detrimentally imaged due to the polarization of the incident radiation can be restored. The use of a so-called SWIFT (Scattered-Wave Included Fourier Transform) correction to the reconstruction algorithm of Eq. (8.1) is one method for accomplishing this, given by [8.4a]:

$$U(\mathbf{r}') \equiv \iiint_K d^3\mathbf{k} \cdot \frac{e^{-i(\mathbf{k}\cdot\mathbf{r}'-kr')}\chi(\mathbf{k})}{f_{Fe}(\Theta_{\mathbf{k}}^{\mathbf{r}'})\sin(\Theta_{\hat{\mathbf{e}}}^{\mathbf{r}'})}. \tag{8.3}$$

Here, one is simply dividing by the strength of the scattered wave associated with an atom along $\mathbf{r}'$. However, doing this type of correction becomes problematic due to the nodes of the Thomson scattering factor $\sin(\Theta_{\hat{\mathbf{e}}}^{\mathbf{r}'})$, such that the integrand in Eq. (8.3) will have divisions by zero. An *ad hoc* solution would then be to limit the SWIFT correction to the angular regions where the Thomson scattering factor is appreciably non-zero [8.27,8.28]. However, we also note that the relative intensities of atomic sites enhanced/diminished by polarization effects can be restored simply by dividing the images by the appropriate enhancement ratios $R_{enh} = U_{polarized}(\mathbf{r}')/U_{unpolarized}(\mathbf{r}')$. Determining this ratio does not require the direct experimental measurement of $\chi(\mathbf{k})$ intensities obtained using polarized and unpolarized incident radiation, as we find from an analysis of exact calculations for various geometries that it can approximated using:

$$R_{enh} = \frac{U_{polarized}(\mathbf{r}')}{U_{unpolarized}(\mathbf{r}')} \approx \frac{\iiint_k d^3\mathbf{k} \cdot \sin(\Theta_{\hat{\mathbf{e}}}^{\mathbf{k}'\equiv\mathbf{r}'})}{\iiint_k d^3\mathbf{k} \cdot \frac{1}{2}\sqrt{1+\cos^2(\Theta_{\mathbf{k}}^{\mathbf{k}'\equiv\mathbf{r}'})}}. \tag{8.4}$$

The enhancement ratio is thus approximated by the relative contribution to an atomic

image at $\mathbf{r}'$ due to the $\mathbf{k}$-space domains in $\chi(\mathbf{k})$ that are selectively enhanced by the polarized Thomson scattering factor. Figures 8.13(c) and 8.14(c) show the reconstructed atomic images of Figs. 8.13(b) and 8.14(b) that have been corrected by dividing out the appropriate approximate polarization (horizontal and vertical, respectively) enhancement factor of Eq. (8.4). The relative intensities between all of the atomic sites in the corrected images of Figs. 8.13(c) and 8.14(c) are now well restored to uniform values, in comparison to the unpolarized atomic images of Fig. 8.12. It is of note that the atomic sites that have been detrimentally affected by the use of polarized incident radiation are discernible in both uncorrected (Figs. 8.13(b) and 8.14(b)) and corrected images (Figs. 8.13(c) and 8.14(c)); merely the relative intensities between all atomic sites have been equalized in the corrected polarized images. As expected, the faint image aberrations in Figs. 8.13(b) and 8.14(b) persist in the corrected images of Figs. 8.13(c) and 8.14(c), due to the overall loss of signal-to-noise in polarized incident radiation $\chi(\mathbf{k})$ data sets, compared to the image reconstructed from the unpolarized incident radiation $\chi(\mathbf{k})$ data set (Fig. 8.12).

8.6. Conclusions

Multiple energy x-ray holography (MEXH) holds much promise in the imaging of local atomic structure surrounding a specific emitter species of interest, as demonstrated here in the first experimental data obtained with it, and for the model system of buried atomic δ-layers. However, there are strong effects in these atomic images due to the Thomson scattering cross section when linearly polarized radiation is used for exciting the fluorescence signal. Utilization of horizontally or vertically polarized incident radiation can emphasize vertical or horizontal atomic structures, respectively. Approximate procedures for correcting for this non-uniformity in image strengths are also discussed. If full three-dimensional atomic structural information is desired from a specific sample, then either unpolarized or circularly polarized radiation should be used for excitation, or the

sample should be mounted such that it can be illuminated by either linear polarization mode relative to the polar and azimuthal rotations being carried out on it. MEXH intensities that would be measured for the case of unpolarized incident radiation also can be determined from the two individual polarized MEXH data sets as obtained over most of the solid-angle above the sample.

References

[8.1] D. Gabor, Nature (London) **161** (1948) 777.

[8.2] A. Szöke, in *Short Wavelength Coherent Radiation: Generation and Applications*, T. Attwood, J. Boker (eds.), AIP Conference Proceedings No. 147, (AIP, New York, 1986), 361.

[8.3] (a) J. J. Barton, Phys. Rev. Lett. **61** (1988) 1356, and Phys. Rev. Lett. **67** (1991) 3106. (b) J. J. Barton and L. J. Terminello, paper presented at the Third International Conference on the Structure of Surfaces, Milwaukee, July 1990, and in *Structure of Surfaces III,* S. Y. Tong, M. A. Van Hove, X. Xide, and K. Takanayagi, eds., (Springer Verlag, Berlin, 1991) p. 107. (c) S. Y. Tong, H. Huang, and C. M. Wei, Phys. Rev. B **46** (1992) 2452, and references therein.

[8.4] (a) B. P. Tonner, Z.-L. Han, G. R. Harp, and D. K. Saldin, Phys. Rev. B **43** (1991) 14423. (b) D. K. Saldin, K. Reuter, P. L. De Andres, H. Wedler, X. Chen, J. B. Pendry, and K. Heinz, Phys. Rev. B **54** (1996) 8172.

[8.5] (a) S. Y. Tong, H. Li, and H. Huang, Phys. Rev. B **51** (1995) 1850. (b) H. Wu and G. J. Lapeyre, Phys. Rev. B **51** (1995) 14549. (c) J. M. Roesler, M. T. Sieger, T.-C. Chiang, Surf. Sci. **329** (1995) L588, and references therein.

[8.6] P. J. Rous and M. H. Rubin, Surf. Sci. **316** (1994) L1068.

[8.7] P. Hofmann, K.-M. Schindler, V. Fritzsche, S. Bao, A. M. Bradshaw, and D. P. Woodruff, J. Vac. Sci. Technol. A **12**, 2045 (1994), Surf. Sci. **337** (1995) 169, and references therein.

[8.8] (a) L. J. Terminello, B. L. Petersen, and J. J. Barton, J. Electron Spectrosc. Relat. Phenom. **75** (1995) 229, and references therein. (b) H. Wu, G. J. Lapeyre, H. Huang, and S. Y. Tong, Phys. Rev. Lett. **71** (1993) 251 and references therein. (c) M. Zharnikov, M. Weinelt, P. Zebisch, M. Stichler, H.-P. Steinrück, Surf. Sci. **334** (1995) 114, and references therein. (d) R. Denecke, R. Eckstein, L. Ley, A. E. Bocquet, J. D. Riley, R. C. G. Leckey, Surf. Sci. **331-333** (1995) 1085. (e) J. G. Tobin, G. D. Waddill, H. Hi, S. Y. Tong, Surf. Sci. **334** (1995) 263, and references therein.

[8.9] (a) H. Li, S. Y. Tong, D. Naumovic, A. Stuck, and J. Osterwalder, Phys. Rev. B **47** (1993) 10036. (b) D. K. Saldin, G. R. Harp, and X. Chen, Phys. Rev. B **48** (1993) 8234, and references therein.

[8.10] (a) Z.-L. Han, S. Hardcastle, G. R. Harp, H. Li, X.-D. Wang, J. Zhang, and B. P. Tonner, Surf. Sci. **258** (1991) 313, and references therein. (b) I. H. Hong, S. C. Shyu, Y. C. Chou, and C. M. Wei, Phys. Rev. B **52** (1995) 16884, and references therein.

[8.11] (a) M. A. Mendez, C. Glück, J. Guerrero. P. L. de Andres, K. Heinz, D. K. Saldin, and J. B. Pendry, Phys. Rev. B **45** (1992) 9402, and references therein. (b) C. M. Wei, S. Y. Tong, H. Wedler, M. A. Mendez, and K. Heinz, Phys. Rev. Lett. **72** (1994) 2434, and references therein.

[8.12] S. Y. Tong, H. Huang, and X. Q. Guo, Phys. Rev. Lett. **69** (1992) 3654.

[8.13] M. Tegze, G. Faigel, Europhys. Lett **16** (1991) 41.

[8.14] P. M. Len, S. Thevuthasan, C. S. Fadley, A. P. Kaduwela, and M. A. Van Hove, Phys. Rev. B **50** (1994) 11275.

[8.15] M. Tegze, G. Faigel, Nature **380** (1996) 49.

[8.16] T. Gog, P. M. Len, G. Materlik, D. Bahr, C. Sanchez-Hanke, and C. S. Fadley, Phys. Rev. Lett. **76** (1996) 3132.

[8.17] T. Gog, R.-H. Menke, F. Arfelli, P. M. Len, C. S. Fadley, G. Materlik, Synch.

Rad. News **9** (1996) 30.

[8.18] P. M. Len, T. Gog, C. S. Fadley, and G. Materlik, Phys. Rev. B **55** (1997) 3323.

[8.19] P. M. Len, C. S. Fadley, and G. Materlik, to appear in *X-ray and Inner-Shell Processes: 17th International Conference*, R. L. Johnson, H. Schmidt-Boeckering, and B. F. Sonntag (eds.), AIP Conference Proceedings No. 389 (AIP, New York, 1997).

[8.20] E. Rotenberg, J. D. Denlinger, private communication.

[8.21] D. K. Saldin, G. R. Harp, B. L. Chen, and B. P. Tonner, Phys. Rev. B **44** (1991) 2480.

[8.22] S. Thevuthasan, G. S. Herman, A. P. Kaduwela, T. T. Tran, Y. J. Kim, R. S. Saiki, and C. S. Fadley, J. Vac. Sci. Technol. A **10** (1992) 2261.

[8.23] P. Hu and D. A. King, Phys. Rev. B **46** (1992) 13615.

[8.24] G. R. Harp, D. K. Saldin, X. Chen, Z.-L. Han, and B. P. Tonner, J. Electron Spectrosc. and Relat. Phenom. **57** (1991) 331.

[8.25] *International Tables for X-ray Crystallography*, ed. K. Lonsdale (Reidel, Dordrecht, 1968), Vol. III.

[8.26] J. Falta, T. Gog, G. Materlik, B. H. Muller, and M. Horn-von Hoegen, Phys. Rev. B **51** (1995) 7598, and references therein.

[8.27] S. Thevuthasan, G. S. Herman, A. P. Kaduwela, T. T. Tran, Y. J. Kim, R. S. Saiki, and C. S. Fadley, J. Vac. Sci. Technol. A **10** (1992) 2261.

[8.28] J. Osterwalder, R. Fasel, A. Stück, P. Aebi, L. Schlapbach, J. Electron Spectrosc. Relat. Phenom. **68** (1994) 1.

Figure captions

Figure 8.1. (a) *Multiple energy x-ray holography* (MEXH). A coherent far field excitation x-ray illuminates and photoexcites an emitter, and part of it scatters off of atoms neighboring the emitter in doing so. The emitting atom senses the interference between the direct wavefront, and wavefronts elastically scattered by the neighboring atoms. The net photoexcitation is then detected by a stationary, large solid-angle fluorescence detector. Moving the far field source over a large solid-angle range builds up a holographic interference pattern. (b) Orientation of the sample (where $\hat{\mathbf{n}}$ is the surface normal ([001]) with respect to the horizontal ($\hat{\mathbf{e}}_1$) polarization vector of the incident radiation $\mathbf{k}$. The polar rotation axis $\hat{\theta}$ is parallel to $\hat{\mathbf{e}}_1$. (c) Schematic $\mathbf{k}$-space representation of the raw measured MEXH $I(\mathbf{k})$ intensity data set for Fe Kα fluorescence from α-Fe_2O_3(001) as excited by horizontally polarized radiation at three energies of k = 4.561Å^{-1}, 4.891Å^{-1}, 5.220Å^{-1} (E = 9.00keV, 9.65keV, 10.30keV). (d) The normalized MEXH $\chi(\mathbf{k})$ data set.

Figure 8.2. Theoretically calculated ratio of image intensities obtained using horizontally polarized incident radiation and image intensities obtained using unpolarized incident radiation on α-Fe_2O_3(001), in (a) the vertical (120) plane, and (b) the horizontal $(00\bar{2})$ plane of 6.89Å below the emitter. The superposition of both inequivalent Fe emitter sites is indicated by a dashed square, and Fe scatterers are indicated by circles. Fe scatterers in the bi-layer just above or below this plane are indicated by dashed circles, and Fe scatterers in relative positions common to both inequivalent Fe emitters are indicated by bold circles. Axes are marked off in 1Å units.

Figure 8.3. Reconstructed α-Fe_2O_3(001) atomic images obtained from an experimental MEXH data set measured with horizontally polarized incident radiation, in (a) the vertical (120) plane, and (b) the horizontal $(00\bar{2})$ plane. The image resolution expected from the

energy and angular ranges of this $\chi(\mathbf{k})$ data set are indicated by the white error bars.

Figure 8.4. As Fig. 8.3, but for images obtained from a theoretical horizontally polarized MEXH data set.

Figure 8.5. Scattering factor magnitudes for $k = 5.220\text{Å}^{-1}$ ($E = 10.30\text{keV}$) x-rays incident on atomic Fe. Θ is the angle between the incident ($\mathbf{k}$) and scattered ($\mathbf{k}'$) wavevectors. (a) Fe atomic scattering factor, in relative units of electrons. (b)-(d) Thomson electron scattering factors, in absolute units of $r_e \equiv 2.818 \times 10^{-5}\text{Å}$, for (b) unpolarized, (c) vertically polarized, and (d) horizontally polarized incident x-rays.

Figure 8.6. Normalized holographic intensities $\chi(\mathbf{k})$ as calculated for Fe Kα fluorescence excited by $k = 5.220\text{Å}^{-1}$ ($E = 10.30\text{keV}$) unpolarized x-rays incident on two different Fe trimers, viewed down along $[00\bar{1}]$. (a) [001] Fe trimer $\chi(\mathbf{k})$. (b) [100] Fe trimer $\chi(\mathbf{k})$.

Figure 8.7. As Fig. 8.6, but for the case of horizontally polarized incident radiation.

Figure 8.8. As Fig. 8.6, but for the case of vertically polarized incident radiation.

Figure 8.9. Reconstructed atomic images obtained from the theoretical unpolarized incident radiation MEXH $\chi(\mathbf{k})$ data sets of Fig. 8.6, for (a) the [001] Fe trimer, and (b) the [100] Fe trimer. Image intensities are scaled in arbitrary units relative to each other. The distances $\mathbf{r}'$ along the trimer axes (whether [001] or [100]) are marked off in 1Å units.

Figure 8.10. As Fig. 8.9, but for images reconstructed from the horizontally polarized incident radiation MEXH $\chi(\mathbf{k})$ data of Fig. 8.7.

Figure 8.11. As Fig. 8.9, but for images reconstructed from the horizontally polarized incident radiation MEXH $\chi(\mathbf{k})$ data of Fig. 8.8.

Figure 8.12. Reconstructed Si(001)/Ge-δ/Si(001) atomic images obtained from a theoretical unpolarized incident radiation MEXH $\chi(\mathbf{k})$ data set, in the vertical $(\bar{1}10)$ plane. The typical equivalent Ge emitter site is indicated by a dashed square, Ge scatterers are indicated by squares, and Si scatterers are indicated by circles. Axes are marked off in 1Å units.

Figure 8.13. (a) Ratio of image intensities obtained used horizontally polarized incident radiation to image intensities obtained using unpolarized incident radiation, in the vertical $(\bar{1}10)$ plane. (b) Reconstructed Si(001)/Ge-δ/Si(001) atomic images obtained from a theoretical horizontally polarized MEXH data set, in the vertical $(\bar{1}10)$ plane. (c) As (b), but corrected for the effects of the polarization of the incident radiation.

Figure 8.14. As Fig. 8.13, but for the case of vertically polarized incident radiation.

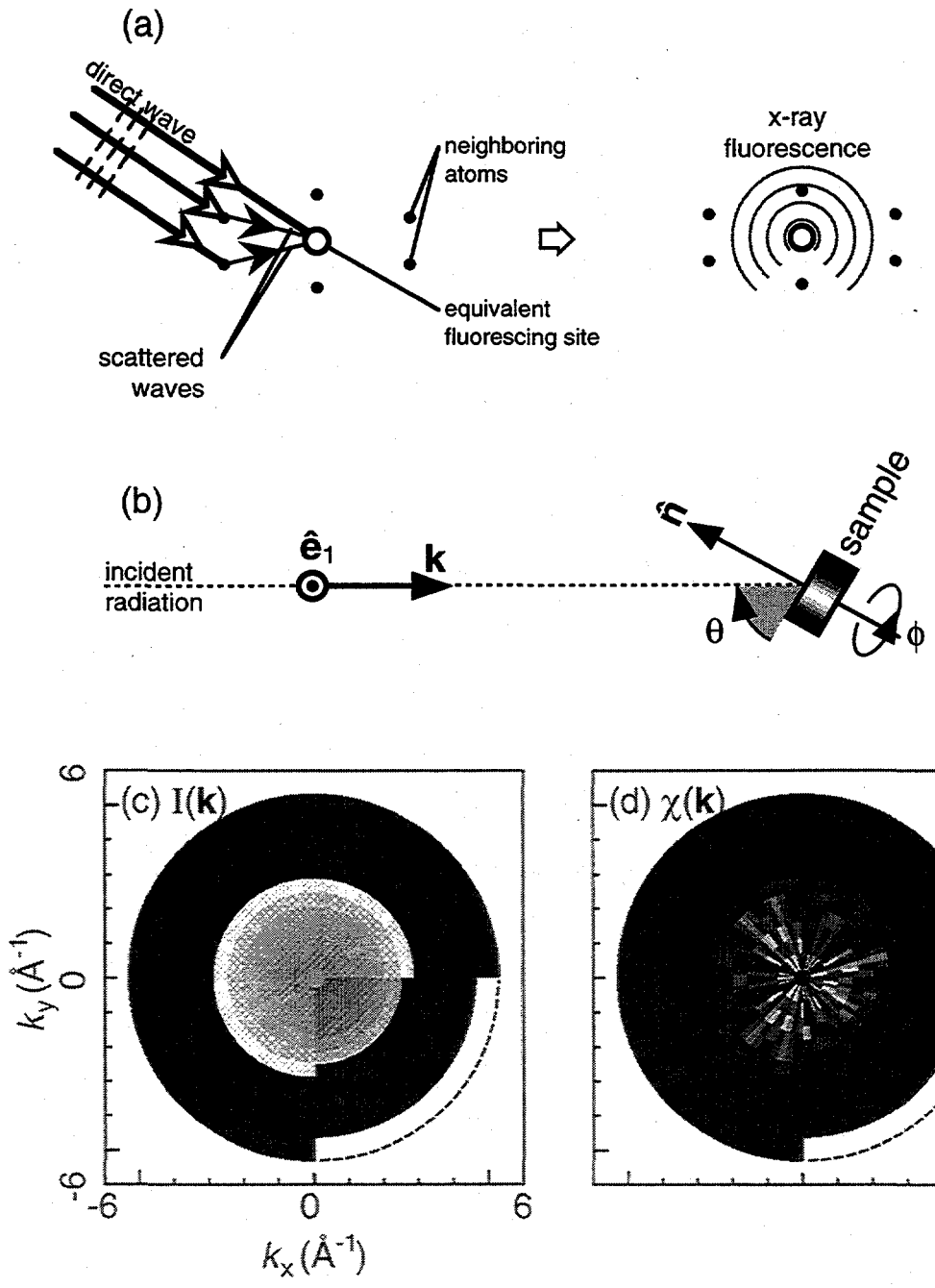

Fig. 8.1

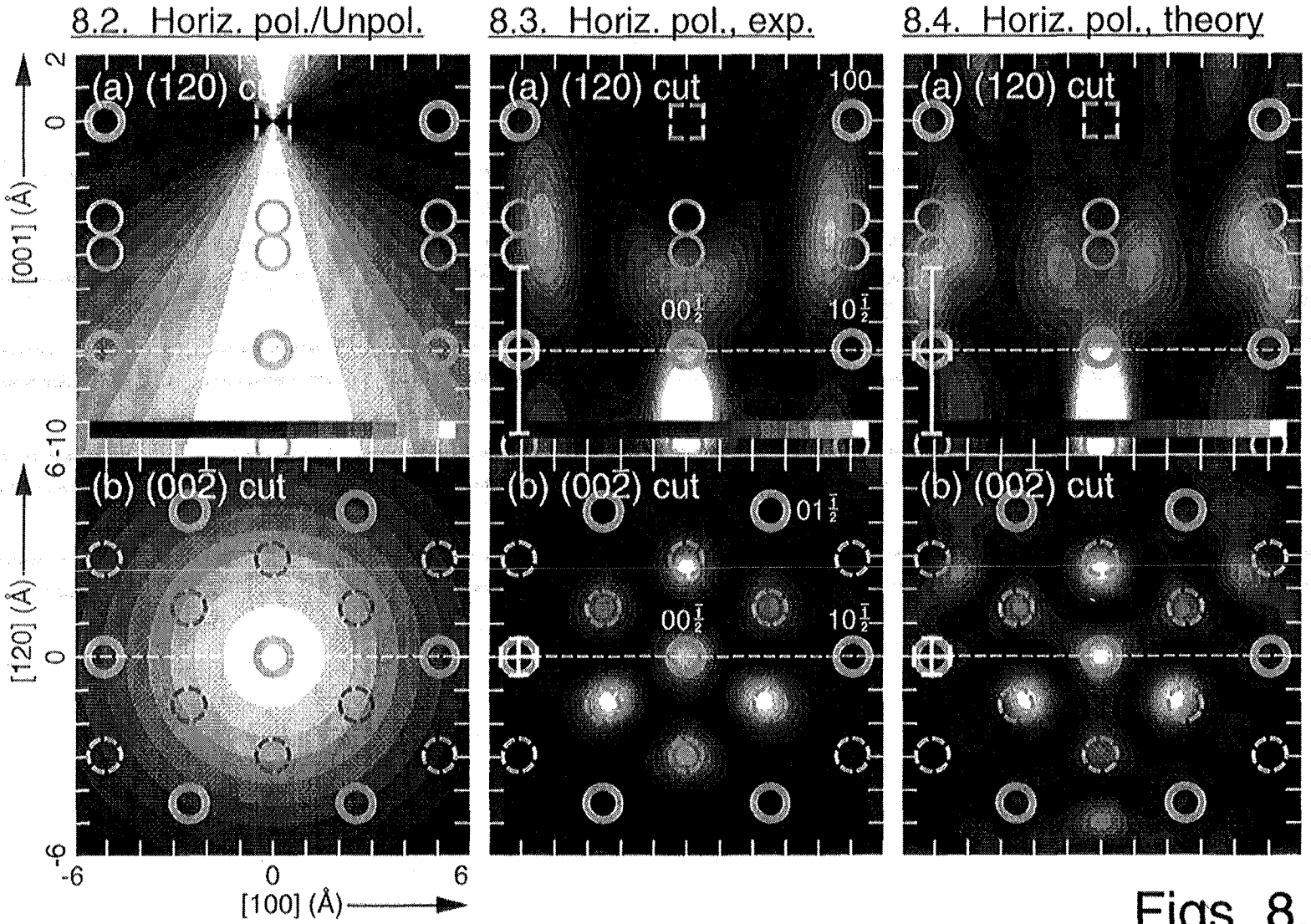

Figs. 8.2-8.4

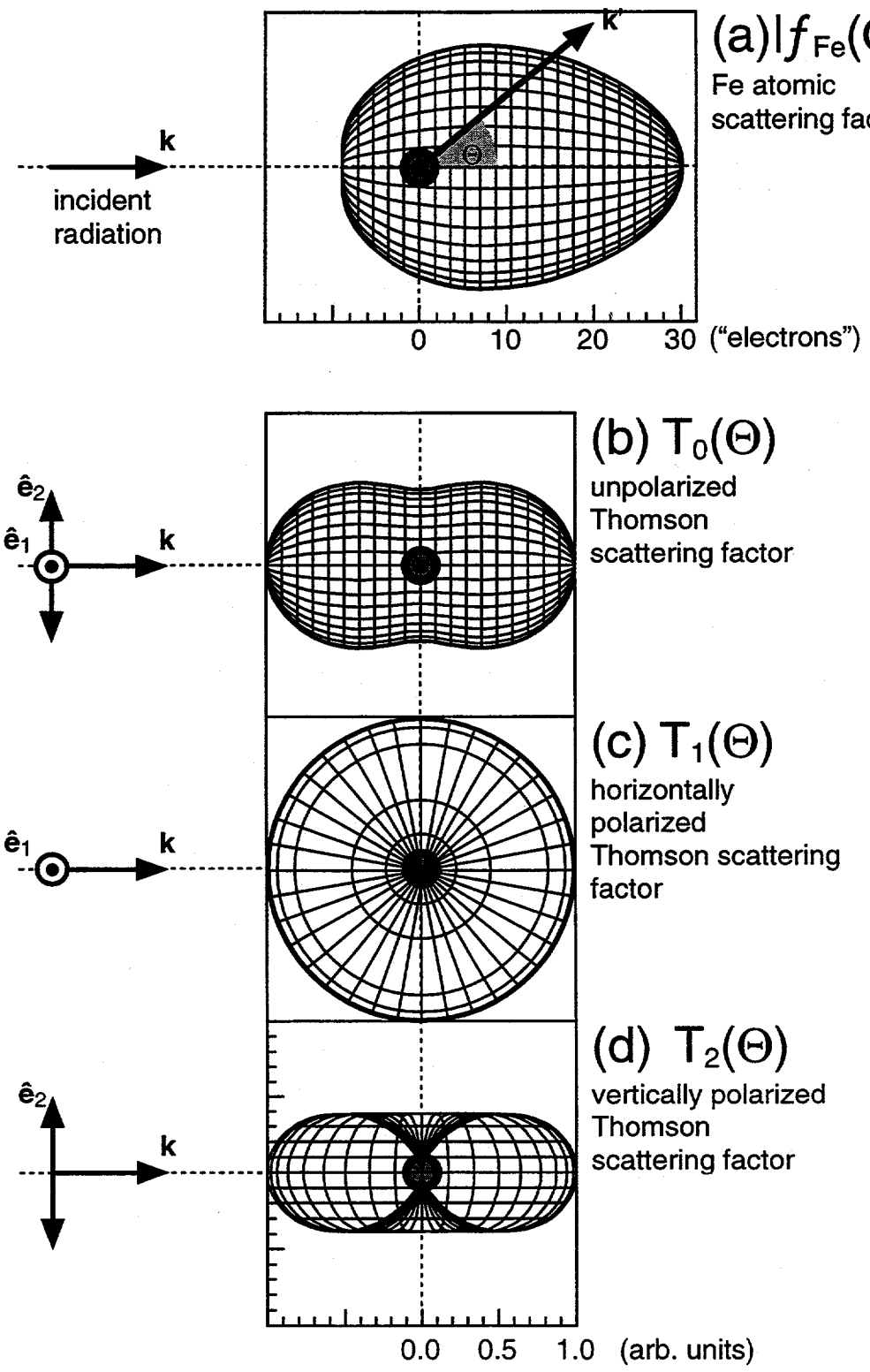

Fig. 8.5

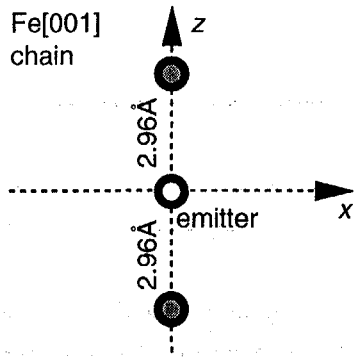

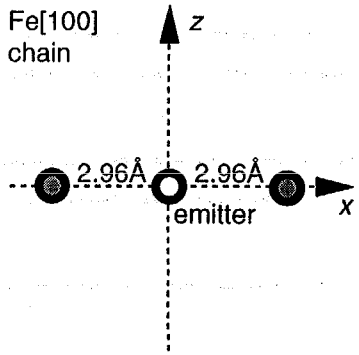

8.6. Unpolarized $\chi(\mathbf{k})$ 8.7. Horiz. polarized $\chi(\mathbf{k})$ 8.8. Vert. polarized $\chi(\mathbf{k})$

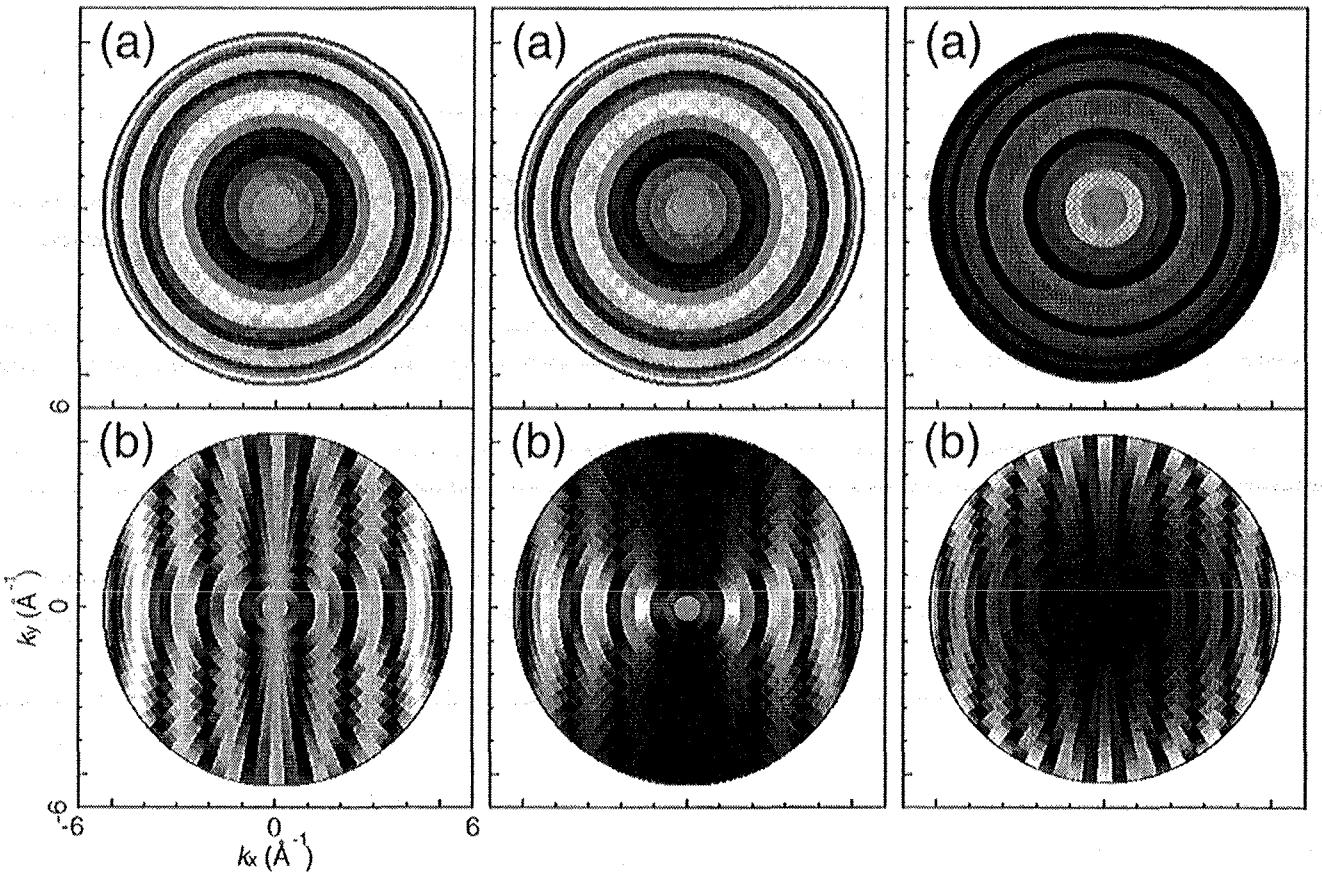

Figs. 8.6-8.8

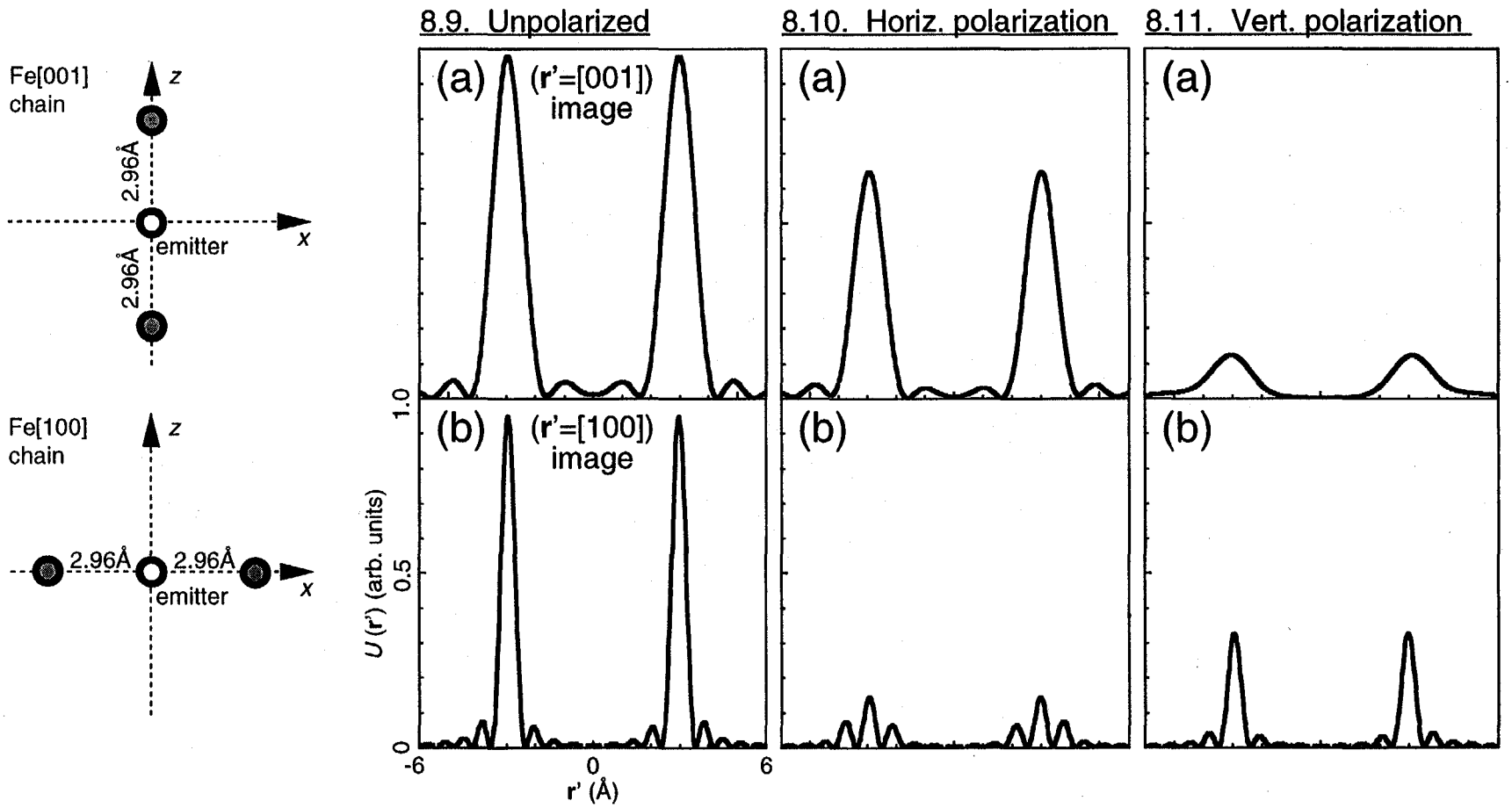

Figs. 8.9-8.11

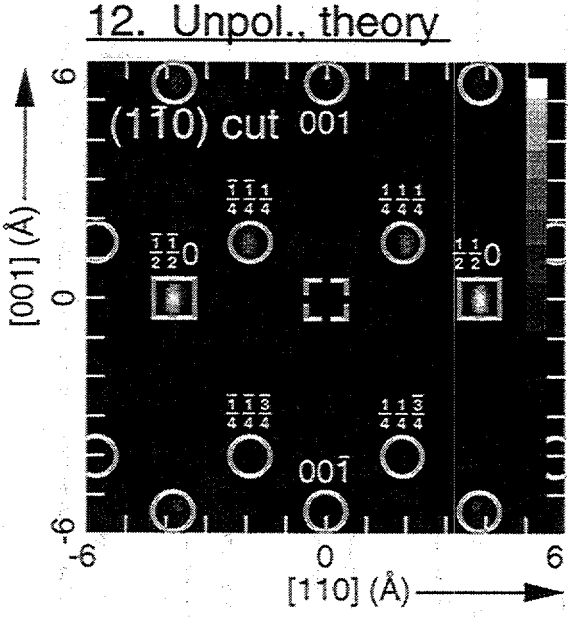

Fig. 8.12

13. Horiz . pol., theory

14. Vert. pol., theory

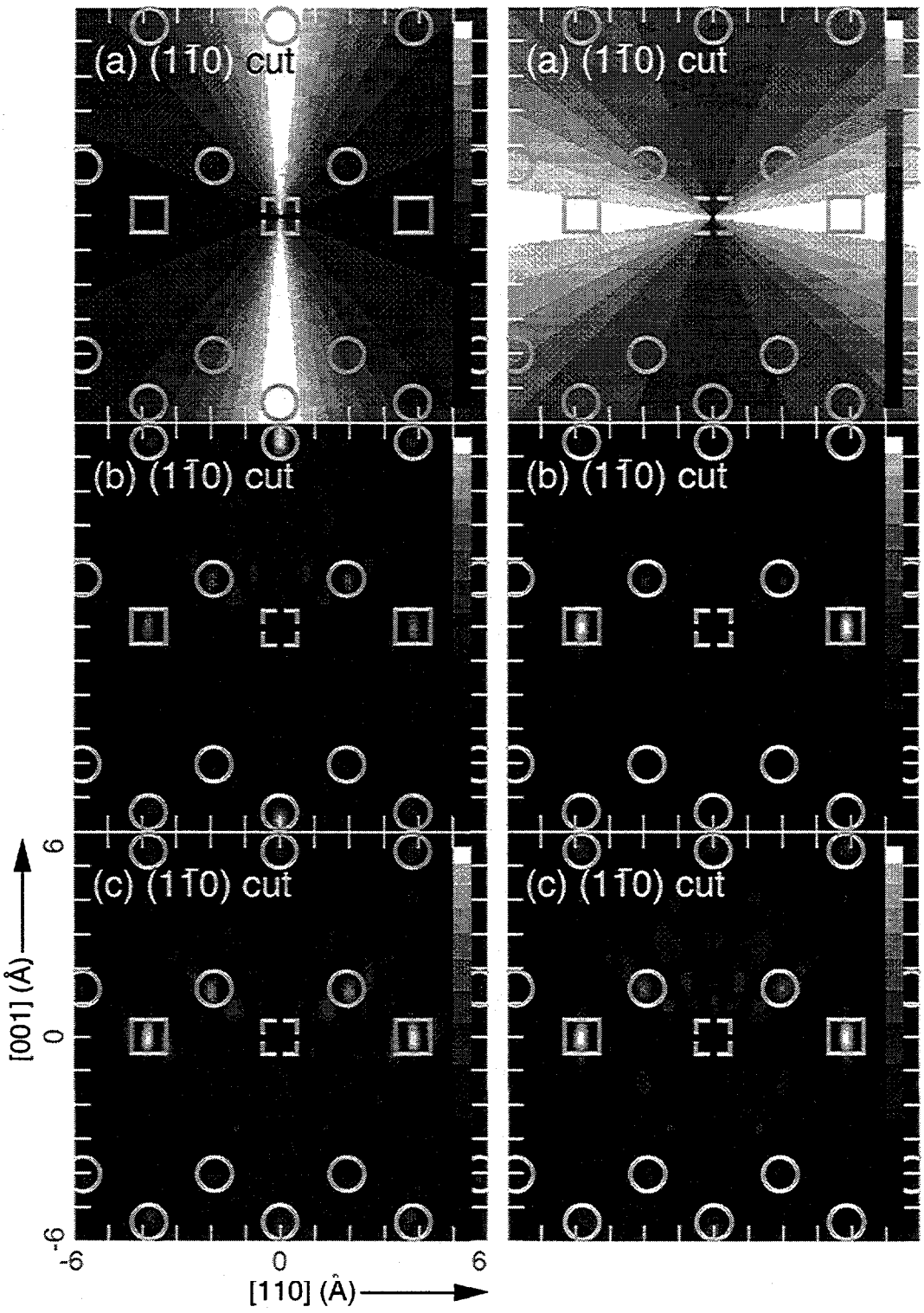

Figs. 8.13-8.14

Chapter 9

Concluding Remarks on the Current and Future Capabilities of Atomic Holography with Electrons and X-Rays

Abstract

We summarize the current status and capabilities of atomic holography using electrons and x-rays, and speculate on the future developments and prospects of these structural probes.

Outline

9.1 Introduction

Since Szöke's proposal ten years ago to implement the holographic principles of Gabor in recording the phases of atomically diffracted photoelectrons and fluorescent x-rays [9.1,9.2], experimental *ab initio* images of atomic structure have been obtained using several proposed reconstruction algorithms [9.3-9.7]. Due to the proof-of-principle nature of these initial efforts to record holographic diffraction intensities from electrons [9.8-9.19] and x-rays [9.20-9.25], the majority of these reconstructed atomic images have been of structures that have already been determined by other means. We will comment on the current status of atomic electron and x-ray holography, possible experimental and theoretical improvements to extend the capabilities of these techniques, and systems that will benefit most uniquely from holographic structural determination.

9.2 The current status and future of atomic electron holography

Figures 9.1(a)-(b) shows the atomic structures of interest that have been fruitfully studied by Atomic electron holography. These structures have been selected for the uniqueness of their equivalent emitter sites (whether the result of core level shifts, or structure, respectively), as well as emphasis on holographic diffraction resulting from a backscattering geometry. Atomic electron holography has notably imaged previously unresolved structures of a surface reconstruction [9.8a] (Fig. 9.1(a)) and different overlayers [9.8b] (Fig. 9.1(b)). These images suffer from position shifts and aberrations due to the non-optical anisotropy of the source and scattered wavefronts, despite analytical correction procedures to the basic reconstruction algorithm of Eq. (1.9) [9.3] (Eqs. (1.10-1.14) [9.4-9.7]), as discussed in Chapters 3-5. The fidelity of forward scattering atomic images from bulk samples and buried interfaces suffer even more from anisotropic wavefront effects. While these image aberrations and position shifts are somewhat tractable for backscattering images, imaging forward scattering atoms will always be problematic, as they will be less resolved than backscattering atomic images even in the total absence of wavefront anisotropy.

This is in contrast to the practice of using *R*-factors for comparing experimental electron diffraction patterns with those calculated from theoretical clusters. Because this technique explicitly includes the effects of source and scattered wavefront anisotropy, it produces structural parameters that are apparently not shifted from those obtained by other structural probes. Thus the accounting for wavefront anisotropy effects is easier in the "normal" case of calculating theoretical diffraction intensities from model clusters, even though it may prove impossible to account these effects to the same degree in the "inverse" case of deconvoluting holographic diffraction patterns to yield atomic images. It is also worth discussing the *R*-factor minimization curves that are obtained by the variation of a structural parameter, such as an epitaxial layer relaxation. Figure 9.2 shows the *R*-

factor curve for varying the vertical relaxation distance of 1ML of epitaxial Cu on Ru(0001) [9.14]. While the vertical relaxation distance with the minimal *R*-factor ($\zeta \approx 1.85\text{Å}$) matches that obtained by other structural probes, note that a second *R*-factor minima is obtained for $\zeta \approx 2.15\text{Å}$, while the uncertainty for either minimum (*i.e.*, FWHM) is comparable to that expected for the vertical [001] image resolution that would be obtained from such a single-wavenumber hologram [9.15]:

$$\delta r \approx \frac{\pi}{\Delta k} \equiv \frac{\pi}{k(\cos\theta_{max} - \cos\theta_{min})} = \frac{\pi}{12.1\text{Å}^{-1}(\sin 90° - \sin 3°)} = 0.27\text{Å}. \qquad (9.1)$$

Thus the structural information obtained by *R*-factor analysis of experimental diffraction patterns with theory yields comparable information to that ideally obtainable from atomic electron holography; but at the same time more directly and effectively accounting for source and scattered wavefront anisotropy.

The problem with using such *R*-factors to judge goodness-of-fit and thus to choose the best structure is that there can be local minima that are not necessarily the absolute minimum (*cf.* the $\zeta \approx 2.15\text{Å}$ minima of Fig. 9.2). The search over various structures can thus get trapped in one of these local minima and never find what is really the best choice for a structure. Thus, the chief motivation for the pursuit of developing atomic electron holography as an adjunct to conventional diffraction methods is in providing a good starting estimate of the local structure so that any subsequent optimization search can be done with confidence that it will not get caught in such a false minimum. That is, if *ab initio* atomic images of good quality can be reconstructed from experimental holographic diffraction data, then these images can provide an unambiguous starting structure to later calculate theoretical diffraction patterns for *R*-factor comparison with the experimental diffraction data.

While the analytical removal of image aberrations and phase shifts from atomic electron holographic images may prove to be limited in scope, there have been several proposals to *experimentally* produce more idealized holographic diffraction patterns. Among them is the recent proposal of Greber and Osterwalder [9.16], whereby positioning a detector near a photoemission node (by minimizing the angle between incident radiation and detector) is expected to result in the suppression of strong forward scattering features in the diffraction patterns, and increased contrast in the more ideal higher-order diffraction fringes. The atomic images reconstructed from these "near-node" holographic diffraction patterns are expected to have increased fidelity, free of the aberrations associated with strong forward scattering effects.

Another promising future application of atomic electron holographyis that it can go beyond obtaining mere structural informationthrough the use of spin detectors or spin-split photoemission so as to image the relative spin environment in materials with local magnetic order [9.17,9.18]. By measuring holographic diffraction patterns at different temperatures, reconstructed images can also reveal structural [9.19] as well as magnetic [9.18] short-range order phase transitions.

9.3 The current status and future of atomic x-ray holography

Figure 9.3 shows various structures of interest that have been and may eventually be fruitfully imaged by atomic x-ray holography. Due to the long extinction length of x-rays, relative to electrons, inelastic attenuation by itself cannot limit the real-space volume of scatterers that contribute to the holographic diffraction intensities [9.20,9.21]. However, the nature of the hologram that is measured, or more specifically, the long-wavelength nature of the modulations that are measured, means that x-ray fluorescence holography is primarily a probe of the short-range atomic structure around a given emitter, just as is the case for photoelectron holography. Thus the structures in Fig. 9.3 have been chosen for their short-range order domains, as well as the uniqueness of equivalent emitter

sites. These structures are presented in rough order of increasing experimental difficulty, and are: (a) mosaic crystals of the type already studied, (b) alloys with compositional disorder but local structural order around a typical higher Z emitter, (c) epitaxial "delta layers" that are a single atom in thickness, (d) dopants which have the same local geometry everywhere, but no long-range order with respect to one another, (e) atomic adsorbates on an ordered substrate surface, with surface defects breaking up the long-range order but short-range order preserved, (f) molecular adsorbates which may not have lateral order with respect to one another, but are all bonded in the same way to the substrate, and (g) biologically active macromolecules which can be crystallized at least in a mosaic fashion and for which the local structure around a particular dilute atomic site (*e.g.* a metal atom) is to be determined.

Atomic x-ray holography, both the single-wavenumber fluorescence type (x-ray fluorescence holography or XFH), and the multiple-wavenumber (inverse) type (multiple-energy x-ray holography or MEXH), have recently been experimentally proven on mosaic crystals such as $SrTiO_3$ [9.22], Fe_2O_3 [9.23,9.24], and Ge [9.25] with relatively little or no of the position shifts or image aberrations seen in comparable atomic electron holographic images. (See Fig. 9.3(a) for a schematic illustration of a mosaic crystal.) Atomic x-ray holography is by no means limited to such bulk samples , and one of its attractive features is in being able to solve certain kinds of problems that are impossible for conventional x-ray diffraction. In addition, these first proof-of-principle papers have caused some confusion and consternation in the conventional x-ray diffraction field [9.26]. Much of this controversy has apparently stemmed from an interpretation of some first papers as claiming that atomic holography is the only means to solve the so-called "phase problem" and thus to get around the trial-and-error nature of structural determinations. However, the phase problem has already been surmounted in conventional x-ray diffraction crystallography by using direct analytical and indirect experimental methods [9.27]. Atomic holography is thus by no means a unique experimental method for

recording diffraction phase information, but it is in fact the most direct one, with the x-ray diffraction approach involving the measurement of many diffracted beams and perhaps also requiring measurements at different wavenumbers and/or with different chemical substitutions in the structure to uniquely determine that absolute phases of all scattered waves. And atomic holography has another key virtue in that the source of the reference wave is atomic in nature and primarily probes the local atomic structure around a given type of emitter. Thus, atomic structures can be determined for systems possessing only short-range-order(*i.e.*, systems with long-range-disorder). Saldin likens the structural information obtained via atomic x-ray holography to what can be seen by a femtoscopic "demon*" atop an atom, brandishing a torch to illuminate its atomic neighborhood [9.28]. Stephens expresses this somewhat less fancifully, if not just as succinctly [9.30], that holography "offers a way of focusing on the deviations from average--the special case that may be buried in an otherwise repeating world."

Due to the fact that the multiple-wavenumber character of MEXH permits obtaining images of higher fidelity than those of single (or few) wavenumber XFH, much of the current research in atomic x-ray holography has focused on MEXH, even with x-ray tubes as incident excitation sources [9.31]. Current MEXH experiments are being carried out on CuAl [9.32], GaAs [9.33], and Cu_3Au [9.34] disordered phase alloys, which have long-range structural order, but no long-range coordination order. Images reconstructed from these MEXH holograms are expected to reveal the average coordination environment of the higher Z sites in these alloys (*i.e.*, the Cu sites in CuAl, and Au sites in Cu_3Au) (Fig. 9.3(b)) and to permit conclusions concerning the possibility of compositional order on a short-range scale.

The current MEXH experiments on bulk samples using solid-state or proportional counter detectors are count rate limited, even with x-ray tube excitation sources. Let us say that we wish to measure a symmetry-reduced single-wavenumber hologram of

* No doubt related in some way to Maxwell's nanoscopic Thermodynamic Demon [9.29].

$N_{total} \approx 10^3$ data points with at least $n \approx 10^7$ counts / data point, so that the fractional statistical noise at each point will be $1/n^{1/2} \approx 0.0003$ and thus much less than the expected holographic modulations of ~0.001-0.003. With a single detector count rate at each data point of $r \approx 10^5$ counts / sec, the total measurement time T will be given by:

$$T \equiv \frac{nN_{total}}{r} \approx 10^5 \text{ seconds} \approx 28 \text{ hours.} \tag{9.2}$$

This is a long experimental time, and it challenges current detector technology. Detection of fluorescence counts to date have either used a non-energy dispersive proportional counter, or an energy dispersive solid-state detector. Both detector schemes result in roughly the same count rate [9.32,9.34]. A proportional counter must count all photons that enter its acceptance window, but it can be coupled with an analyzer crystal to isolate the fluorescence photons via Bragg scattering, such that the detector will only count fluorescence photons. However, analyzer crystals that have been used to date cover only a small part of the total 2π solid angle above the sample. Using a larger solid angle acceptance analyzer crystal geometry would increase the effective single detector count rate r. While a solid-state energy dispersive detector would be able to isolate the fluorescent photons from background photons that enter its acceptance window, the effective single detector count rate r is limited by the fraction of fluorescent photons that it detects, compared to the limiting *integral* amount of photons that it encounters. Thus such a single solid-state detector is capable of detecting fluorescent photons at the same count rate as a single proportional detector/analyzer crystal setup.

An aspect of taking the best experimental data involves the method of scanning angles for a given wavenumber. The initial and simplest approach tried is one of measuring each different azimuthal data point in a polar scan sequentially, with each direction then being counted on only once in the data set [9.32]. However, a better

procedure is to measure the data points in parallel by making many ($\approx 10^2 - 10^3$) azimuthal scans for each polar inclination angle [9.34]. This type of signal accumulation, while work-intensive for the sample and/or detector manipulator, averages out irregularities in the incident x-ray tube or synchrotron excitation source, but still spends the same amount of time overall to acquire counts for each individual azimuthal data point. (This assumes that such scanning can be done without too great a loss of duty cycle while the mechanism is being moved.)

An additional desirous direction of development is using many (and faster) detectors in a parallel array that would decrease data acquisition times in proportion to their numbers by up to two orders of magnitude. Keeping pace with such detector arrays would then also require brighter sources than the beamlines at second generation synchrotrons, and this should lead to further decreased data acquisition times. Thus, it is possible to envisage taking a single x-ray hologram in a fraction of an hour.

Both faster detector arrays and brighter sources will also enable x-ray holograms to be measured from samples with more dilute concentrations of fluorescing species, whether these holograms are measured in the conventional (XFH) or time-reversed (MEXH) mode. As discussed earlier in Chapter 8, the strained vertical environment surrounding a buried epitaxial δ-layer (*e.g.* Ge in Si as discussed earlier) is one such possibility, with the added benefit that many such δ-layers can be sandwiched between thick layers of bulk support crystal, in order to increase the density of equivalent δ-layer fluorescing emitters available in the sample (Fig. 9.3(c)). The strained environments surrounding fluorescing dopant sites could be imaged (Fig. 9.3(d)).

Other dilute emission systems demanding faster detectors and brighter sources would include surface monolayers such as simple (Fig. 9.3(e)) or complex (Fig. 9.3(f)) chemisorbed molecules containing a monolayer of fluorescing emitters. In order to break the long-range order of the monolayer and thus reduce the presence of sharp Bragg-like

diffraction features, the substrate surface could be miscut slightly so as to introduce terraces and steps, or less than full monolayer coverages could be deposited.

Even more ambitious as an ultimate goal is recording x-ray holograms from, and reconstructing atomic-resolution images of, biological molecules (Fig. 9.3(g)). Despite the demand on maximizing count rates in such an experiment, recording holographic as opposed to conventional x-ray diffraction patterns has several advantages in addition to the fact that the wavefront phases are holographically referenced. The first is that, in order for a conventional x-ray diffraction pattern to be recorded, the molecules must be in a nearly perfect crystal of non-trivial size. As higher molecular weight molecules are studied, this experimental sample preparation task becomes more arduous, especially since a new crystal of the molecule of interest must be formed for each type of heavy ion substituted as part of the phase determination [9.35]. In atomic x-ray holography, only orientational order, and not long-range translational order, is required between the molecules in the sample to be studied. Thus these molecules need not be in near-crystalline order, but can be in a liquid crystal phase, assembled in a membrane, or channeled into an external matrix, as long as the molecules are all oriented in the same way with respect to the detector. The second advantage is that similar to the relationship discussed above between normal electron diffraction analyses and atomic electron holography. That is, *R*-factor analyses between theoretical and experimental conventional x-ray diffraction patterns sometimes cannot easily distinguish the relative best fit between unique structural models. But atomic images reconstructed from holographic x-ray diffraction patterns can yield an immediate *ab initio* structure which can then be refined using conventional *R*-factor analysis of theoretical and experimental holographic x-ray diffraction patterns. Thus atomic x-ray holography could be applied to biological molecules for which suitable single crystals could not be synthesized. For systems with good single crystals, it would also serve as an adjunct, rather than a replacement for, conventional x-ray crystallography.

Despite the additional capabilities of multiple-wavenumber MEXH, the recording of holograms from biological molecules may ultimately prove to be more feasible for single-wavenumber XFH instead. This would be via the development of a free-electron laser (FEL) as a successor to fourth-generation synchrotron sources, where an electron packet is linearly accelerated to highly relativistic speeds before being directly injected into a long terminal undulator magnet. The resulting time-integrated intensity from such an FEL in the x-ray region could be 100 times that from current third-generation x-ray undulators on storage rings. While this intense FEL radiation would very quickly destroy any sample it illuminates, an appropriate spatial array of detectors could enable the recording of the instantaneous holographic fluorescent diffraction pattern emitted from the short-lived sample. A comparable MEXH experiment would require rotating the sample relative to the incident beam, and thus be too slow to be able to take advantage of the unprecedented brightness of FEL radiation as a next-generation radiation source.

As for the theoretical aspects of the future of atomic holography, primary consideration should be given to better modeling of the creation of XFH and MEXH holographic intensities. Current models include only single-scattering of an isotropic reference wave off of idealized point-like atoms. More sophisticated modeling would include the anisotropy of L and M emission source waves in XFH, and corrections to account for the near field excitation of the fluorescing emitter in MEXH [9.37,9.38]. Also, since x-ray scattering factors are relatively well-understood, their effect as slight position shifts in reconstructed atomic images may be corrected for in a SWIFT-like algorithm [9.4].

Also, atomic images may be reconstructed as electron density maps by judicious reinterpretation of the original reconstruction algorithm. This would be more closely parallel to, and permit more direct comparisons with, conventional x-ray crystallography.

Further experimental and theoretical studies should also be made to confirm and extend the results of polarized incident radiation in MEXH. Such future experiments

would at first trivially entail measuring MEXH intensities from the same sample, but for different linearly polarized incident radiation modes, and also recording such intensities for elliptically and circularly polarized incident radiation.

9.4 Concluding remarks

In conclusion, holographic atomic imaging with localized single-atom sources of electrons or fluorescent x-rays promises to become an important structural probe that will complement, or in some respects even surpass, conventional diffraction methods or other atomic structural probes. These holographic methods should be applicable to a wide variety of systems of practical and fundamental interest. X-ray holography of either the single-wavenumber fluorescence type (XFH) or the multiple-wavenumber (inverse) type (MEXH) promises to yield more accurate images due to the more ideal scattering of x-rays, although the much weaker diffraction effects observed with x-rays also present challenges in measurement. However, with brighter sources of x-rays at next-generation synchrotron radiation facilities, and the development of faster detectors in parallel arrays, these experimental problems should be surmountable. Thus, much experimental and theoretical work lies ahead if we are to develop both the electron and x-ray techniques to their fullest potential, but the final fulfillment of Gabor's dream for atomic-resolution holography seems well worth the effort.

References

[9.1] A. Szöke, *Short Wavelength Coherent Radiation: Generation and Applications*, T. Attwood, J. Boker (eds.), AIP Conference Proceedings No. 147, (AIP, New York, 1986) 361.

[9.2] D. Gabor, Nature (London) **161** (1948) 777.

[9.3] (a) J. J. Barton, Phys. Rev. Lett. **61** (1988) 1356, and Phys. Rev. Lett. **67** (1991) 3106. (b) J. J. Barton and L. J. Terminello, paper presented at the Third International Conference on the Structure of Surfaces, Milwaukee, July 1990, and in *Structure of Surfaces III*, eds. S. Y. Tong, M. A. Van Hove, X. Xide, and K. Takayanagi (Springer Verlag, Berlin, 1991), 107. (c) S. Y. Tong, H. Huang, and C. M. Wei, Phys. Rev. B **46** (1992) 2452, and references therein.

[9.4] (a) B. P. Tonner, Z.-L. Han, G. R. Harp, and D. K. Saldin, Phys. Rev. B **43** (1991) 14433. (b) D. K. Saldin, K. Reuter, P. L. de Andres, H. Wedler, X. Chen, J. B. Pendry, and K. Heinz, Phys. Rev. B **54** (1996) 8172.

[9.5] (a) S. Y. Tong, H. Li, and H. Huang, Phys. Rev. B **51** (1995) 1850. (b) H. Wu, and G. J. Lapeyre, Phys. Rev. B **51** (1995) 14549.

[9.6] P. J. Rous and M. H. Rubin, Surf. Sci. **316** (1994) L1068.

[9.7] P. Hofmann, K.-M. Schindler, V. Fritzsche, S. Bao, A. M. Bradshaw, and D. P. Woodruff, J. Vac. Sci. Tech. A **12** (1994) 2045, Surf. Sci. **337** (1995) 169, and references therein.

[9.8] (a) M. T. Sieger, J. M. Roesler, D. S. Lin, T. Miller, and T.-C. Chiang, Phys. Rev. Lett. **73** (1994) 3117. (b) J. M. Roesler, M. T. Sieger, and T.-C. Chiang, Surf. Sci. **316** (1994) L1068.

[9.9] (a) L. J. Terminello, B. L. Petersen, and J. J. Barton, J. Electron Spectrosc. Relat. Phenom. **75** (1995) 229, and references therein. (b) H. Wu, G. J. Lapeyre, H. Huang, and S. Y. Tong, Phys. Rev. Lett. **71** (1993) 251, and references therein. (c) M. Zharnikov, M. Weinelt, P. Zebisch, M. Stichler, H.-P. Steinrück, Surf. Sci.

334 (1995) 114, and references therein. (d) R. Denecke, R. Eckstein, L. Ley, A. E. Bocquet, J. D. Riley, R. C. G. Leckey, Surf. Sci. **331-333** (1995) 1085. (e) J. G. Tobin, G. D. Waddill, H. Li, and S. Y. Tong, Surf. Sci. **334** (1995) 263, and references therein.

[9.10] (a) H. Li, S. Y. Tong, D. Naumovic, A. Stuck, and J. Osterwalder, Phys. Rev. B **47** (1993) 10036. (b) D. K. Saldin, G. R. Harp, and X. Chen, Phys. Rev. B **48** (1993) 8234, and references therein.

[9.11] (a) Z.-L. Han, S. Hardcastle, G. R. Harp, H. Li, X.-D. Wang, J. Zhang, and B. P. Tonner, Surf. Sci. **258** (1991) 313, and references therein. (b) I. H. Hong, S. C. Shyu, Y. C. Chou, and C. M. Wei, Phys. Rev. B **52** (1995) 16884, and references therein.

[9.12] (a) M. A. Mendez, C. Glück, J. Guerrero, P. L. de Andres, K. Heinz, D. K. Saldin, and J. B. Pendry, Phys. Rev. B **45** (1992) 9402, and references therein. (b) C. M. Wei, S. Y. Tong, H. Wedler, M. A. Mendez, and K. Heinz, Phys. Rev. Lett. **72** (1994) 2434, and references therein.

[9.13] S. Y. Tong, H. Huang, and X. Q. Guo, Phys. Rev. Lett. **69** (1992) 3654.

[9.14] S. D. Ruebush, Ph. D. Thesis, University of California at Davis, June 1997.

[9.15] G. R. Harp, D. K. Saldin, X. Chen, Z.-L. Han, and B. P. Tonner, J. Electron Spec. and Relat. Phenom. **57** (1991) 331.

[9.16] T. Greber, J. Osterwalder, Chem. Phys. Lett. **256** (1996) 653, and to be published.

[9.17] E. M. E. Timmermans, G. T. Trammell, and J. P. Hannon, Phys. Rev. Lett. **72** (1994) 832.

[9.18] A. P. Kaduwela, Z. Wang, S. Thevuthasan, M. A. Van Hove, and C. S. Fadley, Phys. Rev. B **50** (1994) 9656, and references therein.

[9.19] R. X. Ynzunza, J. Morais, R. Denecke, in preparation.

[9.20] M. Tegze, G. Faigel, Europhys. Lett **16** (1991) 41.

[9.21] P. M. Len, S. Thevuthasan, C. S. Fadley, A. P. Kaduwela, and M. A. Van Hove, Phys. Rev. B **50** (1994) 11275.

[9.22] M. Tegze and G. Faigel, Nature **380** (1996) 49.

[9.23] T. Gog, T., P. M. Len, G. Materlik, D. Bahr, D., C. Sanchez-Hanke, and C. S. Fadley, Phys. Rev. Lett. **76** (1996) 3132.

[9.24] T. Gog., R. H. Menk, F. Arfelli, P. M. Len, C. S. Fadley, and G. Materlik, Synch. Rad. News **9** (1996) 30.

[9.25] P. M. Len, T. Gog, D. Novikov, R. A. Eisenhower, G. Materlik, and C. S. Fadley, submitted to Phys. Rev. B.

[9.26] W. L. Duax, Int. Union Crys. News. **4** (1996) 1.

[9.27] P. M. Len, C. S. Fadley, G. Materlik, to appear in *X-ray and Inner-Shell Processes: 17th International Conference*, R. L. Johnson, H. Schmidt-Boeckering, and B. F. Sonntag (eds.), AIP Conference Proceedings No. 389 (AIP, New York, 1997).

[9.28] D. K. Saldin, Phys. World **9** (1996) 25.

[9.29] P. N. Fahn, Found. Phys. **1** (1996) 71.

[9.30] S. Nadis, Science **272** (1996) 650.

[9.31] M. Tegze and G. Faigel, private communication.

[9.32] T. Gog, private communication.

[9.33] R. A. Eisenhower, private communication.

[9.34] D. Novikov and G. Materlik, private communication.

[9.35] C. Branden, J. Tooze, *Introduction to Protein Crystallography* (Garland Publishing, New York, 1991).

[9.36] L. Fonda, to be published.

[9.37] L. Sorenson, to be published.

Figure captions

Figure 9.1. Schematic representation of atomic structures that have been fruitfully studied using atomic electron holography, together with their expected reconstructed images. (a) Surface reconstructions. (b) Surface overlayers.

Figure 9.2. *R*-factor analysis curve for 1ML epitaxial Cu on Ru(0001) [9.14].

Figure 9.3. Schematic representation of five types of short-range-order atomic structures that have been or could be fruitfully studied using atomic x-ray holography. (a) Mosaic bulk crystals. (b) Disordered phase alloys. (c) Vertically strained, horizontally epitaxial δ-layers. (d) Strained lattice atoms surrounding dopant sites. (e) Atomic adsorbates. (f) Molecular adsorbates. (g) Rotationally aligned (biological) macromolecules with poor long-range translation order.

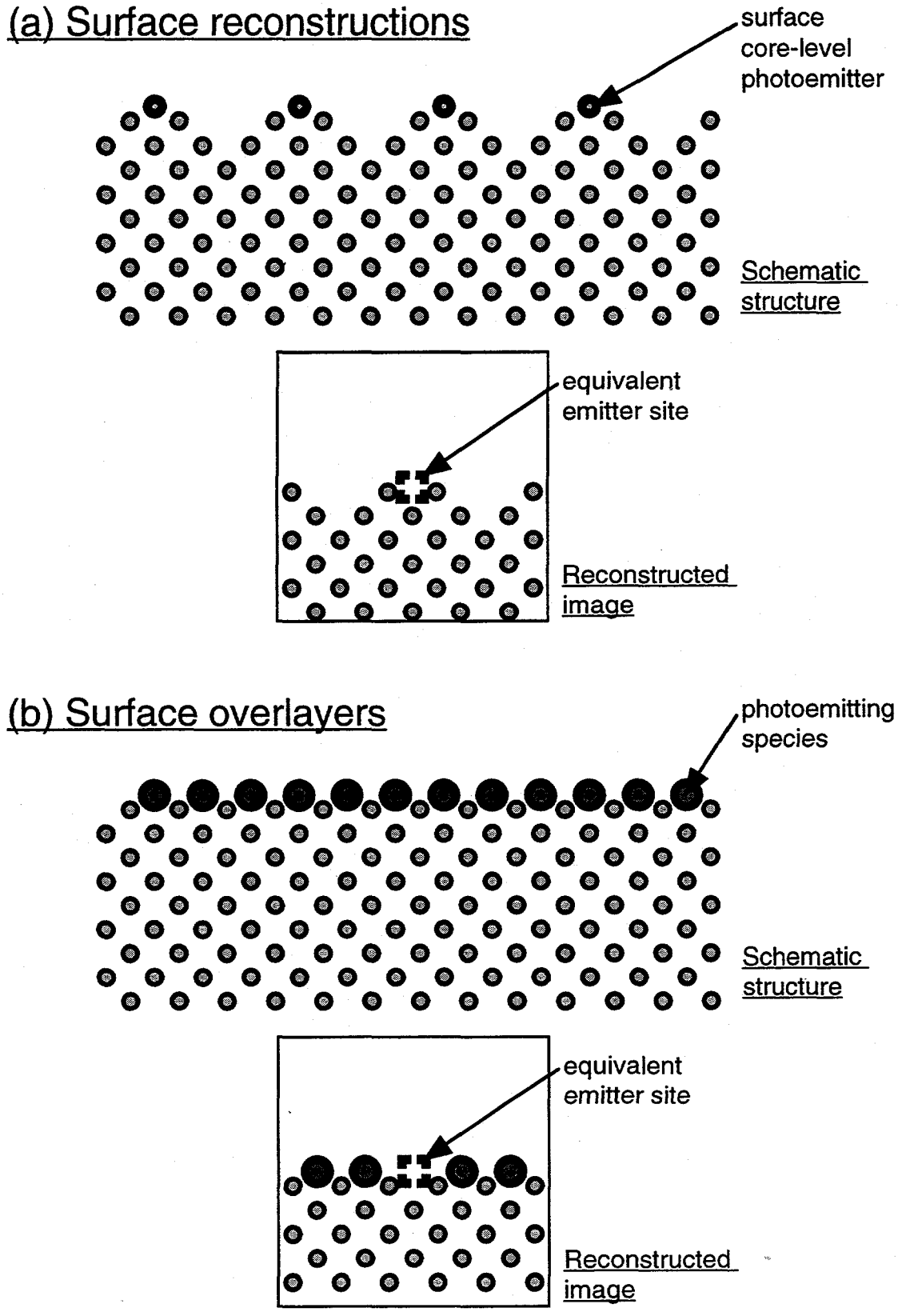

Fig. 9.1

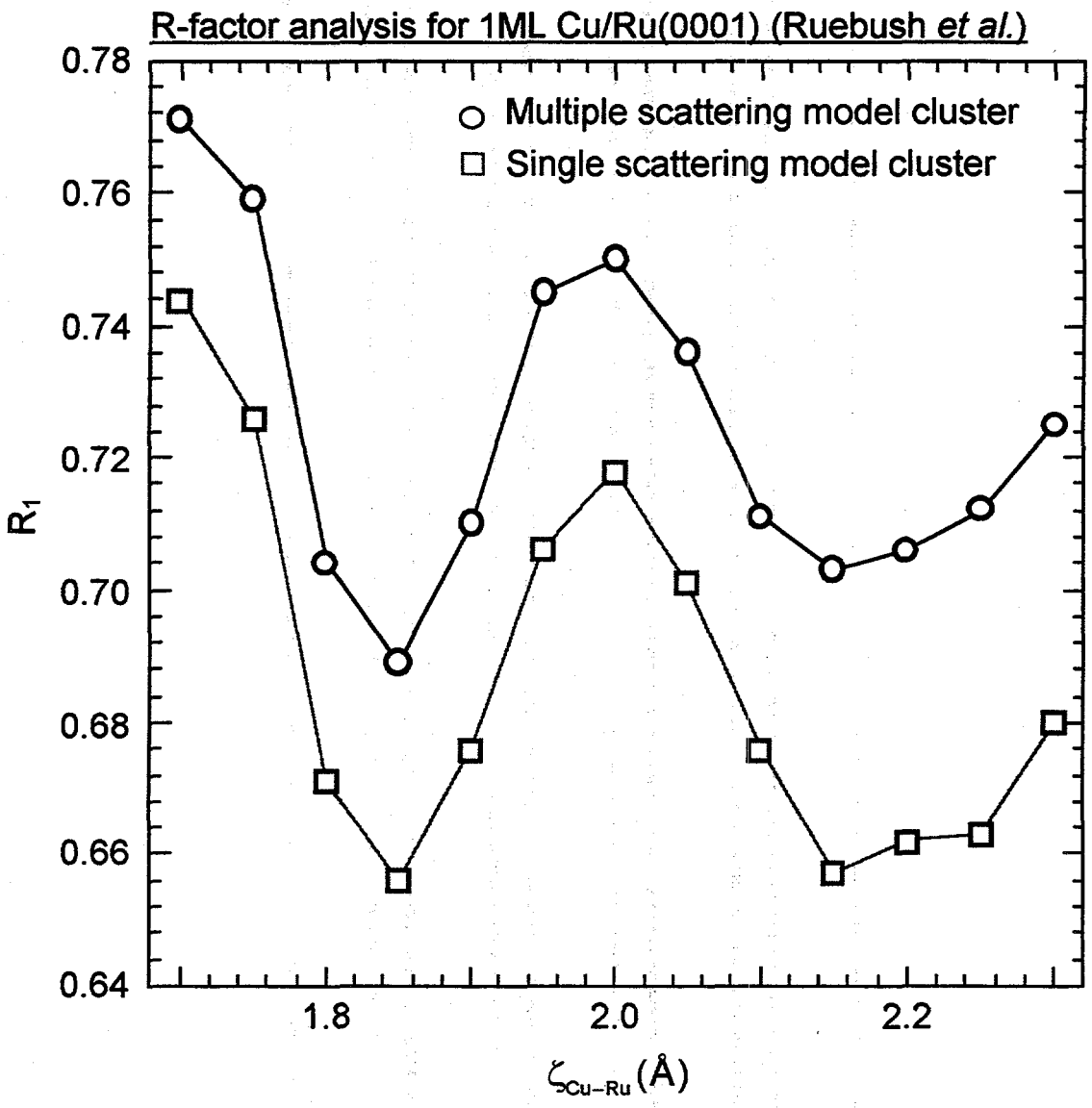

Fig. 9.2

(a) Mosaic crystals

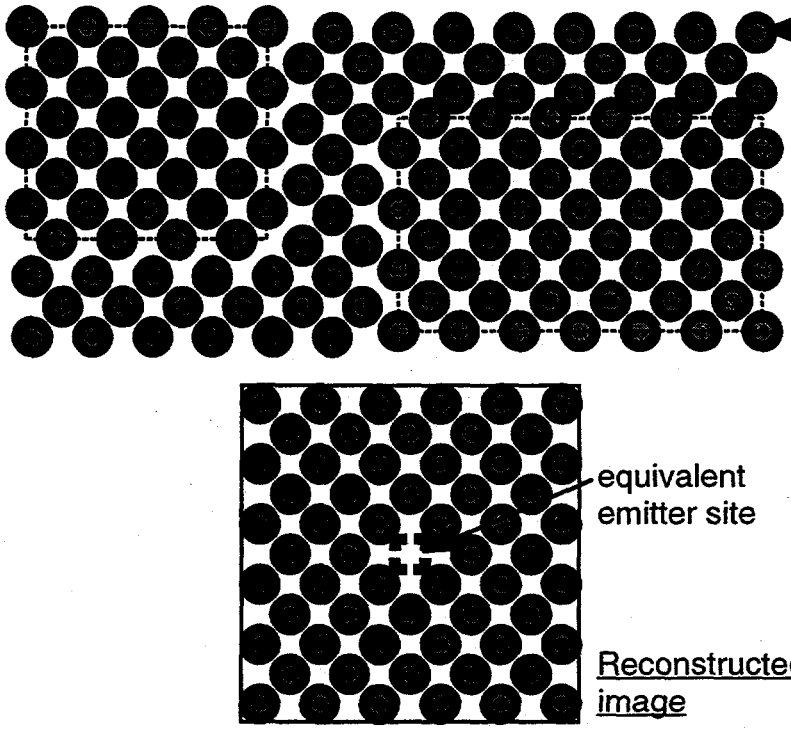

(b) Disordered phase alloys

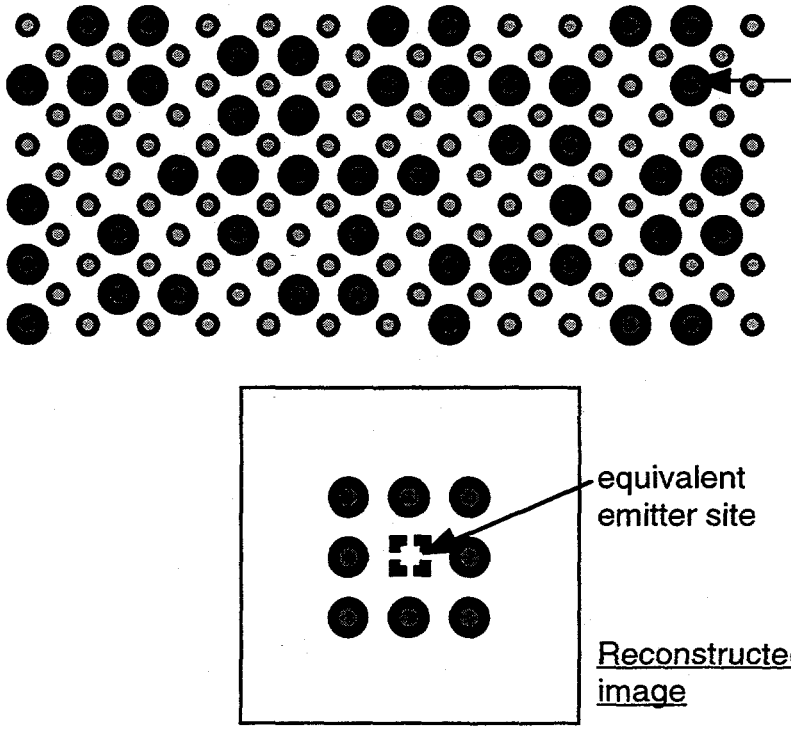

Fig. 9.3(a)-(b)

(c) Epitaxial δ-layers

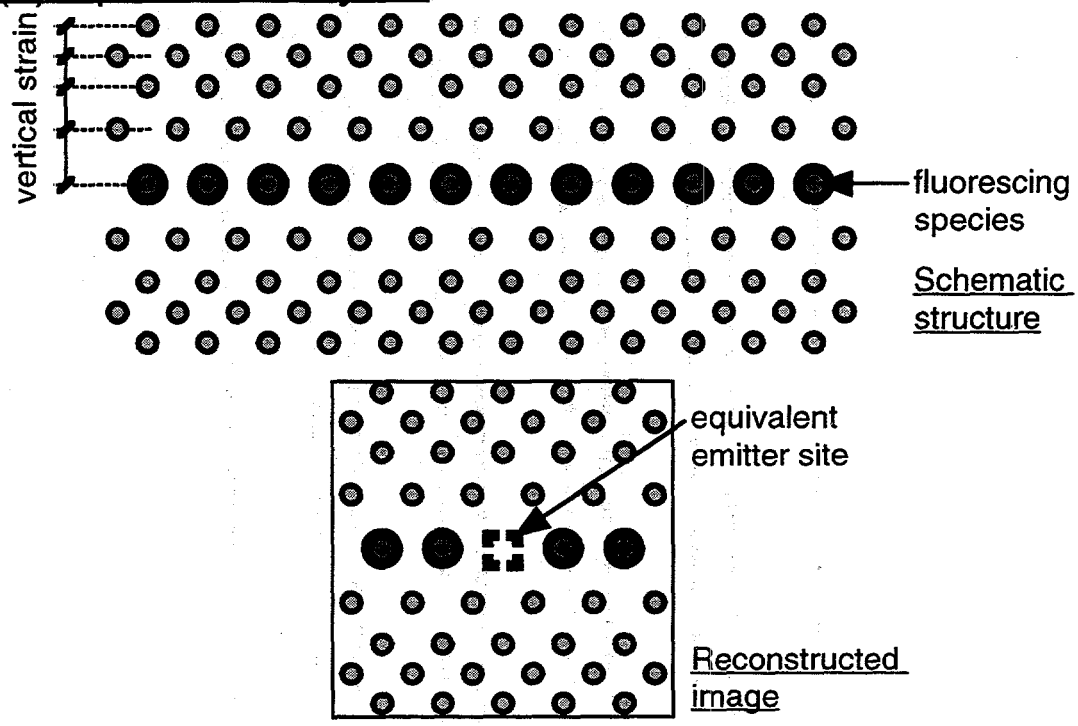

(d) Dopants

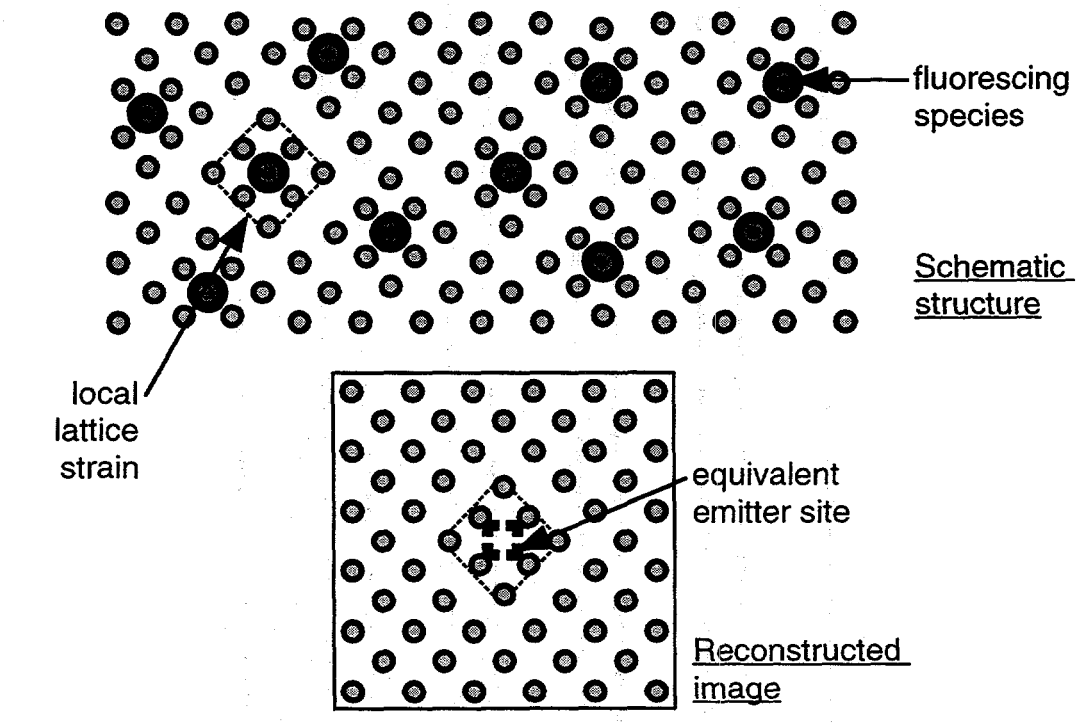

Fig. 9.3(c)-(d)

(e) Atomic adsorbates

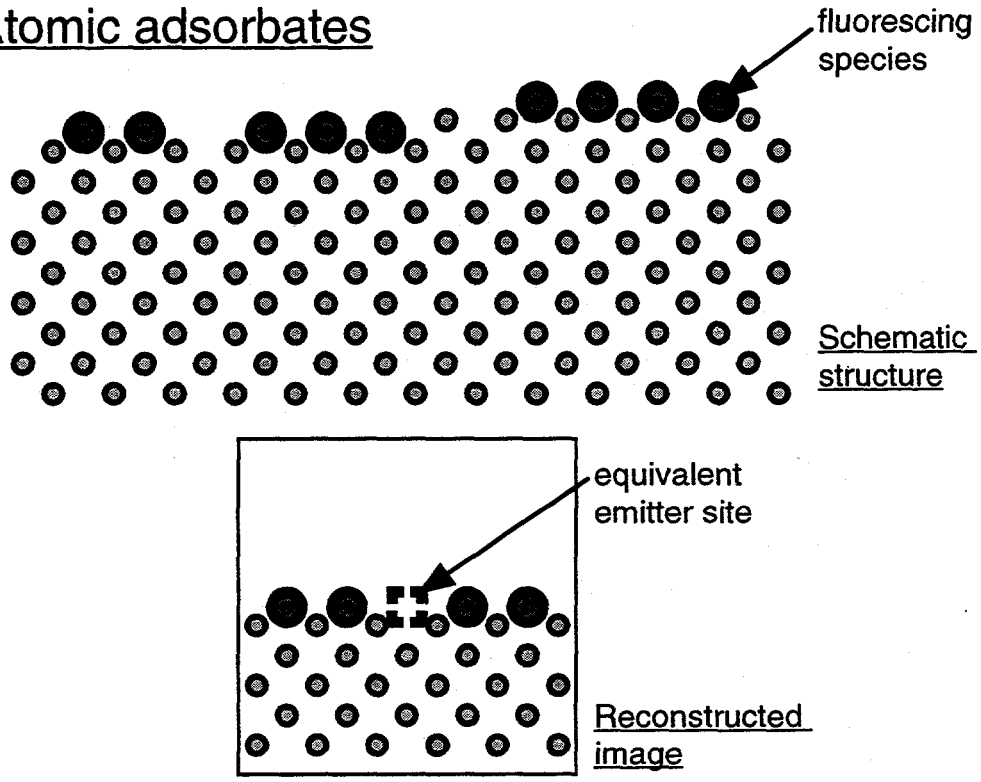

(f) Molecular adsorbates

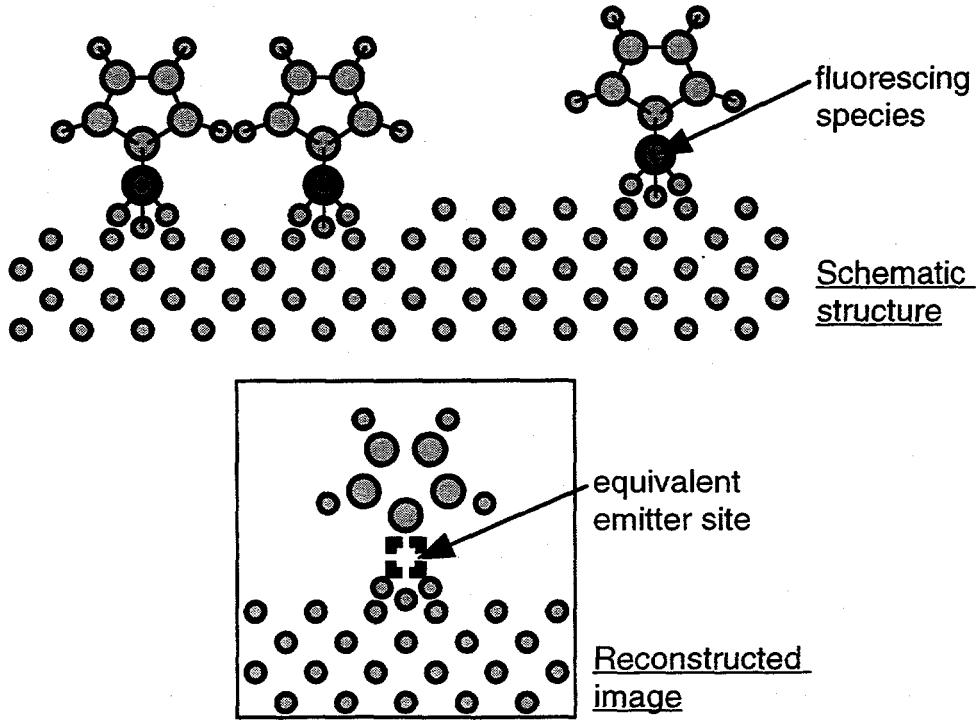

Fig. 9.3(e)-(f)

(g) Biological macromolecules

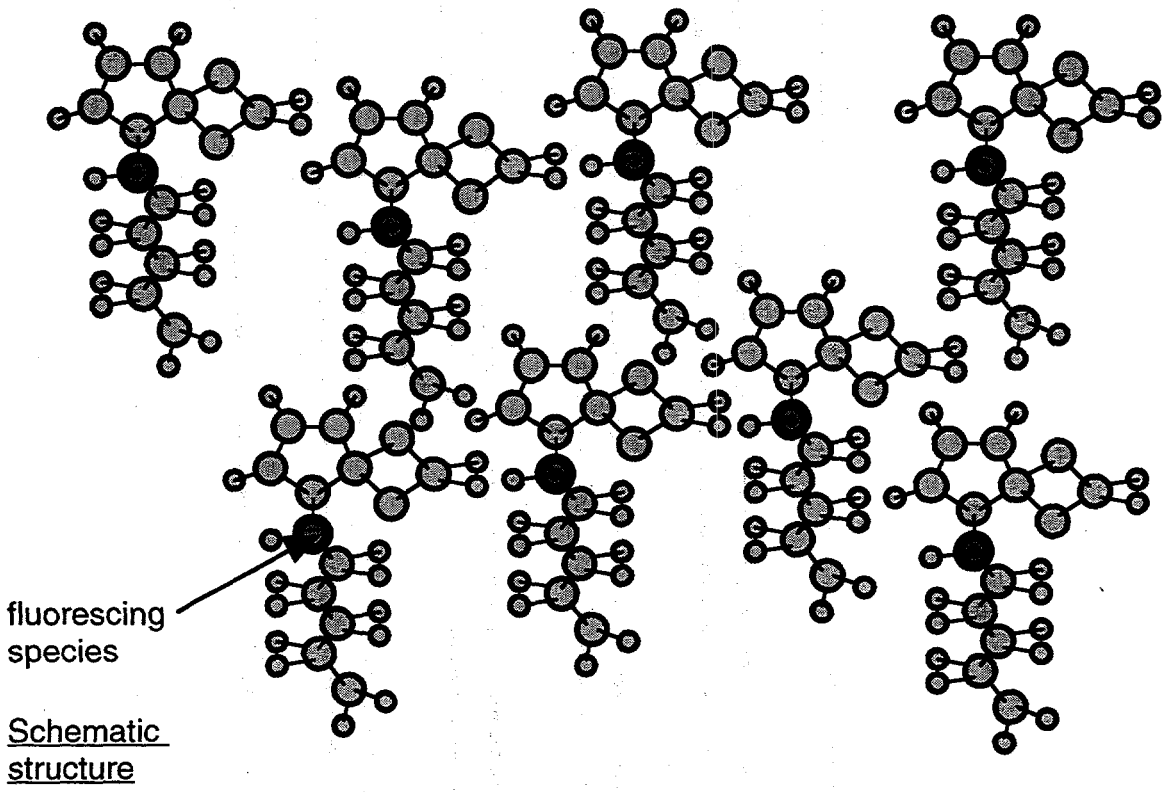

Schematic
structure

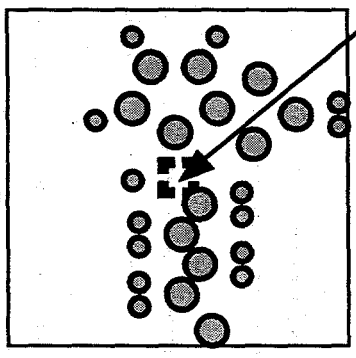

Reconstructed
image

Fig. 9.3(g)